The investigation of 1D nanocrystals confined in carbon nanotubes

Chunyang Nie

Chunyang Nie. The investigation of 1D nanocrystals confined in carbon nanotubes. Material chemistry. Université Paul Sabatier - Toulouse III, 2016. English. NNT : 2016TOU30214 . tel-01540273

HAL Id: tel-01540273
https://theses.hal.science/tel-01540273

Submitted on 16 Jun 2017

THÈSE

En vue de l'obtention du

DOCTORAT DE L'UNIVERSITÉ DE TOULOUSE

Délivré par : Université Toulouse 3 Paul Sabatier (UT3 Paul Sabatier)

Présentée et soutenue par *Chunyang NIE*
Le *23/09/2016*

Titre :

Etude de nanocristaux unidimensionnels confinés dans des nanotubes de carbone

Title :

The investigation of 1D nanocrystals confined in carbon nanotubes

---

ED SDM : Sciences et génie des matériaux - CO034

Unité de recherche :

UMR 5085 CIRIMAT - Centre Interuniversitaire de Recherche et d'Ingénierie des Matériaux
UPR 8011 CEMES-CNRS - Centre d'Elaboration des Matériaux et d'Etudes Structurales

Directeur(s) de Thèse :
Dr. Emmanuel FLAHAUT, Dr. Marc MONTHIOUX

Rapporteurs :

Dr. Brigitte VIGOLO	Institut Jean Lamour	Université de lorraine
Dr. Chris EWELS	Institut de Matériaux Jean ROUXEL	Université de Nantes

Autre(s) membre(s) du jury :

Prof. Alfonso SAN MIGUEL	Université Lyon 1	Président
Prof. Manitra RAZAFINIMANANA	Université Paul Sabatier	Examinateur

Acknowledgements

First and foremost I would like to thank my two supervisors Dr. Emmanuel Flahaut and Dr. Marc Monthioux for their guidance, support and assistance on the research during the last three years, especially the time they gave in the preparation of this thesis during the summer holiday.

I would like to thank Dr. Anne-Marie Galibert and Dr. Brigitte Soula for their help with my experimental work and the discussions with the experimental results.

I wish to acknowledge Dr. Chris Ewels and Dr. Brigitte Vigolo for taking their valuable time to be the Rapporteurs of the thesis, and their comments and remarks on the thesis. I also wish to acknowledge Prof. Alfonso San Miguel and Prof. Manitra Razafinimanana for participating in the jury.

I wish to acknowledge the grant of Chinese Scholoarship Council (CSC) for supporting my PhD study in France.

I wish to acknowledge Dr. Christophe Laurent, Dr Claude Estournes and all Nanocomposites Nanotubes de Carbone team: Dr. Alicia Weibel, Dr. David Mesguich and Professor Alain Peigney in Centre Inter-universitaire de Recherche et d'Ingénierie des Matériaux (CIRIMAT) and Dr. Etienne Snoeck in Centre d'élaboration de matériaux et d'études structurales (CEMES) for giving me the best ambiance and conditions in the lab during my PhD.

I also would like to express my big thank you to Sébastien Joulié and Florent Houdellier for their help with the training on the various kinds of transmission electron microscopes in CEMES, as well as their efforts to maintaining the good running of the microscopes (TEM). Without the microscopes, I could hardly finish my PhD study.

I would like to thank Laure Noé in CEMES for her help with the preparation of TEM grid at the beginning of my thesis and her help with the operation of CM30. Then I would like to thank Lucien Datas in Centre de microcaractérisation Raimond Castaing for the help with taking beautiful TEM images of my samples with the powerful JEOL JEM-ARM200F.

I would like to thank David Neumeyer in CEMES for spending time helping with the sulfurization experiments, discussing with my experiment results and giving me good advises.

I would like to thank Aurélien Masseboeuf for taking time to making holograms of my sample, processing the holograms and explaining me the results. Though nothing interesting has been found thus far, it was a good exploration and experience for me.

I would like to thank Dr. Escoffier Walter and his PhD student Yang Ming in Laboratoire National des Champs Magnétiques Intenses (LNCMI) and Dr. Benjamin Lassagne in Laboratoire de Physique et Chimie des Nano-objets (LPCNO) for their help with the measurements of electrical conductivity of my samples. Though the measurements are still in processing and the full datas are not possible to be represented in this thesis, their work is valuable to my PhD project.

I would like to thank all my colleagues in CIRIMAT (Pierre Lonchambon, Jean François Guillet, Thomas Lorne, …) and in CEMES (David Reyes, Juan Du, Rongrong Wang, Tian Wang, Tingting Xiao, Xiaoxiao Fu, …) for their help and the good time we spent together.

Finally, I would like to thank my family for their support and encourage during all these years.

Amicalement,

Chunyang
Toulouse, France

Table of contents

List of Abbreviations

ADF	Annular dark field
BF	Bright field
BNNTs	Boron nitride nanotubes
CCVD	Catalytic chemical vapour deposition
c-MWCNTs	Concentric multi-walled carbon nanotubes
CNTs	Carbon nanotubes
DWCNTs	Double-walled carbon nanotubes
EELS	Electron energy loss spectroscopy
FWCNTs	Few-walled carbon nanotubes
HAADF	High angle annular dark field
HRTEM	High-resolution transmission electron microscopy
MWCNTs	Multi-walled carbon nanotubes
c-MWCNTs-a	Concentric multi-walled carbon nanotubes prepared by arc discharge
h-MWCNTs	Herringbone multi-walled carbon nanotubes
PDF	Pair distribution function
STEM	Scanning transmission electron microscopy
SWCNTs	Single-walled carbon nanotubes
TEM	Transmission electron microscopy
X-EDS	X-ray energy-dispersive spectroscopy
XPS	X-ray photoelectron spectroscopy
XRD	X-ray diffraction

General Introduction

Carbon nanotubes (CNTs) have attracted since 1991 a lot of attention from the scientific community mainly due to their remarkable physical properties. Most of the current interest is focused on the practical applications of CNTs. To actually use them in various applications, it is often necessary to modify the CNTs in various ways. One of these ways may be to fill them with foreign materials, so that the properties of the host CNTs would be modified due to the interaction with the filling material. Moreover, the templating effect provided by the inner elongated cavity of -CNTs can enforce the inserted materials to adopt a 1D morphology, thus making filling CNTs an alternative route to synthesize 1D nanocrystals/nanowires. Meanwhile, when foreign materials are confined within a limited space, chances are high that deformation of the lattice structure, or even formation of new structures may occur for the encapsulated materials. These possibilities to induce new behaviours or new properties are more likely to occur if the inner cavity of the nanotube is smaller. Therefore, filling single-wall CNTs (SWCNTs) or double-wall (DWCNTs) – which may have an even smaller inner diameter – should be preferably considered as their inner cavity is typically below ~2 nm.

Filling CNTs to prepare X@CNTs hybrids can be achieved by various means and among them the molten phase method is widely employed due to the possibility for high filling rates, simplicity and versatility. Filling CNTs with a liquid is driven by the capillary force generally described by the Young-Laplace equation, but the detailed mechanisms involved in the capillarity filling of CNTs are not clear yet because they depend on different parameters such as the requirement of opening of the nanotubes, the inner diameter and the fact that the wetting properties of CNTs should depend on the texture of the inner tube (concentric tubes, or the so-called herringbone organization).

Even if very simple on the principle, not all compounds can be introduced by the molten phase method due to intrinsic incompatibility (chemical, physical) between the material and the CNTs, or technical limitations of the experimental procedure. To overcome this problem, the strategy of applying post-treatments to CNTs filled with a precursor of the target material can be used. In this way, the synthesis of, for example, metals or sulphides (otherwise generally presenting drawbacks fatal to filling such as poor wetting of CNTs, possible chemical reaction with the host tube, too high melting point… if tentatively directly inserted) nanowires, may be prepared. This work thus aimed to better understand the basics of filling nanotubes with molten materials as well as the mechanisms of chemical reactions performed *in situ* in the inner cavity of the nanotubes. With such a goal, metal iodides have been selected as model compounds because they combine well-matching physico-chemical properties with the high electronic density of iodine, making this element particularly easy to image by high-resolution transmission electron microscopy (HRTEM), a central tool in this work.

Investigations on the properties of individual X@CNT hybrids are quite appealing since the properties of the inserted nanocrystals are expected to differ from that of the bulk material because of their likely different structure, high anisotropy, and surface atoms/core atoms ratio far different from ~0. These potential new properties may also be transferred to the CNTs. Unfortunately, examples of characterisation of such nanostructures is still relatively scarce in the literature, possibly because the facilities and devices for measuring properties of filled CNTs at the microscopic level are not so accessible, or more likely because it is difficult to ensure that the measured nanotube is indeed filled.

This PhD manuscript thus consists of 3 chapters. **Chapter 1** is a general introduction to the filling of carbon nanotubes, describing the state of the art of filling strategies, as well as reporting some examples of properties and applications of filled CNTs. **Chapter 2** reports our investigations (i) of the filling mechanisms when using the molten phase method by considering a variety of filling halide materials (with a focus on iodides and iodine) as well as a variety of host nanotubes (with a focus on DWCNTs) with molten compounds and (ii) of the resulting peculiar X@CNT hybrid nanostructures, with the help of HRTEM, and scanning transmission electron microscopy (STEM) techniques, as well as local probe electron energy loss spectroscopy (EELS). **Chapter 3** deals with three different attempts of *in situ* transformations of selected X@DWCNTs: (i) the *in situ* sulfurization of PbI_2@DWCNTs, (ii) the *in situ* H_2-reduction of FeI_2@DWCNTs and NiI_2@DWCNTs, and (iii) the *in situ* fluorination of FeI_2@DWCNTs. Finally, a general conclusion summarises our results and present our perspectives, in particular the work in progress related to the characterisation of X@DWCNTs hybrids, which could unfortunately not be included in this manuscript.

Chapter 1 General Introduction to Filled Carbon Nanotubes

In 1991, a paper published by Iijima in Nature [1] presenting unambiguous proof of multi-walled carbon nanotubes (MWCNTs) which was discovered in the hard deposit growing at the cathode during electric arc experiments to produce fullerenes had a huge impact on the scientific community back then. Before that, most scientists did not give a second thought to ‘nano’. Ironically, MWCNTs had already been known as early as 1950s [2, 3], and for decades they were merely regarded as hollow carbon filaments - the undesirable byproducts to remove from the processing in the coal and steel industry and also in the nuclear industry. Subsequently in 1993, another work by Iijima with Ichihashi as the co-author reporting the synthesis of single-walled carbon nanotubes (SWCNTs) was published [4]. It is interesting to point out that another team, from IBM, California [5] also reported the formation of SWCNTs at the very same time as the Japanese team. Since then, scientists have devoted their attention to the research on the unique properties of CNTs and the exploration of their applications.

Up to now, many aspects concerning CNTs have been developed maturely. For instance, the synthesis routes for large-scale and diameter-controlled production are well established and supplied commercially, theories to predict various properties of CNTs are well supported by experimental results. Therefore, more and more attention are paid to the actual integration of CNTs in devices and their incorporation in advanced materials and crafts of practical interest. Unfortunately, many challenges with respect to the poor dispersibility, solubility, etc. of CNTs are needed to overcome. One alternative is to modify the CNTs in various ways including adding groups to the surfaces or inserting materials into the cavity and so on. Through the modification, more versatile CNTs are obtained and exhibit more fascinating properties, which can be considered as a third-generation of carbon nanotubes. This new generation of CNTs is named “meta-nanotubes” which is classified into five main categories [6]: functionalized nanotubes (denoted as X-CNTs), decorated nanotubes (denoted as X/CNTs), doped nanotubes (denoted as X:CNTs), filled nanotubes (X@CNTs) and heterogeneous nanotubes (X*CNTs), where X refers to the foreign components associated with nanotubes and which can be chemical functions, phases, atoms or molecules. Compared with the other four kinds, filled nanotubes can be seen as a complement to the full exploitation of the spaces in nanotubes as it only deals with inner cavities. In this manuscript, the subject is focused on the synthesis of X@CNTs, the mechanism of filling CNTs and some related properties of X@CNTs.

1.1 Carbon Nanotubes

To understand the structure of carbon nanotubes, it is better to begin with the simplest one – single-walled carbon nanotubes (SWCNTs). Let us image rolling a graphene sheet, a single-atom-thick hexagonal lattice of sp^2-hybridized carbon atoms, into a cylinder and then adding two hemifullerenes to the two ends of the cylinder to close it. Of course, there are many ways to roll up the graphene into a cylinder thus the indices proposed by Hamada *et al.* [7] to describe the various kinds of SWCNTs are quite useful. As illustrated in Fig 1.1, if the cylinder is formed by overlapping the O atom with the A atom in another ring in the graphene, the helicity vector $\overrightarrow{C_h}$ which is equal to OA can be decomposed into two vectors parallel to the graphene lattice vectors $\overrightarrow{a_1}$ and $\overrightarrow{a_2}$ described in Eq. 1.1:

$$\overrightarrow{C_h} = n\overrightarrow{a_1} + m\overrightarrow{a_2} \tag{1.1}$$

where n and m are Hamada's indices counting the number of hexagons crossed by each vector and $|\overrightarrow{a_1}| = |\overrightarrow{a_2}| = 2.46$ Å = a (the graphene basis [8]). Hence a (5, 2) SWCNTs is formed in Fig 1.1.

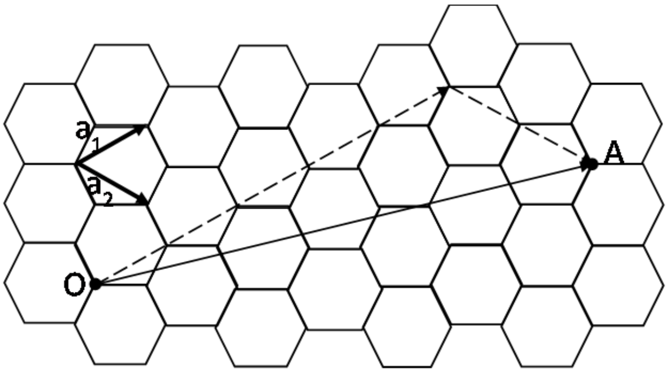

Fig 1.1 - Illustration of how to define a SWCNT by rolling up a graphene sheet with Hamada's indices.

When n is equal to m or n is nil or m is nil, in which case $\overrightarrow{C_h}$ is parallel to one of the symmetry planes of the graphene, two specific nanotubes can be generated: armchair (n=m) and zigzag (n or m=0). Both types of nanotubes possess mirror symmetry and thus are achiral while those tubes with n≠m≠0 are called chiral (Fig. 1.2).

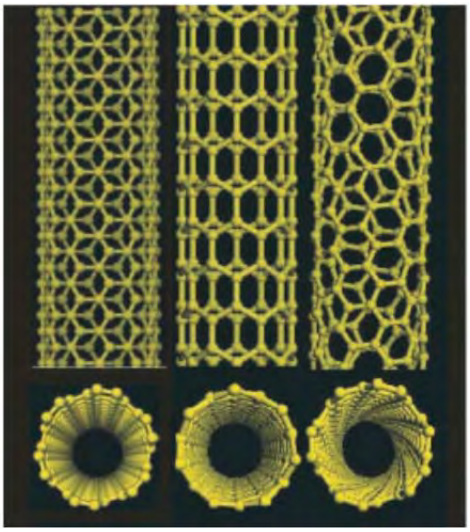

Fig. 1.2 - Examples of three types of SWCNTs, from left to right are armchair, zigzag and chiral, respectively [9].

If we roll several stacked graphene sheets into a cylinder, then a multi-walled carbon nanotube (MWCNT) with concentric texture is obtained. In the case of two rolled graphene sheets, a double-walled carbon nanotube (DWCNT) is formed which can be seen as the intermediate between SWCNTs and MWCNTs that possesses the advantages of both CNTs (Fig. 1.3).

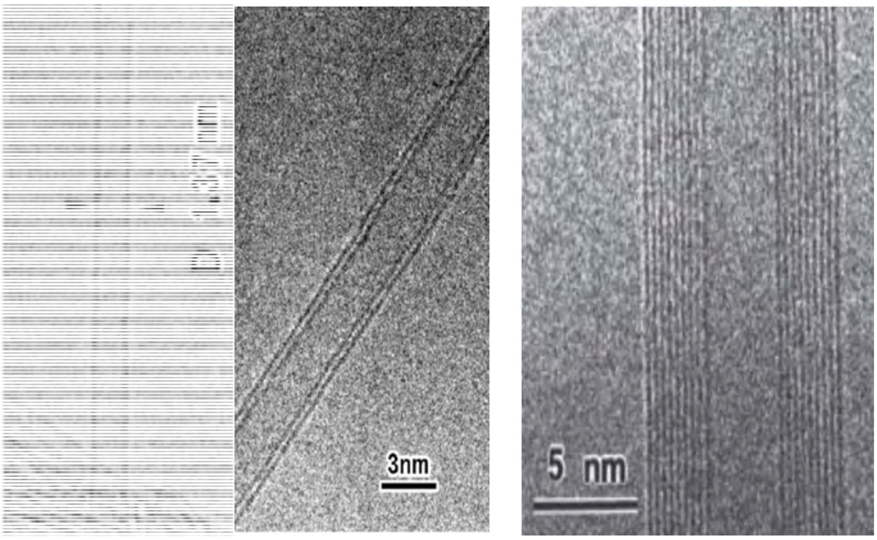

Fig. 1.3 - TEM images of three types of CNTs, from left to right are SWCNTs, DWCNTs and concentric-type MWCNTs, respectively [4, 9, 10].

1.2 Filled Carbon Nanotubes

1.2.1 A Glimpse at the History of Filling CNTs

When MWCNTs became the research focus for physicists, chemists, material scientists and even mathematicians, some attention was paid to the possibility of filling the inner cavity of MWCNTs with various foreign elements or compounds–mainly metals aiming at the synthesis of nanowires. Theoretically, driven by the capillary force the filling can be achieved considering the MWCNTs as nanostraws with diameter in the range of 10-50 nm and the calculations based on Young-Laplace equations predicted the threshold of surface tension for the inserted materials [11, 12] although the validity of this approach in this case can be discussed. In this context, several examples of filling arc-produced MWCNTs were reported in 1993 [13-17]. However, the filling scarcely occurred over length higher than 100 nm for most filled tubes, possibly related to the fact that once the inner hydrostatic pressure equilibrates the outer pressure the filling event stops. Meanwhile, a two-step method including a pre-opening process using oxidizing gas phases [13, 15] or oxidizing acids [18] and then a filling process was proposed. However, studies involving the two-step method came with some problems, such as low filling rates, limited number of species as filling materials, or irreversible damages to the nanotubes. To overcome these drawbacks, *in situ* filling attempts were made which were approached by mixing metal-containing compound like metal oxide [17] or metal carbide [14] with the graphite anode within the arc reactor. In this way, the compounds were encapsulated inside MWCNTs during their growth process. When pure transition metals (Ni, Co, etc.) were selected, SWCNTs were unexpectedly produced [4, 5], making a breakthrough for the scientific community.

Compared to MWCNTs, the diameters of SWCNTs are more than one order of magnitude smaller (typically 1.4 nm) which can be seen as truly nano-world objects. Consequently, the interest in filling SWCNTs is much greater than that previously shown for filling MWCNTs. In spite of the efforts made by researchers from different laboratories, it took five years after the first filling of MWCNTs for the first successful encapsulation of Ru by SWCNTs to be published by University of Oxford [19] (Fig.1.4a), immediately followed by the discovery of SWCNTs filled with fullerenes (‘peapods’) resulting from the collaboration between University of Pennsylvania and CEMES in France [20] (Fig.1.4b). In the former case, a mild process with concentrated HCl solution was used to open the SWCNTs first and then $RuCl_3$ compound was deliberately introduced into SWCNTs via a wet chemistry method; a subsequent reduction in a H_2 stream was carried out in order to get Ru metal. However, the displayed transmission electron microscope (TEM) images (Fig. 1.4a) were confusing as isolated filled SWCNTs instead of ropes of SWCNTs are hardly seen thus making it difficult to tell whether the filling occurred in the cavity of SWCNTs or in the interstitial space in the ropes, as well as to tell whether the ends of tubes were open. Later, the Oxford team modified the filling conditions by soaking the pristine SWCNTs into molten mixtures of KCl-UCl_4 or AgCl-AgBr [21]. Surprisingly, continuous crystals filling the tubes were found in abundance for both mixtures as evidenced by high resolution TEM (HRTEM) images. Subsequently, various halides including lanthanide halides $LnCl_3$ [22], alkali iodides [23-27], $ZrCl_4$ [28], $AgCl_xI_{1-x}$ [29] etc. were attempted to fill SWCNTs or DWCNTs by this team. In 2001, Mittal *et al.* [30] performed the filling of SWCNTs with chromium oxide at room temperature, which is the first example of filling SWCNTs with oxides. Another example of Sb_2O_3-filled SWCNTs [31, 32] was reported by Oxford in the same year. Following the two studies, other oxides and hydroxides (KOH and CsOH [33]) were also introduced into SWCNTs, sometimes with a quite high filling rate (e.g. 80-90% for PbO). However, as most oxides have low solubility in harmless solvents or high melting point, they are not as favorable as halides for filling. Nitrates, on the other hand, were also popular compounds for filling SWCNTs. One interesting example reporting SWCNTs filled with double-helix chains of iodine by Fan *et al.* [34] should be noted here, which was the pioneering work on filling CNTs with atoms. Intriguingly, in their previous study [35], the authors only investigated the effect of iodine-doping on SWCNTs materials, not realizing that the molten iodine can help opening the ends of SWCNTs thereby entering the SWCNT cavities. Based on this research, a similar structure was assumed for encapsulated Cs chains prepared later [36]. However, due to the limited resolution of TEM achieved at that time, iodine chains were not so unambiguously observed and the following studies using similar methods as in [34] more or less focused on the charge transfer between iodine and CNTs through other characterizations rather than imaging iodine chains directly [37-40]. It is only in 2007 that Guan *et al.* demonstrated single, double or even triple chains of iodine confined in SWCNTs by means of HRTEM technique [41]. Recently, the formation of other atom chains (sulfur chains [42] and selenium chains [43]) encapsulated within SWCNTs or DWCNTs was also reported.

The story for peapods (C_{60}@SWCNTs) is different. Though reported in the same year as $RuCl_3$/Ru@SWCNTs, they were not deliberately synthesized but were actually by-products from the purification and annealing treatments on raw SWCNTs materials produced from the pulsed laser vaporization method (PLV) [20, 44-46]. These spontaneously formed peapods during the post synthesis process were questioned for a while, as the spontaneous formation could also be achieved during the synthesis of SWCNTs within plasma when arc discharge method was used [47, 48]. As a result, attempts to prepare C_{60}@SWCNTs with a controlled synthesis were made by annealing the mixture of acid-treated SWCNTs and fullerenes in vacuum which led to much higher filling yield of 50-100% [49-53] than that for peapods produced during regular SWCNTs synthesis (less than 10%) [46, 48].

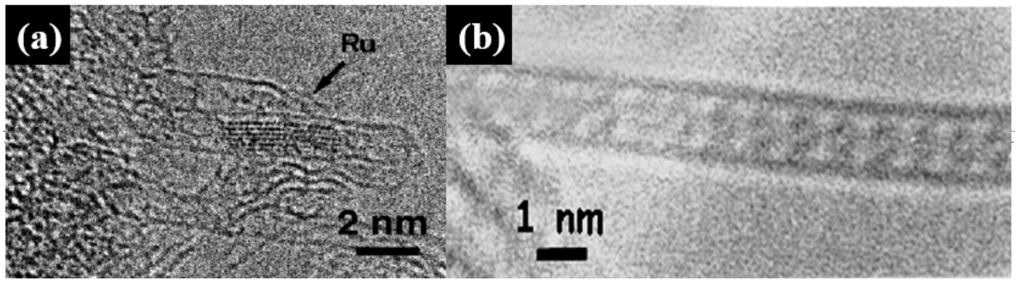

Fig. 1.4 - TEM images of the two firstly reported examples regarding to filling SWCNTs in 1998 (a) Ru@SWCNTs, the metal Ru was reduced from the initially introduced $RuCl_3$ [19]; (b) C_{60}@SWCNTs (peapods) [20].

Beyond these experimental fillings, some 'virtual' filling examples are simulated on the basis of theoretical calculations. For instance, by modeling the confinement of water in SWCNTs, new ice phases not seen in bulk ice and a solid-liquid critical point are suggested [54]. Likewise, the insertion of Na and K atoms [55] or DNA molecules [56], the formation of metals nanowires or semiconductor nanowires within SWCNTs [57-62] and related properties are predicted using ab initio molecular dynamics simulations or other simulations. It should be pointed out that the fillings of these materials are actually performed either with MWCNTs without exhibiting intriguing behaviors or with SWCNTs/DWCNTs but nanowires are not obtained in that case.

Apart from introducing solid and liquid into CNTs, filling CNT with gases is also reported but considered as a controversial issue. Those works dealing with the filling of hydrogen are inspired by the potential applications of CNTs as H_2 containers [63, 64], while other gases are rarely attempted for filling but Xe [65], O_2 and N_2 [66]. However, several possible sites including inner cavities in CNTs contribute to the absorption of gas molecules and the exact location of the absorbed molecules is unable to be demonstrated so far. Therefore, details about the filling with gases will not be introduced in following sections.

1.2.2 The Motivations with Filling CNTs

What makes filling CNTs so special? Firstly, the inner cavity of nanotubes can act as a template or ‘nanomould’, and/or as a ‘nanoreactor’ (i.e. for the chemical transformation of an inserted material) for the synthesis of nanomaterials. Due to the confinement situation in CNT cavity, inserted materials are enforced to adopt the one-dimensional (1D) morphology. Especially, the templating of SWCNTs or DWCNTs can promote the formation of 1D materials with very small diameter and high aspect ratio. Furthermore, the encapsulation of CNTs is found to be a shelter for the contained materials from reactions with the surrounding medium, typically oxidation by contact with air, as well as dissolution of the confined material in aqueous or non-aqueous solvents. In this regard, filling CNTs is considered as a possible approach to obtain nanowire-like materials that could never exist if not encapsulated. Indeed, it has been demonstrated that metallic nanowires of 1 nm in diameter would rapidly turn into oxide nanowires or would even possibly collapse when attempting to remove the carbon sheath from filled SWCNTs [67]. In both cases, the possibility of losing any peculiar property is high. In general, phase growth within a very confined space offers a chance to enforce and stabilize new combinations of chemical elements, novel crystal structures for regular chemical phases and to deform and stress lattices within regular structures.

Once new 1D nanomaterials are formed, new, alter or enhanced physical properties are anticipated for them. The latter expectation arises from the stabilization of otherwise impossible new chemical compositions, structures or morphologies. Typical examples includes (i) the ballistic transport behavior from the one-dimensional structures, which prevents electron scattering; (ii) the immense surface-atom to core-atom ratios, which may even reach an infinite value, (e.g. all the atoms of the structure can effectively be ‘surface atoms’), and (iii) the protection by the carbon shell from the disturbance of absorbed molecules on the surface. Representative expectations and achievements benefit from nanowires prepared from magnetic elements or compounds and charge-transfer electronic interactions with the encapsulating graphene lattice and the guest materials.

In an opposite manner, in case the encapsulated phases do not exhibit any peculiar property, filling can then be utilized as a special approach for external reactants to access the filling materials, thus controlling the behavior of the latter by controlling the interaction kinetics with the surrounding medium. However, there is a risk that the chemical reactivity of the filling material may be more or less inhibited despite of the nanosize as a result of the presence of the carbon sheath. On the other hand, this modified behavior relating to chemical reactivity may occur in a positive manner for some applications, for example, slowing down diffusion kinetic and/or chemical reactivity may be very valuable in fields such as chemical catalysis, drugs or pesticide delivery, and so on.

Overall, new phases, new structures, new properties, and/or new behaviors are very likely to be induced by confining foreign materials in CNTs. More specifically, any of these features will be more likely if the size of the tube cavity is smaller. Hence, filling SWCNTs and DWCNTs whose inner cavity is generally below 2 nm is preferably considered for scientists and the examples given below are mainly related to filling SWCNTs/DWCNTs.

1.2.3 Filling Strategy

Generally speaking, there are two possible routes for filling CNTs at present, in-situ filling and ex-situ filling. For ex-situ filling route, guest materials can be introduced into CNT cavities as a liquid or vapour depending on their physical properties including solubility, melting point, boiling point and of course, decomposition temperature, which should not be reached. Thus, two popular methods employed during the ex-situ filling process are the gas phase method and the liquid phase method. Details about the filling strategy are described in the following sections.

1.2.3.1 In Situ Filling Route

Filling nanotubes in situ is interesting because the filling and growth of CNTs is integrated into a one-step synthesis procedure. In this way, the nanotube sheath remains intact and, depending on the synthesis process, closed (for arc-prepared CNTs) or opened at one end only (for CCVD-prepared CNTs) are formed, consequently isolating as much as possible the encapsulated material from the surrounding post-synthesis environment. Meanwhile, elements with high melting point or high surface tension which are unfavorable for filling by wetting methods (see next) are sometimes allowed to fill CNTs through in-situ routes.

In fact, in-situ filling mainly occurs spontaneously during the synthesis of MWCNTs, either during the electric arc process [68] or the CCVD process [69]. For the latter, specific conditions are required to trap and encapsulate the excess metal catalyst which is critical for growing nanotubes, thereby making it limited. Because catalysts for carbon formation are typically transition metals such as Co, Fe and Ni, metal-filled MWCNTs can be synthesized this way (Figs. 1.5 a and b). Examples involving encapsulation of other materials such as Mg_3N_2 [70], Sn [71], Ge [72], Cu [73] and Fe_3C [74] by the CCVD method can also be found in the literature. However, since most catalysts used for CNTs are ferromagnetic metals, in this sense this method can be taken as an efficient way to produce ferromagnetic nanowires encapsulated in nanotubes [69, 75-78] otherwise difficult to obtain (see next).

In an electric arc process, first the powder of the desired element or the mixture of it with graphite is compacted into a coaxial hole drilled within the graphite anode, then the electric arc is run under conditions similar to that used to produce fullerenes and finally partially filled MWCNTs are usually collected as a cathode deposit. However, the efficiency and control of the filling process is lower than for the CCVD-related method, possibly arising from the huge temperature gradients in arc-related processes. In addition, early works dealing with in situ filling by electric arc method reported that the presence of sulfur played a key role in the formation of filled nanotubes [68, 79]. In contrast to the CCVD-based method, electric arc method is hardly able to achieve the encapsulation of transition metals within MWCNTs though some rare examples may be found [79]. On the other hand, many other elements such as Yb, Dy or Ge, and so on, can be successfully introduced into MWCNTs during the electric arc process (Fig. 1.5 c and d). Therefore, the CCVD method and the electric method conveniently complement each other.

Regardless that many materials can be confined in MWCNTs via in situ filling by considering either methods, multi-element compounds involving oxide, salts, etc. are not permitted to be inserted into nanotubes because of the restricted number of species able to play the role of a catalyst for the CCVD process or because of the high temperature involved for the electric arc process, which is a major disadvantage. Another disadvantage is that filling SWCNTs by this route is scarcely possible and when it is, a small amount of filled nanotubes are obtained. Only a few examples involving the electric arc process are found in the literature. One is the incidental discovery of peapods [20] described above and the other one is the encapsulation of Bi in SWCNTs by mixing a few percent of both Co (as catalyst) and Bi with the graphite anode, as previously described [80]. To overcome these drawbacks exhibited by in situ filling, specifically the challenge for filling SWCNTs, ex situ processes have thus emerged, as we will see in the next section.

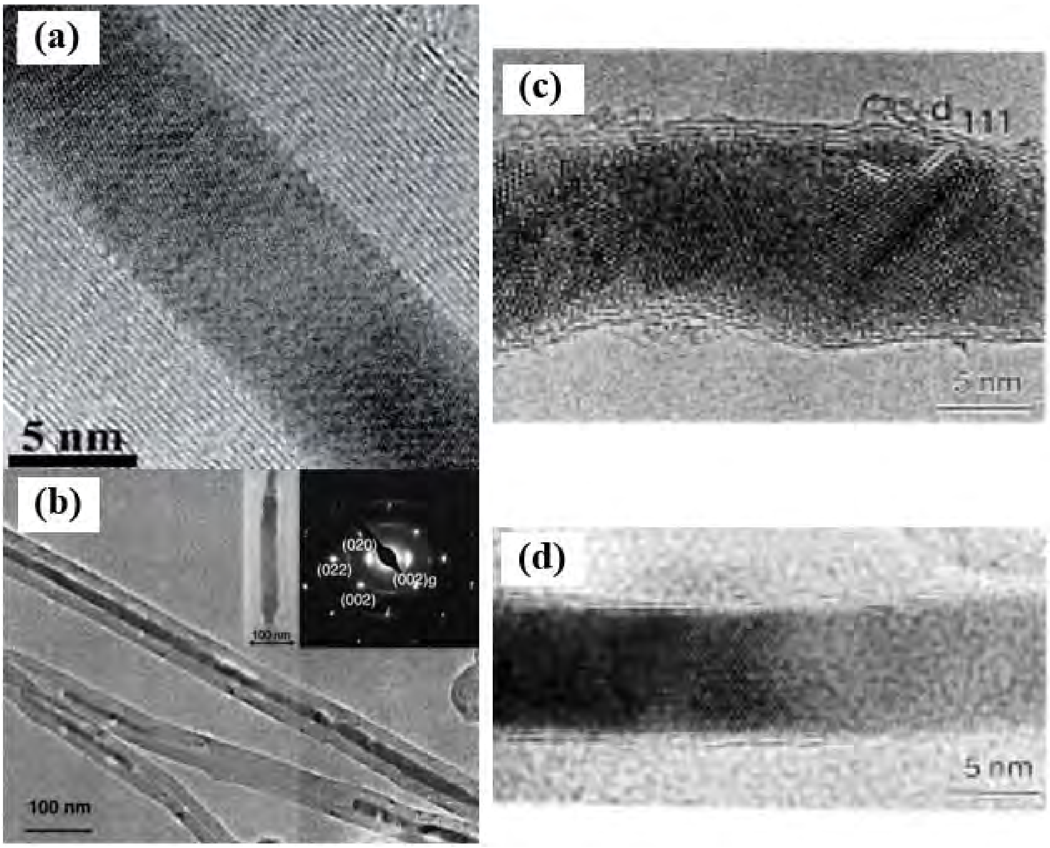

Fig. 1.5 - (a) HRTEM image of a α-Fe filled MWCNTs prepared by CCVD process [81]; (b) TEM image of Co nanowires encapsulated inside nanotubes prepared by CCVD process. The inset displays an encapsulated nanowire and the corresponding SAED pattern showing the presence of f.c.c.-Co structure. [75]; *HRTEM images of filled CNTs produced by arc-discharge when a 99.4% graphite anode is doped with: (c) Ge and (d) Yb. In the case of Ge (c), the filling material is polycrystalline and encapsulated in only 2 or 3 graphitic layers. Pure Ge microcrystals in a <110> projection can be seen on the left and right parts of the nanowire and typical microtwins and stacking faults of the <111> dense atomic layers are frequently observed [79].*

1.2.3.2 Ex situ Filling Route

Ex situ filling is a very versatile route as it possibly allows nearly any kind of material to be inserted into nearly any kind of nanotubes. During this process, the capillary property of nanotubes is fully exploited. Various ex situ filling means employed in the literature will be described in detail subsequently. As illustrated, one-step or multi-step procedures are carried out to realize the ex situ filling, not mentioning the final cleaning step by means of washing or heating in dynamic vacuum which is necessary for all ex situ methods to remove the non-encapsulated material.

1.2.3.2.1 Previous Opening of the Tubes

Unless the initial CNTs prepared under certain specific conditions are thus naturally opened or single-step filling procedures are performed, the first requirement for ex situ filling of nanotubes is to open them. To achieve this, two ways are widely employed including (i) thermal treatments in oxidizing gas atmosphere (air, O_2, O_3 or CO_2) [13, 82, 83] or (ii) reaction with liquid reactants that are oxidizing for polyaromatic carbon materials, typically, acids such as HNO_3, H_2SO_4, or a mixture of both [18]. Other oxidizing agents like supercritical water [82], $KMnO_4$, H_2O_2 [84], Br_2 [85], HF/BF_3 mixture, aqueous OsO_4, OsO_4-$NaIO_4$ [86], or activation with alkali hydroxide [87] are also reported in literature. Beyond the two main ways, mechanical ball milling or electrochemical treatment can also open the CNTs. However, liquid phase oxidation intends to generate residuals that may more or less cover the nanotubes, hence impeding the subsequent filling or characterization. In this regard, gas phase oxidation is generally preferred. Meanwhile, these oxidizing treatments can also be used to purify, functionalize or shorten CNTs.

Given that the graphene lattice possesses comparatively high inertness toward chemical oxidation, opening normally occurs at the location of structural defects or high strain. For MWCNTs, pentagons are obviously found at their tips which enables the opening, while the wall structure is almost impossible to be opened because the possibility that the defects from each graphene wall are located at the same site where the opening takes place are extremely low. On the contrary, the tips and the side walls of SWCNTs are both potential sites for opening which are proved by TEM investigation or other ways in some early studies [88].

1.2.3.2.2 Filling by Gas Phase Methods

Filling nanotubes via gaseous phase is carried out by heating an evacuated and sealed Pyrex or quartz vessel that contains the previously opened nanotubes together with the desired filling material up to the vaporization or sublimation temperature of the filling material, or slightly above. Materials with low vaporization or sublimation temperature (C_{60}, S, Se, etc.) are normally inserted into nanotubes in this way [42, 45, 89]. For filling materials exhibiting high electronic affinity with the graphene lattice such as fullerenes, insertion into the interior of SWCNTs are proved to be driven by surface diffusion [53] and it depends largely on temperature and time instead of the partial pressure of filling material vapor. However, there is a limitation of the maximum temperature for the formation of peapods because the open ends or sidewall defects of the nanotubes may be closed again and the residence time of C_{60} on the nanotube surface will decrease at high temperature thus hindering the entering of C_{60} into the cavity of SWCNTs. On the other hand, a long processing time, in the range of several hours to two days, will promote the achievement of high filling rates (sometimes close to 100%) if an excess of fullerenes is supplied. For other insertions of materials with low electronic affinity to the graphene lattice such as $ZrCl_4$ [90], Se [89], Re_xO_y [91], the filling mechanism is related to capillary condensation. Therefore, the partial pressure of the inserted material can influence the filling rate, as illustrated in [89]. Examples of filling by this method are displayed in Fig. 1.6.

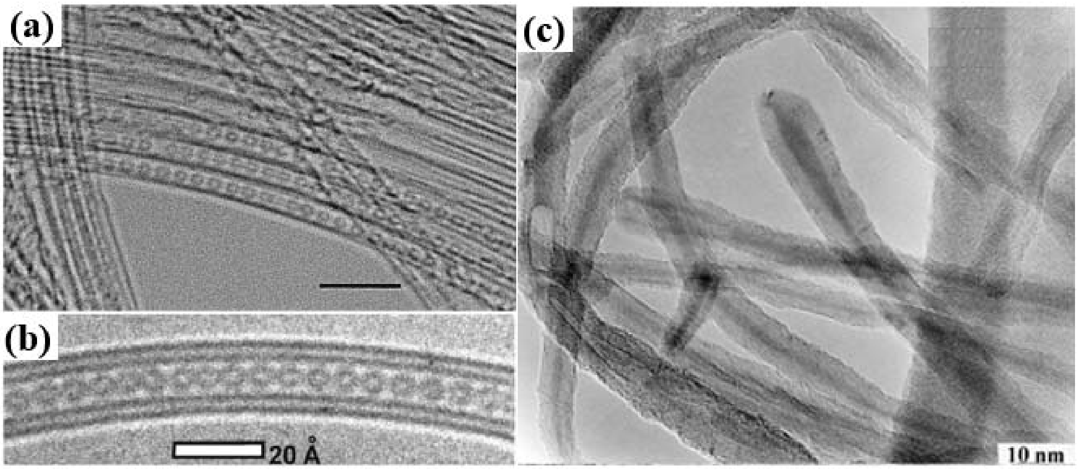

Fig. 1.6 - HRTEM images of (a) C_{60}@SWCNTs prepared by annealing SWCNTs and C_{60} at 1100°C for 14h [46]; (b) C_{60}@DWCNTs prepared by annealing DWCNTs and C_{60} altogether in a closed vessel at various temperatures in the range of 200-520°C for 48h [92]; (c) Se@MWCNTs prepared by heating MWCNTs and Se at 500°C for 1h [89].

The gas phase route has several advantages including its relatively simple operation (opening by air oxidation), its ability for a high filling rate and high homogeneity of the filling material, as well as the absence of any requirement for a surface tension threshold (as opposed to the liquid phase method, see the next section). It can be applied to SWCNTs and MWCNTs, although examples of MWCNTs filled by the gas phase route are rarely reported in the literature [89, 92, 93]. On the contrary, this method is not applicable to the guest material with vaporization or sublimation temperature higher than ca. 1000°C-1200°C, otherwise healing of the nanotubes openings and/or reaction with carbon will possibly occur. Additionally, inserting compound such as salts which typically will decompose once vaporized or sublimed are not favored this way.

1.2.3.2.3 Filling by Liquid Phase Methods

Filling via the liquid phase process is induced by capillary wetting as illustrated by the Young-Laplace law depicting the physical interaction between the filling liquid and the encapsulating hollow solid. In this process, the suspension or solution of the filling material or molten material are widely employed. In the case of the suspension and solution method (see next), a solvent is involved hence wettability is not considered as a key factor as surface tensions of the usual solvents are less than 80 mN m^{-1}. However, herein the effect of viscosity should be taken into account, yet relevant research works are scarcely found.

The *suspension method* is dedicated to filling nanotubes with nanoparticles. The loading of particles are achieved by immersing the opened CNTs in the suspension containing guest nanoparticles at room temperature and subsequently evaporating the liquid in the suspension. The second step is assumed to drive a continuous flow of fresh suspension from the outside to the inside of the tubes. Therefore, the combination of capillary force and evaporation is possibly responsible for the high filling efficiency by this method. However, related examples (Fig. 1.7) only involve MWCNTs and are quite limited so far [94, 95]. One possible reason is that nanoparticles less than 1 nm large in diameter are barely able to be produced for filling pre-opened SWCNTs and preparations of large nanoparticles are not well-established yet though some species are now commercially available (e.g. Sigma-Aldrich). Anyhow, this field is attractive because of the high filling efficiency and it is still at the primary stage, thus interesting developments are anticipated.

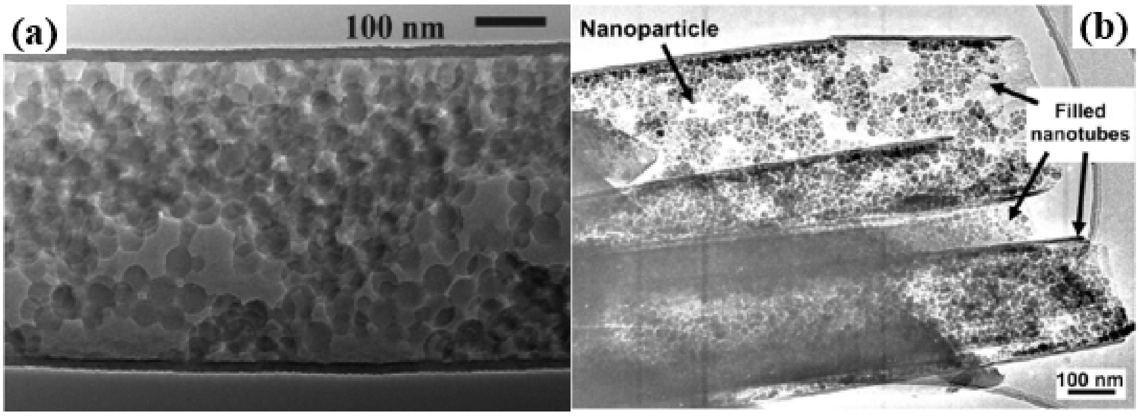

Fig. 1.7 - TEM images of MWCNTs filled with (a) polystyrene nanobeads via bringing MWCNTs into contact with the related suspension in ethylene glycol and deionized water [94]; (b) Fe_3O_4 *nanoparticles via bringing MWCNTs into contact with organic- or water-based ferrofluids [95].*

The *solution method* is quite similar to the former and it is carried out by soaking the opened CNTs into a concentrated solution of the desired material instead of the suspension. Hence, the solubility of the desired material in the corresponding solvent should be considered before the filling. Although a wide variety of materials are permitted to be introduced into the nanotubes via this method, it is actually seen as a candidate when the gas phase route and molten phase route (see next) are not suitable due to the inappropriate physical properties of the desired filling material, or when filling at room temperature is needed for some reasons (e.g., thermal fragility of the substrate, or surrounding device). Compared with the other two methods, a lower filling efficiency is achieved [96] and more steps are required. For instance, filling CNTs with inorganic compounds by the solution method requires subsequent post-treatments (most often calcination as in [97] or reduction as in [19, 80, 98] but also other treatments such as photolysis or electron irradiation, as in [90, 91]) to obtain the hybrid nanotubes with the desired chemical composition. However, encapsulating organic molecules like dye [99], dipoles [100], carotenoids [101], biomolecules [102, 103] inside CNTs is recently a hot topic and it is mainly achieved by the solution method which is an efficient approach and only consists of two steps (opening and filling).

Generally speaking, a prior opening of CNTs is needed for filling by the solution method, while in some specific cases the opening and filling of nanotubes can be merged into a single step. In other words, opening and filling process can occur simultaneously. For instance, a one-step filling process consisting of heating a mixed solution containing closed nanotubes, metal (e.g. Ni, Sm) nitrates and nitric acid is reported by Chen *et al.* [104]. Another example is related to the synthesis of CrO_x@SWCNTs by soaking raw SWCNTs from arc within a super-saturated solution of CrO_3 in concentrated HCl, in which case the CrO_2Cl_2, as a product from the reaction between CrO_3 and HCl, accounts for the opening of SWCNTs.

Overall, the solution method is useful for confining molecules, various nanoparticles, nanorods or nanocrystals within nanotubes (Fig. 1.8) and has been widely employed since its first utilization for filling SWCNTs with $RuCl_3$ as mentioned in [19]. However, very long nanowires are hardly obtained via this method, which can be a drawback. Moreover, the concomitant filling with the solvent molecules cannot be avoided which prevents the achievement of high filling rate.

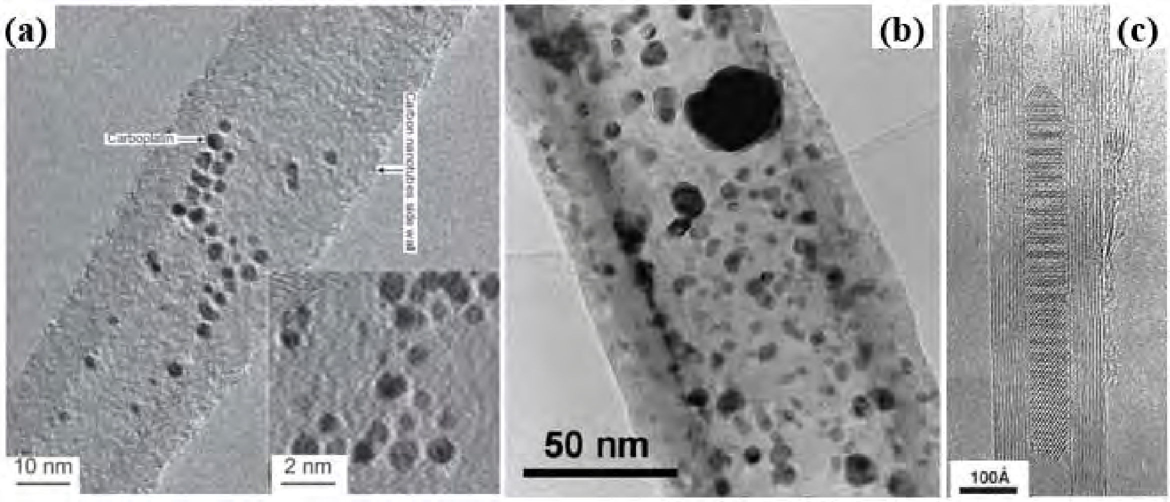

Fig. 1.8 - TEM images of (a) MWCNTs filled with carboplatin prepared by placing a suspension of opened MWCNTs into carboplatin solution [103]; (b) MWCNTs filled with Pd nanoparticles prepared by immersing opened MWCNTs into Pd salt solution followed by a calcination and reduction process [105]; (c) MWCNTs filled with a single Sm_2O_3 *crystal prepared by heating a mixed solution containing closed nanotubes,* $Sm(NO_3)_3$ *and nitric acid [104].*

The *molten phase method* is performed in an identical way to the gas phase method, that is putting the previously opened (or not, see next) nanotubes together with the desired filling material in a quartz vessel sealed under vacuum, and then heating up the whole. Differing from the gas phase method, the target temperature in this method is above (~30–100°C higher) the melting point of the filling material. The duration of the heating can last as long as 1–3 days (see [106-108]) though this maybe shorter for some low viscosity materials. Such long duration are necessary to account for the slow filling kinetics (specifically within SWCNTs) arising from the high viscosity that the molten material may exhibit. Similar to the gas phase method, materials with high melting point such as metals and lanthanides are not suitable for filling nanotubes by the molten phase method, therefore chemical derivatives of the targeted elements to be encapsulated exhibiting lower melting points are the preferred materials for the filling steps. Subsequently, post-treatments for transforming the intermediate compounds into the targeted filling materials are carried out. However, interesting behaviors of one-dimensional crystals were able to be observed for such intermediate hybrid materials (see next).

When halides are attempted to be introduced into nanotubes, it is surprisingly found that filling succeeds even when starting from closed nanotubes, as reported by the Oxford group as early as in 1999 [109]. Hence they proposed that the chemical activity of the halides toward polyaromatic carbon can be used to open the nanotubes during the filling process, thus making the preliminary opening step needless, which is demonstrated in most of their subsequent filling experiments [25-27, 110] (Fig. 1.9). However, this is mainly valid for SWCNTs (and DWCNTs in a few occasions), for the reasons related to the number of walls already discussed above. It is worth noting that molten iodine is also demonstrated to help to open SWCNTs [34].

In summary, the molten phase method was among the first methods used to fill MWCNTs (with PbO [15]) and has been very popular for filling various types of nanotubes due to the possibility for high filling rates (e.g. a filling rate as high as 70% was reported for filling SWCNTs with KI [25]), simplicity (one to three steps, depending on the goal and the material to fill) and versatility. As opposed to the solution method, continuous nanowires up to several micrometers (if starting nanotubes exhibit lengths more than several micrometers) can be synthesized via this process. On the other hand, the application of the molten phase method is limited when the surface tension of the desired filling material at its melting point is too high (i.e. > 170 $mN.m^{-1}$ [12]).

Finally, the assisted filling methods are also reported for filling nanotubes in the literature. For instance, Mittal *et al.* [111] proposed that, when using UV irradiation on the solution of halides ($FeCl_3$, $MoCl_3$, and I) in chloroform, the induced chlorine moieties can promote the attack of the SWCNTs, allowing the filling to proceed from the dissolved material. Another example proposed by Jeong *et al.* [36, 112] illustrated the combined encapsulation of fullerenes and Cs atoms within SWCNTs by irradiating with Cs or C_{60} plasmas the stainless steel substrate connected to a bias-voltage on which SWCNTs were previously deposited. Though not many assisted filling methods have been developed so far, more original and/or simpler and/or efficient ways to synthesized filled nanotubes should be encouraged in the future.

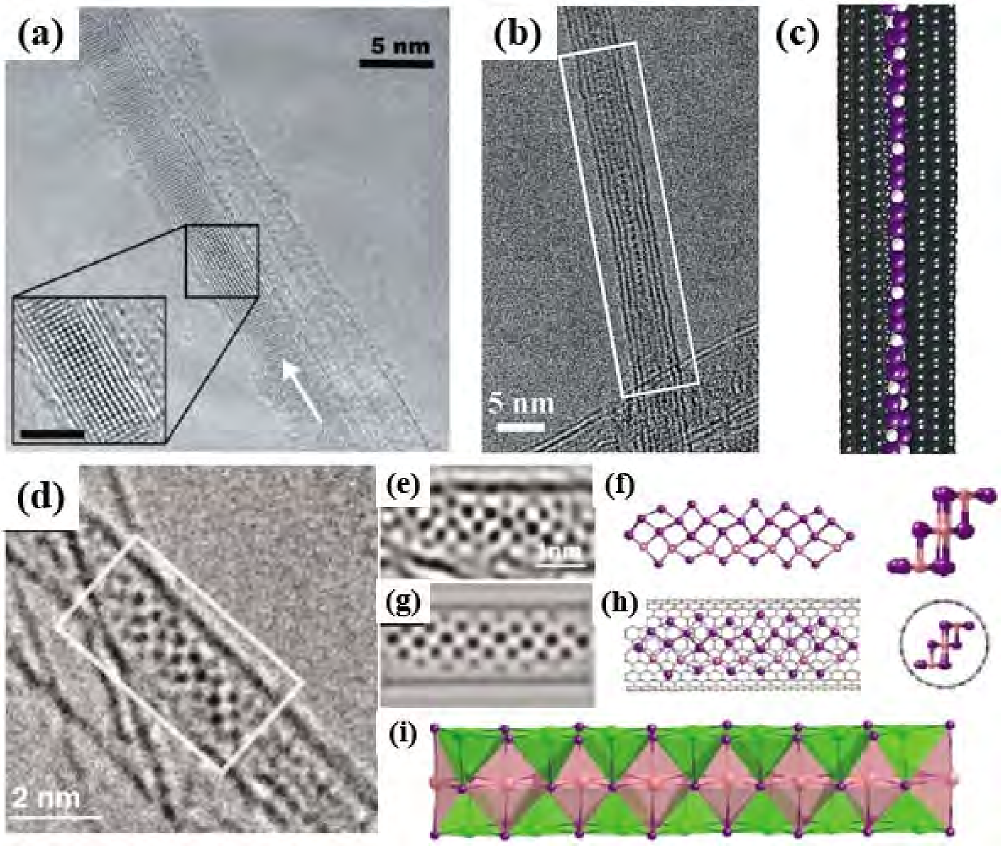

Fig. 1.9 - Examples of CNTs filled with halides via a one-step molten phase method (without prior opening). (a) A DWCNT filled with crystalline CsI (diameter of the inner tube, 3.9 nm; diameter of the outer tube, 4.7 nm). The inset image shows the rocksalt structure of the encapsulated CsI. Scale bar is 2 nm [26]; (b) and (c) HRTEM image of a triple-walled carbon nanotube filled with a helically twisting 2 × 1 × ∞ HgI_2 crystal and the simulated structure model of the crystal [24]; (d) to (i) a 1D BaI_2 chain encapsulated in a SWCNT: (d) and (e) HRTEM images, (f) side-on and end-on views of the atom positions derived from the lattice image, (g) Scherzer focus simulation of derived composite, (h) side-on and end-on views of the composite, (i) coordination model derived for a 1D BaI_2 chain [113].

1.2.4 Species Encapsulated within CNTs

In principle, every type of material including atoms, molecules and phases can be inserted into the CNT cavity and experimentally, successful insertions of atoms, molecules, elements, and compounds have been achieved up to now. In this manuscript, representative papers in which direct proof of filling such as TEM imaging are provided will be introduced, while other related references in which the fillings are merely confirmed by spectroscopic investigations will not be mentioned here.

1.2.4.1 Atoms (Isolated, or as Chains)

When atoms are introduced into nanotubes, it is nearly impossible for them to remain isolated due to their relative instability. Meanwhile, demonstrating the presence of isolated atoms in SWCNTs or DWCNTs is experimentally challenging. Hence, the encapsulated atoms tend to form elongated crystals as nanowires (see next) or single atom wide chains, although only a few examples related to the latter can be found in the literature. The first example was iodine, which was observed to adopt a double-helix structure [34]. In the following works involving iodine filling [36, 114], besides double chain, single and triple iodine chains were demonstrated as well (Figs. 1.10 a and b).

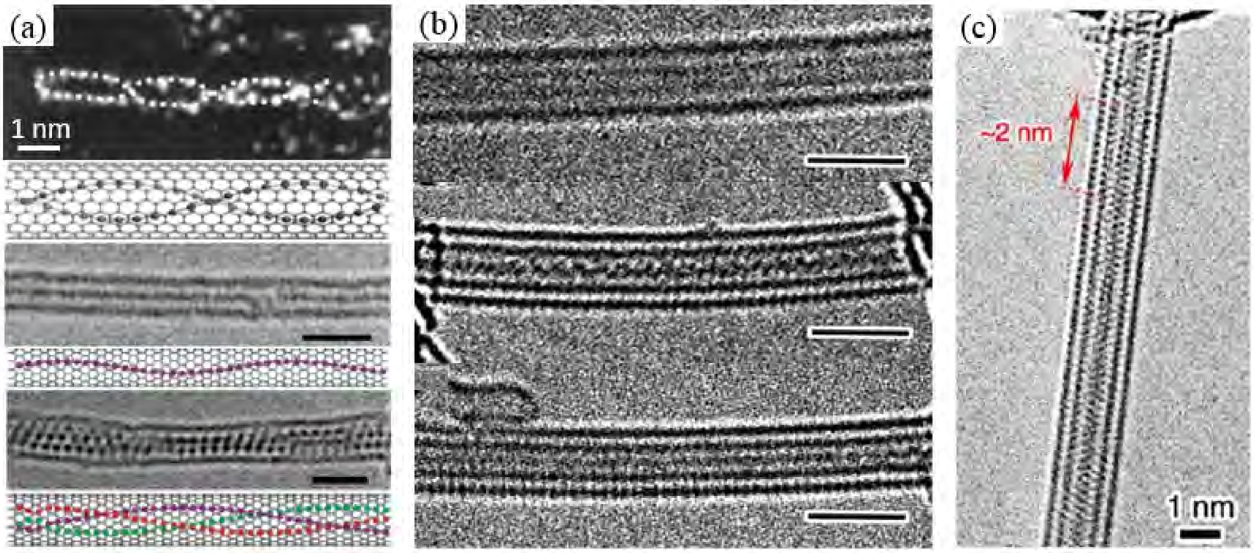

Fig. 1.10 - First column (a), from top to bottom: the first example of SWCNTs filled with a double-helix chain of iodine atoms, as evidenced by means of high-resolution Z contrast TEM, then HRTEM image of a SWCNT filled with a single iodine chain, then HRTEM image of a SWCNT filled with a triple-helix iodine chain. The corresponding structure models (side view) are provided for each case below the related images. Scale bar is ~1.5 nm [34, 41]; Second column (b): HRTEM images of sulfur chains with linear (first and third images) or zigzag (second image) conformation inside a SWCNT or a DWCNTs, scale bar is ~2 nm [42]; (c) HRTEM image of a DWCNT filled with a double-helix Se chain displaying a pitch length of ~ 2 nm [43].

One thing to point out is that iodine crystal is observed – instead of single-atom chain -when the host SWCNT has a large diameter as shown in [36, 114], yet such a configuration is very rare. Interestingly, when attempt to dope the C_{60}@SWCNTs with iodine was made, a bent I_2 chain intercalated into the fullerenes inside a SWCNT was observed in addition to the embedded iodine atoms among two adjacent fullerene molecules [115]. The formation of these structures could be attributed to the obstruction of fullerenes on the filling pathway and the bonding of the inserted atoms, which also resulted in the observation of isolated Cs atoms and K atoms in peapods [116, 117]. A chain structure was also proposed for the encapsulated Cs within SWCNTs prepared by Jeong *et al*. [36], inspired by the pioneering work of iodine filling [34]. Recently, a Japanese group reported the synthesis of linear sulfur chains [42] and double helices of selenium [43] inside CNTs (Fig. 1.10 b and c), both of which were totally different from the atomic arrangement in bulk elements. These progresses may indicate the potential development of a new branch of chemistry for the above elements.

1.2.4.2 Molecules (Isolated, or as Chains)

When molecules are intended to be inserted into nanotubes, the cavity size of the host nanotubes should be taken into account if the diameter of guest molecule is large (e.g. more than 2 nm) which may not be accommodated by a SWCNT or DWCNT. So far, filling nanotubes with molecules principally involves SWCNTs except for some scarce examples concerning the loading of drugs into MWCNTs. The first molecules ever introduced into SWCNTs were fullerenes, thereby forming the so-called nanopeapods as mentioned above. Later on, many fullerene derivative fillings have been performed including higher fullerenes (C_{70} [118], C_{78} and C_{90} [119]), fullerene epoxide ($C_{60}O$ [120]), endohedral fullerenes ($Gd@C_{82}$ and $Dy@C_{82}$ [119], $N@C_{60}$ [121], $Sc_3N@C_{80}$ and $Er_xSc_{3-x}N@C_{80}$ [122], $Dy_3N@C_{80}$ [123], $La@C_{82}$ and $La_2@C_{82}$ [124], $Sm@C_{82}$ [125], $Sc_2@C_{84}$ [126], $Gd_2@C_{92}$ [127], $Ce@C_{82}$ [128], D_{5d}-C_{80} and I_h-$Er_3N@C_{80}$ [129], $Sc_3C_2@C_{80}$ [130]), fullerenes functionalized with ester $C_{61}(COOH)_2$ or carboxylic groups $C_{61}(COOEt)_2$ [131], heterofullerenes ($C_{59}N$ azafullerene [132]), as well as ^{13}C isotope enriched fullerene peapods [133]. Besides the linear fullerene chain, a ‘silo’ configuration can also form when fullerenes are encapsulated inside large diameter nanotubes [92].

Although CNT is considered as a 1D material, the synthesis of linear carbon chains (also called carbyne) only one atom wide and the presence of *sp* hybridization has always been another goal for scientists to achieve [134]. It has been accomplished by initially filling CNTs with polyyne [135] or adamantane [136] molecules and then subsequently annealing the filled nanotubes in vacuum to promote the fusion of the encapsulated molecules, somehow in a similar fashion to the coalescence behavior of peapods (see section 1.2.6). The carbyne is theoretically predicted to possess higher strength, elastic modulus and stiffness than other members in the carbon family including diamond, carbon nanotubes and graphene, which will motivate more efforts on its synthesis at bulk scale.

Apart from fullerenoids as the most popular filling molecules, other organic molecules have also been successfully inserted into nanotubes (Fig. 1.11 a and b), such as metallocenes [122, 137-143], octasiloxane [120], *ortho*-carborane and related molecules [144, 145], fulvalenes [146], Zn-diphenylporphyrin [118, 147], Pt-porphyrin, rhodamin-6G, and chlorophyll [147], β-carotene [101], squarylium (SQ) dye [99], and α–sexithiophene [148].

A peculiar example with regard to the insertion of discrete molecular anion into DWCNTs was reported by Sloan *et al.* [149]. The inserted $[W_6O_{19}]^{2-}$ "Lindqvist ion" which belongs to the family of inorganic polyoxometalate (POM) ions exhibits a nonspheroidal shape and thus can lock into position within sterically matched nanotube capillaries. Owing to these advantages, the constituent W_6 cation framework in the ion can be directly imaged by means of HRTEM (Fig. 1.11 c and d).

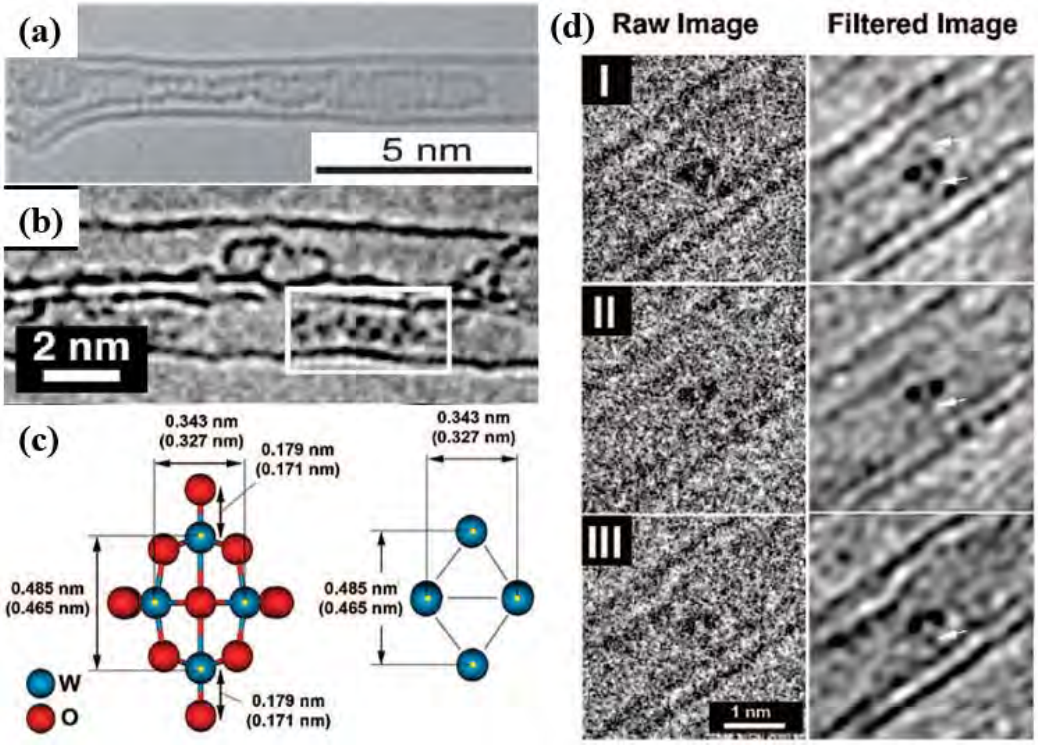

Fig. 1.11 - (a) HRTEM image of a SWCNT filled with α–sexithiophene molecule by gas phase method, two parallel chains formed by the molecules are shown [148]; (b) HRTEM image of a short chain of ortho-carborane molecules formed within a ~ 1.6 nm diameter SWCNT [150]; (c) shows structure models of the $[W_6O_{19}]^{2-}$ *anion with oxygen included (left) and excluded (right);(d) a sequence of HRTEM images (left) obtained from a single* $[W_6O_{19}]^{2-}$ *anion locked into position within the capillary of a DWCNT shown with Fourier-filtered images (right) [149].*

Furthermore, a possible electronic interaction between the nanotube and the encapsulated anion can be verified on the condition that expansion between the two atom columns each containing just a pair of W atoms was observed.

1.2.4.3 Pure Elements (as Nanowires or Nanoparticles)

Except for the formation of chains when elements such as iodine, sulfur, or selenium are inserted into SWCNTs or DWCNTs, nanocrystals are obtained when other elements (mostly when metals are involved) are encapsulated within SWCNTs or DWCNTs. For instance, the synthesis of confined Ru nanowires [19], Bi nanowires [80], Ag nanowires [19, 97, 98, 151, 152], Au nanowires [98], Pt nanowires [98], Pd nanowires [98], La nanowires [153], Eu nanowires [154, 155], Co nanoparticles [156], Fe nanoparticles/nanowires [137, 157, 158], Ni nanocluster [159, 160] have been reported in the literature (Fig. 1.12).

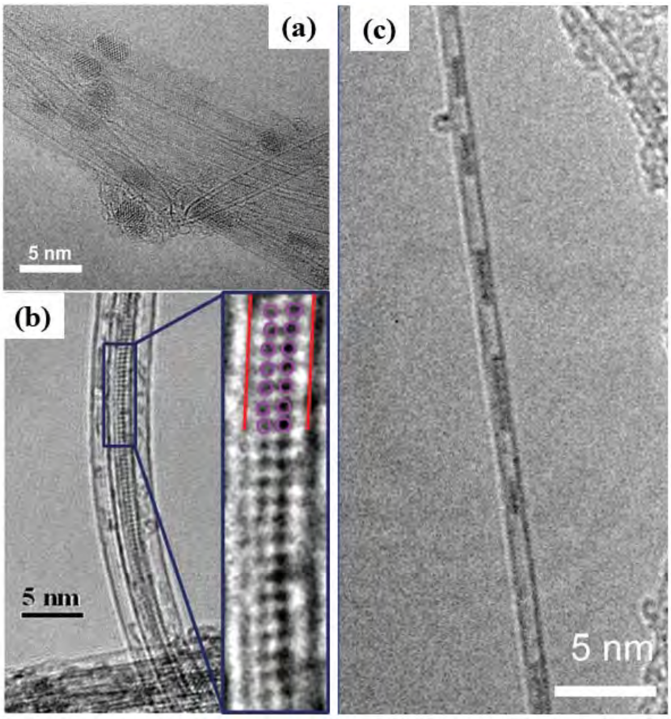

Fig. 1.12 - HRTEM images of (a) Ni clusters filled SWCNTs obtained by annealing initial $NiCp_2$-filled SWCNTs at 500 °C for 2 hours [159]; (b) SWCNTs filled with Eu nanowires (left) and magnified image (right). In the magnified image, red lines correspond to the side wall of the SWCNT, and purple circles correspond to the Eu atoms [154]; (c) a Co-nanoparticle-filled SWCNT [156].

Among these, only Bi and Eu nanowires are directly prepared by filling SWCNTs with pure metals, others are prepared via in situ transformations on the hybrid nanotubes filled with intermediate compounds (e.g. salts). Nanowires of transition metals (e.g. Co, Fe, Ni) may exhibit remarkable magnetic properties while they are barely produced yet, thus more explorations are required. It should be pointed out that in [157, 158], no clear evidence demonstrating the presence of iron nanowires was given, at least from the TEM and HAADF images. However, lanthanum nanowires with typical length of ~10 nm are claimed to be obtained by heating the $La_2@C_{80}$ peapods to trigger the coalescence of metallofullerene molecules. This may give some hints for generating other one-dimensional metallic wires.

1.2.4.4 Compounds (as Chains, Nanowires, or Nanoparticles)

When the desired filling elements possess high melting points and/or high surface tension at the molten state, filling SWCNTs or DWCNTs with compounds can be taken as an efficient alternative. Additionally, filling compounds in solutions may also be the option when a low-temperature filling process is needed or when the elements considered are poorly soluble. The favorite compounds for filling SWCNTs (or DWCNTs) are halides because of their versatility (including fluorides, chlorides, bromides, and iodides), moderate melting points (usually less than 1000 °C), good solubility in many usual solvents (chloroform, water, etc.) and the distinctive ability (compared with other desired filling compounds) to open the nanotube and then fill the nanotube simultaneously. Up to now, halides of a wide range of elements (alkali metals [24, 26, 27], alkaline earth metals [25, 99], transition metals [24, 25, 98, 113, 157, 158, 161-163], lanthanides [22, 113], post-transition metals [164, 165] and their mixtures [21, 25, 29]) have been successfully inserted into SWCNTs (or DWCNTs) mainly by the Oxford Group (see Fig. 1.9), which is one of the most active groups involved principally in filling SWCNTs with inorganic compounds since 1998 [19], as well as other groups around the world.

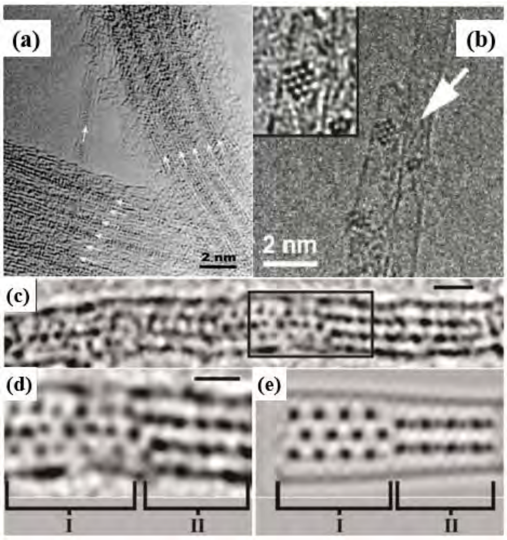

Fig. 1.13 - (a) HRTEM image of SWCNTs filled with PbO. White arrows point to nanotubes filled with lead oxide, a high filling rate≥70% was reported [108]; (b) HRTEM image and detail of UO_2 clusters inside SWCNTs [33]; (c)-(e) TEM image and detail of CsOH crystals inside SWCNTs (scale bar = 1.0 nm), and corresponding Scherzer defocus simulated TEM image [33].

Besides halides, filling SWCNTs (or DWCNTs) with nitrates such as $AgNO_3$ [151, 152, 166], $Bi(NO_3)_3$ [80], $UO_2(NO_3)_2$ [33], oxides including CrO_3 [30], Sb_2O_3 [31, 32], PbO [108], Re_xO_y [91], UO_2 [33], hydroxides (KOH and CsOH [33]), HgTe [167], $MnTe_2$[168], GeTe [169] have also been reported in the literature (Fig. 1.13).

1.2.5 Filling Mechanisms

Although many filling examples have been reported so far, the filling mechanisms are not clearly understood yet, especially in respect to filling via liquid phase method which is frequently used in this manuscript. It is initially assumed that the nanocapillary wetting for filling of nanotubes can also be described by the equation of Young and Laplace, as shown below:

$$\Delta \mathrm{P} = \gamma \left(\frac{1}{R_1} + \frac{1}{R_2}\right) \tag{1.2}$$

where ΔP refers to the pressure difference, γ refers to the surface tension, R_1 and R_2 refer to the two radii of curvature for a curved surface. When the phenomenon of capillary rise occurs in a nanotube, the liquid wets the wall of the nanotube and a meniscus will be formed at the end of the capillary rise, as illustrated in Fig. 1.14.

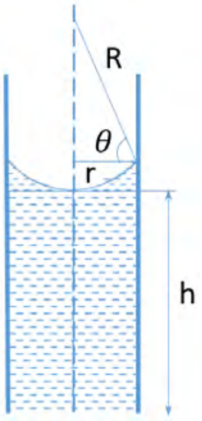

Fig. 1.14 - Illustration of a capillary rise

If the meniscus is taken to be spherical in shape and the liquid meets the circularly cylindrical capillary wall at some angle θ, Eq. 1.2 then becomes

$$\Delta \mathrm{P} = \frac{2\gamma cos\theta}{r} \tag{1.3}$$

where r refers to the radius of the capillary. Meanwhile, the pressure difference also equals the hydrostatic pressure drop in the column of liquid in the capillary. Thus $\Delta \mathrm{P} = \Delta \mathrm{\rho} \mathrm{gh}$, where $\Delta\rho$ denotes the difference in density between the liquid and gas phase, g is the acceleration due to gravity and h denotes the height of the meniscus above the liquid surface. Eq. 1.3 may write

$$\mathrm{h} = \frac{2\gamma cos\theta}{r\Delta \mathrm{\rho g}} \tag{1.4}$$

…which is also known as the Jurin's law since the XVIIIth Century. It can be seen that if θ (also called as contact angle) is larger than 90° h will be negative, which indicates that an external pressure is required to drive the capillary. Hence, only if the contact angle is below 90° can a spontaneous capillarity action occur (however, a recent study demonstrates the possibility of capillary adsorption of metal nanodroplets with $\theta > 90°$ by SWCNTs stemming from the calculation). On the other hand, the contact angle can be derived from Eq. 1.5:

$$\cos\theta = \frac{\gamma_{SV} - \gamma_{SL}}{\gamma} \tag{1.5}$$

where γ_{SV} and γ_{SL} refer to the tensions at the solid-vapor and solid-liquid interfaces, respectively. However, relevant data on the two tensions are not easy to obtain thus making the calculation of contact angle difficult.

In the early days, Dujardin *et al.* [12] investigated the wetting and capillarity of MWCNTs regarding various elements. Their results implied that only materials with low surface tension at melting point could wet the nanotubes then be drawn inside the nanotubes and a cut-off point for surface tension was between 100~200 mN/m. The latter could then provide an upper limit to the effect of Jurin's law (see eq. 1.4 above) which indicates in principle that the filled length h increases as surface tension γ increases. Likewise, if we go back to Eq. 1.4, it is found that h is inversely proportional to r, thereby, for a given liquid, a longer capillary rise should be observed for narrow tubes than for large tubes, meaning higher filling efficiency. However, this is not in accordance with the conclusions from early works dealing with filling with liquids, while comparing MWCNTs with a narrow and wide inner cavity, respectively. Ugarte *et al.* [170] claimed that only nanotubes with inner diameter ≥4 nm were filled while nanotubes with inner diameter of ~1-2 nm were not filled when filling MWCNTs with molten silver nitrate was carried out. Furthermore, following the discovery of SWCNTs several early attempts to fill SWCNTs with molten materials did not succeed [171]. Hence, it is suggested that the equation of Young and Laplace established for sub-millimeter capillaries may not be valid for the sub-nanometer capillaries (‘nanocapillarity’). Until 1999, higher filling yield was observed for regular SWCNTs (inner diameter ~1.4 nm on average) than for MWCNTs when molten materials were used for filling. Likewise, narrow nanotubes were found to be firstly filled during the filling process of Se vapor [89] and the filling efficiency of Bi via the gas and liquid routes was found to be higher for SWCNTs than for MWCNTs [80]. Overall, very high filling rates were achieved when materials involving PbI_2 [164], KI [25] and PbO [108] were inserted into SWCNTs and the existence of nanocapillarity can thus be confirmed.

Despite the success in filling SWCNTs, factors involved in the filling process and how they affect the final filling efficiency are not clearly defined. Since the capillarity of nanotubes is directly related to the surface energies of interaction between the liquid and the solid surface of nanotubes, wetting issue should be taken into consideration firstly. Nevertheless, there are high chances that discrepancies between nanowetting and regular macrowetting may occur. For instance, though surface tension of the filling material is suggested as a determining factor for successful filling by Dujardin *et al.* [12], several studies reported that the introduction of molten material with high surface tension results in higher filling efficiency compared with the introduction of material with low surface tension [25]. In addition, it was recently proposed [6] that viscosity which is considered to only affect the wetting dynamics in macrowetting is likely to play an important role in nanowetting, while the effect of gravity which is considered in macrowetting will not be taken into account in nanowetting because the related weights of the tiny amount of liquid involved is negligible with respect to capillary forces. The proposed factor, viscosity, which may influence the nanowetting, is deduced from the fact that whatever the tube diameter, friction forces increasingly oppose the wetting forces because the tube/liquid contact surface where the friction forces take place increases as the liquid proceeds in the tube, while the gas/liquid/solid contact line where the capillary forces take place remain constant. Finally the cease of the liquid progression is induced once the capillary forces equilibrate the friction forces.

It is likely that viscosity and/or nanowetting are not the only criteria to consider for controlling the filling of nanotubes. The configuration of the filling materials when entering into the cavity of nanotubes should be understood, as a complex may form for certain molten salts or solvated molecules which may not be accommodated by nanotubes with inner diameter below ~1nm due to their large size. Moreover, the intrinsic saturating vapour pressure value of the guest materials is suggested to be important when the molten phase method is used [172]. Though the filling temperature is maintained below the boiling point of the filling material, partial vapour pressure actually develops in the sealed vessel which is likely to push the molten material into the cavity of nanotubes. In this sense, materials with high saturating vapour pressure should provide high filling efficiency (assuming that other parameters are equal). Such an aspect has not been investigated yet. Aside from above, local conditions may play an important role as well, as probably the only reason why, within the same filling experiments, some nanotubes are found extensively filled, whereas adjacent ones with open ends are found empty (frequently observed in our work).

1.2.6 Behaviors, Properties and Applications

As stated above, a large variety of filling experiments has been performed during the short period of development of filling CNTs, especially regarding to filling SWCNTs, while experimental proofs indicating the peculiar properties of X@SWCNTs are relatively rare. Meanwhile, most theoretical work has been focused on the anticipated possibility to tune the SWCNT band gap owing to the inserted material, or to modulate the band gap of the inserted material owing to the enforced structural deformations, while few efforts have been devoted to theoretically predict the electronic properties of filled CNTs (except peapods). So far, simulations of the formation of KI crystals [173], spontaneous filling process of DNA [56], encapsulation of acetylene molecules and their polymerization within SWCNTs [174], modeling of SWCNTs filled water [54], simulations of structural transition of Cu nanowires [175] and electrical transport property of Ge nanowires [62] encapsulated in SWCNTs, quantum chemical simulation of the electronic properties and chemical bonding of the hybrid $(Sc, Ti, V)_8C_{12}$@(12, 0)SWCNTs [174], calculations on the modified electronic properties of SWCNTs inserted by Ag or CrO_3 [176], and many predictions concerning the magnetic properties of transition metal filled SWCNTs, specifically Fe [57, 59-61, 177], have been carried out. With more and more attention attracted to this research field, we can expect discoveries of new properties of filled SWCNTs and progress of theories on these hybrid SWCNTs in the future.

1.2.6.1 Peculiar in-Tube Behavior (diffusion, coalescence, crystallization)

Thanks to the unidirectional confinement given by the inner cavity of carbon nanotubes, especially SWCNTs and DWCNTs, many peculiar in-tube behaviours of the filling material are induced either spontaneously upon filling or by imposing an external stress after filling (annealing, irradiation). As one of the first two synthesized X@SWCNTs, the intriguing behaviours of peapods have been extensively investigated. In the first report on peapods [20], it was found that the encapsulated fullerene molecules coalesce into smaller tubular structures with a capped end when exposed to a 100 kV electron beam in a TEM (Fig.1.15).

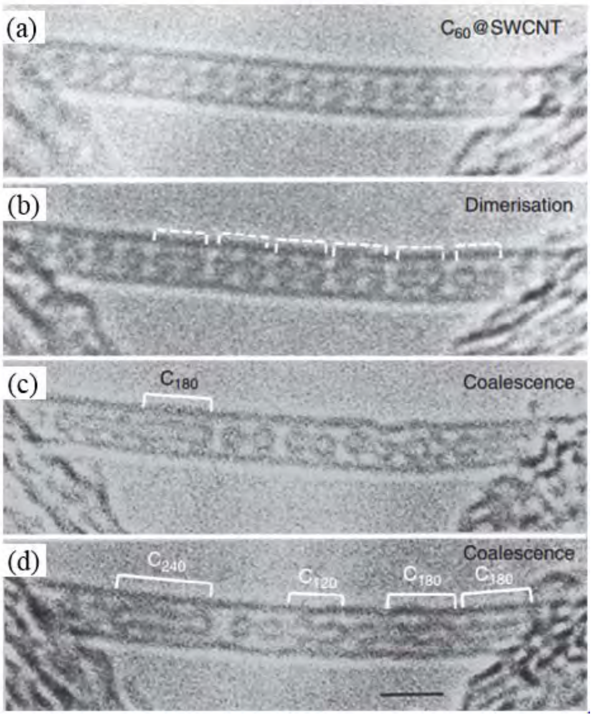

Fig. 1.15 - Sequence of HRTEM images (100 kV, ~300 seconds between images) illustrating the progressive coalescence of a chain of C_{60} *molecules within a 1.4 nm diameter SWCNT under the irradiation. (a) starting situation, showing a well periodic display of the fullerenes; (b) pairs of* C_{60} *are seen indicating the initiation of dimerization; (c)coalescence starts, yet not uniformly; (c) coalescence proceeds and longer capsules are formed. Scale bar 2 nm [178].*

Subsequently, more electron beam-induced behaviors were discovered. In a partially filled SWCNTs, diffusion of the fullerene molecules were observed inside the cavity [45] (Fig.1.16), while in a SWCNT filled with densely packed fullerenes two adjacent molecules tended to dimerize [45, 178], as illustrated in Figs. 1.15. Further, with prolonged irradiation, the dimers coalesced into higher, elongated fullerenes and ultimately ‘two-wall, coaxial tubes’ (CAT) were obtained [45, 178], which were close to double-walled carbon nanotubes (DWCNTs), whose structure had been described prior to the discovery of peapods [179]. The irradiation-induced coalescence is understood as the overcome of activation barrier thanks to the energy brought by the electron beam.

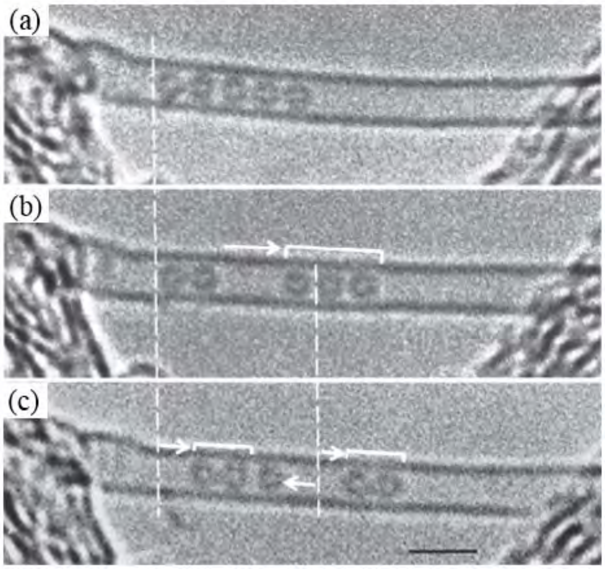

Fig. 1.16 - Sequence of HRTEM images (100 kV, ~30 seconds between images) displaying the diffusion of the encapsulated C_{60} molecules within a 1.4 nm diameter SWCNT under the irradiation. (a) Starting situation, showing a chain consisting of five fullerenes. (b) The five fullerenes suddenly split into two ensembles, one consisting of three fullerenes moves to the right, leaving behind the other one consisting of two fullerenes. (c) One fullerene from the right ensemble jumps back to the left ensemble thus leaving the right ensemble consisting of two fullerenes. Meanwhile, both ensembles have slightly moved to the right. Scale bar 2 nm [45].

It is noticeable that such behaviours were not observed for fullerenes in bulk fullerite when electron irradiated. Other kinds of treatments including thermal annealing [126, 180], combinations of thermal annealing and electron irradiation [181, 182] and photon (laser) irradiation [183-188] can also supply the needed energy and thus cause the coalescence. Among these, annealing the as-synthesized peapods at high temperature in dynamic vacuum may be thought of as a potential way to produce DWCNTs in macroscopic amounts. However, destruction of the tubular morphology and subsequent transformation of the whole peapod material into a graphite-like material may also occur during the thermal annealing as a thermodynamics requirement. Similarly, depending on the amount of energy supplied and the way it is supplied during the combining process of irradiation and thermal annealing, coalescence of confined C_{60} into an inner SWCNT or damage to the peapods will also occur.

Unlike peapods, others nanocrystals confined within CNTs seldom exhibit such dynamic behaviours under the irradiation by an electron beam, except the clusterization of $ZrCl_4$ crystals [90] and the steady rotation of Re_xO_y clusters [91] which were observed inside SWCNTs. As opposed to the fusion of fullerenes, $ZrCl_4$ nanocrystals undergo a progressive dissociation from chains into clusters resulting from the exposure to electron beam. It is speculated that the irradiation can induce the elimination of halide ions in small volume crystals, thus promoting the rearrangement and shrinkage of the crystal remnants. This may also explain the rotation of Re_xO_y cluster arising from the loss of oxygen instead of halide ions. Regarding the structural transformation occurring inside the nanotubes, the encapsulated crystals behave differently from fullerenes. Recently, by taking advantage of a double-aberration-corrected (scanning) transmission electron microscope (S/TEM), Giusca *et al.* [169] recorded the evolution of a SWCNT filled with GeTe crystals under the irradiation of a 80 kV electron beam and a back-and-forth motion as well as phase transformation from amorphous to crystalline for the confined crystals without damaging the host nanotube were observed. In addition, a transformation from a double-helix structure to a single-helix structure for encapsulated Se within a DWCNT resulted from electron beam irradiation [43].

On the other hand, when attempts to remove the carbon sheath from X@SWCNTs are made, several kinds of halide crystals lose the nanowire morphology [67] which demonstrates that the formation of nanowire morphology enforced by confining crystals inside SWCNTs can be also considered as a specific behavior of such hybrid SWCNTs. In addition, pronounced structural modifications for the materials encapsulated within SWCNTs with respect to their bulk state without encapsulation can be generated, which is another specific, peculiar behavior. For instance, preferred orientation with respect to the nanowire elongation axis, systematically reduced coordination, lattice expansion and/or contraction are commonly observed, and new crystal structures are occasionally found. Preferred orientation exhibited by the crystals of binary or higher order compounds [24] is believed to be driven by stoichiometry and reduced coordination is apparently a consequence of the sterically confined space in which the encapsulated crystals have to grow, which may also account for the lattice expansion in the radial direction as observed for KI [27] and CrO_x [30]. Lattice distortions along the wire axis are less likely to occur because the confinement is relatively nil in this specific direction while discrepancy is found in numerous filling examples including KI@SWCNTs [23] and Sb_2O_3@SWCNTs [31, 32]. Such lattice contractions are supposed to correspond to the Poisson effect, which is well known in bulk material mechanics. In all, the observed lattice distortions are prominent and may reach 14% or more. Even in C_{60}@SWCNTs, the C_{60}-C_{60} distance is decreased from 1 nm in fullerite to 0.97 nm for encapsulated C_{60} chains [189]. Contrary to the fact that the inserted compounds can adopt low dimensional configurations within the cavity of nanotubes, it should be impossible for the compounds to form three-dimensional or layered (depending on the radius of atoms involved) structures as in bulk state in the limited space available in SWCNTs and DWCNTs (for those with small inner diameters). However, when wide space is provided as in MWCNTs, single-layered PbI_2 nanotubes is successfully obtained starting from molten PbI_2 as demonstrated in [190]. This work is inspired by a previous study [191] showing that in wide inorganic WS_2 nanotubes, not only does the layered PbI_2 (introduced from the liquid phase) revert to its bulk structure type but the latter distorts in order to allow the encapsulated iodide crystallizing onto the inner wall of the WS_2 capillary, forming a core-shell nanotubular structure.

Additionally, even in the same batch of filling experiment the structure type for a given compound may vary with the size of the inner cavity in the nanotube capillaries [113, 164, 192, 193]. Ultimately, structural constraints can be such that new structures are created, for instance, peculiar features such as unusual symmetry are exhibited by $HoCl_3$ [172], CrO_3 [30], $NdCl_3$ [110], CoI_2 [161] and BaI_2 [193] (Figs. 1.17(a) and 1.17(b)). Despite the previous work reporting the formation of $2\times2\times\infty$ and $3\times3\times\infty$ CsI crystal in 1.4 nm and 1.6 nm diameter SWCNTs respectively [24], truly 1D CsI chains of one-atom thickness encapsulated within DWCNTs with inner cavity less than 1 nm have been reported recently [194] and are clearly imaged by microscope showing the alternate arrangements of Cs and I atoms (Fig. 1.17(d-f)).

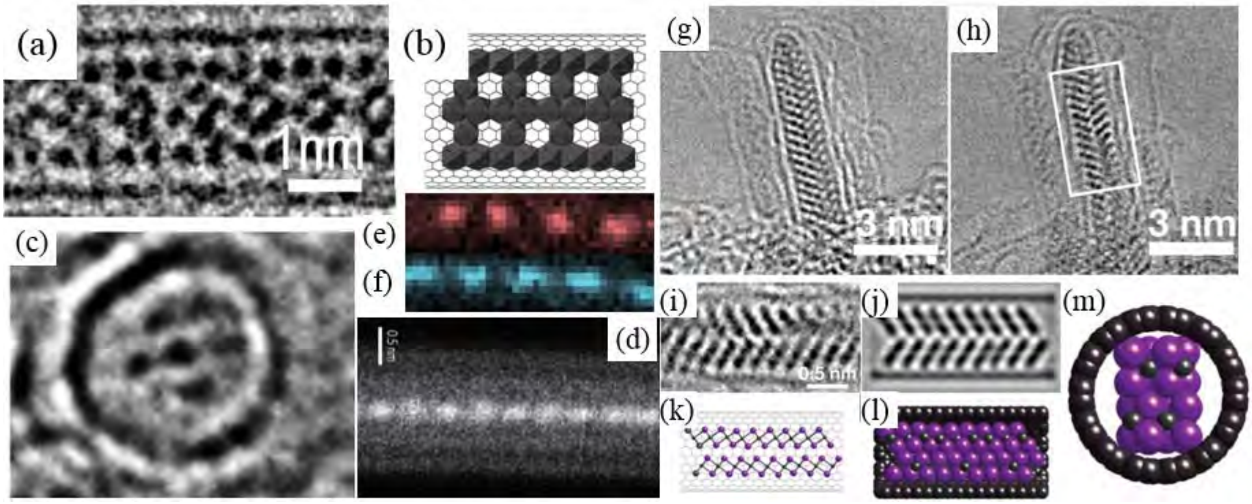

Fig. 1.17 - (a) and (b) HRTEM image of a SWCNT filled with $NdCl_3$ crystals showing the unusual structure and the simulated structure model [22]; (c) HRTEM image of a cross-section of a SWCNT filled with $HoCl_3$ exhibiting a somewhat five-fold symmetry, yet deformed. Based on the observed structural similarities with $NdCl_3$ as described in (a), each dark spot is assumed to a projection of a single 1D chain of $HoCl_x$ polyhedra [172]; (d) ADF image of a CsI chain encapsulated within a DWCNT and related EELS chemical maps of Cs (e) and I (f), respectively, constructed from the image in (d) [194]; (g) and (h) HRTEM images of a tip of a SWCNT hosting PbI_2 focused at two different values of the objective lens; (i) enlarged image of the boxed area in (h); (j) the simulated image corresponding to (i) based on the suggested structural model of PbI_2 crystals in (k); (l) and (m) ball and stick models of the structure modelled in (k), as a side and end views respectively [164].

Other atomic chains such as CsCl, CsF, NaI and $AuBr_3$ can also be duplicated by the same method for producing CsI chains. Such 1D ionic crystals are predicted to show remarkable optical properties and may be used as a component of quantum devices. Finally, it was found that the ability of the inserted material to crystallize may not only relate to the available inner space, but also relate to the deformability of the tube wall. Indeed, small diameter SWCNTs were observed to show oval cross-sections in order to accommodate the confined crystal structure (CoI_2 [161] or PbI_2 [164]). Accordingly, PbI_2 was found to be amorphous when the inner diameter of the host DWCNTs is as small as those SWCNTs, probably associated with the greater structural rigidity of these DWCNTs with respect to SWCNTs, thereby unable to distort and permit the crystal structure to develop.

1.2.6.2 Electronic Properties (Transport, Magnetism and others)

It is natural to anticipate that the structural features stated above exhibited by the filling materials arising from encapsulation will give rise to spectacular physical properties, such as electronic properties, optical properties, etc.. Meanwhile, the interaction between the host nanotubes and filling materials may also result in peculiar properties. In few cases, the intrinsic properties from the filling materials may transfer to the nanotubes making the whole hybrid nanotubes exhibit interesting properties, for example, by filling with ferromagnetic materials the hybrid nanotubes become ferromagnetic as well. However, studies on the properties of filled SWCNTs or DWCNTs are relatively limited despite the achievements of high filling rates which are suitable for structural investigations, possibly as a result of the impurity content (e.g. catalysts, which are often ferromagnetic as well) in the carbon materials that may interfere with the investigation. On the other hand, necessary nanolithography facilities and specifically-designed measurement devices for investigating an individual filled-nanotube are not so common and easily accessible. Besides above difficulties, in order to explain and understand the observed phenomena, the structural characterization of the very same X@CNTs before and/or after property measurements is requested to ascertain the extent of filling and the structural features of the encapsulating nanotubes, which is not routine yet.

So far, a majority of the published work is focused on the various properties of peapods and related materials such as transport properties [49, 188, 195-197], optical properties [198], vibrational properties [51, 199] and magnetic properties [200]. The first transport studies were performed on the buckypaper of Gd@C_{82}-filled SWCNTs. The temperature-dependent resistance for the metallofullerene and C_{60} peapods, and for the pristine SWCNTs were compared (Fig. 1.18a) and it was found that the peapod films have a higher resistance than the pristine SWCNTs sample which was attributed to electrostatic scattering or the presence of disorder induced by the fullerenes. Later on, transport measurements on isolated SWCNT peapods were carried out and the similar power-law-like nature of the low temperature conductivity as found in the bucky-paper measurements was confirmed for an individual C_{60}@SWCNT [195]. In addition, the peapods were found to behave as a regular array of individual quantum dots below 30 K, which was assigned to the local changes arising from the presence of encapsulated fullerenes [201]. The optical properties related to the peapods were studied by the Pichler group employing optical absorption spectroscopy and EELS and a small downshift of 14 meV in the peapods with respect to the empty SWCNTs was observed, which may be related to the presence of fullerenes [198]. The downshift is suggested as a consequence of a small increase of the SWCNT diameter or a change in the inter-tube interaction. C_{60} vibrations in the peapods were proved by means of Raman spectroscopy [200] and transport measurements [197, 202] and the magnetic resonance of peapods was investigated by electron spin resonance (ESR) and nuclear magnetic resonance (NMR). For the latter, the magnetism of the peapods originates from encapsulated magnetic fullerenes including N@C_{60} [203] and $C_{59}N$ [204].

Compared with peapods, reports on the intriguing properties shown by the SWCNTs or DWCNTs filled with other materials are less abundant in the literature. The first study on the electrical conductivity measurement of filled SWCNTs can be dated back to 1998 when attempts to immerse the SWCNT mats in molten iodine were made [35]. It was found that the resistance of the filled SWCNTs decreased sharply compared to the pristine SWCNTs and charge transfer between iodine and SWCNTs was evidenced by Raman scattering. However, intercalation of iodine in the interstitial spaces within SWCNT bundles is induced as well during the iodine treatment, which can also contribute to - or, more likely, can be mostly responsible for - the enhancement of electron transport. Same conclusions can be drawn from a recent study dealing with the iodination of SWCNT films by iodine gases [114]. For other X@SWCNT hybrids in which cases the filling positions are ascertained, interactions between the encapsulated materials and the host SWCNTs are demonstrated, resulting in charge transfer (*e.g.* Ag@SWCNTs [176], CrO_x@SWCNTs [176], AgCl@SWCNTs [205], CuCl/Br/I@SWCNTs [206-208], $CdCl_2/Br_2/I_2$@SWCNTs [209]), increase of transmittance (*e.g.* CuCl@SWCNTs [163]), reduction of band gap (*e.g.* $MnTe_2$@SWCNTs [168]), energy transfer-induced modification of optical adsorption range (*e.g.* SQ@SWCNTs [99])

To better understand the mechanism of interaction in a X@SWCNT, theoretical works involving first-principles *ab initio* density functional theory (DFT) is necessary to be developed. In this regard, the nature of interactions between SWCNTs and inserted transition-metal metallocene molecules (i.e. $Fe/CoCp_n$) has been investigated by using first-principles density functional pseudo-potential calculations [210]. The obtained results demonstrate that the composites were stabilized via weak π-stacking and CH↔ π interactions and the binding energy is inversely dependent on the diameter of the encapsulating SWCNT. In the case of $CoCp_2$@SWCNTs, an additional electrostatic contribution due to the charge transfer from cobaltocene to SWCNT controls the interaction. Experimentally, Raman spectroscopic analysis has been conducted on SWCNTs filled with $CoCp_2$ [141], as well as $FeCp_2$ [211, 212] or $CeCp_3$ [213] while charge transfer was found for all three samples.

Regarding the occurrence of new properties induced by the encapsulated materials instead of the mere enhancement of the nanotube properties, which is one of the motivations for filling CNTs, relevant discoveries except peapods are few so far but explorations are ongoing. One remarkable work by Carter *et al.* [167] reported a semiconducting property for the HgTe nanowires confined inside SWCNTs, which is different from the bulk semi-metallic HgTe. This modified electronic structure for HgTe is considered to be induced from the formation of new coordination geometry for encapsulated HgTe nanocrystals, as a consequence of space constraints imposed by SWCNTs. According to the HRTEM images and the corresponding simulated structure models, the Hg atoms are suggested to be trigonally coordinated and Te atoms are half-octahedrally coordinated, in contrast to the tetrahedral coordination for both atomic species in bulk HgTe. The semiconducting character of HgTe is verified on the basis of DFT calculations and no significant interaction between confined HgTe nanocrystal and SWCNT is demonstrated. Another breakthrough work is related to the synthesis of conducting linear sulfur chains inside SWCNTs and DWCNTs, which opposes to the fact that bulk sulfur is insulating at ambient conditions and only becomes metallic at ultrahigh pressures exceeding ~90 GPa [42]. The presence of sulfur chains was verified by HRTEM images and it is found that the size of cavity within nanotubes can affect the geometries of confined chains, which are further proved by XRD analysis. Meanwhile, the display of sulfur as two parallel single-atom-wide linear chains inside a SWCNT is very stable even at 800K while the zigzag chain or single linear chain inside a DWCNT undergoes a phase transition at 650K. Both thermodynamic behaviours are totally different from that displayed by bulk sulfur. The conducting character of those 1D sulfur chains is directly revealed from the measurements of resistivity on the empty and S-filled CNT films. As shown in Fig. 1. 18b, all the tested samples including empty metallic SWCNTs (M-SWCNTs in the figure) exhibit an inverse dependence of resistivity on temperature and a significant resistance decrease as a result of sulfur encapsulation is observed for both SWCNTs and DWCNTs.

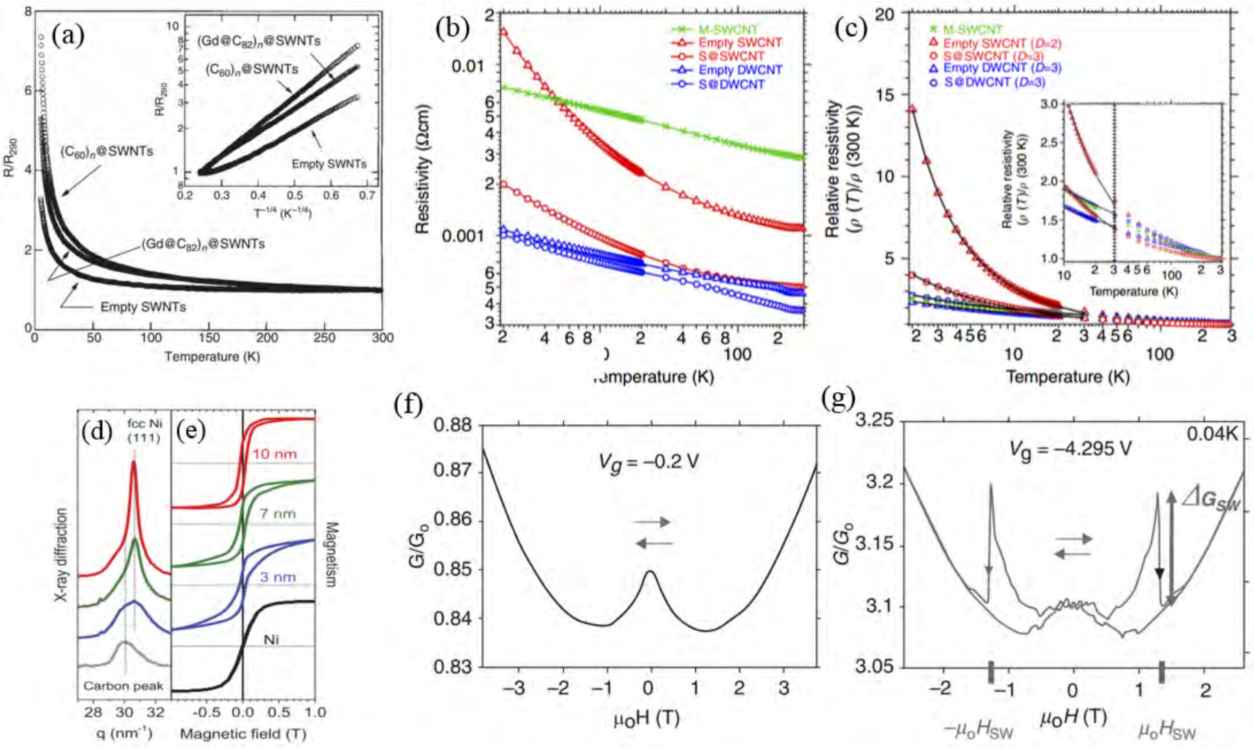

Fig. 1.18 (a) Temperature dependence of the resistance for buckypapers of (Gd@C_{82})@SWCNT, C_{60}@SWCNT, and empty SWCNTs. Inset is a semi-logarithmic plot against $T^{-1/4}$ [49]; (b) and (c) Relationship between temperature and resistivity as well as relative resistivity (normalized by the T=300 K value) for films prepared with empty SWCNTs, S@SWCNTs, empty DWCNTs and S@DWCNTs, in comparison with pristine M-SWCNTs. In (c), hopping model is used to fit the curves of the above samples (black solid line) except M-SWCNTs whose curve could not be reproduced by the model and D refers to the dimensionality of electron hopping in these systems. The enlarged relative resistivity curves for temperature between 10 and 300 K are shown in the inset of (c) [42]; (d) X-ray diffraction profiles for nickel clusters confined in SWCNTs with diameter of 3 nm, 7 nm and 10 nm respectively. The diffraction profile of empty SWCNTs is also shown; (e) magnetization curves for the same materials as measured by SQUID at 5 K. The magnetization curve of bulk Ni is also show; (f) and (g) Variation of conductance as a function of cycling magnetic field measured on isolated Co@SWCNT bundles contacted (with Pd) following the transistor-type device, for an angle of 25° between the direction of the outer magnetic field and the elongation axis of the contacted bundle, and at a temperature

of 40 mK. (f) as seen, 90% of the devices do not show a hysteretic behaviour, whatever the gate voltage. (g) as seen, 10% of the devices show a hysteretic behavior with two conductance jumps in the curve at the same absolute magnetic field value.

From a theoretical standpoint, *ab initio* density functional theory is used to calculate the stability and electronic properties of the hybrid S@SWCNTs and the results indicate that the encapsulated S chain and host SWCNT are both metallic and the total conductance of S@SWCNTs is approximately equal to the sum of the quantum conductances of the isolated S chain and the isolated nanotube, which can support the experimental observations. These calculations also imply that no significant bonding or charge transfer occurs between the sulfur chain and the SWCNT, which is different from the observations in other hybrid systems described above.

The magnetic behavior of filled SWCNTs is another fascinating aspect which has also attracted huge attention in spite of the experimental work is smaller [137, 157, 158, 214] than the theoretical one [59, 60, 175, 177]. For instance, iron nanowires encapsulated within SWCNTs are predicted to still maintain the intrinsic ferromagnetic property regardless of the reduced coordination number of Fe atoms in the nanowires and the magnetism is subsequently transferred to the whole hybrid material. Recently, nickel clusters encapsulated in SWCNTs has been synthesized and their magnetic behaviours have been investigated [160]. It is found that these clusters exhibit superparamagnetism and larger coercivity than bulk Ni, indicating the formation of single domain magnets (Fig. 1.18c). Another example regarding to the interaction between the encapsulated Co nanoparticle and the host SWCNT was also reported, in which case the Co nanoparticles were unambiguously evidenced to be confined in the interior of SWCNTs [156]. A transistor-type device was fabricated based on the hybrid Co@SWCNTs and the occurrence of magneto-resistance effects when operated at temperatures close to absolute zero in cycling magnetic field conditions was observed (Figs. 1.18(f) and 1.18(g)). As the radial dimension of the Co nanoparticles within the narrow SWCNTs is minimized while their proportion of surface atoms is multiplied, a perpendicular or oblique main direction of magnetization with respect to the elongation axis is induced, which counters what was found for large Co wires filling MWCNTs [75].

1.2.6.3 Applications

So far, the reported practical applications of filled CNTs mainly deal with employing CNTs as vehicles for molecular delivery in biomedicine. For instance, targeted drugs are loaded inside CNTs firstly and then the nanocomposites are delivered to certain tissue or somewhere else [103, 215, 216], in which case, nanotubes are merely considered as nanocontainers. In addition, CNTs filled with contrast agents can be used for biomedical imaging such as in vivo observations by magnetic resonance imaging (MRI). For example, SWCNTs attached with Gd^{3+} complex [217] and iron oxide nanoparticles [218] are both investigated by MRI and they are demonstrated to show a dramatically enhanced imaging contrast as a result of the absence of any organic component and the enrichment of the magnetic atom (or compound) concentration.

Besides the biomedical applications, filled CNTs are also used for other fields including as catalyst supports, components in energy storage devices, field electron emitters, magnetic force microscopy (MFM) probes, etc. For example, Rh particles confined inside MWCNTs are reported to exhibit significantly enhanced catalytic activity for converting CO and H_2 into ethanol [219]. Meanwhile, much higher (more than one order of magnitude) formation rate of ethanol inside the cavity of nanotubes is observed with respect to that on the outside of nanotubes. Such a synergetic confinement effect has subsequently been reported for other catalysts such as iron [220], and titanium [221]. The first demonstrated application of filled SWCNTs for energy storage device was related to the utilization of CrO_x@SWCNTs as electrode material for symmetric supercapacitor device, in which case, unprecedented charging rates up to 1 V/s were observed, attributed to Faradaic reactions between the confined CrO_x nanocrystals and the acidic electrolyte [222]. However, other demonstrations of X@CNT-based energy storage devices mostly relate to filled MWCNTs, such as the use of SnO_2@MWCNTs for lithium-ion battery [222, 223] while other X@SWCNT-based energy devices could be barely found in the literature. One of the practical applications of CNTs has been their use as field emitters, which is associated to their intrinsic properties and the relatively convenient growth of 2D CNT arrays on a flat or curved substrate. Therefore, once nanotubes are filled with materials which can also serve as emission source, enhanced field-emission performances are expected for the hybrid X@CNTs when the work function of hybrid X@CNTs decreases. For instance, GaN-filled nanotubes synthesized by the in-situ CVD method enhanced by microwave plasma were investigated as field emitters, and they were found to produce high as well as stable currents [224]. In addition, field emission properties of CNTs filled with germanium [225], iron oxide [226] and ferromagnetic nanowires (FeNi) [227] were reported as well, and these hybrid systems are suggested as promising candidates for field emission displays. All the above studies are concentrated on filled MWCNTs rather than SWCNTs, probably arising from the simpler preparation and higher mechanical stability of MWCNTs compared to SWCNTs during the electron emission event. On the other hand, magnetic CNTs stemming from encapsulations of magnetic materials are found to be suitable for probes of magnetic force microscopy (MFM) and exhibit longer lifetime with respect to conventional magnetically coated probes thanks to the protection from oxidation by carbon shells. As a result of the challenge in preparing SWCNTs filled with magnetic nanowires, only Fe@MWCNTs has been tested as probe for magnetic imaging thus far [69, 228-230].

Regarding the electronic properties of filled SWCNTs as described in section 1.2.6.2, especially concerning peapods, promising applications in single spin devices are expected though progress in this area is slow. Meanwhile, the ability of SWCNTs or DWCNTs to change or alter the crystallographic state of the filling material because of their narrow cavities, as observed for various hybrid X@SWCNT/DWCNT systems involving BaI_2@SWCNTs [193], CoI_2@SWCNTs [161], HgTe@SWCNTs [167] and PbI_2@DWCNTs [164], thereby inducing the possibility to tune the band gap of the filling material, may lead to the potential development in sensors applications.

1.3 Conclusion

Filling CNTs is a promising field due to the feasibility of inserting molecules and synthesizing 1D nanomaterials including nanowires, nanoparticles, atomic chains, and the discovery of peculiar properties leading to potential new applications. The progress made in this field as described above also promotes the development of nanoscience and nanotechnology. In spite of the achievements to date, many issues are needed to overcome. For example, although more and more materials have been introduced into the CNTs successfully, very few studies have been devoted to the investigation of the parameters which may control the filling process described in section 1.2.5. Data on the physical properties of filling materials including surface tension, viscosity and vapour pressure are not easy to find in the literature (especially at the melting point) and most of the related literature was published in the early days. Thus, comprehensive studies on the physical properties of the filling materials are needed in order to understand the filling mechanism. In addition, chemical properties though not discussed in the literature yet may also play a role in the filling process and should be taken into account as well. Few attention is focused on the physical properties of SWCNTs or DWCNTs filled with compounds or elements although peculiar crystalline structures of the encapsulated materials or atomic chains have already been observed, possibly due to the fact that there are often different kinds of structures present simultaneously in a given sample, so it is rather difficult to clearly propose a structure/properties relationship. In the case of hybrid DWCNTs, it is also possible that the modification on the properties of the inner nanotube(s) arising from the filling is not so significant and may be screened by the outer tube, thus not being observed at macroscopic level. However, the measurement at microscopic level on the physical properties of the encapsulated crystal within an individual nanotube is not easy to carry out because of the requirement of advanced facilities such as nanolithography for fabricating electrodes on a SiO_2 substrate, superior TEM to locate the individual filled-tube on the substrate (100% filling rate was hardly achieved so far!) and specifically-designed devices for measuring. Meanwhile, microscopic investigation on the interaction between an individual host nanotube and its internal guest material or the modification on the energy band gap of the encapsulated crystals is scarce at the current stage, which somehow limits the practical applications of X@CNTs. Moreover, nanowires of transition metals are expected to exhibit interesting magnetic properties differing from the bulk metals while successful synthesis of such nanowires encapsulated within SWCNTs or DWCNTs is few. Hence, further work on the preparation of SWCNTs or DWCNTs filled with metals was the motivation for this work.

References

[1] S. Iijima, Helical microtubules of graphitic carbon, nature, 354 (1991) 56-58.

[2] M. Monthioux, V.L. Kuznetsov, Who should be given the credit for the discovery of carbon nanotubes?, Carbon, 44 (2006) 1621-1623.

[3] L. Radushkevich, V. Lukyanovich, O strukture ugleroda, obrazujucegosja pri termiceskom razlozenii okisi ugleroda na zeleznom kontakte, Zurn Fisic Chim, 26 (1952) 88-95.

[4] S. Iijima, T. Ichihashi, Single-shell carbon nanotubes of 1-nm diameter, (1993).

[5] D. Bethune, C. Klang, M. De Vries, G. Gorman, R. Savoy, J. Vazquez, R. Beyers, Cobalt-catalysed growth of carbon nanotubes with single-atomic-layer walls, (1993).

[6] M. Monthioux, Carbon meta-nanotubes: Synthesis, properties and applications, John Wiley & Sons, 2011.

[7] N. Hamada, S.-i. Sawada, A. Oshiyama, New one-dimensional conductors: graphitic microtubules, Physical Review Letters, 68 (1992) 1579.

[8] T.W. Odom, J.-L. Huang, P. Kim, C.M. Lieber, Atomic structure and electronic properties of single-walled carbon nanotubes, Nature, 391 (1998) 62-64.

[9] R.H. Baughman, A.A. Zakhidov, W.A. de Heer, Carbon nanotubes--the route toward applications, science, 297 (2002) 787-792.

[10] W. Li, J. Wen, M. Sennett, Z. Ren, Clean double-walled carbon nanotubes synthesized by CVD, Chemical Physics Letters, 368 (2003) 299-306.

[11] M.R. Pederson, J.Q. Broughton, Nanocapillarity in fullerene tubules, Physical Review Letters, 69 (1992) 2689.

[12] E. Dujardin, T. Ebbesen, H. Hiura, K. Tanigaki, Capillarity and wetting of carbon nanotubes, Science, 265 (1994) 1850-1852.

[13] P. Ajayan, T. Ebbesen, T. Ichihashi, S. Iijima, K. Tanigaki, H. Hiura, Opening carbon nanotubes with oxygen and implications for filling, Nature, 362 (1993) 522-525.

[14] S. Seraphin, D. Zhou, J. Jiao, J.C. Withers, R. Loutfy, Selective encapsulation of the carbides of yttrium and titanium into carbon nanoclusters, Applied physics letters, 63 (1993) 2073-2075.

[15] P.M. Ajayan, Capillarity-induced filling of carbon nanotubes, Nature, 361 (1993) 333-334.

[16] Y. Saito, T. Yoshikawa, Bamboo-shaped carbon tube filled partially with nickel, Journal of crystal growth, 134 (1993) 154-156.

[17] S. Seraphin, D. Zhou, J. Jiao, J.C. Withers, R. Loutfy, Yttrium carbide in nanotubes, (1993).

[18] S. Tsang, Y. Chen, P. Harris, M. Green, A simple chemical method of opening and filling carbon nanotubes, Nature, 372 (1994) 159-162.

[19] M.H. Green, The opening and filling of single walled carbon nanotubes (SWTs), Chemical Communications, (1998) 347-348.

[20] B.W. Smith, M. Monthioux, D.E. Luzzi, Encapsulated C60 in carbon nanotubes, Nature, 396 (1998) 323-324.

[21] D. Wright, A.E. York, K. Coleman, M.H. Green, J. Hutchison, Capillarity and silver nanowire formation observed in single walled carbon nanotubes, Chemical Communications, (1999) 699-700.

[22] C. Xu, J. Sloan, G. Brown, S. Bailey, V.C. Williams, S. Friedrichs, K.S. Coleman, E. Flahaut,

J.L. Hutchison, R.E. Dunin-Borkowski, 1D lanthanide halide crystals inserted into single-walled carbon nanotubes, Chemical Communications, (2000) 2427-2428.

[23] R.R. Meyer, J. Sloan, R.E. Dunin-Borkowski, A.I. Kirkland, M.C. Novotny, S.R. Bailey, J.L. Hutchison, M.L. Green, Discrete atom imaging of one-dimensional crystals formed within single-walled carbon nanotubes, Science, 289 (2000) 1324-1326.

[24] J. Sloan, A.I. Kirkland, J.L. Hutchison, M.L. Green, Aspects of crystal growth within carbon nanotubes, Comptes Rendus Physique, 4 (2003) 1063-1074.

[25] G. Brown, S. Bailey, M. Novotny, R. Carter, E. Flahaut, K. Coleman, J. Hutchison, M. Green, J. Sloan, High yield incorporation and washing properties of halides incorporated into single walled carbon nanotubes, Applied Physics A, 76 (2003) 457-462.

[26] P.M. Costa, S. Friedrichs, J. Sloan, M.L. Green, Imaging lattice defects and distortions in alkali-metal iodides encapsulated within double-walled carbon nanotubes, Chemistry of materials, 17 (2005) 3122-3129.

[27] J. Sloan, M. Novotny, S. Bailey, G. Brown, C. Xu, V. Williams, S. Friedrichs, E. Flahaut, R. Callender, A. York, Two layer 4: 4 co-ordinated KI crystals grown within single walled carbon nanotubes, Chemical Physics Letters, 329 (2000) 61-65.

[28] G. Brown, S.R. Bailey, J. Sloan, C. Xu, S. Friedrichs, E. Flahaut, K.S. Coleman, J.L. Hutchison, R.E. Dunin-Borkowski, M.L. Green, Electron beam induced in situ clusterisation of 1D ZrCl4 chains within single-walled carbon nanotubes, Chem. Commun., (2001) 845-846.

[29] J. Sloan, M. Terrones, S. Nufer, S. Friedrichs, S.R. Bailey, H.-G. Woo, M. Rühle, J.L. Hutchison, M.L. Green, Metastable One-Dimensional AgCl1-x I x Solid-Solution Wurzite "Tunnel" Crystals Formed within Single-Walled Carbon Nanotubes, Journal of the American Chemical Society, 124 (2002) 2116-2117.

[30] J. Mittal, M. Monthioux, H. Allouche, O. Stephan, Room temperature filling of single-wall carbon nanotubes with chromium oxide in open air, Chemical physics letters, 339 (2001) 311-318.

[31] S. Friedrichs, R.R. Meyer, J. Sloan, A.I. Kirkland, J.L. Hutchison, M.L. Green, Complete characterisation of a Sb2O3/(21,− 8) SWNT inclusion composite, Chemical Communications, (2001) 929-930.

[32] S. Friedrichs, J. Sloan, M.L.H. Green, J.L. Hutchison, R.R. Meyer, A.I. Kirkland, Simultaneous determination of inclusion crystallography and nanotube conformation for aSb2O3/single−wallednanotube composite, Physical Review B, 64 (2001).

[33] N. Thamavaranukup, H.A. Höppe, L. Ruiz-Gonzalez, P.M. Costa, J. Sloan, A. Kirkland, M.L. Green, Single-walled carbon nanotubes filled with M OH (M= K, Cs) and then washed and refilled with clusters and molecules, Chemical communications, (2004) 1686-1687.

[34] X. Fan, E.C. Dickey, P. Eklund, K. Williams, L. Grigorian, R. Buczko, S. Pantelides, S. Pennycook, Atomic arrangement of iodine atoms inside single-walled carbon nanotubes, Physical review letters, 84 (2000) 4621.

[35] L. Grigorian, K. Williams, S. Fang, G. Sumanasekera, A. Loper, E.C. Dickey, S. Pennycook, P. Eklund, Reversible intercalation of charged iodine chains into carbon nanotube ropes, Physical

review letters, 80 (1998) 5560.

[36] G.-H. Jeong, R. Hatakeyama, T. Hirata, K. Tohji, K. Motomiya, T. Yaguchi, Y. Kawazoe, Formation and structural observation of cesium encapsulated single-walled carbon nanotubes, Chem. Commun., (2003) 152-153.

[37] N. Bendiab, R. Almairac, S. Rols, R. Aznar, J.-L. Sauvajol, I. Mirebeau, Structural determination of iodine localization in single-walled carbon nanotube bundles by diffraction methods, Physical Review B, 69 (2004) 195415.

[38] J. Cambedouzou, J.-L. Sauvajol, A. Rahmani, E. Flahaut, A. Peigney, C. Laurent, Raman spectroscopy of iodine-doped double-walled carbon nanotubes, Physical Review B, 69 (2004) 235422.

[39] K.R. Kissell, K.B. Hartman, P.A. Van der Heide, L.J. Wilson, Preparation of I2@ SWNTs: synthesis and spectroscopic characterization of I2-loaded SWNTs, The Journal of Physical Chemistry B, 110 (2006) 17425-17429.

[40] T. Michel, L. Alvarez, J.-L. Sauvajol, R. Almairac, R. Aznar, J.-L. Bantignies, O. Mathon, EXAFS investigations of iodine-doped carbon nanotubes, Physical Review B, 73 (2006) 195419.

[41] L. Guan, K. Suenaga, Z. Shi, Z. Gu, S. Iijima, Polymorphic structures of iodine and their phase transition in confined nanospace, Nano letters, 7 (2007) 1532-1535.

[42] T. Fujimori, A. Morelos-Gomez, Z. Zhu, H. Muramatsu, R. Futamura, K. Urita, M. Terrones, T. Hayashi, M. Endo, S.Y. Hong, Y.C. Choi, D. Tomanek, K. Kaneko, Conducting linear chains of sulphur inside carbon nanotubes, Nat Commun, 4 (2013) 2162.

[43] T. Fujimori, R.B. Dos Santos, T. Hayashi, M. Endo, K. Kaneko, D. Tománek, Formation and properties of selenium double-helices inside double-wall carbon nanotubes: experiment and theory, ACS nano, 7 (2013) 5607-5613.

[44] M. Monthioux, B. Smith, B. Burteaux, A. Claye, J. Fischer, D. Luzzi, Sensitivity of single-wall carbon nanotubes to chemical processing: an electron microscopy investigation, Carbon, 39 (2001) 1251-1272.

[45] B.W. Smith, M. Monthioux, D.E. Luzzi, Carbon nanotube encapsulated fullerenes: a unique class of hybrid materials, Chemical Physics Letters, 315 (1999) 31-36.

[46] B. Burteaux, A. Claye, B.W. Smith, M. Monthioux, D.E. Luzzi, J.E. Fischer, Abundance of encapsulated C 60 in single-wall carbon nanotubes, Chemical Physics Letters, 310 (1999) 21-24.

[47] Y. Zhang, S. Iijima, Z. Shi, Z. Gu, Defects in arc-discharge-produced single-walled carbon nanotubes, Philosophical magazine letters, 79 (1999) 473-479.

[48] J. Sloan, R.E. Dunin-Borkowski, J.L. Hutchison, K.S. Coleman, V.C. Williams, J.B. Claridge, A.P. York, C. Xu, S.R. Bailey, G. Brown, The size distribution, imaging and obstructing properties of C 60 and higher fullerenes formed within arc-grown single walled carbon nanotubes, Chemical Physics Letters, 316 (2000) 191-198.

[49] K. Hirahara, K. Suenaga, S. Bandow, H. Kato, T. Okazaki, H. Shinohara, S. Iijima,

One-dimensional metallofullerene crystal generated inside single-walled carbon nanotubes, Physical Review Letters, 85 (2000) 5384.

[50] H. Kataura, Y. Maniwa, T. Kodama, K. Kikuchi, K. Hirahara, S. Iijima, S. Suzuki, W. Kratschmer, Y. Achiba, Fullerene-peapods: Synthesis, Structure and Raman Spectroscopy, in: AIP Conference Proceedings, IOP INSTITUTE OF PHYSICS PUBLISHING LTD, 2001, pp. 251-255.

[51] H. Kataura, Y. Maniwa, T. Kodama, K. Kikuchi, K. Hirahara, K. Suenaga, S. Iijima, S. Suzuki, Y. Achiba, W. Krätschmer, High-yield fullerene encapsulation in single-wall carbon nanotubes, Synthetic Metals, 121 (2001) 1195-1196.

[52] K. Suenaga, M. Tence, C. Mory, C. Colliex, H. Kato, T. Okazaki, H. Shinohara, K. Hirahara, S. Bandow, S. Iijima, Element-selective single atom imaging, Science, 290 (2000) 2280-2282.

[53] B.W. Smith, D.E. Luzzi, Formation mechanism of fullerene peapods and coaxial tubes: a path to large scale synthesis, Chemical Physics Letters, 321 (2000) 169-174.

[54] K. Koga, G. Gao, H. Tanaka, X.C. Zeng, Formation of ordered ice nanotubes inside carbon nanotubes, Nature, 412 (2001) 802-805.

[55] A.A. Farajian, K. Ohno, K. Esfarjani, Y. Maruyama, Y. Kawazoe, Ab Initio study of dopant insertion into carbon nanotubes, The Journal of chemical physics, 111 (1999) 2164-2168.

[56] H. Gao, Y. Kong, D. Cui, C.S. Ozkan, Spontaneous insertion of DNA oligonucleotides into carbon nanotubes, Nano Letters, 3 (2003) 471-473.

[57] G. Peng, A. Huan, Y. Feng, Energetic and magnetic properties of transition-metal nanowire encapsulated BxCyNz composite nanotubes, Applied physics letters, 88 (2006) 3117.

[58] C.-K. Yang, J. Zhao, J.P. Lu, Magnetism of transition-metal/carbon-nanotube hybrid structures, Physical review letters, 90 (2003) 257203.

[59] M. Weissmann, G. García, M. Kiwi, R. Ramírez, C.-C. Fu, Theoretical study of iron-filled carbon nanotubes, Physical Review B, 73 (2006) 125435.

[60] Y.-J. Kang, J. Choi, C.-Y. Moon, K. Chang, Electronic and magnetic properties of single-wall carbon nanotubes filled with iron atoms, Physical Review B, 71 (2005) 115441.

[61] N. Fujima, T. Oda, Structures and magnetic properties of iron chains encapsulated in tubal carbon nanocapsules, Physical Review B, 71 (2005) 115412.

[62] X. Zhang, H. Li, K.M. Liew, The structures and electrical transport properties of germanium nanowires encapsulated in carbon nanotubes, Journal of Applied Physics, 102 (2007) 073709.

[63] A.D.K. Jones, T. Bekkedahl, Storage of hydrogen in single-walled carbon nanotubes, Nature, 386 (1997) 377.

[64] S. Farhat, B. Weinberger, F.D. Lamari, T. Izouyar, L. Noe, M. Monthioux, Performance of carbon arc-discharge nanotubes to hydrogen energy storage, Journal of nanoscience and nanotechnology, 7 (2007) 3537-3542.

[65] A. Kuznetsova, J. Yates Jr, J. Liu, R. Smalley, Physical adsorption of xenon in open single walled carbon nanotubes: Observation of a quasi-one-dimensional confined Xe phase, The Journal of Chemical Physics, 112 (2000) 9590-9598.

[66] A. Fujiwara, K. Ishii, H. Suematsu, H. Kataura, Y. Maniwa, S. Suzuki, Y. Achiba, Gas adsorption in the inside and outside of single-walled carbon nanotubes, Chemical Physics Letters, 336 (2001) 205-211.

[67] J. Bendall, A. Ilie, M. Welland, J. Sloan, M. Green, Thermal stability and reactivity of metal halide filled single-walled carbon nanotubes, The Journal of Physical Chemistry B, 110 (2006) 6569-6573.

[68] A. Loiseau, F. Willaime, Filled and mixed nanotubes: from TEM studies to the growth mechanism within a phase-diagram approach, Applied surface science, 164 (2000) 227-240.

[69] F. Wolny, T. Mühl, U. Weissker, K. Lipert, J. Schumann, A. Leonhardt, B. Büchner, Iron filled carbon nanotubes as novel monopole-like sensors for quantitative magnetic force microscopy, Nanotechnology, 21 (2010) 435501.

[70] J. Hu, Y. Bando, J. Zhan, C. Zhi, D. Golberg, Carbon nanotubes as nanoreactors for fabrication of single-crystalline Mg3N2 nanowires, Nano letters, 6 (2006) 1136-1140.

[71] L. Jankovic, D. Gournis, P.N. Trikalitis, I. Arfaoui, T. Cren, P. Rudolf, M.-H. Sage, T.T. Palstra, B. Kooi, J. De Hosson, Carbon nanotubes encapsulating superconducting single-crystalline tin nanowires, Nano letters, 6 (2006) 1131-1135.

[72] E. Sutter, P. Sutter, Au‐Induced Encapsulation of Ge Nanowires in Protective C Shells, Advanced Materials, 18 (2006) 2583-2588.

[73] L. Dong, X. Tao, L. Zhang, X. Zhang, B.J. Nelson, Nanorobotic spot welding: controlled metal deposition with attogram precision from copper-filled carbon nanotubes, Nano Letters, 7 (2007) 58-63.

[74] L. Sun, F. Banhart, A. Krasheninnikov, J. Rodriguez-Manzo, M. Terrones, P. Ajayan, Carbon nanotubes as high-pressure cylinders and nanoextruders, Science, 312 (2006) 1199-1202.

[75] R. Kozhuharova, M. Ritschel, D. Elefant, A. Graff, A. Leonhardt, I. Mönch, T. Mühl, S. Groudeva-Zotova, C.M. Schneider, Well-aligned Co-filled carbon nanotubes: preparation and magnetic properties, Applied surface science, 238 (2004) 355-359.

[76] R. Lv, F. Kang, J. Gu, X. Gui, J. Wei, K. Wang, D. Wu, Carbon nanotubes filled with ferromagnetic alloy nanowires: lightweight and wide-band microwave absorber, Applied Physics Letters, 93 (2008) 223105.

[77] A. Leonhardt, S. Hampel, C. Mueller, I. Moench, R. Koseva, M. Ritschel, D. Elefant, K. Biedermann, B. Buechner, Synthesis, Properties, and Applications of Ferromagnetic‐Filled Carbon Nanotubes, Chemical vapor deposition, 12 (2006) 380-387.

[78] A. Leonhardt, M. Ritschel, R. Kozhuharova, A. Graff, T. Mühl, R. Huhle, I. Mönch, D. Elefant, C. Schneider, Synthesis and properties of filled carbon nanotubes, Diamond and related materials, 12 (2003) 790-793.

[79] N. Demoncy, O. Stephan, N. Brun, C. Colliex, A. Loiseau, H. Pascard, Filling carbon nanotubes with metals by the arc-discharge method: the key role of sulfur, The European Physical Journal B-Condensed Matter and Complex Systems, 4 (1998) 147-157.

[80] C.-H. Kiang, J.-S. Choi, T.T. Tran, A.D. Bacher, Molecular nanowires of 1 nm diameter from

capillary filling of single-walled carbon nanotubes, The Journal of Physical Chemistry B, 103 (1999) 7449-7451.

[81] C. Müller, D. Golberg, A. Leonhardt, S. Hampel, B. Büchner, Growth studies, TEM and XRD investigations of iron‐filled carbon nanotubes, physica status solidi (a), 203 (2006) 1064-1068.

[82] J.-Y. Chang, A. Ghule, J.-J. Chang, S.-H. Tzing, Y.-C. Ling, Opening and thinning of multiwall carbon nanotubes in supercritical water, Chemical physics letters, 363 (2002) 583-590.

[83] J. Simmons, B. Nichols, S. Baker, M.S. Marcus, O. Castellini, C.-S. Lee, R. Hamers, M. Eriksson, Effect of ozone oxidation on single-walled carbon nanotubes, The journal of physical chemistry B, 110 (2006) 7113-7118.

[84] K. Hernadi, A. Siska, L. Thien-Nga, L. Forro, I. Kiricsi, Reactivity of different kinds of carbon during oxidative purification of catalytically prepared carbon nanotubes, Solid State Ionics, 141 (2001) 203-209.

[85] Y.K. Chen, M.L. Green, J.L. Griffin, J. Hammer, R.M. Lago, S.C. Tsang, Purification and opening of carbon nanotubes via bromination, Advanced Materials, 8 (1996) 1012-1015.

[86] B. Satishkumar, A. Govindaraj, J. Mofokeng, G. Subbanna, C. Rao, Novel experiments with carbon nanotubes: opening, filling, closing and functionalizing nanotubes, Journal of Physics B: Atomic, Molecular and Optical Physics, 29 (1996) 4925.

[87] E. Raymundo-Pinero, P. Azais, T. Cacciaguerra, D. Cazorla-Amorós, A. Linares-Solano, F. Béguin, KOH and NaOH activation mechanisms of multiwalled carbon nanotubes with different structural organisation, Carbon, 43 (2005) 786-795.

[88] M. Monthioux, Filling single-wall carbon nanotubes, Carbon, 40 (2002) 1809-1823.

[89] J. Chancolon, F. Archaimbault, A. Pineau, S. Bonnamy, Filling of carbon nanotubes with selenium by vapor phase process, Journal of nanoscience and nanotechnology, 6 (2006) 82-86.

[90] G. Brown, S.R. Bailey, J. Sloan, C. Xu, S. Friedrichs, E. Flahaut, K.S. Coleman, M.L.H. Green, J.L. Hutchison, R.E. Dunin-Borkowski, Electron beam induced in situ clusterisation of 1D ZrCl4 chains within single-walled carbon nanotubes, Chemical Communications, (2001) 845-846.

[91] P.M. Costa, J. Sloan, T. Rutherford, M.L. Green, Encapsulation of Re x O y clusters within single-walled carbon nanotubes and their in tubulo reduction and sintering to Re metal, Chemistry of materials, 17 (2005) 6579-6582.

[92] A.N. Khlobystov, D.A. Britz, A. Ardavan, G.A.D. Briggs, Observation of ordered phases of fullerenes in carbon nanotubes, Physical review letters, 92 (2004) 245507.

[93] T. Fröhlich, P. Scharff, W. Schliefke, H. Romanus, V. Gupta, C. Siegmund, O. Ambacher, L. Spiess, Insertion of C 60 into multi-wall carbon nanotubes—a synthesis of C 60@ MWCNT, Carbon, 42 (2004) 2759-2762.

[94] B.M. Kim, S. Qian, H.H. Bau, Filling carbon nanotubes with particles, Nano Letters, 5 (2005) 873-878.

[95] G. Korneva, H. Ye, Y. Gogotsi, D. Halverson, G. Friedman, J.-C. Bradley, K.G. Kornev,

Carbon nanotubes loaded with magnetic particles, Nano letters, 5 (2005) 879-884.

[96] L. Noé, M. Monthioux, Liquid phase synthesis of “peapods” at room temperature, in: International Conference on Carbon “Carbon’04, 2004.

[97] Z. Zhang, B. Li, Z. Shi, Z. Gu, Z. Xue, L. Peng, Filling of single-walled carbon nanotubes with silver, Journal of Materials Research, 15 (2000) 2658-2661.

[98] A. Govindaraj, B. Satishkumar, M. Nath, C.N.R. Rao, Metal nanowires and intercalated metal layers in single-walled carbon nanotube bundles, Chemistry of Materials, 12 (2000) 202-205.

[99] K. Yanagi, K. Iakoubovskii, H. Matsui, H. Matsuzaki, H. Okamoto, Y. Miyata, Y. Maniwa, S. Kazaoui, N. Minami, H. Kataura, Photosensitive function of encapsulated dye in carbon nanotubes, Journal of the American Chemical Society, 129 (2007) 4992-4997.

[100] N. Nobel, Dipoles align inside a nanotube, (2015).

[101] K. Yanagi, Y. Miyata, H. Kataura, Highly Stabilized β‐Carotene in Carbon Nanotubes, Advanced Materials, 18 (2006) 437-441.

[102] Y. Ren, G. Pastorin, Incorporation of hexamethylmelamine inside capped carbon nanotubes, Advanced Materials, 20 (2008) 2031-2036.

[103] S. Hampel, D. Kunze, D. Haase, K. Krämer, M. Rauschenbach, M. Ritschel, A. Leonhardt, J. Thomas, S. Oswald, V. Hoffmann, Carbon nanotubes filled with a chemotherapeutic agent: a nanocarrier mediates inhibition of tumor cell growth, (2008).

[104] M.á.H. Green, Synthesis of carbon nanotubes containing metal oxides and metals of the d-block and f-block transition metals and related studies, Journal of Materials Chemistry, 7 (1997) 545-549.

[105] J.-P. Tessonnier, L. Pesant, G. Ehret, M.J. Ledoux, C. Pham-Huu, Pd nanoparticles introduced inside multi-walled carbon nanotubes for selective hydrogenation of cinnamaldehyde into hydrocinnamaldehyde, Applied Catalysis A: General, 288 (2005) 203-210.

[106] G. Brown, S.R. Bailey, M. Novotny, R. Carter, E. Flahaut, K.S. Coleman, J.L. Hutchison, M.L.H. Green, J. Sloan, High yield incorporation and washing properties of halides incorporated into single walled carbon nanotubes, Applied Physics A: Materials Science & Processing, 76 (2003) 457-462.

[107] B. Satishkumar, A. Taubert, D. Luzzi, Filling single-wall carbon nanotubes with d-and f-metal chloride and metal nanowires, Journal of nanoscience and nanotechnology, 3 (2003) 159-163.

[108] M. Hulman, H. Kuzmany, P.M. Costa, S. Friedrichs, M.L. Green, Light-induced instability of PbO-filled single-wall carbon nanotubes, Applied physics letters, 85 (2004) 2068-2070.

[109] J. Sloan, D. Wright, A.E. York, K. Coleman, M.H. Green, J. Hutchison, Capillarity and silver nanowire formation observed in single walled carbon nanotubes, Chemical Communications, (1999) 699-700.

[110] C. Xu, J. Sloan, G. Brown, S. Bailey, V.C. Williams, S. Friedrichs, K.S. Coleman, E. Flahaut, M.L.H. Green, J.L. Hutchison, R.E. Dunin-Borkowski, 1D lanthanide halide crystals inserted into single-walled carbon nanotubes, Chemical Communications, (2000) 2427-2428.

[111] J. Mittal, M. Monthioux, H. Allouche, Synthesis of SWNT-based hybrid nanomaterials from

photolysis-enhanced chemical processes, in: Twenty-Fifth Biennial Conference on Carbon, Lexington, KY. Novel/14.2, 2001.

[112] G.-H. Jeong, R. Hatakeyama, T. Hirata, K. Tohji, K. Motomiya, N. Sato, Y. Kawazoe, Structural deformation of single-walled carbon nanotubes and fullerene encapsulation due to magnetized-plasma ion irradiation, Applied Physics Letters, 79 (2001) 4213-4215.

[113] J. Sloan, A.I. Kirkland, J.L. Hutchison, M.L. Green, Integral atomic layer architectures of 1D crystals inserted into single walled carbon nanotubes, Chemical Communications, (2002) 1319-1332.

[114] A. Tonkikh, V. Tsebro, E. Obraztsova, K. Suenaga, H. Kataura, A. Nasibulin, E. Kauppinen, E. Obraztsova, Metallization of single-wall carbon nanotube thin films induced by gas phase iodination, Carbon, 94 (2015) 768-774.

[115] L. Guan, K. Suenaga, T. Okazaki, Z. Shi, Z. Gu, S. Iijima, Coalescence of C60 molecules assisted by doped iodine inside carbon nanotubes, Journal of the American Chemical Society, 129 (2007) 8954-8955.

[116] B.-Y. Sun, Y. Sato, K. Suenaga, T. Okazaki, N. Kishi, T. Sugai, S. Bandow, S. Iijima, H. Shinohara, Entrapping of exohedral metallofullerenes in carbon nanotubes:(CsC60) n@ SWNT nano-peapods, Journal of the American Chemical Society, 127 (2005) 17972-17973.

[117] L. Guan, K. Suenaga, Z. Shi, Z. Gu, S. Iijima, Direct imaging of the alkali metal site in K-doped fullerene peapods, Physical review letters, 94 (2005) 045502.

[118] H. Kataura, Y. Maniwa, M. Abe, A. Fujiwara, T. Kodama, K. Kikuchi, H. Imahori, Y. Misaki, S. Suzuki, Y. Achiba, Optical properties of fullerene and non-fullerene peapods, Applied Physics A: Materials Science & Processing, 74 (2002) 349-354.

[119] T. Shimada, Y. Ohno, T. Okazaki, T. Sugai, K. Suenaga, S. Kishimoto, T. Mizutani, T. Inoue, R. Taniguchi, N. Fukui, Transport properties of C 78, C 90 and Dy@ C 82 fullerenes-nanopeapods by field effect transistors, Physica E: Low-dimensional Systems and Nanostructures, 21 (2004) 1089-1092.

[120] A.N. Khlobystov, D.A. Britz, G.A.D. Briggs, Molecules in carbon nanotubes, Accounts of chemical research, 38 (2005) 901-909.

[121] F. Simon, H. Kuzmany, H. Rauf, T. Pichler, J. Bernardi, H. Peterlik, L. Korecz, F. Fülöp, A. Jánossy, Low temperature fullerene encapsulation in single wall carbon nanotubes: synthesis of N@ C 60@ SWCNT, Chemical physics letters, 383 (2004) 362-367.

[122] D.E. Luzzi, B.W. Smith, R. Russo, B. Satishkumar, F. Stercel, N. Nemes, Encapsulation of metallofullerenes and metallocenes in carbon nanotubes, in: ELECTRONIC PROPERTIES OF MOLECULAR NANOSTRUCTURES: XV International Winterschool/Euroconference, AIP Publishing, 2001, pp. 622-626.

[123] H. Shiozawa, H. Rauf, T. Pichler, M. Knupfer, M. Kalbac, S. Yang, L. Dunsch, B. Büchner, D. Batchelor, H. Kataura, Effective valency of Dy ions in Dy3N@ C80 metallofullerenes and peapods, in: ELECTRONIC PROPERTIES OF NOVEL NANOSTRUCTURES: XIX International Winterschool/Euroconference on Electronic Properties of Novel Materials, AIP Publishing, 2005, pp. 325-328.

[124] K. Suenaga, K. Hirahara, S. Bandow, S. Iijima, T. Okazaki, H. Kato, H. Shinohara, Core-level spectroscopy on the valence state of encaged metal in metallofullerene-peapods, in: ELECTRONIC PROPERTIES OF MOLECULAR NANOSTRUCTURES: XV International Winterschool/Euroconference, AIP Publishing, 2001, pp. 256-260.

[125] T. Okazaki, K. Suenaga, K. Hirahara, S. Bandow, S. Iijima, H. Shinohara, Electronic and geometric structures of metallofullerene peapods, Physica B: Condensed Matter, 323 (2002) 97-99.

[126] K. Suenaga, T. Okazaki, C.-R. Wang, S. Bandow, H. Shinohara, S. Iijima, Direct Imaging of S c 2@ C 84 Molecules Encapsulated Inside Single-Wall Carbon Nanotubes by High Resolution Electron Microscopy with Atomic Sensitivity, Physical review letters, 90 (2003) 055506.

[127] K. Suenaga, R. Taniguchi, T. Shimada, T. Okazaki, H. Shinohara, S. Iijima, Evidence for the intramolecular motion of Gd atoms in a Gd2@ C92 nanopeapod, Nano Letters, 3 (2003) 1395-1398.

[128] K. Shibata, Y. Rikiishi, T. Hosokawa, Y. Haruyama, Y. Kubozono, T. Uruga, A. Fujiwara, H. Kitagawa, Y. Iwasa, Structural and electronic properties of Ce@ C 82, Physical Review B, 68 (2003) 094104.

[129] Y. Sato, K. Suenaga, S. Okubo, T. Okazaki, S. Iijima, Structures of D 5 d-C80 and I h-Er3n@ C80 fullerenes and their rotation inside carbon nanotubes demonstrated by aberration-corrected electron microscopy, Nano Letters, 7 (2007) 3704-3708.

[130] S. Sato, S. Seki, G. Luo, M. Suzuki, J. Lu, S. Nagase, T. Akasaka, Tunable charge-transport properties of Ih-C80 endohedral metallofullerenes: investigation of La2@ C80, Sc3N@ C80, and Sc3C2@ C80, Journal of the American Chemical Society, 134 (2012) 11681-11686.

[131] D.A. Britz, A.N. Khlobystov, J. Wang, A.S. O'Neil, M. Poliakoff, A. Ardavan, G.A.D. Briggs, Selective host–guest interaction of single-walled carbon nanotubes with functionalised fullerenes, Chemical communications, (2004) 176-177.

[132] F. Simon, H. Kuzmany, J. Bernardi, F. Hauke, A. Hirsch, Encapsulating C 59 N azafullerene derivatives inside single-wall carbon nanotubes, Carbon, 44 (2006) 1958-1962.

[133] F. Simon, C. Kramberger, R. Pfeiffer, H. Kuzmany, V. Zólyomi, J. Kürti, P. Singer, H. Alloul, Isotope engineering of carbon nanotube systems, Physical review letters, 95 (2005) 017401.

[134] J. Heath, Q. Zhang, S. O'Brien, R. Curl, H. Kroto, R. Smalley, The formation of long carbon chain molecules during laser vaporization of graphite, Journal of the American Chemical Society, 109 (1987) 359-363.

[135] C. Zhao, R. Kitaura, H. Hara, S. Irle, H. Shinohara, Growth of linear carbon chains inside thin double-wall carbon nanotubes, The Journal of Physical Chemistry C, 115 (2011) 13166-13170.

[136] J. Zhang, Y. Feng, H. Ishiwata, Y. Miyata, R. Kitaura, J.E. Dahl, R.M. Carlson, H. Shinohara, D. Tománek, Synthesis and transformation of linear adamantane assemblies inside carbon nanotubes, ACS nano, 6 (2012) 8674-8683.

[137] Y.F. Li, R. Hatakeyama, T. Kaneko, T. Izumida, T. Okada, T. Kato, Electrical properties of ferromagnetic semiconducting single-walled carbon nanotubes, Applied Physics Letters, 89

(2006) 083117.

[138] L. Guan, K. Suenaga, S. Iijima, Smallest carbon nanotube assigned with atomic resolution accuracy, Nano Letters, 8 (2008) 459-462.

[139] H. Qiu, Z. Shi, Z. Gu, J. Qiu, Controllable preparation of triple-walled carbon nanotubes and their growth mechanism, Chemical Communications, (2007) 1092-1094.

[140] D.M. Guldi, M. Marcaccio, D. Paolucci, F. Paolucci, N. Tagmatarchis, D. Tasis, E. Vάzquez, M. Prato, Single ‐ Wall Carbon Nanotube – Ferrocene Nanohybrids: Observing Intramolecular Electron Transfer in Functionalized SWNTs, Angewandte Chemie, 115 (2003) 4338-4341.

[141] L.-J. Li, A. Khlobystov, J. Wiltshire, G. Briggs, R. Nicholas, Diameter-selective encapsulation of metallocenes in single-walled carbon nanotubes, Nature Materials, 4 (2005) 481-485.

[142] L. Guan, Z. Shi, M. Li, Z. Gu, Ferrocene-filled single-walled carbon nanotubes, Carbon, 43 (2005) 2780-2785.

[143] H. Shiozawa, T. Pichler, A. Grϋneis, R. Pfeiffer, H. Kuzmany, Z. Liu, K. Suenaga, H. Kataura, A Catalytic Reaction Inside a Single ‐ Walled Carbon Nanotube, Advanced Materials, 20 (2008) 1443-1449.

[144] D.A. Morgan, J. Sloan, M.L.H. Green, Direct imaging of o-carborane molecules within single walled carbon nanotubes, Chemical Communications, (2002) 2442-2443.

[145] M. Koshino, T. Tanaka, N. Solin, K. Suenaga, H. Isobe, E. Nakamura, Imaging of single organic molecules in motion, Science, 316 (2007) 853-853.

[146] T. Takenobu, T. Takano, M. Shiraishi, Y. Murakami, M. Ata, H. Kataura, Y. Achiba, Y. Iwasa, Stable and controlled amphoteric doping by encapsulation of organic molecules inside carbon nanotubes, Nature materials, 2 (2003) 683-688.

[147] H. Kataura, Y. Maniwa, T. Kodama, K. Kikuchi, S. Suzuki, Y. Achiba, K. Sugiura, S. Okubo, K. Tsukagoshi, One ‐ dimensional System in Carbon Nanotubes, in: MOLECULAR NANOSTRUCTURES: XVII International Winterschool Euroconference on Electronic Properties of Novel Materials, AIP Publishing, 2003, pp. 349-353.

[148] M.A. Loi, J. Gao, F. Cordella, P. Blondeau, E. Menna, B. Bάrtovά, C. Hέbert, S. Lazar, G.A. Botton, M. Milko, Encapsulation of Conjugated Oligomers in Single ‐ Walled Carbon Nanotubes: Towards Nanohybrids for Photonic Devices, Advanced Materials, 22 (2010) 1635-1639.

[149] J. Sloan, G. Matthewman, C. Dyer-Smith, A.-Y. Sung, Z. Liu, K. Suenaga, A.I. Kirkland, E. Flahaut, Direct imaging of the structure, relaxation, and sterically constrained motion of encapsulated tungsten polyoxometalate Lindqvist ions within carbon nanotubes, Acs Nano, 2 (2008) 966-976.

[150] D.A. Morgan, J. Sloan, M.L. Green, Direct imaging of o-carborane molecules within single walled carbon nanotubes, Chem. Commun., (2002) 2442-2443.

[151] E. Borowiak-Palen, Silver intercalated carbon nanotubes, 786 (2005) 236-239.

[152] P. Corio, A. Santos, P. Santos, M. Temperini, V. Brar, M. Pimenta, M. Dresselhaus,

Characterization of single wall carbon nanotubes filled with silver and with chromium compounds, Chemical physics letters, 383 (2004) 475-480.

[153] L. Guan, K. Suenaga, S. Okubo, T. Okazaki, S. Iijima, Metallic wires of lanthanum atoms inside carbon nanotubes, Journal of the American Chemical Society, 130 (2008) 2162-2163.

[154] R. Nakanishi, R. Kitaura, P. Ayala, H. Shiozawa, K. de Blauwe, P. Hoffmann, D. Choi, Y. Miyata, T. Pichler, H. Shinohara, Electronic structure of Eu atomic wires encapsulated inside single-wall carbon nanotubes, Physical Review B, 86 (2012) 115445.

[155] R. Kitaura, R. Nakanishi, T. Saito, H. Yoshikawa, K. Awaga, H. Shinohara, High‐Yield Synthesis of Ultrathin Metal Nanowires in Carbon Nanotubes, Angewandte Chemie International Edition, 48 (2009) 8298-8302.

[156] J.-P. Cleuziou, W. Wernsdorfer, T. Ondarcuhu, M. Monthioux, Electrical detection of individual magnetic nanoparticles encapsulated in carbon nanotubes, ACS nano, 5 (2011) 2348-2355.

[157] E. Borowiak-Palen, E. Mendoza, A. Bachmatiuk, M.H. Rummeli, T. Gemming, J. Nogues, V. Skumryev, R.J. Kalenczuk, T. Pichler, S.R.P. Silva, Iron filled single-wall carbon nanotubes – A novel ferromagnetic medium, Chemical Physics Letters, 421 (2006) 129-133.

[158] J. Jorge, E. Flahaut, F. Gonzalez-Jimenez, G. Gonzalez, J. Gonzalez, E. Belandria, J.M. Broto, B. Raquet, Preparation and characterization of α-Fe nanowires located inside double wall carbon nanotubes, Chemical Physics Letters, 457 (2008) 347-351.

[159] M.V. Kharlamova, M. Sauer, T. Saito, Y. Sato, K. Suenaga, T. Pichler, H. Shiozawa, Doping of single-walled carbon nanotubes controlled via chemical transformation of encapsulated nickelocene, Nanoscale, 7 (2015) 1383-1391.

[160] H. Shiozawa, A. Briones-Leon, O. Domanov, G. Zechner, Y. Sato, K. Suenaga, T. Saito, M. Eisterer, E. Weschke, W. Lang, Nickel clusters embedded in carbon nanotubes as high performance magnets, Scientific reports, 5 (2015).

[161] E. Philp, J. Sloan, A.I. Kirkland, R.R. Meyer, S. Friedrichs, J.L. Hutchison, M.L. Green, An encapsulated helical one-dimensional cobalt iodide nanostructure, Nature materials, 2 (2003) 788-791.

[162] M. Chernysheva, A. Eliseev, A. Lukashin, Y.D. Tretyakov, S. Savilov, N. Kiselev, O. Zhigalina, A. Kumskov, A. Krestinin, J. Hutchison, Filling of single-walled carbon nanotubes by CuI nanocrystals via capillary technique, Physica E: Low-dimensional Systems and Nanostructures, 37 (2007) 62-65.

[163] P.V. Fedotov, A.A. Tonkikh, E.A. Obraztsova, A.G. Nasibulin, E.I. Kauppinen, A.L. Chuvilin, E.D. Obraztsova, Optical properties of single‐walled carbon nanotubes filled with CuCl by gas‐phase technique, physica status solidi (b), 251 (2014) 2466-2470.

[164] E. Flahaut, J. Sloan, S. Friedrichs, A.I. Kirkland, K. Coleman, V. Williams, N. Hanson, J. Hutchison, M.L. Green, Crystallization of 2H and 4H PbI2 in carbon nanotubes of varying diameters and morphologies, Chemistry of materials, 18 (2006) 2059-2069.

[165] J. Sloan, S. Friedrichs, E. Flahaut, G. Brown, S. Bailey, K. Coleman, C. Xu, M. Green, J. Hutchison, A. Kirkland, The characterization of sub-nanometer scale structures within single

walled carbon nanotubes, in: ELECTRONIC PROPERTIES OF MOLECULAR NANOSTRUCTURES: XV International Winterschool/Euroconference, AIP Publishing, 2001, pp. 277-282.

[166] E. Borowiak-Palen, M. Ruemmeli, T. Gemming, T. Pichler, R. Kalenczuk, S. Silva, Silver filled single-wall carbon nanotubes—synthesis, structural and electronic properties, Nanotechnology, 17 (2006) 2415.

[167] R. Carter, J. Sloan, A.I. Kirkland, R.R. Meyer, P.J. Lindan, G. Lin, M.L. Green, A. Vlandas, J.L. Hutchison, J. Harding, Correlation of structural and electronic properties in a new low-dimensional form of mercury telluride, Phys Rev Lett, 96 (2006) 215501.

[168] L.-J. Li, T.-W. Lin, J. Doig, I. Mortimer, J. Wiltshire, R. Taylor, J. Sloan, M. Green, R. Nicholas, Crystal-encapsulation-induced band-structure change in single-walled carbon nanotubes: photoluminescence and Raman spectra, Physical Review B, 74 (2006) 245418.

[169] C.E. Giusca, V. Stolojan, J. Sloan, F. Börrnert, H. Shiozawa, K. Sader, M.H. Rümmeli, B. Büchner, S.R.P. Silva, Confined crystals of the smallest phase-change material, Nano letters, 13 (2013) 4020-4027.

[170] D. Ugarte, A. Chatelain, W. De Heer, Nanocapillarity and chemistry in carbon nanotubes, Science, 274 (1996) 1897.

[171] E. Dujardin, T.W. Ebbesen, A. Krishnan, M.M. Treacy, Wetting of single shell carbon nanotubes, Advanced Materials, 10 (1998) 1472-1475.

[172] M. Monthioux, E. Flahaut, J.-P. Cleuziou, Hybrid carbon nanotubes: strategy, progress, and perspectives, Journal of materials research, 21 (2006) 2774-2793.

[173] M. Wilson, P.A. Madden, Growth of ionic crystals in carbon nanotubes, Journal of the American Chemical Society, 123 (2001) 2101-2102.

[174] G. Kim, Y. Kim, J. Ihm, Encapsulation and polymerization of acetylene molecules inside a carbon nanotube, Chemical physics letters, 415 (2005) 279-282.

[175] Y. Guo, Y. Kong, W. Guo, H. Gao, Structural transition of copper nanowires confined in single-walled carbon nanotubes, Journal of Computational and Theoretical Nanoscience, 1 (2004) 93-98.

[176] S.B. Fagan, A. Souza Filho, J. Mendes Filho, P. Corio, M. Dresselhaus, Electronic properties of Ag-and CrO 3-filled single-wall carbon nanotubes, Chemical physics letters, 406 (2005) 54-59.

[177] M. Weissmann, G. Garcia, M. Kiwi, R. Ramirez, Theoretical study of carbon-coated iron nanowires, Physical Review B, 70 (2004) 201401.

[178] D.E. Luzzi, B.W. Smith, Carbon cage structures in single wall carbon nanotubes: a new class of materials, Carbon, 38 (2000) 1751-1756.

[179] M. Dresselhaus, G. Dresselhaus, R. Saito, Physics of carbon nanotubes, Carbon, 33 (1995) 883-891.

[180] S. Bandow, M. Takizawa, K. Hirahara, M. Yudasaka, S. Iijima, Raman scattering study of double-wall carbon nanotubes derived from the chains of fullerenes in single-wall carbon

nanotubes, Chemical Physics Letters, 337 (2001) 48-54.

[181] C. Arrondo, M. Monthioux, K. Kishita, M. Le Lay, In‐situ coalescence of aligned C60 molecules in Peapods, in: ELECTRONIC PROPERTIES OF NOVEL NANOSTRUCTURES: XIX International Winterschool/Euroconference on Electronic Properties of Novel Materials, AIP Publishing, 2005, pp. 329-332.

[182] Y. Sakurabayashi, M. Monthioux, K. Kishita, Y. Suzuki, T. Kondo, M. Le Lay, Tailoring double‐wall carbon nanotubes?, in: MOLECULAR NANOSTRUCTURES: XVII International Winterschool Euroconference on Electronic Properties of Novel Materials, AIP Publishing, 2003, pp. 302-305.

[183] C. Kramberger, A. Waske, K. Biedermann, T. Pichler, T. Gemming, B. Büchner, H. Kataura, Tailoring carbon nanostructures via temperature and laser irradiation, Chemical physics letters, 407 (2005) 254-259.

[184] M. Kalbáč, L. Kavan, L. Juha, S. Civiš, M. Zukalová, M. Bittner, P. Kubát, V. Vorlíček, L. Dunsch, Transformation of fullerene peapods to double-walled carbon nanotubes induced by UV radiation, Carbon, 43 (2005) 1610-1616.

[185] P. Puech, F. Puccianti, R. Bacsa, C. Arrondo, V. Paillard, A. Bassil, M. Monthioux, E. Flahaut, F. Bardé, W. Bacsa, Ultraviolet photon absorption in single-and double-wall carbon nanotubes and peapods: Heating-induced phonon line broadening, wall coupling, and transformation, Physical Review B, 76 (2007) 054118.

[186] P. Puech, F. Puccianti, R. Bacsa, C. Arrondo, M. Monthioux, W. Bacsa, V. Paillard, A. Bassil, F. Barde, Thermal transfer in SWNTs and peapods under UV-irradiation, Physica Status Solidi-B-Basic Solid State Physics, 244 (2007) 4064-4068.

[187] M. Berd, P. Puech, A. Righi, A. Benfdila, M. Monthioux, Resonant Laser‐Induced Formation of Double‐Walled Carbon Nanotubes from Peapods under Ambient Conditions, Small, 8 (2012) 2045-2052.

[188] V. Prudkovskiy, M. Berd, E. Pavlenko, K. Katin, M. Maslov, P. Puech, M. Monthioux, W. Escoffier, M. Goiran, B. Raquet, Electronic coupling in fullerene-doped semiconducting carbon nanotubes probed by Raman spectroscopy and electronic transport, Carbon, 57 (2013) 498-506.

[189] M. Yoon, S. Berber, D. Tománek, Energetics and packing of fullerenes in nanotube peapods, Physical Review B, 71 (2005) 155406.

[190] L. Cabana, B. Ballesteros, E. Batista, C. Magén, R. Arenal, J. Oró‐Solé, R. Rurali, G. Tobias, Synthesis of PbI2 Single‐Layered Inorganic Nanotubes Encapsulated Within Carbon Nanotubes, Advanced Materials, 26 (2014) 2016-2021.

[191] R. Kreizman, S.Y. Hong, J. Sloan, R. Popovitz‐Biro, A. Albu‐Yaron, G. Tobias, B. Ballesteros, B.G. Davis, M.L. Green, R. Tenne, Core–shell PbI2@ WS2 inorganic nanotubes from capillary wetting, Angewandte Chemie International Edition, 48 (2009) 1230-1233.

[192] J. Sloan, S. Friedrichs, R.R. Meyer, A.I. Kirkland, J.L. Hutchison, M.L. Green, Structural changes induced in nanocrystals of binary compounds confined within single walled carbon nanotubes: a brief review, Inorganica chimica acta, 330 (2002) 1-12.

[193] J. Sloan, S.J. Grosvenor, S. Friedrichs, A.I. Kirkland, J.L. Hutchison, M.L. Green, A One‐Dimensional BaI2 Chain with Five‐ and Six‐Coordination, Formed within a Single‐Walled Carbon Nanotube, Angewandte Chemie International Edition, 41 (2002) 1156-1159.

[194] R. Senga, H.-P. Komsa, Z. Liu, K. Hirose-Takai, A.V. Krasheninnikov, K. Suenaga, Atomic structure and dynamic behaviour of truly one-dimensional ionic chains inside carbon nanotubes, Nature materials, 13 (2014) 1050-1054.

[195] P. Utko, J. Nygard, M. Monthioux, L. Noé, Sub-Kelvin transport spectroscopy of fullerene peapod quantum dots, Applied physics letters, 89 (2006) 3118.

[196] H. Hongo, F. Nihey, M. Yudasaka, T. Ichihashi, S. Iijima, Transport properties of single-wall carbon nanotubes with encapsulated C 60, Physica B: Condensed Matter, 323 (2002) 244-245.

[197] P. Utko, R. Ferone, I. Krive, R. Shekhter, M. Jonson, M. Monthioux, L. Noé, J. Nygård, Coupling between Electronic and Vibrational Excitations in Carbon Nanotubes Filled with C60 Fullerenes, Acta Physica Polonica A, 120 (2011) 839-841.

[198] X. Liu, T. Pichler, M. Knupfer, M. Golden, J. Fink, H. Kataura, Y. Achiba, K. Hirahara, S. Iijima, Filling factors, structural, and electronic properties of C 60 molecules in single-wall carbon nanotubes, Physical Review B, 65 (2002) 045419.

[199] T. Pichler, H. Kuzmany, H. Kataura, Y. Achiba, Metallic polymers of C 60 inside single-walled carbon nanotubes, Physical review letters, 87 (2001) 267401.

[200] F. Simon, D. Quintavalle, A. Jánossy, B. Náfrádi, L. Forró, H. Kuzmany, F. Hauke, A. Hirsch, J. Mende, M. Mehring, Metallic bundles of single‐wall carbon nanotubes probed by electron spin resonance, physica status solidi (b), 244 (2007) 3885-3889.

[201] A. Eliasen, J. Paaske, K. Flensberg, S. Smerat, M. Leijnse, M.R. Wegewijs, H.I. Jørgensen, M. Monthioux, J. Nygård, Transport via coupled states in a C 60 peapod quantum dot, Physical Review B, 81 (2010) 155431.

[202] P. Utko, R. Ferone, I.V. Krive, R.I. Shekhter, M. Jonson, M. Monthioux, L. Noé, J. Nygård, Nanoelectromechanical coupling in fullerene peapods probed by resonant electrical transport experiments, Nature communications, 1 (2010) 37.

[203] T.A. Murphy, T. Pawlik, A. Weidinger, M. Höhne, R. Alcala, J.-M. Spaeth, Observation of atomlike nitrogen in nitrogen-implanted solid C 60, Physical review letters, 77 (1996) 1075.

[204] F. Simon, H. Kuzmany, B. Náfrádi, T. Fehér, L. Forró, F. Fülöp, A. Jánossy, L. Korecz, A. Rockenbauer, F. Hauke, Magnetic fullerenes inside single-wall carbon nanotubes, Physical review letters, 97 (2006) 136801.

[205] G. Chen, J. Qiu, H. Qiu, Filling double-walled carbon nanotubes with AgCl nanowires, Scripta Materialia, 58 (2008) 457-460.

[206] A. Eliseev, L. Yashina, N. Verbitskiy, M. Brzhezinskaya, M. Kharlamova, M. Chernysheva, A. Lukashin, N. Kiselev, A. Kumskov, B. Freitag, Interaction between single walled carbon nanotube and 1D crystal in CuX@ SWCNT (X= Cl, Br, I) nanostructures, Carbon, 50 (2012) 4021-4039.

[207] A. Kumskov, V. Zhigalina, A. Chuvilin, N. Verbitskiy, A. Ryabenko, D. Zaytsev, A. Eliseev, N.

Kiselev, The structure of 1D and 3D CuI nanocrystals grown within 1.5–2.5 nm single wall carbon nanotubes obtained by catalyzed chemical vapor deposition, Carbon, 50 (2012) 4696-4704.

[208] N. Kiselev, A. Kumskov, V. Zhigalina, N. Verbitskiy, L. Yashina, A. Chuvilin, A. Vasiliev, A. Eliseev, The structure and electronic properties of copper iodide 1D nanocrystals within single walled carbon nanotubes, in: Journal of Physics: Conference Series, IOP Publishing, 2013, pp. 012035.

[209] M. Kharlamova, L. Yashina, A. Lukashin, Charge transfer in single-walled carbon nanotubes filled with cadmium halogenides, Journal of Materials Science, 48 (2013) 8412-8419.

[210] E.L. Sceats, J.C. Green, Noncovalent interactions between organometallic metallocene complexes and single-walled carbon nanotubes, The Journal of chemical physics, 125 (2006) 154704-154704.

[211] X. Liu, H. Kuzmany, P. Ayala, M. Calvaresi, F. Zerbetto, T. Pichler, Selective Enhancement of Photoluminescence in Filled Single - Walled Carbon Nanotubes, Advanced Functional Materials, 22 (2012) 3202-3208.

[212] M. Sauer, H. Shiozawa, P. Ayala, G. Ruiz-Soria, X. Liu, A. Chernov, S. Krause, K. Yanagi, H. Kataura, T. Pichler, Internal charge transfer in metallicity sorted ferrocene filled carbon nanotube hybrids, Carbon, 59 (2013) 237-245.

[213] H. Shiozawa, T. Pichler, C. Kramberger, M. Rümmeli, D. Batchelor, Z. Liu, K. Suenaga, H. Kataura, S.R.P. Silva, Screening the missing electron: nanochemistry in action, Physical review letters, 102 (2009) 046804.

[214] C.Z. Loebick, M. Majewska, F. Ren, G.L. Haller, L.D. Pfefferle, Fabrication of discrete nanosized cobalt particles encapsulated inside single-walled carbon nanotubes, The Journal of Physical Chemistry C, 114 (2010) 11092-11097.

[215] C. Tripisciano, S. Costa, R. Kalenczuk, E. Borowiak-Palen, Cisplatin filled multiwalled carbon nanotubes–a novel molecular hybrid of anticancer drug container, The European Physical Journal B, 75 (2010) 141-146.

[216] M. Arlt, D. Haase, S. Hampel, S. Oswald, A. Bachmatiuk, R. Klingeler, R. Schulze, M. Ritschel, A. Leonhardt, S. Fuessel, Delivery of carboplatin by carbon-based nanocontainers mediates increased cancer cell death, Nanotechnology, 21 (2010) 335101.

[217] B. Sitharaman, K.R. Kissell, K.B. Hartman, L.A. Tran, A. Baikalov, I. Rusakova, Y. Sun, H.A. Khant, S.J. Ludtke, W. Chiu, Superparamagnetic gadonanotubes are high-performance MRI contrast agents, Chem. Commun., (2005) 3915-3917.

[218] J.H. Choi, F.T. Nguyen, P.W. Barone, D.A. Heller, A.E. Moll, D. Patel, S.A. Boppart, M.S. Strano, Multimodal biomedical imaging with asymmetric single-walled carbon nanotube/iron oxide nanoparticle complexes, Nano letters, 7 (2007) 861-867.

[219] X. Pan, Z. Fan, W. Chen, Y. Ding, H. Luo, X. Bao, Enhanced ethanol production inside carbon-nanotube reactors containing catalytic particles, Nature materials, 6 (2007) 507-511.

[220] W. Chen, Z. Fan, X. Pan, X. Bao, Effect of confinement in carbon nanotubes on the activity of Fischer-Tropsch iron catalyst, Journal of the American Chemical Society, 130 (2008)

9414-9419.

[221] H. Zhang, X. Pan, J.J. Liu, W. Qian, F. Wei, Y. Huang, X. Bao, Enhanced Catalytic Activity of Sub‐nanometer Titania Clusters Confined inside Double‐Wall Carbon Nanotubes, ChemSusChem, 4 (2011) 975-980.

[222] G. Lota, E. Frackowiak, J. Mittal, M. Monthioux, High performance supercapacitor from hybrid-nanotube-based electrodes, Chem. Phys. Lett, (2006).

[223] H. Zhang, H. Song, X. Chen, J. Zhou, H. Zhang, Preparation and electrochemical performance of SnO_2@ carbon nanotube core–shell structure composites as anode material for lithium-ion batteries, Electrochimica Acta, 59 (2012) 160-167.

[224] L. Liao, J. Li, C. Liu, Z. Xu, W. Wang, S. Liu, X. Bai, E. Wang, Field emission of GaN-filled carbon nanotubes: high and stable emission current, Journal of nanoscience and nanotechnology, 7 (2007) 1080-1083.

[225] G.A. Domrachev, A.M. Ob'edkov, B.S. Kaverin, A.A. Zaitsev, S.N. Titova, A.I. Kirillov, A.S. Strahkov, S.Y. Ketkov, E.G. Domracheva, K.B. Zhogova, MOCVD Synthesis of Germanium Filled “Diamondlike” Carbon Nanotubes and Microtubes from Organogermanium Precursors and Their Field‐Emission Properties, Chemical Vapor Deposition, 12 (2006) 357-363.

[226] C. Yang, Y. Li-Gang, W. Ming-Sheng, Z. Qi-Feng, W. Jin-Lei, Low-field emission from iron oxide- filled carbon nanotube arrays, Chinese Physics Letters, 22 (2005) 911.

[227] R. Lv, F. Kang, D. Zhu, Y. Zhu, X. Gui, J. Wei, J. Gu, D. Li, K. Wang, D. Wu, Enhanced field emission of open-ended, thin-walled carbon nanotubes filled with ferromagnetic nanowires, Carbon, 47 (2009) 2709-2715.

[228] F. Wolny, U. Weissker, T. Mühl, A. Leonhardt, S. Menzel, A. Winkler, B. Büchner, Iron-filled carbon nanotubes as probes for magnetic force microscopy, Journal of Applied Physics, 104 (2008) 064908.

[229] A. Winkler, T. Mühl, S. Menzel, R. Kozhuharova-Koseva, S. Hampel, A. Leonhardt, B. Büchner, Magnetic force microscopy sensors using iron-filled carbon nanotubes, Journal of applied physics, 99 (2006) 104905.

[230] F. Wolny, U. Weissker, T. Mühl, M.U. Lutz, C. Müller, A. Leonhardt, B. Büchner, Stable magnetization of iron filled carbon nanotube MFM probes in external magnetic fields, Journal of Physics: Conference Series, IOP Publishing, 2010, pp. 112011.

Chapter 2 Investigation on the filling mechanisms of DWCNTs with foreign phases and of the resulting peculiar structures of the latter

2.1 Introduction

Although various examples of fillings of CNTs have been reported already, filling mechanisms are not well understood yet, especially when considering the molten phase method. As described in chapter 1, though early works proposed that the filling of CNTs can be described by a nanocapillary wetting effect driven by Laplace equation [1,2], factors which may play a role in the filling process are many (e.g., morphology of CNTs, surface tension, viscosity, vapour pressure, etc. [3]) and which ones are the most relevant is not clear yet. Therefore, two goals were targeted. One was to tentatively understand better the filling mechanisms, what previous works have more or less failed to do so far. This will be treated in this Chapter. Another was to investigate the ability of the encapsulated phases to be transformed *in situ* by chemical routes, and this will be treated in Chapter 3.

In this chapter, filling CNTs with various metal halides as well as iodine via the molten phase method was performed and the filling rate achieved in each case was estimated from high-resolution transmission electron microscopy (HRTEM) data. Halides were selected as filling materials because early studies demonstrated that raw SWCNTs with closed ends could be directly filled with molten halides or iodine, thereby skipping the preliminary opening process, and revealing the chemical reactivity of halides or iodine towards aromatic carbon [4,5]. This makes the molten phase method favourable for synthesizing CNTs filled with halide or iodine crystals due to the simplicity of the related filling procedure. Hence, the molten phase method was employed in our work for filling CNTs.

First, based on previous results from the literature showing that filling CNTs with molten PbI_2 was able to achieve high filling rates, we have attempted to assess the importance in the filling process of CNT-related parameters such as the number of walls, CNT inner diameter, and inner CNT surface energetics. To do so, various types of CNTs including DWCNTs, few-walled CNTs (FWCNTs) with concentric texture, MWCNTs with herringbone texture, and boron nitride nanotubes (BNNTs) were filled with PbI_2. Second, to evaluate the influence of possibly relevant physical and chemical properties of filling materials on the filling mechanisms and rate, DWCNTs were chosen as host tubes because they are more robust than SWCNTs due to the protection of outer walls while the inner cavity of DWCNTs can be as small as or even smaller than that of SWCNTs, which is more likely to promote peculiar structures, hence peculiar properties. Then, filling DWCNTs with a series of metal halides (mostly iodides, but also $PbCl_2$, PbF_2, etc.) as well as iodine was performed while data on the filling material properties were gathered from the literature.

2.2 Preparing/gathering host CNTs and BNNTs

2.2.1 CCVD synthesis of DWCNTs/FWCNTS

The DWCNTs were prepared by a well-established CCVD method in our group [6-8]. The catalyst used for the growth of DWCNTs is a mixed oxide of Mg, Co and Mo, whose formula can be written as $Mg_{0.99}Co_{0.0075}Mo_{0.0025}O$. This catalyst was prepared by a combustion route using citric acid as the fuel. First, three precursors, ammonium heptamolybdate, cobalt nitrate and magnesium nitrate were added into an aqueous citric acid solution. After full dissolution of the precursors, the solution was transferred into a crystallising dish and placed into an oven (with open door) preheated at 550°C for 15 min. The combustion occurred and a solid product was obtained. Due to the incomplete decomposition of citric acid, a calcination step is required to eliminate the residual carbon contamination in the solid product. Thereby, the obtained product was ground into a homogeneous powder and then heated in a furnace under air flow at 450°C for 1h.

An alumina boat filled with the as-prepared catalyst powder was placed in the middle of a horizontal tubular furnace, in H_2/CH_4 atmosphere (18 mol.% CH_4, 15 L/h). H_2 is used to selectively reduce the oxide in the catalyst and CH_4 acts as the carbon source. H_2 is also needed to moderate the decomposition of CH_4 at 1000°C. The furnace was heated to 1000°C from RT at a heating rate of 300°C/h and then immediately cooled down to RT with a rate of 300°C/h, without dwell at 1000°C.

FWCNTs were prepared by the same CCVD method as described above except for some experimental parameters which were modified. For instance, the composition of the catalyst used for growing FWCNTs can be described as $Mg_{0.9}Co_{0.033}Mo_{0.067}O$, and the content of CH_4 in the

H_2/CH_4 mixture was increased to 36 mol.% (twice as much than what was used for growing DWCNTs).

2.2.2 Extraction of DWCNTs/FWCNTs

In order to separate the carbon nanotubes from the catalyst after the CCVD process, an extraction process is required. The MgO in the obtained composite powder can be easily removed by dissolution in concentrated hydrochloric acid (HCl 37%). Meanwhile, the unreacted metal nanoparticles (Co, Mo) during the CCVD process which are not surrounded by carbon shells or present into the CNTs can also be eliminated by HCl. Because the reaction between Co particles and acid can produce $CoCl_4^{2-}$ during the extraction process, a blue colour was observed. HCl is known to be a non-oxidizing acid thus no damage to the CNTs or carbon shells occurred in this step.

After leaving the composite powder in acid solution for the night, the suspension was filtered by a Millipore vacuum system using a cellulose nitrate membrane with a pore size of 0.45 µm. Then the solid was washed with deionized water for several times until neutral pH was obtained. The powder was recovered on the membrane and transferred into a glass vial. A small amount of deionized water was added into the vial and the vial was sonicated for several seconds to disperse the powder. Subsequently, the suspension was frozen, and then the sample was finally freeze-dried.

Fig. 2.1 shows typical TEM images of raw DWCNTs before filling. Although Fig. 2.1 illustrates the variety of phases and morphologies present in the material, the large majority of the tubes are DWCNTs indeed. They exhibit the concentric texture, consistently with the limited number of walls. The inner and outer diameters of the DWCNTs ranged from 0.5 to 2.5 nm (most frequently 1-2 nm) and from 1.2 to 3.2 nm, respectively [8]. A few CNTs with more than 2 walls are also present as illustrated in Fig. 2.1c.

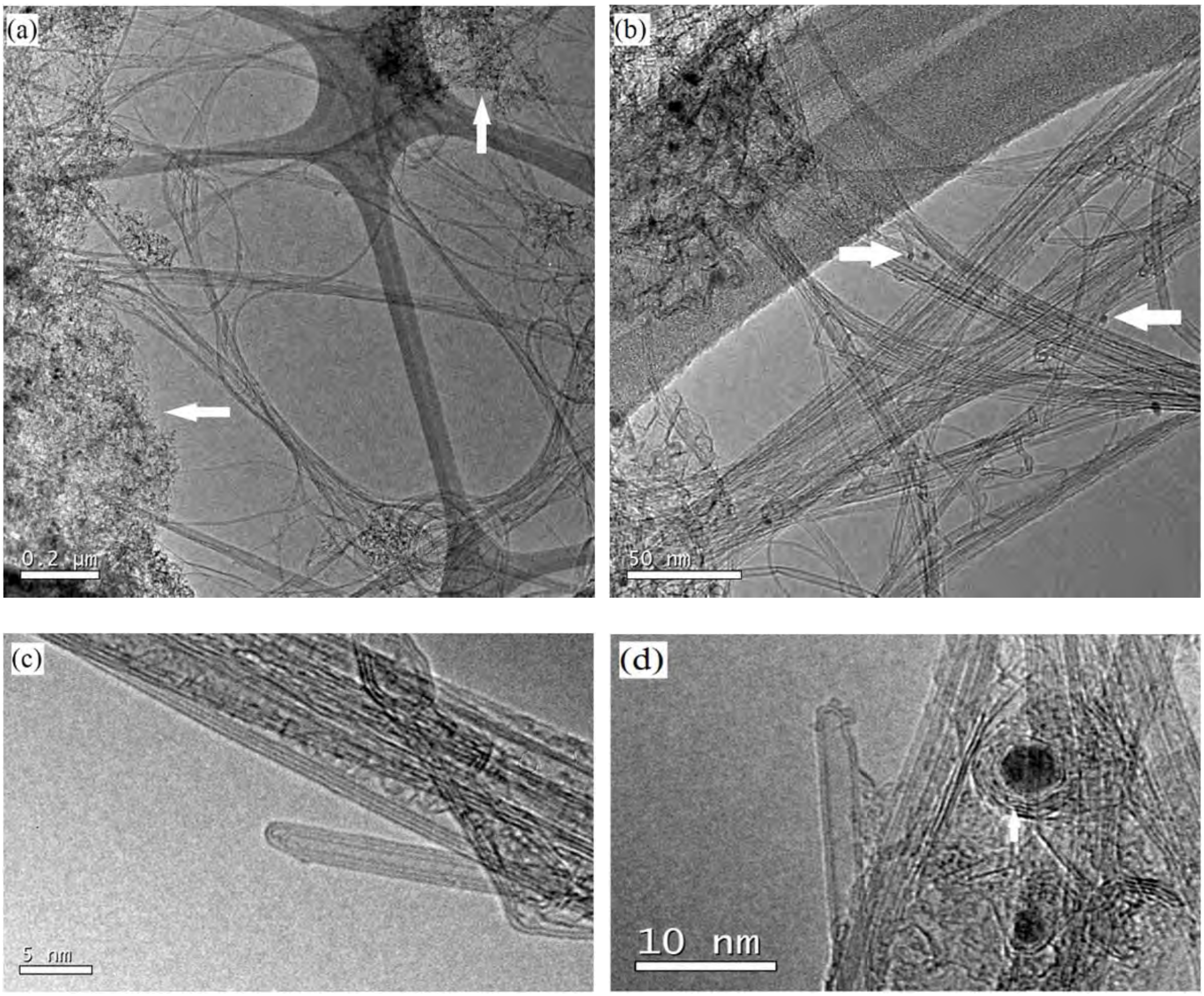

Fig. 2.1 - TEM images of raw DWCNTs showing (a) "diaphanous" carbon (arrows, see text); (b) metal nanoparticles (arrows); (c) a 3-wall nanotube with closed tip and a 4-wall tube; (d) a double-walled nanotube with closed tip and residual cobalt catalyst nanoparticles encapsulated in carbon shells (white arrow).

Then, Fig. 2.2 shows typical TEM images and histograms representing the distribution of number of walls and inner and outer diameters for raw FWCNTs before filling. It can be seen that among 93 individual CNTs, most of the tubes have 2~6 walls with inner diameters ranging from 0.5 to 6 nm with the most represented diameters in the range 1.5-3.5 nm.

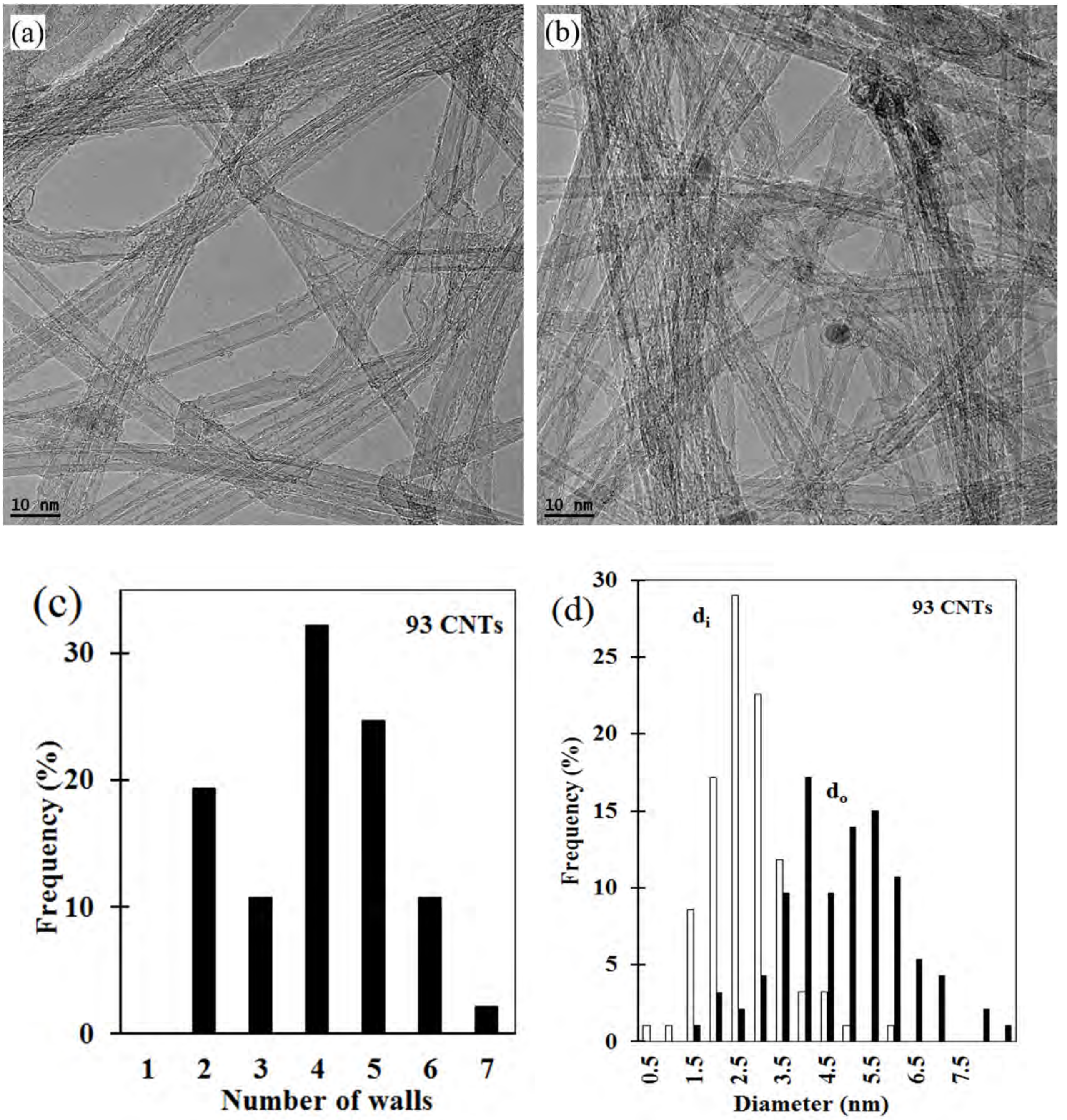

Fig. 2.2 - (a) and (b) are HRTEM images of FWCNTs showing the presence of tubes with 2~6 walls; (c) and (d) are distributions of the numbers of walls and inner (d_i) and outer (d_o) diameters for the whole population (established from 93 individual CNTs).

2.2.3 Nanotubes from external suppliers

Purified SWCNTs prepared by the arc process (Nanocarblab, Russia) were used. They exhibit a large majority of tubes with the regular 1.3-1.4 nm diameter, and the oxidative purification process has induced openings large enough for allowing sublimated C_{60} (0.7 nm diameter) to enter the

SWCNT cavity. Also, two other kinds of MWCNTs were used for filling in this chapter. One of them exhibited the concentric texture and was produced by the arc discharge method (Nanoledge, France), denoted as c-MWCNTs-a. They mostly exhibit inner diameters in the range 2-10 nm and a large number of walls, typically higher than 10. The other one exhibited the herringbone texture and was produced by the floating catalyst CCVD method (Pyrograf-III grade from Applied Sciences Inc.), denoted as h-MWCNTs. The average outer diameter of the h-MWCNTs ranges from 125 to 150 nm and the average inner diameter ranges from 50 nm to 70 nm. Those were selected because, as opposed to many other h-MWCNT batches from other sources, the bamboo texture, which usually comes along with the herringbone texture, is rare here (and the bamboo texture is obviously unwanted because the presence of compartments delimiting the inner cavity is detrimental to the filling)

HRTEM images of c-MWCNTs-a are shown in Fig. 2.3 and it can be seen that most CNTs have more than 10 graphene walls showing a ‘concentric’ texture.

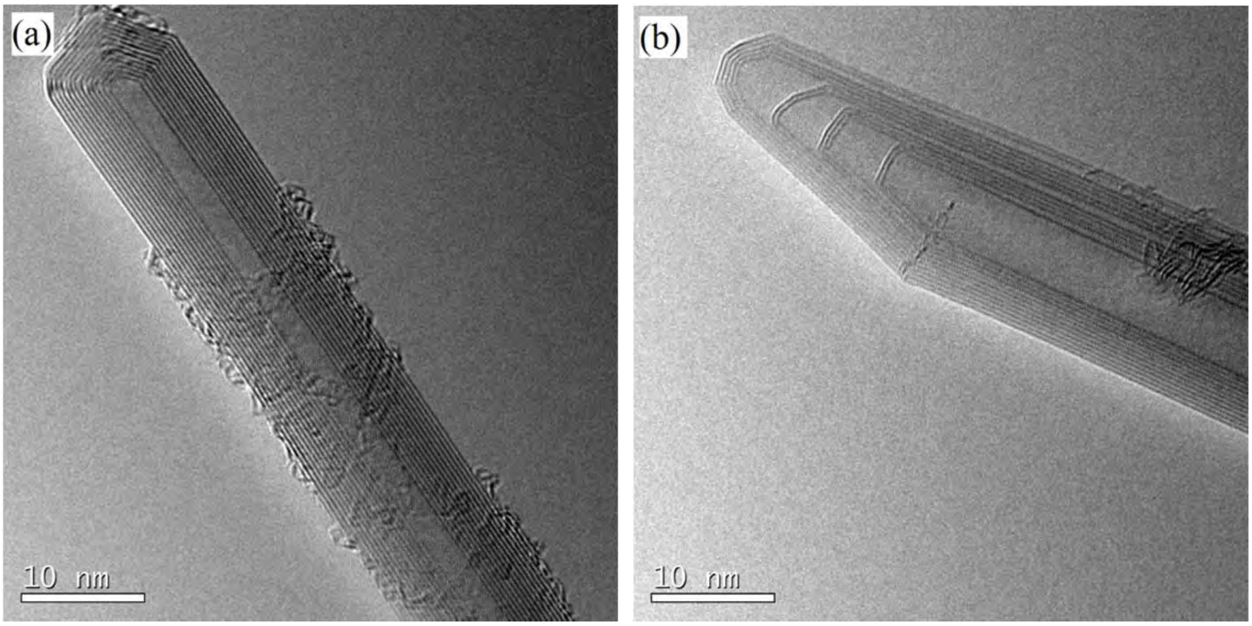

Fig. 2.3 - HRTEM images of c-MWCNTs-a showing (a) a 13-wall CNT with closed tip and (b) a 12-wall CNT with closed tip.

TEM images of h-MWCNTs are illustrated in Fig. 2.4. As seen, tubes with open tips or closed tips are both present in the sample (see Fig, 2.4a) and the inner graphene walls of the tube are oblique to the tube axis forming the ‘herringbone’ texture (see Fig. 2.4b). It is worth noting that the original h-MWCNT tube, in which the graphene nanotexture is perfect, was subsequently coated by a pyrolytic carbon layer in which graphenes are more or less concentrically displayed while their nanotexture is much lower than for the inner part. This double texture is typical for the ASI Pyrograf-III product.

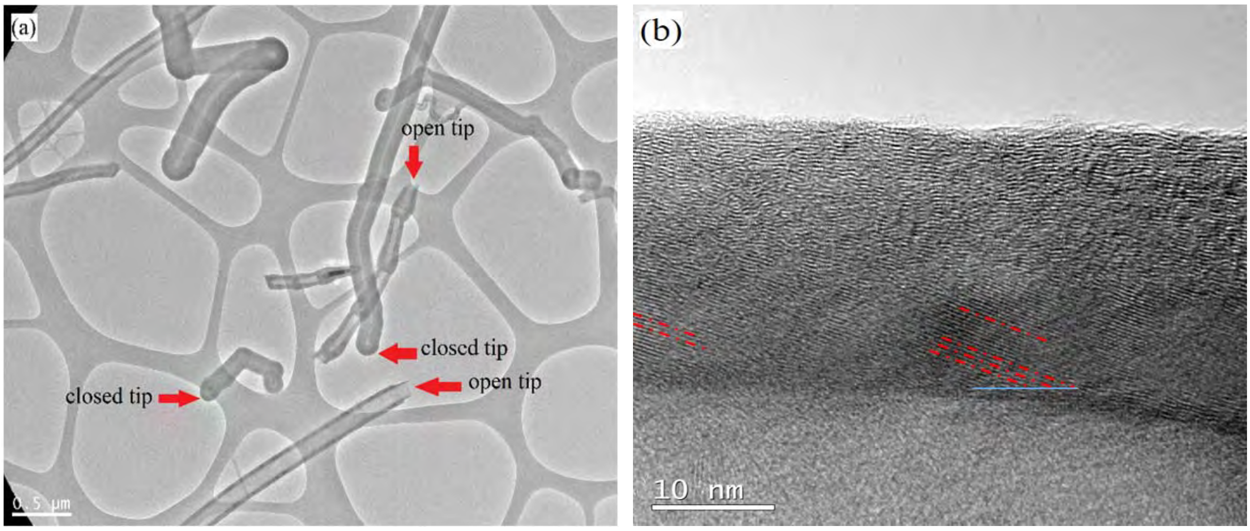

Fig. 2.4 - (a) TEM images of h-MWCNTs showing that the tubes are often opened at one end; (b) HRTEM image of one of the CNTs exhibiting the 'herringbone' texture in the inner part of the wall (see text), the dashed red lines indicate the orientation of the graphitic planes making the tube wall and the blue line is parallel to the tube axis.

BNNTs were produced (and given for free by the BNNT, LLC, USA) by the high temperature/high pressure method with 50 wt% of BNNTs and 50 wt% of hexagonal boron nitride in the product. The BN nanotubes in the product typically have 1~5 walls, yet most frequently 2-4. The inner diameters of most BN nanotubes range from 1 to 7.5 nm with the most represented diameters in the range 1.2-3 nm, while the outer diameters range from 1.6 to 10 nm with the most represented diameters in the range 2.2-4.5 nm. A BNNT is a structural analogue to a CNT, while B and N atoms entirely substitute C atoms alternatively in a graphene with almost no change in atomic spacing [9]. Alike the DWCNTs described above, the BNNTs used in this work correspond to an inhomogeneous mixture of nanotubes and nanoparticles entangled as a spider-web-like network (Fig. 2.5a-b). The nanotubes are either isolated or organized in small bundles (2-10 tubes), with lengths ranging from several hundreds of nanometers up to several microns among the entangled network. Most nanotubes are close-ended while a few tubes have opened tips (Fig. 2.5c and d). It is possible that the opening occurred while the sample was ground (mortar and pestle) in order to be used: as provided, the sample is looking like large "raw cotton" balls which cannot be proceeded. Gentle grinding allows obtaining a powder which can be used for further experiments. In addition, some tubes are filled with amorphous material which is supposed to also be boron nitride (Fig. 2.5c and d).

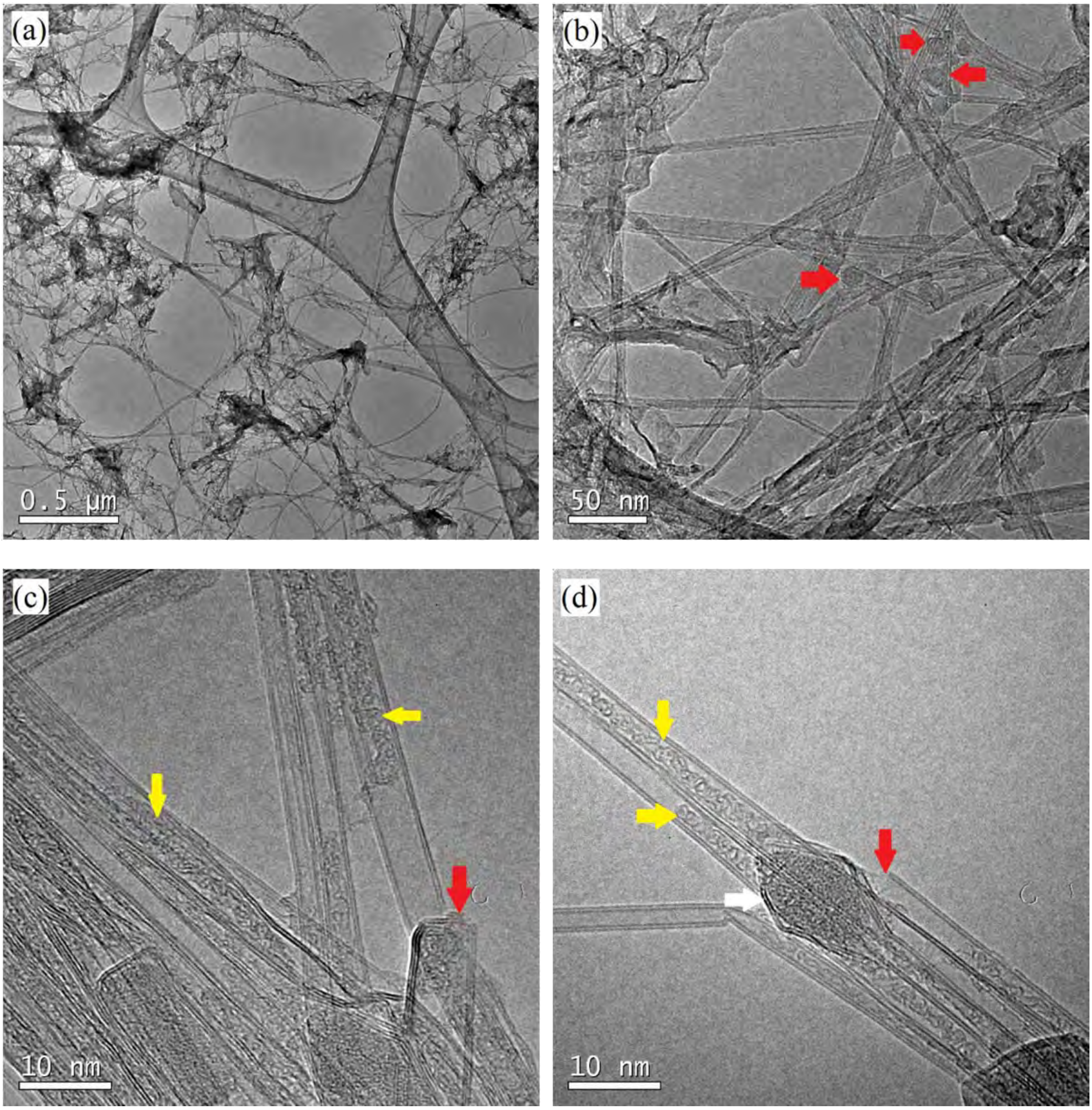

Fig. 2.5 - TEM images of BNNTs showing (a) a spider web network formed by the entangled tubes; (b) the presence of nanoparticles (red arrowed); (c) a 3-wall BNNT with closed tip (red arrowed) and tubes filled with what is likely to be amorphous boron nitride (yellow arrowed); (d) a double-walled nanotube with open tip (red arrowed), tubes filled with amorphous boron nitride (yellow arrowed) and a boron nanoparticle encapsulated by BN shells (white arrowed).

2.3 Synthesis of X@CNTs or X@BNNTs (X = halide or iodine)

First, dry, raw CNTs or BNNTs along with the desired filling material, with a molar ratio of 1/1.3 (DWCNTs/halides or iodine), were ground in a mortar together to obtain a homogeneous mixture. Then the mixture was transferred into a quartz ampoule (6 mm diameter) using a glass funnel. As many of the filling materials are hygroscopic or sensitive to air, the above steps were performed in a tent under N_2 atmosphere. Subsequently, the ampoule was evacuated down to a reduced pressure of 20 Pa and kept subjected to this dynamic vacuum for 2 h. Finally, the ampoule was sealed with a flame and placed into a furnace. The heating program of the furnace was set as followings: from room temperature (RT) to 30°C above the melting point (Mp, see Table 2.1) of the filling material at 5°C/min, then 24h dwell time, then down to 20°C below Mp at 0.1°C/min, then down to 120°C below Mp at 1°C/min, then down to RT at 5°C/min.

For FWCNTs, c-MWCNTs-a and h-MWCNTs, only filling with PbI_2 was performed. For BNNTs, fillings with PbI_2 and NiI_2 were performed and for the latter, the dwell time was 6h. For DWCNTs, the halides used for filling are listed in Table 2.1.

Table 2.1: Filling temperature for the various halides (and iodine) used as filling materials

Filling material	AgI	CdI_2	CoI_2	FeI_2	KI	LiI	NiI_2	PbI_2	$PbCl_2$	PbF_2	SnI_2	*iodine*
Filling T° (°C)	588	417	550	617	711	499	827	432	531	854	350	140/827

For iodine, two filling temperatures were used: 140°C and 827°C (same temperature as for NiI_2) and the as-prepared samples were denoted as I@DWCNTs_140 and I@DWCNTs_827, respectively. At 827°C, iodine is no longer a liquid but a vapour. When the heating process was completed, the ampoule was taken out of the furnace and opened. The composite powder taken out from the ampoule was ground into fine powder and then dispersed in a suitable solvent which can dissolve the filling material (see Table 2.2).

Table 2.2: Solvents used for washing in various filling experiments

Filling material	AgI	CdI_2	CoI_2	FeI_2	KI	LiI	NiI_2	PbI_2	$PbCl_2$	PbF_2	SnI_2	*iodine*
Solvent	$Na_2S_2O_3$[a]	H_2O	H_2O	HCl (37%)	H_2O	H_2O	H_2O	$Na_2S_2O_3$[a] CH_3COOH	HNO_3 (6M)	HNO_3 (6M)	CH_3CH_2OH (absolute)	CH_3CH_2OH (absolute)

[a]*in solution, in proportions 1:20 for [filling material]:[$Na_2S_2O_3$]*

With the molar ratio we used, the filling material was in a large excess and washing was necessary to remove the non-encapsulated material. To facilitate the dissolution, an ultrasonication bath was used. The suspension was filtered and washed with the corresponding solvent repeatedly for several times to make sure that the filling material outside the nanotubes was removed. The washed solid was finally freeze-dried. If an organic solvent was used for washing, the product was dried in an oven at 80°C instead of by lyophilisation.

The halides used to fill CNTs or BNNTs are listed in Table 2.2 along with the corresponding solvents used for washing in each experiment. For FeI_2 which can easily be oxidized in air, concentrated hydrochloric acid solution (37%) was used for washing. For AgI and PbI_2, sodium thiosulfate solution was chosen for washing because the reaction between $S_2O_3^{2-}$ ion and the metal iodide can give the soluble thiosulfate complex of Ag or Pb [10,11]. In the case of PbI_2, after washing twice with $Na_2S_2O_3$ solution, acetic acid solution (pH=2) was used subsequently to wash the PbI_2@DWCNT film left on the membrane with a controlled slow filtration rate. Due to the solubility product constant K_{sp} of lead acetate which is higher than that of lead iodide, lead iodide can dissolve in acetic acid under dynamic equilibrium state with the help of filtration. It should be noted that lead iodide does not dissolve in the acetic acid solution under static equilibrium state.

A synoptics summarizing all the filling experiments carried out during this work can be found on the page hereafter.

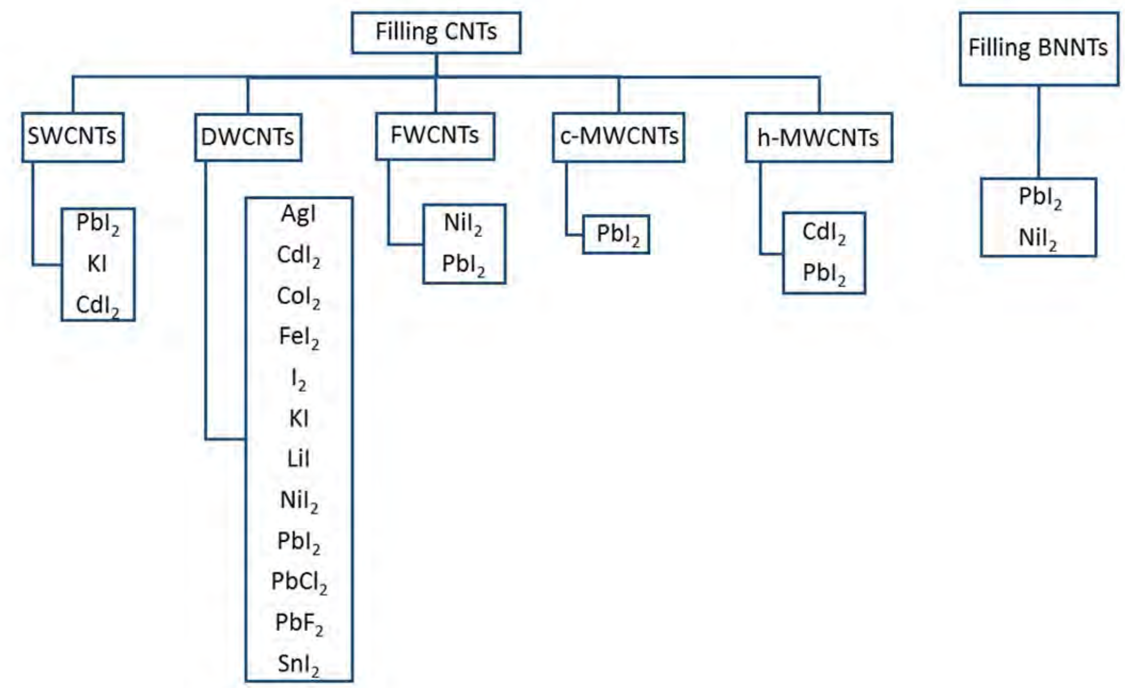

2.4 Electron microscopy characterization on the X@CNTs and X@BNNTs

All the filled CNTs/BNNTs (as well as the starting materials, as already shown in Figures 2.1 to 2.5) were imaged by HRTEM with a FEI Tecnai-F20 microscope (100 kV) equipped with a Cs corrector for the objective lens and occasionally with a Philips CM30 microscope (150 kV) with a LaB_6 gun source. A JEOL JEM-ARM200F microscope (80 kV, occasionally 200kV as indicated on the related image captions) equipped with a STEM and Cs corrector for the condenser lens was used for ADF images and EELS analysis. To prepare the TEM specimen, samples were dispersed in ethanol using sonication bath firstly. Then one or two drops were deposited onto a copper grid (200 mesh) coated with a lacey-type carbon film on the surface using a glass pipette. After the evaporation of the ethanol on the grid, the specimen is ready for observation by TEM. To estimate the filling rate of each hybrid-CNT/BNNT sample, more than 30 HRTEM images randomly selected from area showing isolated tubes (filled or not) were acquired per sample, from which the filling rate was defined as the ratio of the total length of filled tubes over the total length of (filled + unfilled) tubes measurable on each image, which is more accurate (even if not perfect) than the usual simple, visual global estimation from a series of images which is usually performed. However, due to the inherent limitations of the method used, we estimate that the filling rates are accurate within a ± 5% range (absolute %). It should be noted that in the case of PbI_2@h-MWCNTs, the filling rate was estimated from TEM images of the unwashed sample while it was found that the encapsulated PbI_2 was partly washed out during the TEM specimen preparation. Indeed, the penetration of the solvent (either ethanol from TEM grid preparation or $Na_2S_2O_3$ in water) creates bubbles and menisci (see Fig. 2.9b), which is assumed to come with partial removal of the filling material. As a matter of fact, the amount of bubbles observed in the washed sample was higher than in the unwashed sample. The estimated filling rates achieved with DWCNTs are shown in Table 2.3. For filling with iodine, only the filling rate of I@DWCNTs_140 was estimated.

Table 2.3: Estimated filling rates of DWCNTs reached with a variety of iodides (and iodine)

Filling material	AgI	CdI_2	CoI_2	FeI_2	KI	LiI	NiI_2	PbI_2	$PbCl_2$	PbF_2	SnI_2	iodine
Estimated filling rate (%)	38±5	22±5	14±5	27±5	<1	<1	51±5	32±5	1~5	<1	34±5	27±5 (140°C)

The estimated filling rates achieved for PbI_2@DWCNTs, PbI_2@FWCNTs, PbI_2@c-MWCNTs-a, PbI_2@h-MWCNTs, PbI_2@BNNTs and NiI_2@BNNTs are shown in Table 2.4 along with data on the average inner diameters of the host tubes.

Table 2.4: Estimated filling rates achieved for PbI_2@CNTs, PbI_2@BNNTs and NiI_2@BNNTs, and some characteristics of host tubes

sample	*PbI_2@ SWCNTs*	*PbI_2@ DWCNTs*	*PbI_2@ FWCNTs*	*PbI_2@ c-MWNTs-a*	*PbI_2@ h-MWCNTs*	*PbI_2@ BNNTs*	*NiI_2@ BNNTs*
Estimated filling rate (%)	32±5	32±5	25±5	<1	20±5	<1	0
Most frequent nb of walls	1	2	2-6	> 10	Not appropriate	2-4	2-4
Most frequent inner diameters	1.35 nm	1-2 nm	1.5-3.5 nm	2-10 nm	50-70 nm	1.2-3 nm	1.2-3 nm

Fig. 2.6 displays low-magnification TEM images of AgI@DWCNTs and PbI_2@DWCNTs, before washing and after washing. By comparison, it is found that the material embedding the CNTs in the sample before washing is absent after washing, indicating that the washing step is efficient to remove the excess (non-encapsulated) metal iodide. It is also the case for each of the other filling experiments with the other filling materials (yet the related TEM images are not shown).

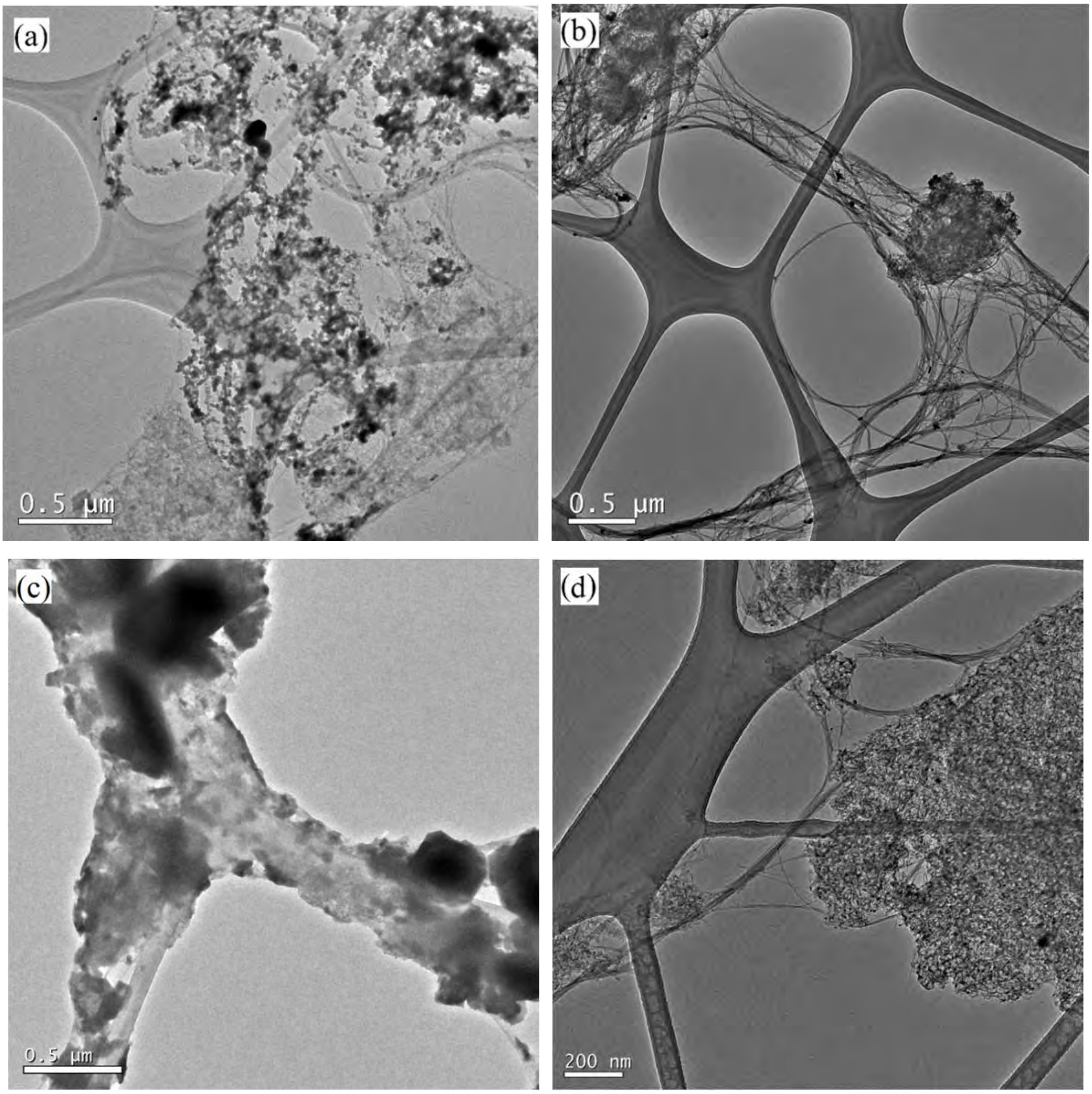

Fig. 2.6 - low-magnification TEM images of AgI@DWCNTs (a) before washing, (b) after washing, and PbI_2*@DWCNTs (c) before washing, (d) after washing.*

Fig. 2.7 shows typical HRTEM images for all the filled DWCNTs. It can be seen that the desired filling material was successfully inserted within the nanotubes and well crystallized inside the nanotubes in each case except for PbF_2 which did enter the CNT cavity but failed crystallising, confirming the ability of metal halides and iodine to open CNTs, at least those with a limited number of walls such as DWCNTs. DWCNTs are filled continuously with the halides even up to micrometres sometimes. Results obtained with SWCNTs were similar for all the filling materials attempted (see the synoptics of filling experiments in section 2.3) hence they will not illustrated.

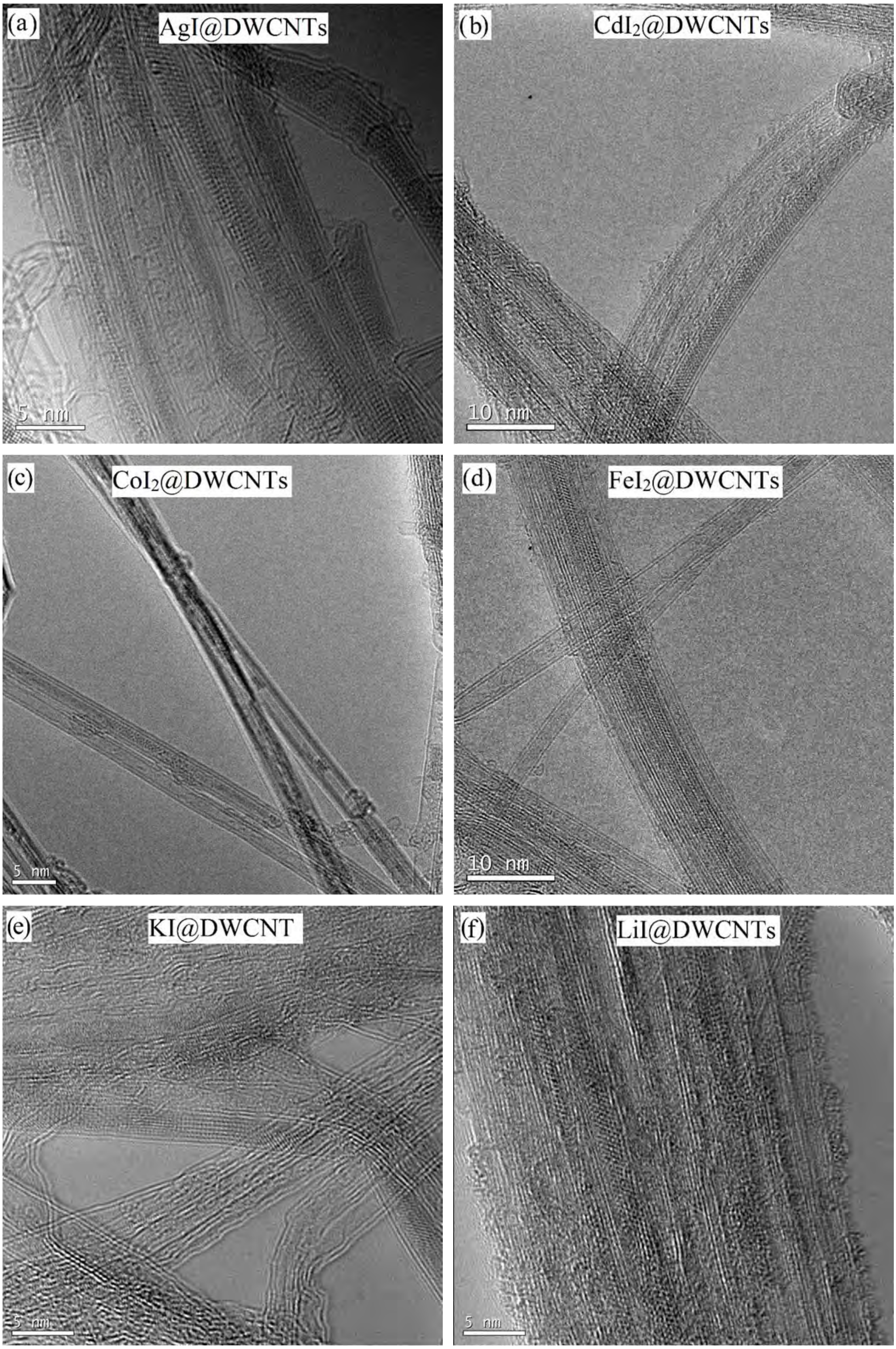
(a)
AgI@DWCNTs
5 nm
(b)
CdI_2@DWCNTs
10 nm
(c)
CoI_2@DWCNTs
5 nm
(d)
FeI_2@DWCNTs
10 nm
(e)
KI@DWCNT
5 nm
(f)
LiI@DWCNTs
5 nm

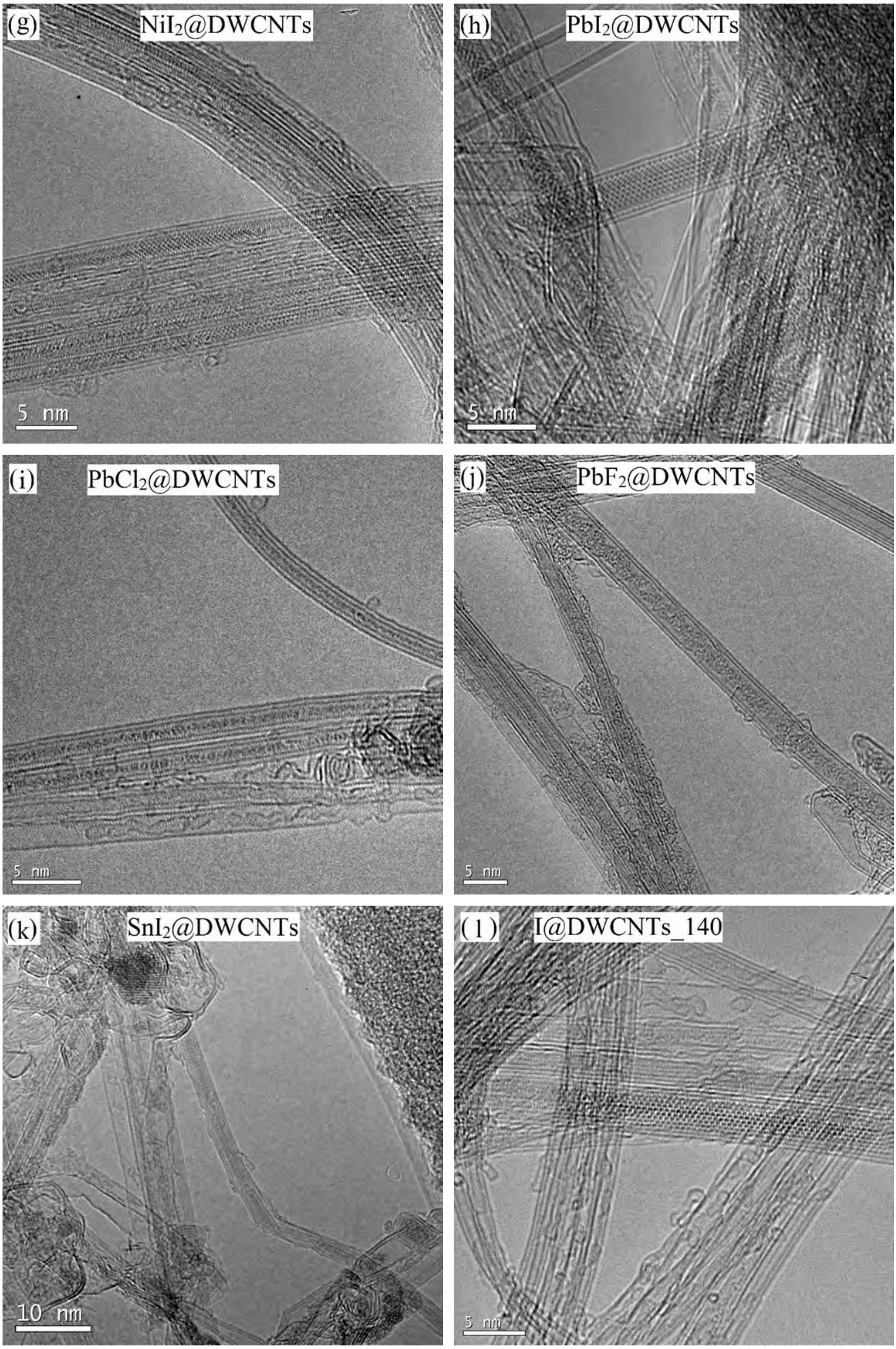
(g)
NiI$_2$@DWCNTs
5 nm
(h)
PbI$_2$@DWCNTs
5 nm
(i)
PbCl$_2$@DWCNTs
5 nm
(j)
PbF$_2$@DWCNTs
5 nm
(k)
SnI$_2$@DWCNTs
10 nm
(l)
I@DWCNTs_140
5 nm

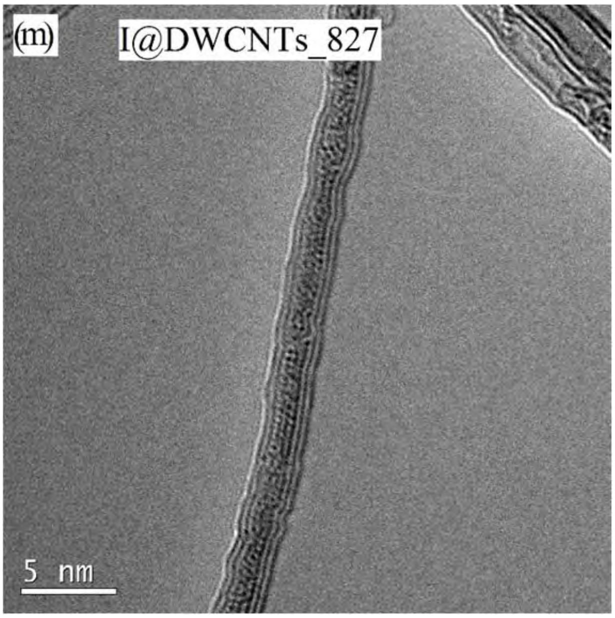

Fig. 2.7 - HRTEM images of single or bundled DWCNTs filled with (a) AgI crystals, (b) CdI_2 crystals, (c) CoI_2 crystals, (d) FeI_2 crystals, (e) KI crystals, (f) LiI crystals, (g) NiI_2 crystals, (h) PbI_2 crystals, (i) $PbCl_2$ crystals, (j) amorphous PbF_2, (k) SnI_2 crystals and (l) iodine crystals in I@DWCNTs_140 and (m) iodine crystals in I@DWCNTs_827.

Typical HRTEM images of PbI_2@FWCNTs and PbI_2@c-MWCNTs-a are shown in Fig. 2.8. In the case of PbI_2@FWCNTs, besides the commonly observed encapsulated PbI_2 nanowires, a continuous coating by PbI_2 of the inner CNT surface of CNTs with large inner cavity is occasionally observed, thereby forming an inner encapsulated PbI_2 nanotube (Fig. 2.8b). Such PbI_2 nanotubes can be synthesized in large amounts by filling open-ended MWCNTs with molten PbI_2 as reported by Cabana *et al.* [12]. In the case of PbI_2@c-MWCNTs-a, it is an overall statement that CNTs with less than 6 walls were filled while tubes with a higher number of walls were not (Figs. 2.8c-d).

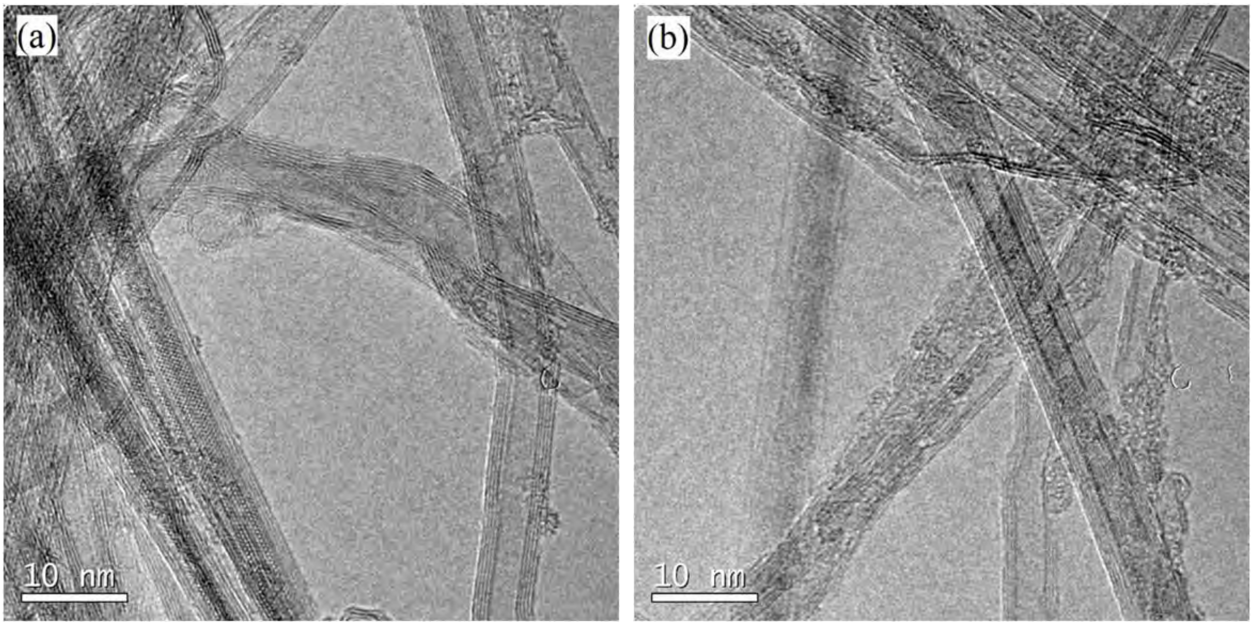

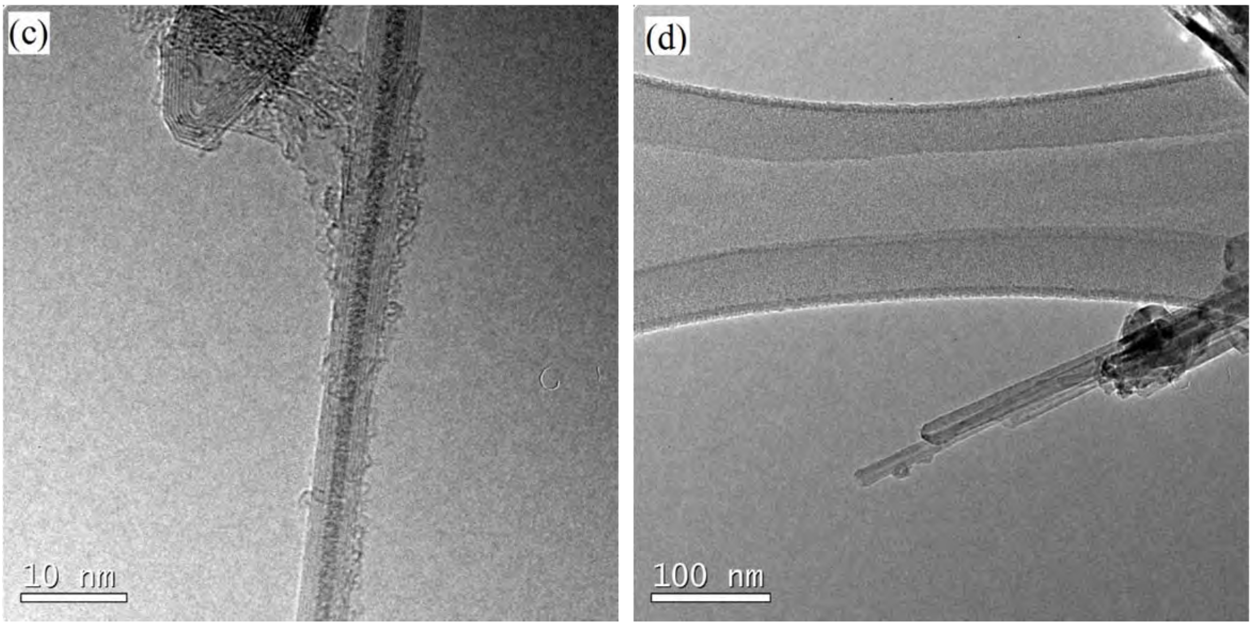

Fig. 2.8 - HRTEM images of PbI_2@FWCNTs illustrating (a) a PbI_2 nanowire encapsulated within a 4-walled CNT and (b) a PbI_2 nanotube encapsulated within a 4-walled CNT; TEM images of PbI_2@c-MWCNTs-a showing (c) a 5-wall CNT filled with a PbI_2 nanowire and (d) unfilled CNTs with more than 6 walls.

Regarding PbI_2@h-MWCNTs, the unwashed sample and washed sample were both investigated by electron microscope. Before washing, many tubes are filled with continuous PbI_2 nanorods over long distances, in particular when they do not exhibit the bamboo texture (Fig. 2.9a), while some tubes are filled with PbI_2 'bubbles' after washing (Fig. 2.9b) (the PbI_2 nature was ascertained by X-EDS).

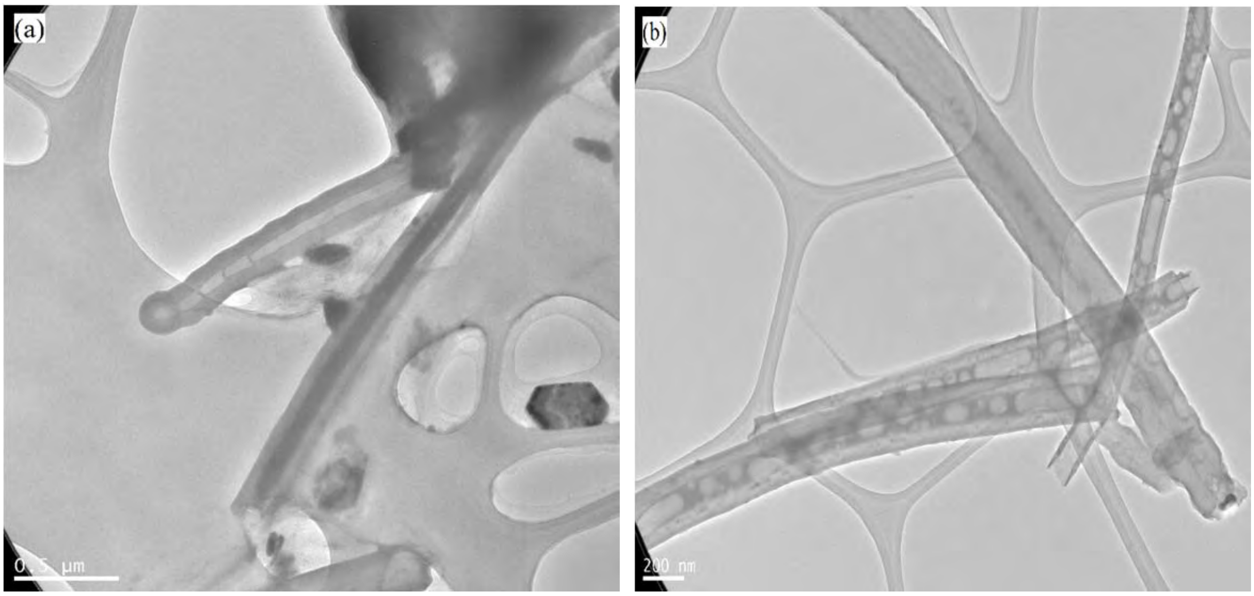

Fig. 2.9 - (a) TEM image of unwashed PbI_2@ h-MWCNTs showing a continuously filled large tube and (b) TEM image of washed PbI_2@h-MWCNTs showing four tubes filled with PbI_2 'bubbles'.

In addition, the amount of filled tubes in the washed sample is decreased compared to unwashed sample. Apparently, the washing step can partly empty the filled tubes due to the dissolution of encapsulated PbI_2 in the washing solvent. The washing out of PbI_2 for PbI_2@h-MWCNTs is ascribed to the open ends and large inner cavity of the host tubes, which allows the solvent to freely enter the tubes and then form solvation spheres within the tubes. This is consistent with the observation that such a washing-out behavior was not observed for CNTs exhibiting smaller diameters such as DWCNTs and FWCNTs filled with halides.

In the case of PbI_2@BNNTs, some rare tubes are filled with elongated nanocrystals (Fig. 2.10a) while some are filled with small clusters (Fig. 2.10b). The formation of PbI_2 clusters inside the BNNT arises from the presence of boron nitride 'plugs' which hinders the capillary rise of PbI_2 inside the tube.

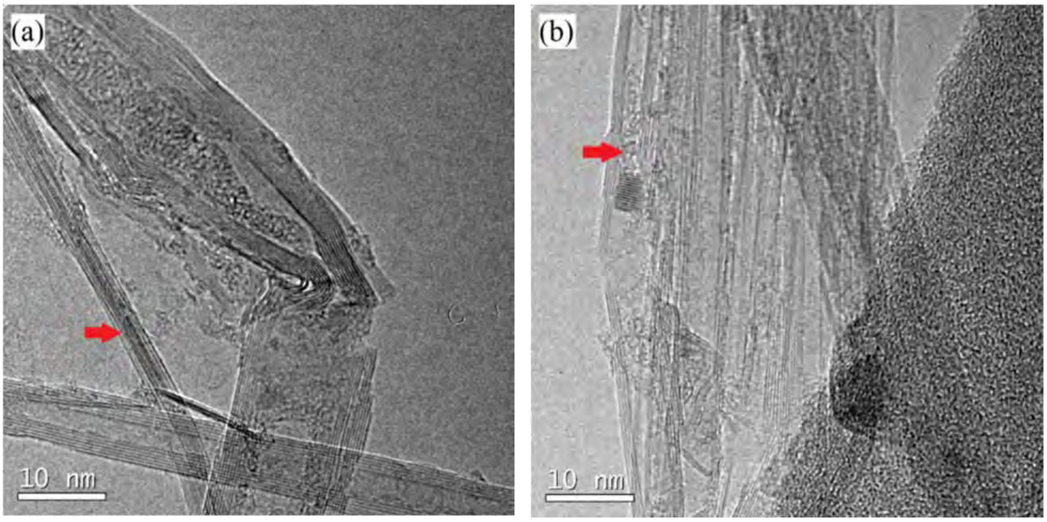

Fig.2.10 - HRTEM images of PbI_2@BNNTs showing (a) a BN tube filled with long crystals (red arrowed) and (b) encapsulation of a cluster stopped by amorphous boron nitride at one end (red arrowed) within a BN tube.

Although high resolution bright field imaging is able to reveal the presence of filling materials sometimes with atomic resolution, ADF imaging was much more efficient in this by providing much higher contrast. Hence, in the following, many of the images will be ADF type, despite this imaging mode is not favourable to imaging the DWCNT walls because of the low contrast (low scattering) generated by carbon atoms.

In the case of filling attempts with NiI_2, NiI_2@DWCNTs are duly observed along with a minor occurrence of I@DWCNTs as revealed by EELS analysis (see Figure 2.11). The reason of this dual chemical nature – I and NI_2 – of the filling materials will be addressed in section 2.7.

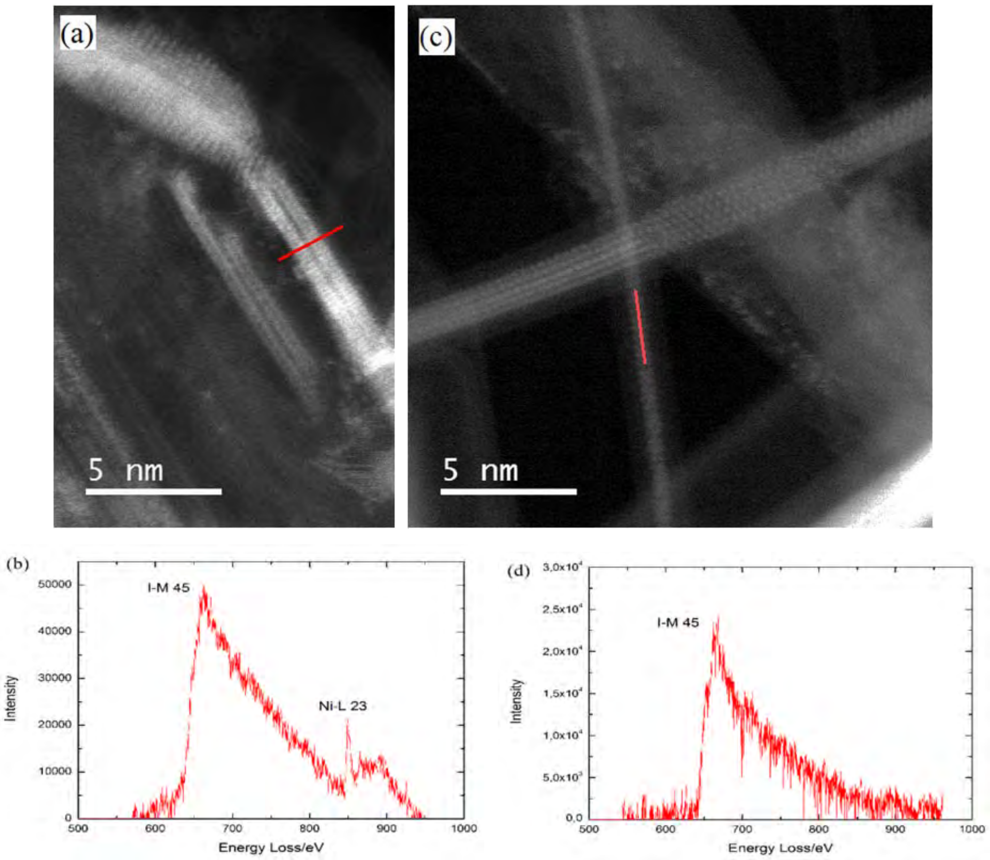

Fig. 2.11 - NiI_2 filling experiments. All images are from the same sample batch: (a) Annular Dark Field (ADF) image of NiI_2@DWCNTs showing the crystal structure of the encapsulated NiI_2. The split aspect with two crystallized bodies separated by a large gap was found typical of NiI_2 crystals; (b) EEL spectrum obtained by summing the spectra collected along the red line indicated in (a) confirming that the crystal is NiI_2; (c) ADF image of a DWCNT filled with a crystal whose structure is different from that in (a) and is consistent with encapsulated iodine, as proposed in [13]; (d) EEL spectrum obtained by summing the spectra collected along the red line indicated in (c) confirming that the encapsulated crystal is pure iodine.

Regarding NiI_2@BNNTs, it was surprisingly found that the web-like network of BNNTs was destroyed after filling (Fig. 2.12a and b). In addition, a filling experiment involving heating the mixture of NiI_2 and BNNTs at 827°C for 24h was also performed resulting in almost no BNNTs remaining in the final product. As this did not happen when filling BNNTs with PbI_2, this is a peculiar behavior which, again, appears to be related to NiI_2. This heavy alteration of the BNNTs of course prevented the encapsulation of NiI_2 to occur, and remaining BNNTs appear to be unfilled, yet opened (Fig. 2.12c-d). However, as described earlier, it is not possible to tell if this opening is an additional process due to the interaction with NiI_2 or if these open BNNTs were already present in the starting (ground) material used for filling.

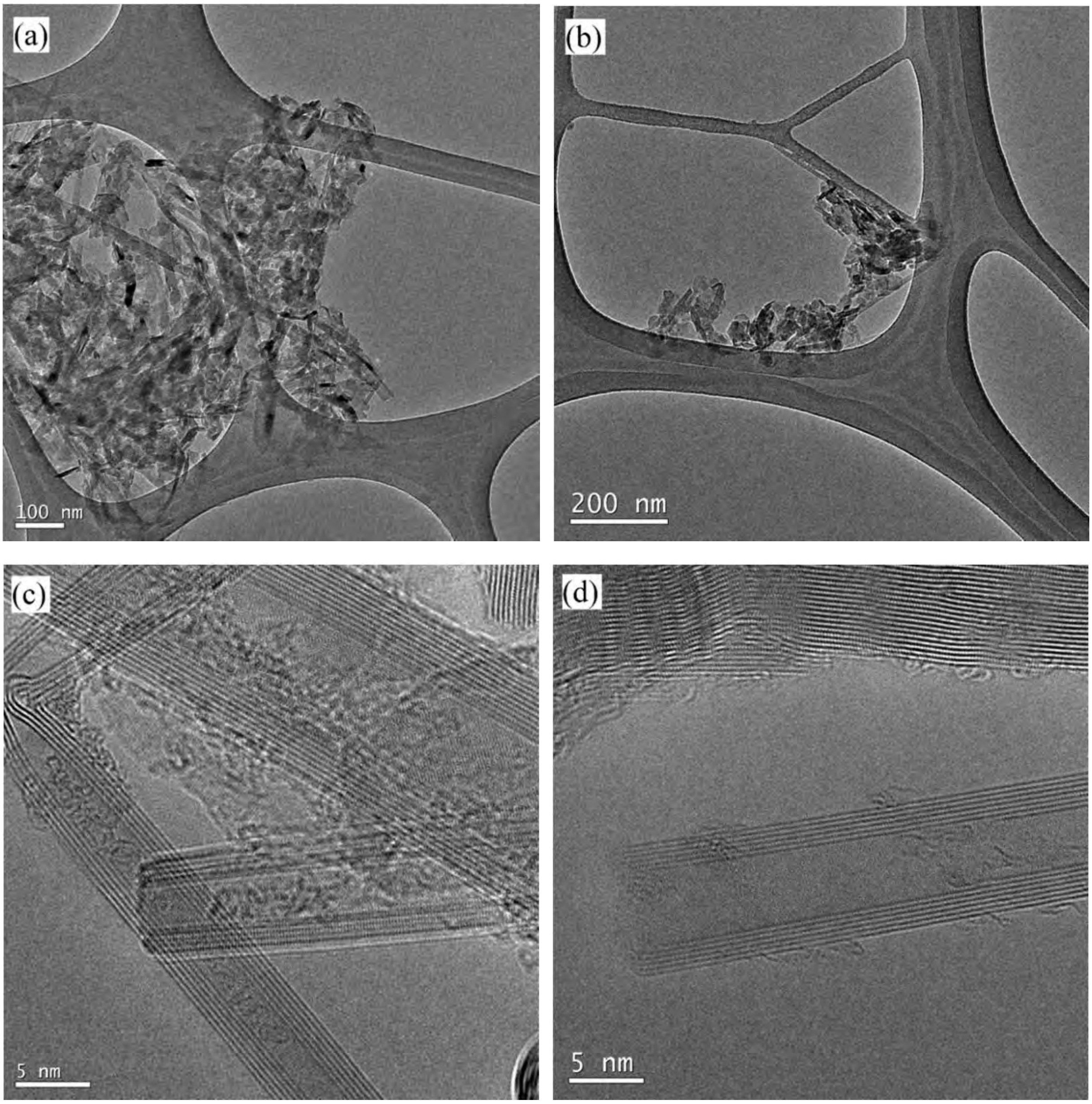

Fig. 2.12 - (a) and (b) TEM images of NiI_2@BNNTs showing the destroyed network of BNNTs after filling; (c) and (d) HRTEM images of some remaining BNNTS from the NiI_2@BNNTs experiment showing that they are unfilled, even if opened.

2.5 Structures of NiI_2 and iodine confined within CNTs

2.5.1 Encapsulated NiI_2

Both the HRTEM and ADF images show that NiI_2 is well crystallized within the cavity of CNTs and elongates along the axis of CNTs continuously, up to several micrometres. Nominally, NiI_2 conforms to the layered $CdCl_2$ structural archetype and only forms R-3mH structure (Fig. 2.13).

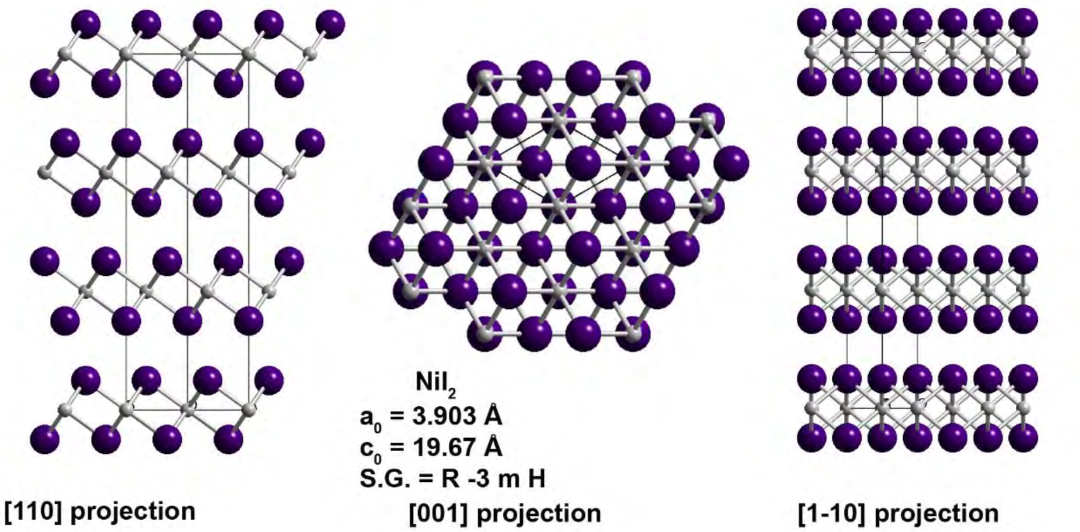

Fig. 2.13 - Crystal structure and common projections observed for NiI_2 *[14]. In this figure, iodine is depicted by purple spheres and nickel is depicted by white spheres.*

The type of crystal observed for encapsulated NiI_2 is broadly similar to that previously reported for PbI_2 encapsulated within SWCNTs or DWCNTs [15] which also forms the $CdCl_2$ (3R) R-3mH structure but much more commonly forms the CdI_2 (2H) P-3m1 structure although both consist of 2D layers of MI_2 (M= Pb, Ni) separated by Van der Waals gaps (i.e. similar to MoS_2, WS_2, $NiCl_2$ etc.). However, the crystallization of NiI_2 in CNTs behaves more regularly than that of PbI_2 as the latter forms different polytypes depending on the diameter of the host CNT [15]. Nearly all the encapsulated NiI_2 crystals can be related to the R-3mH structure with 4-5 atoms thick or more depending on the inner diameter of the host CNT. Meanwhile, many NiI_2 crystals are observed to be twisted within the same nanotube. For instance, the fragments in region **I** and **II** in Fig. 2.14 (see insets) show different projections of the same structure. Both fragments do not exhibit the same width, suggesting that the tube cross-section should correspondingly exhibit an oval instead of circular profile, and that the oval profile is twisted along the tube axis, as previously observed in the literature for other encapsulated crystals [16,17]. The corresponding simulated ADF images and models derived from both regions (Fig. 2.15) reveal that fragment **II** is imaged parallel to a fairly unusual projection ([21-0.5]) with respect to the bulk R-3mH structure in Fig. 2.13, and the orientation of fragment **I** is perpendicular to that of fragment **II** (see end-on view). In addition, NiI_2 crystals in region **I** is 5-atom-thick, thereby differing from the 4-atom-thick fragment **II**, which possibly arises from the expansion of inner cavity of the host DWCNT or, alternatively, makes the tube cross-section adopt an oval shape to accommodate the crystal dimension variation, as previously suggested. Another example of twisted NiI_2 crystals is illustrated in Fig. 2.16.

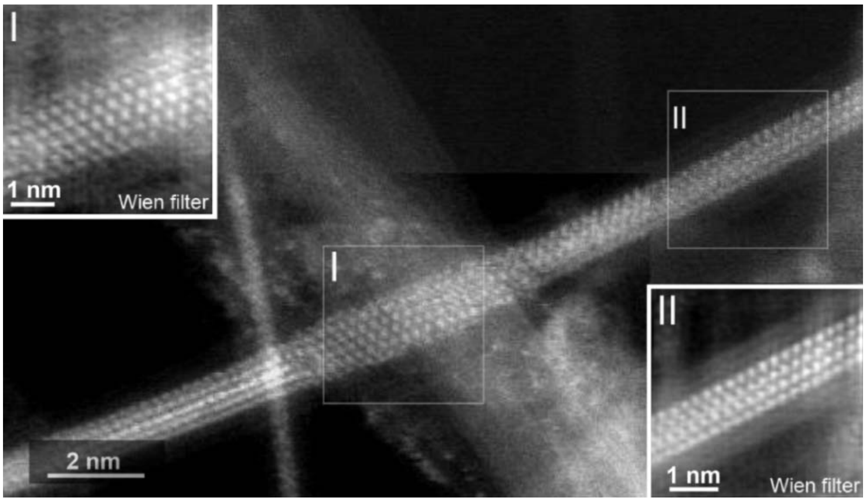

Fig. 2.14 - ADF image of an encapsulated NiI_2 nanocrystal. The insets are two 'Wien' filtered images of boxed regions I and II, which are produced using the 'HRTEM Filter' program developed by D. R. G. Mitchell (see http://www.dmscripting.com/hrtem_filter.html).

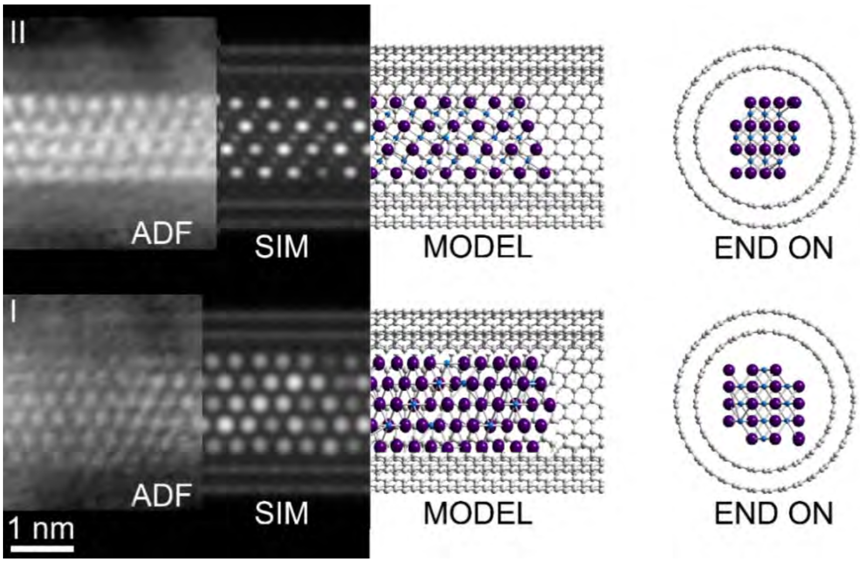

Fig. 2.15 - ADF = Details of the inset images in Fig. 2.14, SIM = corresponding simulations of the ADF images; MODEL = corresponding structure models (side views), for both regions ***I*** *and* ***II*** *in Fig. 2.13. END-ON = corresponding cross-section views of the NiI_2 fragments inside DWCNTs. In this figure, iodine is depicted by purple spheres and nickel is depicted by blue spheres.*

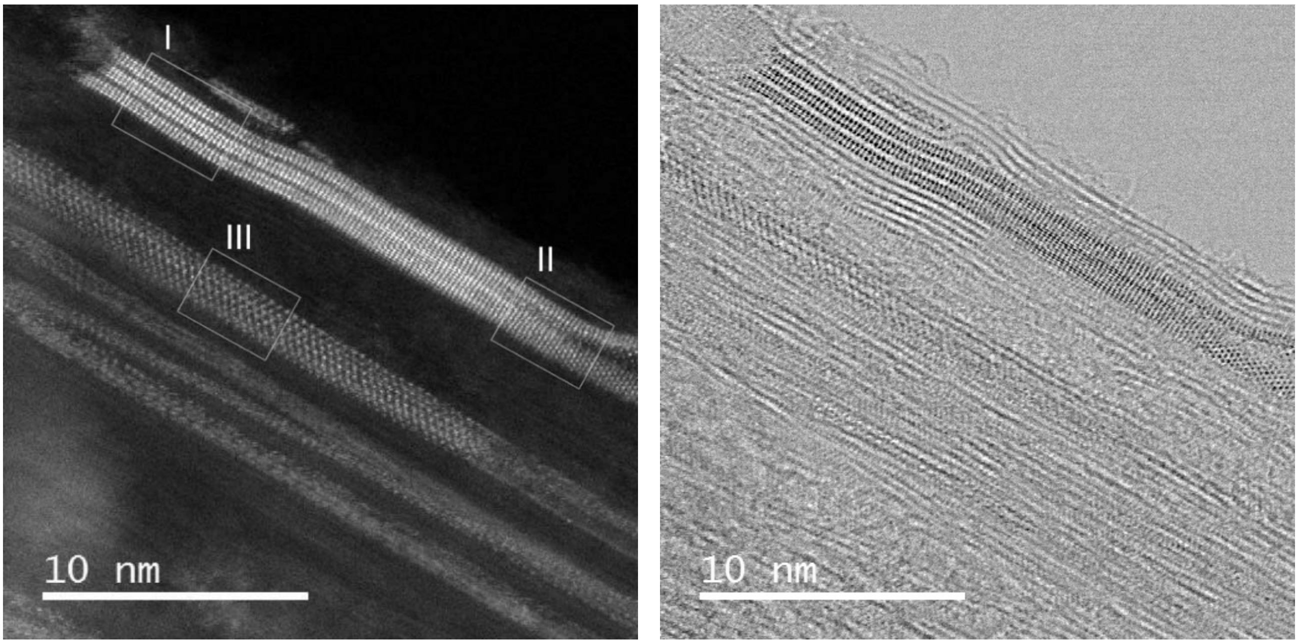

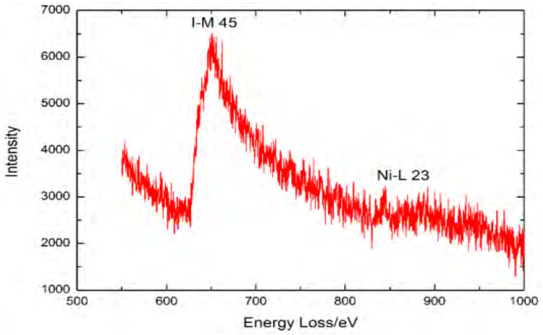

Fig. 2.16 - ADF (left) and HRTEM (right) images of the same encapsulated NiI_2 *nanocrystals showing different projected structures in regions* ***I, II*** *and* ***III****.*

For the confined NiI_2 nanowires at the top of the ADF image in Fig. 2.16, a three-strip microstructure is unambiguously seen in region **I**, whereas at region **II**, the microstructure splits into two but is also rotated (see Fig. 2.16). Apparently, fragment **I** corresponds to the combination of three 2D NiI_2 crystal layers viewed along [1-10] projection (see Fig. 2.17, far right) as suggested by the corresponding simulation and model (Fig. 2.17). When it comes to region **II**, the fragment is slightly rotated with respect to fragment **I** (by ca. 15°), as indicated by the structure model (Fig. 2.17). Meanwhile, the splitting of fragment **II** should be due to the ‘opening up’ of the host CNT, as observed in the bright field image (Fig.2.16b). Beside the twisted structure, another intriguing feature is also observed for NiI_2 crystals, as shown in region **III** in Fig. 2.17. According to the simulated ADF image (Fig. 2.17, bottom), Fragment **III** is suggested to be viewed along [001] direction, which should induce that some atoms at the periphery of the fragment appear dimmer than others (white arrows) due to a smaller atom column thickness which lowers the level of scattered intensity. However, this does not show up in the related real ADF image.

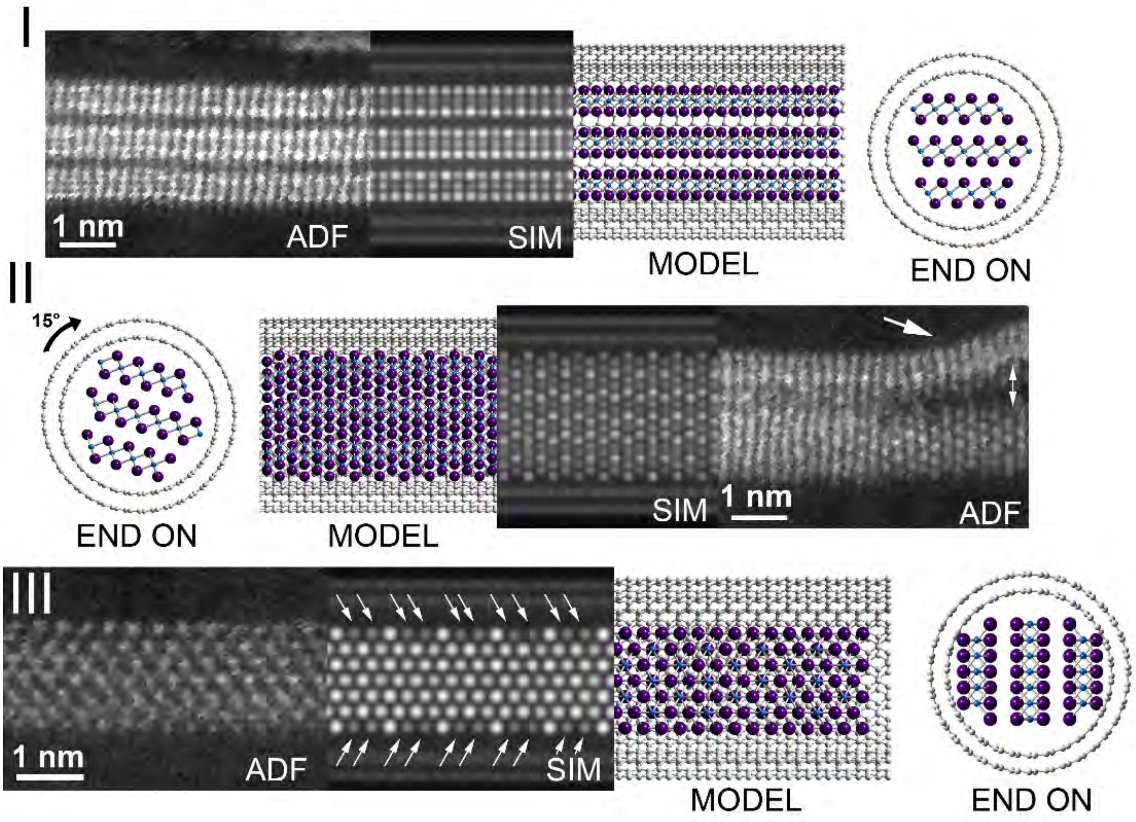

Fig. 2.17 - ADF = Details of the inset images in Fig. 2.16; SIM = corresponding simulation of the ADF images; MODEL = corresponding structure models (side views) for regions ***I, II*** *and* ***III*** *in Fig. 2.17; END-ON = corresponding space-filling cross-section views of the* NiI_2 *fragments inside DWCNTs. On the right side of the experimental image of region II (arrowed area), we see that the structure has indeed peeled apart. Arrows in the simulated ADF image for fragment III point out the presence of some Ni atom pairs which appear dimmers than neighbouring ones. In this figure, iodine is depicted by purple spheres and nickel is depicted by blue spheres.*

2.5.2 Encapsulated iodine

Besides the NiI_2-filled tubes, a significant amount of CNTs in the NiI_2@DWCNT sample are observed to be filled with beautiful atomic chains whose atoms were identified to be iodine by EELS analysis. Chains can be single, double, or triple, in good agreement with previous observations [5,13]. They are induced by the entering of iodine vapours produced from the spontaneous decomposition of NiI_2 into the CNT cavity. It is worth mentioning that those tubes containing iodine chains have a much smaller inner diameter compared to the NiI_2-filled tubes, possibly indicating a preference of iodine for narrow space. The selectivity towards the size of CNTs during the filling process with iodine vapour may be explained by the capillary condensation phenomena, as previously suggested in the case of filling with selenium vapour, which behaves similarly [18].

Fig. 2.18 presents typical ADF images, corresponding simulated ADF images, and a structural model of 1D-iodine chains. It can be seen (Figs. 2.18a-b and 2.18e-f) that straight iodine chains are commonly observed and the spacing between the iodine atoms are measured to be ~0.29 nm on the average, similar to the I-I distance reported in [19].

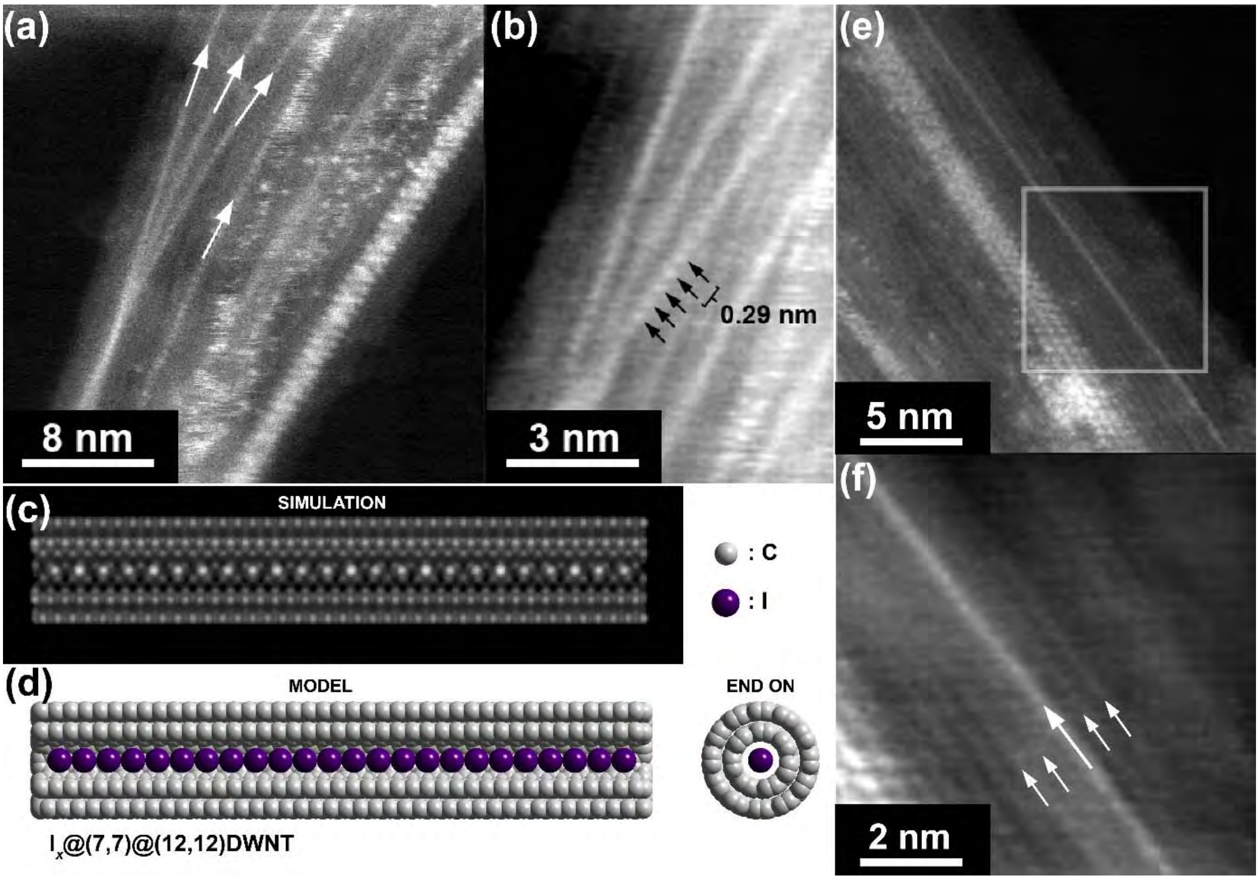

Fig. 2.18 - (a) ADF image of a bundle of CNTs from NiI_2@DWCNT sample with at least four 1D iodine-chains (arrowed) visible. (b) Detail from (a) indicating measured distances between I atoms in a chain. (c) and (d) are a simulated ADF image and the corresponding structural model of a 1D iodine-chain inside a (7,7)@(12,12) DWCNT. The wall helicities of the model for the DWCNT are derived from (e) and (f) where the DWCNT walls are visible. Indeed, (e) and (f) show an ADF image and a detail of it respectively, showing a DWCNT which contains a 1D iodine chain (large white arrow) in-between the two walls of the DWCNT (small white arrows). Note that in order to accommodate the 1D iodine chain, the inner SWCNT must fit perfectly around the chain in order to retain a linear structure.

Complementary experiments were carried-out as reference, consisting in attempting to fill DWCNTs with molten iodine and iodine vapour. Those experiments have generated samples I@DWCNTs_140 and I@DWCNTs_827 respectively. The filling behaviour of iodine was found similar, as illustrated by Figure 2.19.

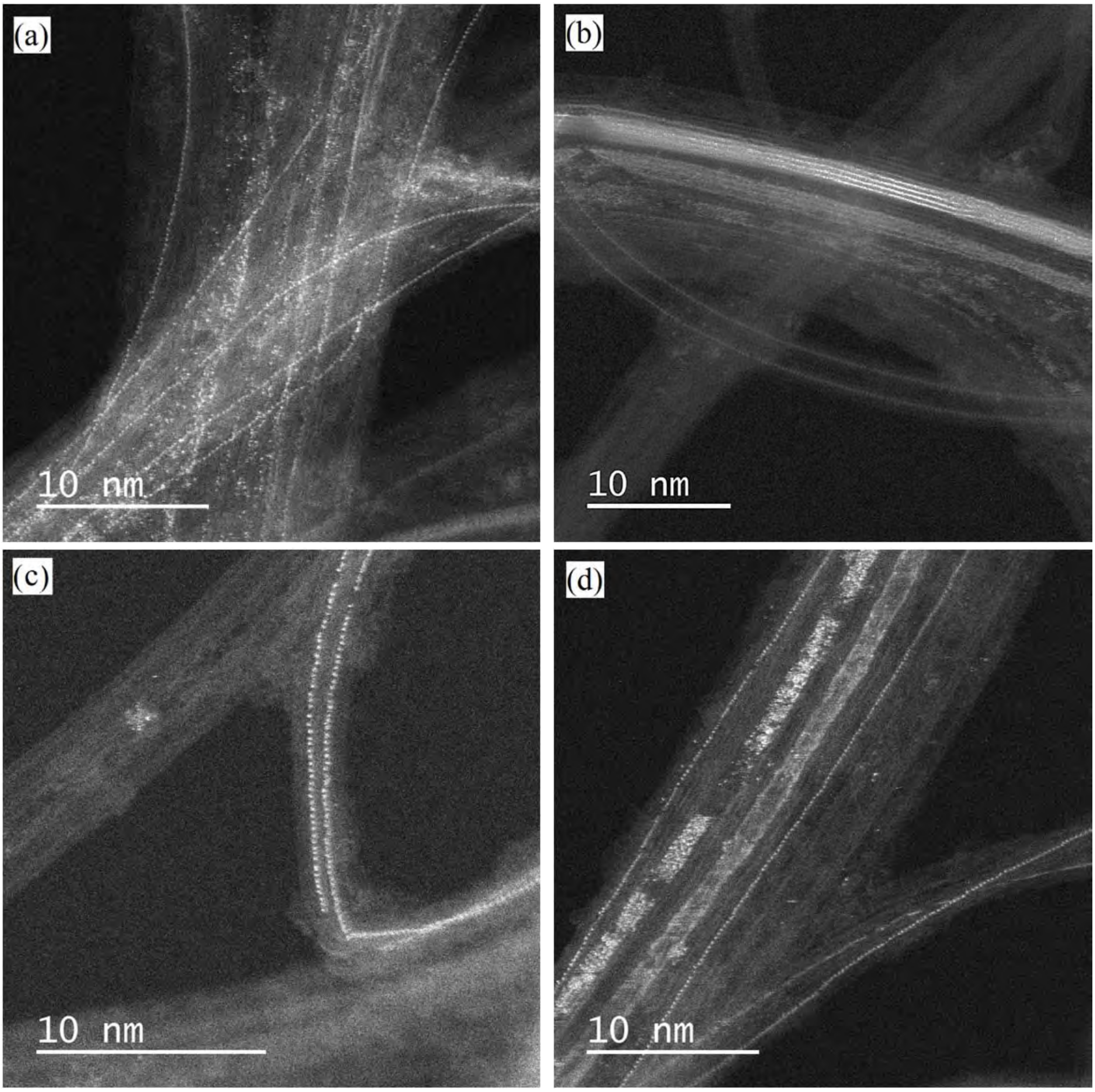

Fig. 2.19 - ADF images (STEM operated at 200 kV) of I@DWCNTs_140 showing: (a) several single iodine chains, (b) two single iodine chains as wells as other structures in the background, and I@DWCNTs_827 showing: (c) two single iodine chains, (d) several single iodine as well as other structures in the background .

The atomic arrangement of iodine chains was better resolved in the ADF images of I@DWCNTs_140 and I@DWCNTs_827 (Fig. 2.19) by increasing the accelerating voltage from 80 kV (for sample NiI_2@DWCNTs, as in Figs. 2.11, 2.14, 2.16 and 2.18) to 200 kV. These ADF images clearly confirm that the encapsulated single iodine-chains adopt a linear and straight configuration instead of the helical configuration suggested by Guan et al. [13]. Meanwhile, other polymorphic structures of iodine confined within CNTs demonstrated by Guan et al. [13] are also observed in samples I@DWCNTs_140 and I@DWCNTs_827. For instance, helical double-chains of iodine encapsulated within a DWCNT are unambiguously presented in Fig. 2.20.

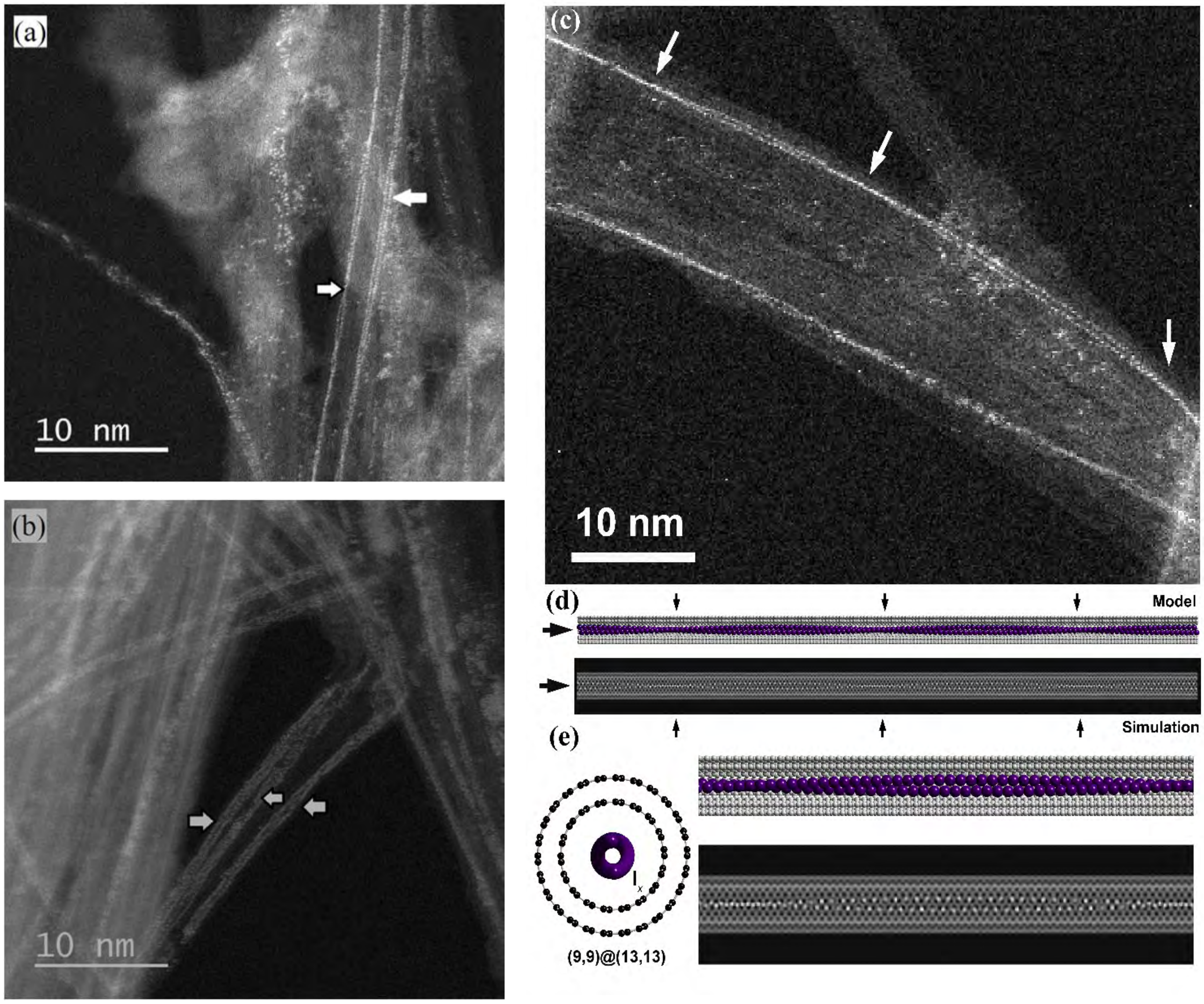

Fig. 2.20 - Examples of encapsulated twin helical chains of iodine. (a) and (c) in sample I@DWCNTs_140 (white arrows); (b) in sample I@DWCNTs_827 (white arrowed). In (c) three nodes along the helical double iodine chain are arrowed. (d) Structural model (top) and simulated ADF image (bottom) of the double chain in (c) with the three nodes indicated by small arrows. (e) End-on (cross-section) structural model and enlargement of a region between two nodes.

The maximum separation of the two chains in Fig. 2.20c is measured at ~0.26 nm, which is smaller than that reported for double helix of iodine encapsulated within SWCNTs (0.65 nm in [5] and 0.49 nm in [13]) which is likely to be due to the smaller inner cavity of our DWCNTs (below ~1 nm) with respect to the SWCNTs used in [5, 13]. Hence, the pitch of the double helix may depend on the inner diameter of the host CNT. In addition, the distance between two adjacent nodes in the helix shown in Fig. 2.20c is not the same, i.e. 8 nm for the first two nodes at top left and

13 nm for the two nodes at top right. Such a helix in a DWCNT with different periodicities is often found in our sample and for helixes confined in different tubes, they show different periodicities (see Fig. 2.20a). Compared to I@DWCNTs_140, less helical chains are observed in I@DWCNTs_827, which may be related to the fact that iodine molecules in iodine vapour tend to dissociate into iodine radicals at high temperature [20] instead of I^+ and I_n^- species in the case of molten iodine [5]. Monoatomic iodine may prefer to adopt a straight line configuration once confined within CNTs. However, the mechanism of the preferred formation of single chains or helical double-chains of iodine atoms instead of nanocrystals is not clear yet. Intercalation of iodine chains into the interstitial channels in DWCNTs ropes is also observed and clearly evidenced by comparing the ADF image and BF STEM image, as shown in Fig. 2.21.

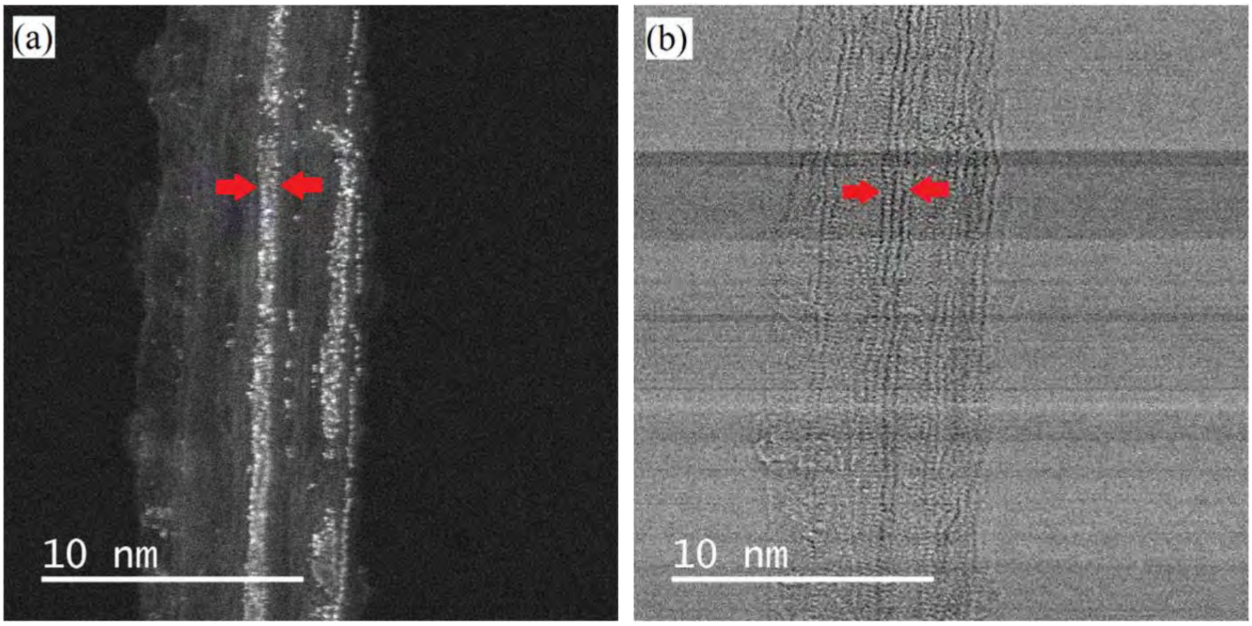

Fig. 2.21 - ADF image and the corresponding BF STEM image show the presence of intercalated iodine chains (arrowed) between in the interstitial channel of two CNTs in a small bundle. The tube structure appears highly defective, as a result from using TEM conditions with high energy electron beam (200 keV) which is able to damage the tubes.

When the inner diameter of the host CNT is in the range of 1 nm or more, both amorphous-like phase (Fig. 2.22) and ordered phases of iodine other than linear chains (Fig. 2.23 and 2.24) are observed in sample I@DWCNTs_140 and I@DWCNTs_827.

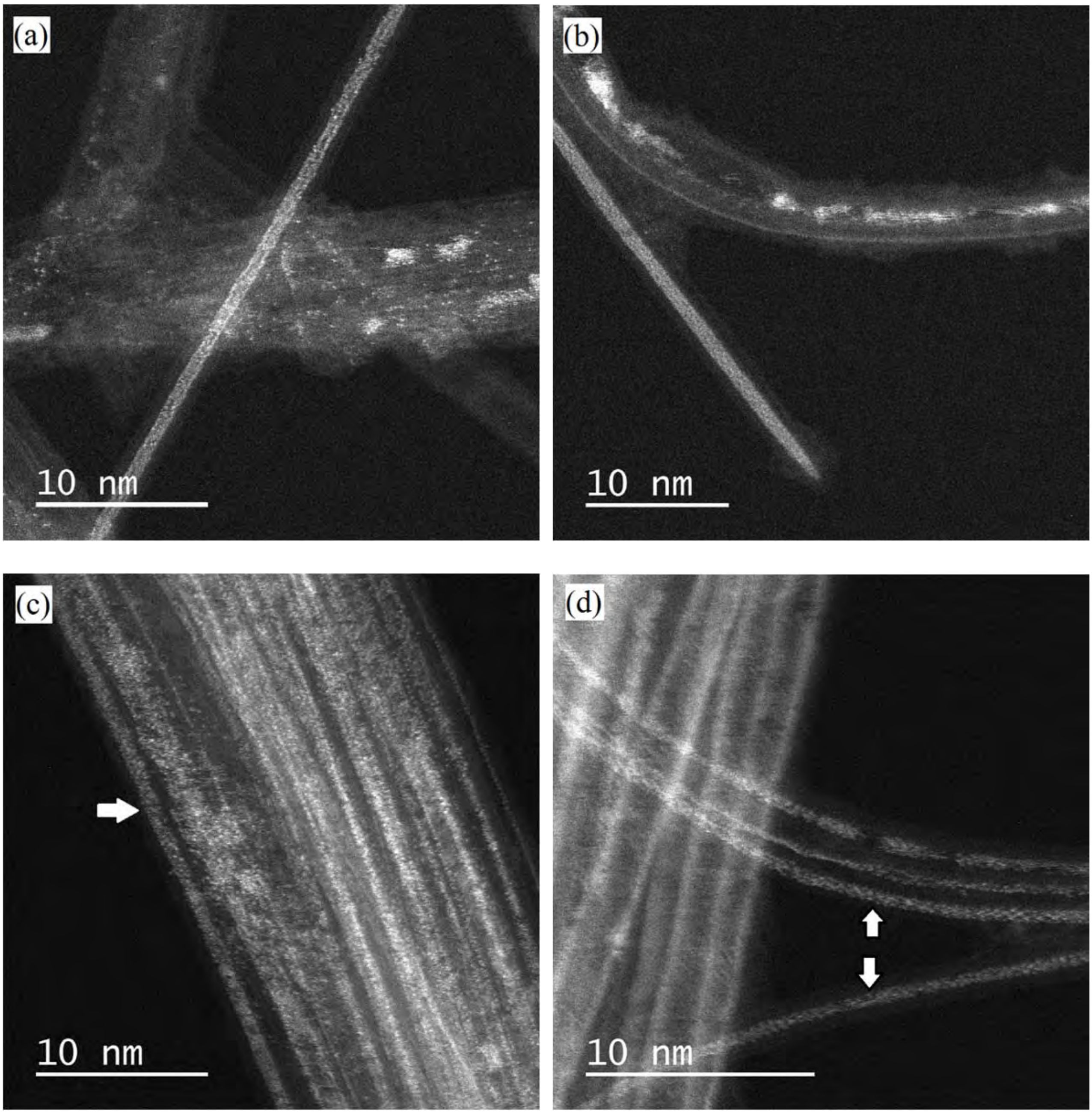

Fig. 2.22 - ADF images (acquired at 200 kV) of amorphous-like iodine present in (a) I@DWCNTs_140 and (b)-(d) I@DWCNTs_827 (white arrows), respectively;

The iodine ordered phase observed in Fig. 2.23a-c exhibit similar features as the Phase III structure proposed by Guan et al. [13]. This phase was supposed by Guan et al. to be a transition phase generated from the transformation of triple-helix iodine chains under the electron beam irradiation, as described in [13]. As we have most often used the STEM mode which required a convergent beam with higher dose of electrons (in addition often operated at 200 kV) than the parallel beam used for HRTEM (in addition operated at 120 kV only) in [13], it is possible that triple-helix iodine chains were present in the materials but did not survive under the irradiation and quickly evolve into this "Phase III" structure. This phase was also observed to be not stable under the electron beam and this could be the reason why we also observed amorphous-like iodine filling in ADF (STEM) images operated at 200 kV (Fig. 2.22). Therefore, the phase transformation of triple-helix iodine chains is ongoing during the TEM observation, which may account for the commonly observed blurred iodine crystals and scarcely observed triple-helix iodine chains in our samples (one ADF image illustrating a possible triple iodine helical-chain is shown in Fig. 2.23d).

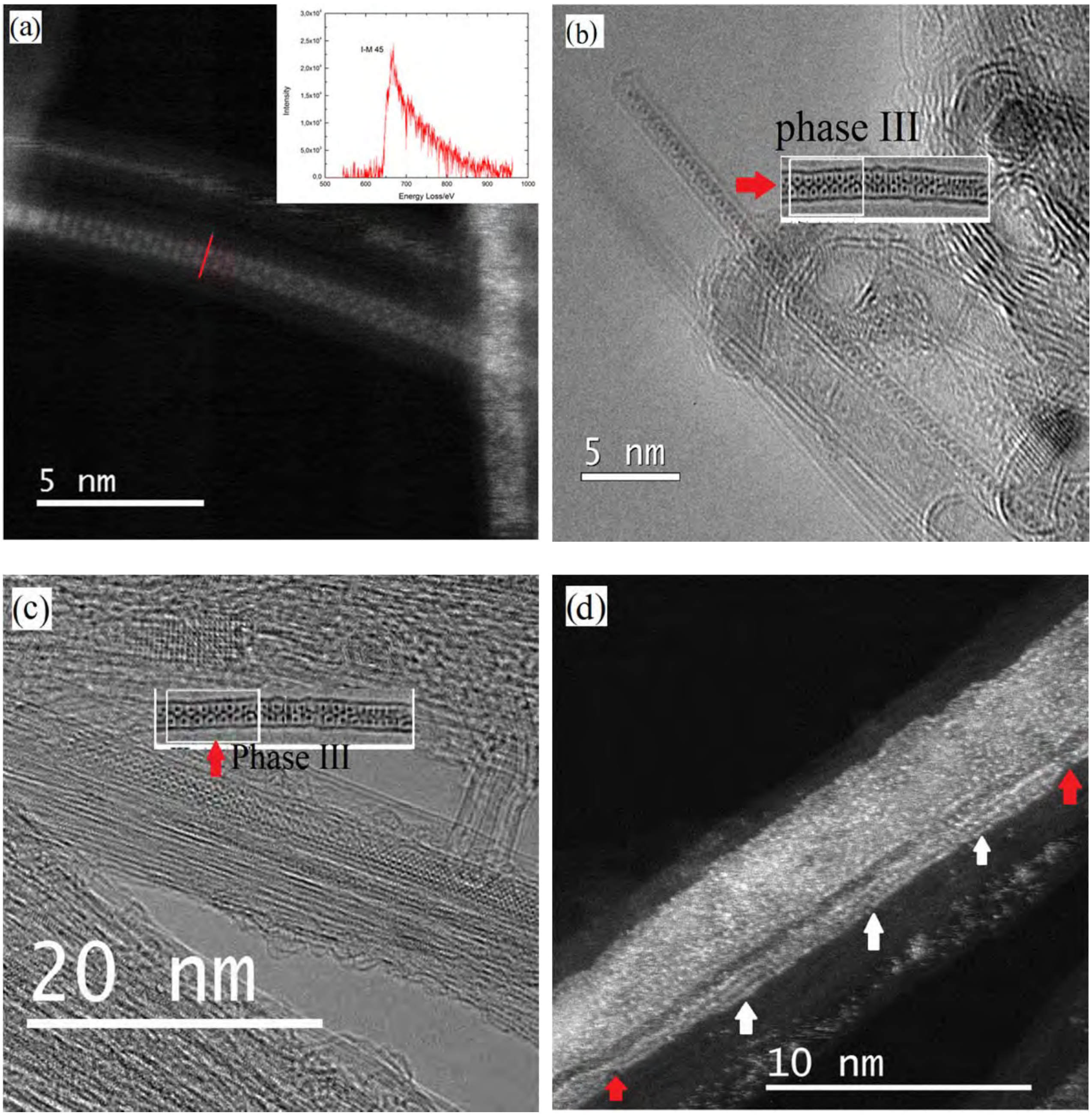

Fig. 2.23 - (a) ADF image (acquired at 80 kV) of an ordered phase of iodine present in Ni@DWCNTs_500_7 (see Chapter 3), the inset in (a) is the EEL spectrum obtained by summing the spectra collected along the red line across the

filled tube, identifying the filling as pure iodine; (b) and (c) HRTEM images (acquired at 100 and 200 kV respectively) showing an ordered phase of iodine in sample NiI_2*@DWCNTs. This phase resembles the iodine Phase III structure proposed by Guan et al [11] which is shown in both images as an inset (see text); (d) ADF image (acquired at 200 kV) of a triple iodine helical-chains (the two nodes of the chains are indicated by red arrows, the configuration of the triple-chains can be seen clearly in white-arrowed region).*

When the inner diameter of the host CNT is larger than 1.5 nm, encapsulated iodine chains are no longer observed but crystalline iodine with identical structure to the bulk orthorhombic iodine crystals may fully develop, as found in the case of I@DWCNTs_140 and I@DWCNTs_827, which is in agreement with the work by Guan et al. [13]. An example is provided in Fig. 2.24a as an ADF image of a crystalline iodine filling in a triple-walled CNT with an inner cavity of around 1.71 nm (measured in BF mode, Fig. 2.24b). The filling material exhibits four parallel lines inside the CNT whose average spacing is about 0.368 nm, close to the 0.359 nm {200} *d*-spacing of orthorhombic iodine [20]. Only one example of such an encapsulated iodine crystal with the orthorhombic structure was reported in the literature [13], and our observations are fully consistent with it (Figure 2.25). In addition, crystalline iodine containing up to 6 parallel lines were also observed inside large CNTs (Fig. 2.24c and d). The average spacing of the parallel lines is also measured to be around 0.368 nm for the thicker iodine crystals.

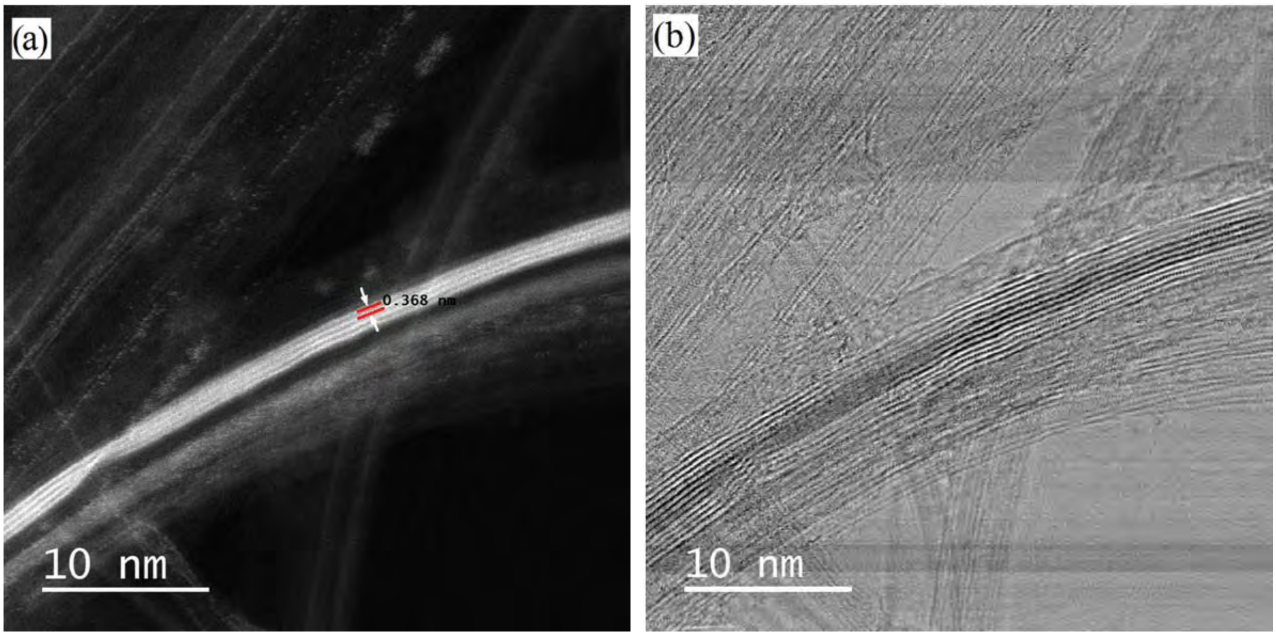

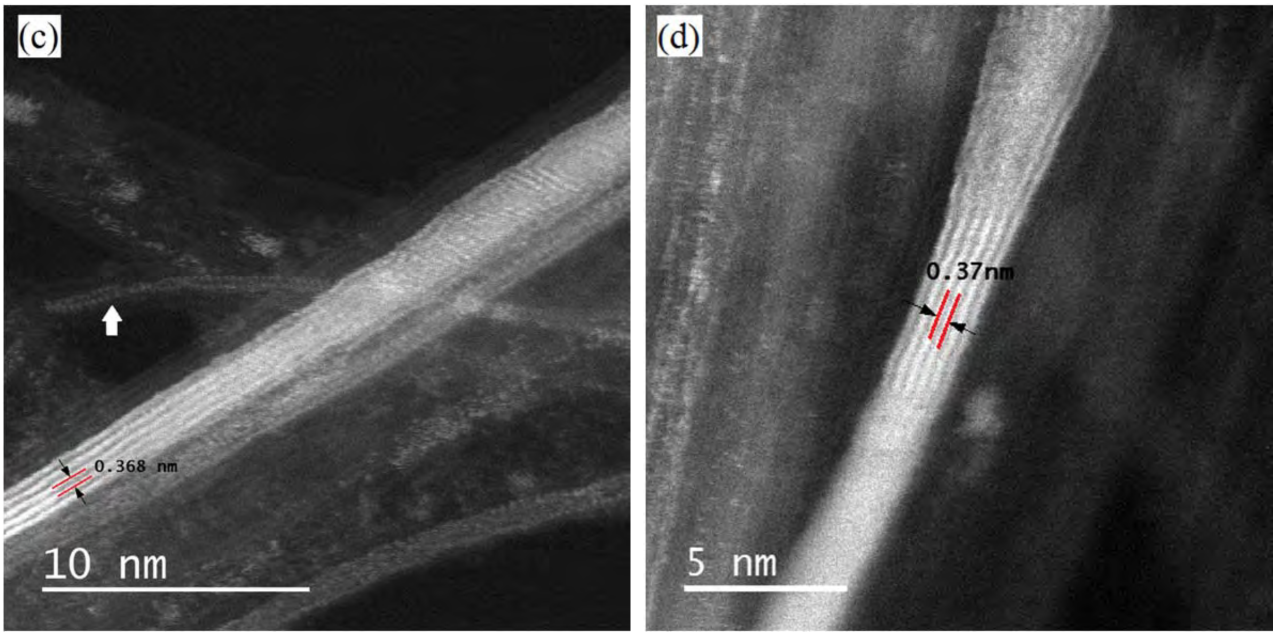

Fig. 2.24 - Iodine crystals with the orthorhombic structure of different thickness present in sample I@DWCNTs_140 (see text): (a) ADF image and (b) BF image (both acquired at 200 kV) of an iodine crystal consisting of four parallel lines; ADF images (acquired at 200 kV) of an iodine crystal consisting of five parallel lines (c) and six parallel lines (d), in (c), a double-helix of iodine is indicated by a white arrow in the background.

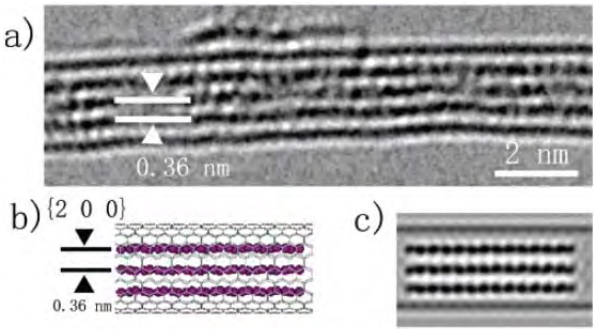

Fig. 2.25 - Crystalline iodine confined in a 1.55 ± 0.05 nm SWCNT as reported in [13]: (a) HR-TEM image (120 kV); (b) Schematic model based on the orthorhombic iodine (bulk crystal) encapsulated in a SWCNT with the <010> direction parallel to the tube axis and the <001> direction parallel to the electron beam. (c) The corresponding simulated image.

Finally, a new configuration for iodine filling confined within CNTs which has not been reported in the literature was occasionally observed in I@DWCNTs_140 and I@DWCNTs_827, and even in sample NiI_2@DWCNTs (Figures 2.26a-d).

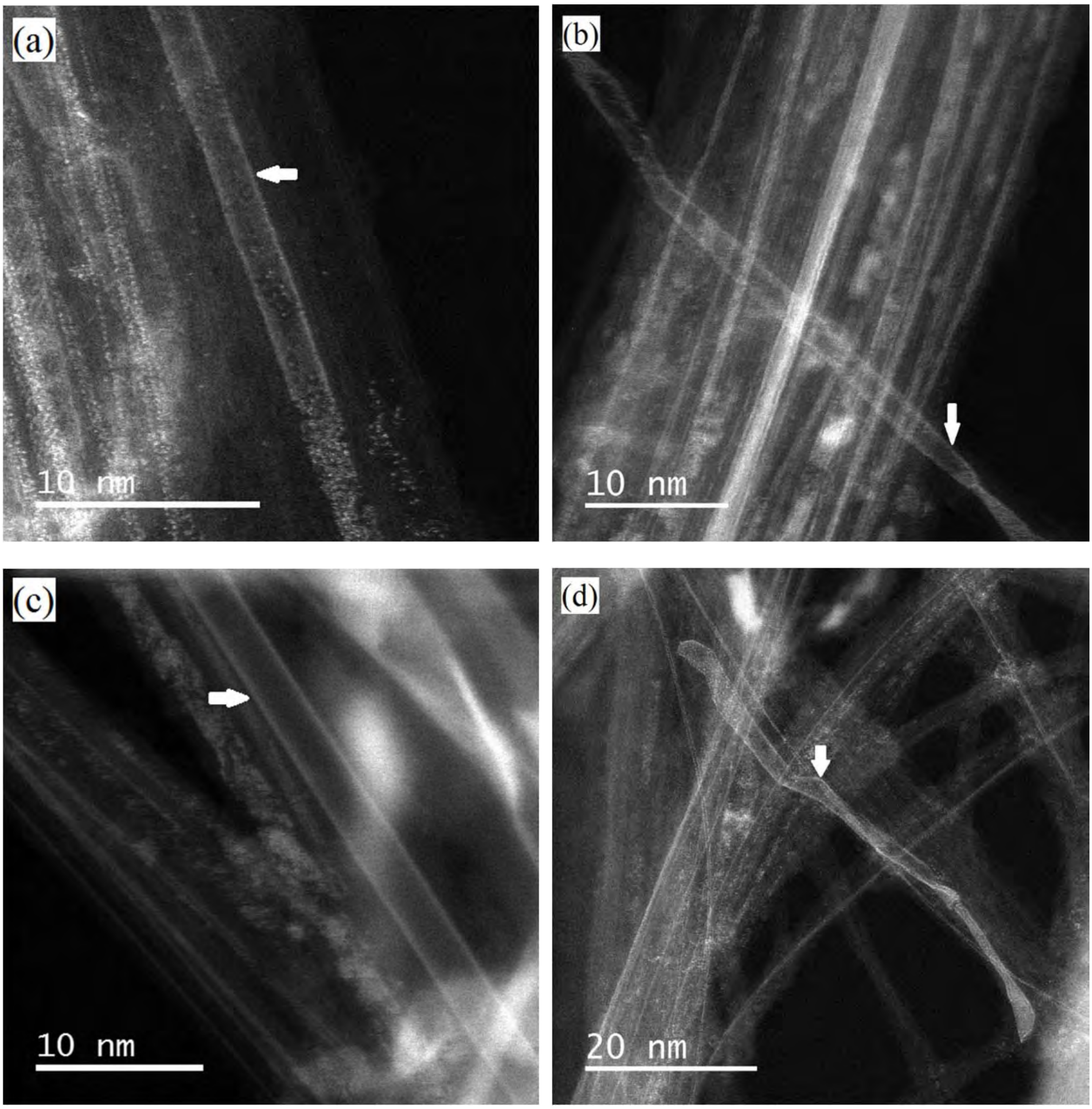

Fig. 2.26 - ADF images of inner iodine nanotubes (white arrows) found: (a) and (b) in I@DWCNTs_827; (c) in NiI$_2$@DWCNTs; (d) in I@DWCNTs_140.

It generally occurred when host CNTs exhibit rather large diameters, and can be described in two ways: (i) either as a coating of the host CNT inner surface by iodine, thereby resulting in making an inner iodine nanotube whose wall is probably amorphous, somehow resembling the inner PbI$_2$ nanotube illustrated in Fig.2.8b; (ii) or as a large yet flattened tube whose flattening event has created SWCNT-like channels at both edges, subsequently filled by iodine (Figure 2.27a-b).

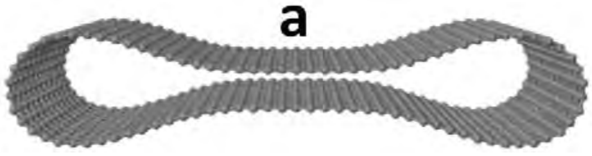

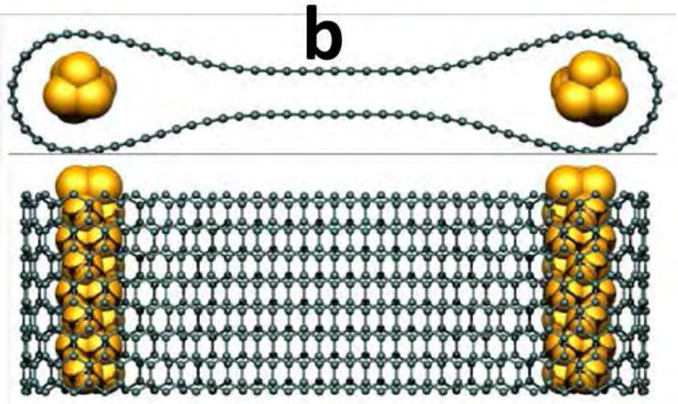

Fig. 2.27 – (a) Model of a large SWCNT once flattened, thereby exhibiting edge channels. (b) Cross-section and top views of a flattened tube as in (a), with the edge channels filled with a foreign material. Models provided by C. Ewels (IMN, Nantes).

Such large and flattened tubes have already been reported in the literature [21] for both SWCNTs and DWCNTs, and fullerene molecules have been already demonstrated to be able to fill their edge channels [22, 23]. Because of the observed irregular shapes (see Fig. 2.26d) which is quite consistent with the aspect of ribbon-like objects once folded and bent, and because of the dark contrast exhibited by the center of each of the tubes involved, which is barely consistent with the existence of an inner iodine tube (which would cause the contrast to look brighter than it is, we believe), we presume that the cases imaged in figure 2.26 do correspond to the sketch depicted in Figure 2.27b.

2.5.3 Summary regarding the various structural states of encapsulated iodine

In summary, peculiar structures can be obtained when materials are encapsulated within CNTs, such as atomic iodine chains either single and straight or twins (or triple) and helical, iodine crystals with structure differing from that of bulk iodine, iodine crystals with orthorhombic structure as in bulk, and iodine nanotubes which may not exist without the protection of the carbon sheath. Table 2.5 summarizes the possible configurations of iodine when encapsulated and their conditions of occurrence.

Hence, when filling DWCNTs with iodine, the configuration of iodine may vary dramatically as the inner diameter of the host CNT varies. As opposed to filling experiments starting from pure iodine, either molten or vapour, it is possible that the amount of iodine available at once is not enough for generating the double and triple helical chain configurations, thereby explaining why we rarely observed them in sample NiI$_2$@DWCNTs, as well the transitory Phase III structure presumably derived from them.

Table 2.5: Summary of the various morphologies, structure, and occurrence of iodine when encapsulated in CNTs.

Filling materials and sample name → ↓ Structural state ↓	Molten iodine (140°C) (I@DWCNTs_140)	Molten NiI$_2$ (827°C) (NiI$_2$@DWCNTs)	Iodine vapour (827°C) (I@DWCNTs_827)	Comments
Single chain	Abundant	Abundant	Abundant	Straight morphology, inside smallest tubes (< ~1nm) or in grooves between (outside) tubes of any diameter
Double chain	Present	No	Rare	Always helical
Triple chain	Rare	Rare	Rare	Always helical
Phase III structure [13]	Present	Rare	Present	For CNTs with inner diameters larger than 1 nm. Presumably resulting from the electron irradiation effect on triple iodine chains in TEM
Orthorhombic	Frequent	No	Present	For CNTs with inner diameters larger than 1.5 nm. Similar to bulk.
Amorphous	Rare	Present	Present Systematic for largest tubes (> ~2nm)	In tubes with intermediate inner diameters (~1.5 to ~2.5nm). Filling is sometimes segmented. Presumably resulting from the electron irradiation effect on Phase III structure in TEM
Iodine inner nanotube (amorphous)	Rare	Rare	Rare	In largest tubes only (inner diameter > ~2nm)
Comments	ADF STEM operated at 200kV	ADF STEM operated at 80kV BF TEM operated at 100kV	ADF STEM operated at 200kV BF TEM operated at 100kV	

However, alternatively, the absence of orthorhombic structure in the NiI$_2$@DWCNTs sample could be explained because large inner cavities are necessary for the structure to develop, which could not occur since the large tubes were preferentially filled with NiI$_2$.

On the other hand, it would be of great interest to perform measurements on the physical properties of DWCNTs filled with iodine chains, iodine crystals or iodine nanotubes and further make a comparison among them, if only these different structures could be prepared separately, or located and recognized within the CNTs before studying them individually.

2.6 Filling mechanisms

The influence of the filling materials characteristics will be discussed first, then that of the host nanotubes characteristics.

2.6.1 Physical and chemical properties of the filling materials

Physical parameters such as surface tension, viscosity, melting point, boiling point, and vapour pressure of the filling materials were gathered from the literature when available. Data on the surface tension of these metal iodides are scarcely reported in the literature because the experimental measurement of surface tension is rather difficult, specifically at molten state. A theoretical model proposed by Aqra [24] is thus employed in our study to calculate the surface tension of the inserted metal iodides, as shown in Eq. 2.1:

$$\gamma = \varphi^{-1}\left(\frac{V_s}{V}\right)^2 kT\left[\frac{0.0481E_s}{RT}\right]$$

$$\text{where } V \text{ or } V_s = \frac{M}{\rho} \text{ and } \varphi = \frac{\sqrt{3}}{2}\left(\frac{\sqrt{2}V_s}{N}\right)^{2/3} \qquad (2.1)$$

where γ is the surface tension (mJ/m^2), φ is the area occupied (cm^2/atom), M is molar mass, ρ is the density, V and V_s are the molar volumes at a given temperature and at the melting point, N is the Avogadro's number (6.02×10^{23}atoms/mol), k is the Boltzmann constant (1.38×10^{-23}J/K), T is the absolute temperature (K), R is the universal gas constant (8.31 J/(K· mol)) and E_s is the heat of sublimation. The calculated values of surface tension for CdI_2, CoI_2, FeI_2, NiI_2 and PbF_2 at their melting points are presented in ref. [24] and for AgI, KI, LiI, SnI_2 and $PbCl_2$, values of surface tension at melting point are reported in ref. [25] and [26]. For PbI_2, value of E_S is reported in the literature [27] and its surface tension is calculated using Eq. 2.1.

The relationship between viscosity η ($\mathrm{mN\cdot s/m^2}$) and temperature T (K) for AgI, CdI_2, KI, LiI and $PbCl_2$ are reported in ref. [28], as described in Eqs. 2.2 to 2.6:

AgI: $\eta=0.1481\exp(22004.02413/RT)$ (2.2)

CdI_2: $\eta=0.082084\exp(29472.58908/RT)$ (2.3)

KI: $\eta=0.1023\exp(20521.2734/RT)$ (2.4)

LiI: $\eta=0.1265\exp(17386.23343/RT)$ (2.5)

$PbCl_2$: $\eta=0.05619\exp(28292.68134/RT)$ (2.6)

where R is the universal gas constant.

In Section 2.5, we have observed that attempting to fill DWCNT material with NiI_2 has actually resulted in filling with NiI_2 but also in filling with pure iodine. This indicates that NiI_2 certainly experienced early decomposition during the filling step before the melting temperature is reached [29] thereby releasing gaseous iodine. Therefore, the Gibbs free energies ΔG_1^0 of the decomposition reaction for all the halide materials MX_y (X= F, Cl and I) used for the filling attempts into their elements M and halogen are reported in Table 2.6. ΔG_1^0 values were obtained from the software HSC Chemistry 6. It should be noted that the filling temperature used for PbF_2 was 854°C, at which temperature the corresponding ΔG_1^0 of its decomposition reaction is similar to what it is at 827°C. Therefore, only the ΔG_1^0 value at 827°C is shown in Table 2.6 in order to make a comparison among all the filling materials.

Table 2.6: ΔG_1^0 at 827°C for reaction $MX_y=M+\frac{y}{2}X_2$ (MX_y is the filling material, X= F, Cl and I).

Filling material	KI	PbF_2	LiI	$PbCl_2$	CdI_2	AgI	PbI_2	SnI_2	FeI_2	CoI_2	NiI_2
ΔG_1^0(kJ/mol)	530.5	510.5	465.9	210.6	123.2	101.6	94.4	69.0	57.5	26.9	1.5

It appears clearly that NiI_2 exhibit a significantly smaller Gibbs free energy of this reaction (~1.5 kJ/mol) compared to the other metal halides (ranging from ~27 to 530 kJ/mol).

Regarding the vapour pressure, data for various compounds at different temperature can be found both in the SGPS database and in Factsage software. Vapour pressure values for all the halide materials are reported in Table 2.7 below (see Section 2.7.2) along with all the gathered or calculated property values we have obtained. It is worth noting that NiI_2 exhibits a significantly higher vapour pressure value at the melting temperature compared to all the other metal halides, and one may wonder which effect this could have with respect to the filling mechanism. This is in full agreement with the fact that NiI_2 exhibits by far the smallest Gibbs free energy over all the filling material. This is also consistent with the fact that a slight decomposition of FeI_2 occurred during the filling process since a few iodine-filled nanotubes were also observed in the sample FeI_2@DWCNTs, which can also be explained by the small Gibbs free energy (the third smallest among all the filling materials, see Table 2.6) for the decomposition reaction of FeI_2. On the other hand, iodine-filled nanotubes were not observed in sample CoI_2@DWCNTs though the Gibbs free energy for the decomposition reaction of CoI_2 is the second smallest among all the filling materials (see Table 2.6). This could be due to the fact that higher free energy was required for the equilibrium between CoI_2 and its elements (Co, I_2) during the filling process than the value displayed in Table 2.6 since the actual filling temperature used for CoI_2 (see Table 2.1) was much lower than 827°C, at which the Gibbs free energy was calculated.

Redox potentials of the filling materials at melting point were also investigated and we will see why in next section. Since the redox potentials vary with temperature, in order to make relevant the comparison between all the metal iodides, the redox potential of each corresponding [metal iodide / metal] couple was calculated at 827°C, which is the highest temperature used among all the filling conditions. From now on, the "redox potential" will always refer to the potential of the couple [metal iodide / metal]. The calculation of each couple [metal iodide / metal] is derived from the following equations:

$$2MI = M + I_2 \quad \text{(for monoiodide)} \quad \text{or} \quad MI_2 = M + I_2 \quad \text{(for diiodide)} \qquad (2.7)$$

$$I_2 + 2e^- = 2I^- \qquad (2.8)$$

$$MI + e^- = M + I^- \quad \text{(for monoiodide)} \quad \text{or} \quad MI_2 + 2e^- = M + 2I^- \quad \text{(for diiodide)} \qquad (2.9)$$

As seen, equation (2.9) = $\frac{1}{2}$equation (2.8) + $\frac{1}{2}$equation (2.7) in the case of monoiodide or equation (2.9) = equation (2.8) + equation (2.7) in the case of diiodide. Thus, the Gibbs free energy for equation (2.9), ΔG_3^0 equals to $\frac{1}{2}(\Delta G_1^0 + \Delta G_2^0)$ in the case of monoiodide or equals to $(\Delta G_1^0 + \Delta G_2^0)$ in the case of diiodide. ΔG_1^0 are reported in Table 2.6 and ΔG_2^0 is considered equal to 0. Meanwhile, the relationship between ΔG_3^0 and the redox potential of the molten salts ($E^0_{MI/M}$ or $E^0_{MI_2/M}$) can be described as ΔG_3^0= -F$E^0_{MI/M}$ or ΔG_3^0= -2F$E^0_{MI_2/M}$. Therefore, the redox potential of molten salt can be derived to be -$\frac{\Delta G_1^0}{2F}$, where F is the Faraday constant (96500 C/mol). Taking AgI for example, its corresponding ΔG_1^0 at 827°C is 101.595 kJ/mol (see Table 2.6), thus the redox potential at 827°C is calculated to be ($-\frac{101.595\ kJ/mol}{2\times96500\ C/mol} = -0.526\ V$) as reported in Table 2.7.

2.6.2 Discussion

First of all, the various metal iodides were ranked according to their filling rates estimated from TEM observations (see section 2.5), as reported in Table 2.7. It appears that they dispatch into 4 main groups whose filling rates do not overlap taking into account the measurement accuracy: NiI_2 enables the highest filling rate (~50%), then AgI, SnI_2, PbI_2 and FeI_2 belong to a group with filling rates ranging from ~27 to ~38%, then CdI_2 and CoI_2 come next with filling rates in the range ~14-22%, and finally LiI and KI belong to the last group with filling rates lower than 1%. Meanwhile, in order to provide the TEM-based filling rate estimate with some support, as it is an important parameter on which the discussion will be based on, the weight percent of metal in the MI_x@DWCNT was investigated by elemental analysis for some hybrid-DWCNT samples, and the results are as follows: 13.31 wt% of Ni in NiI_2@DWCNTs, 3.69 wt% of Pb in PbI_2@DWCNTs, 1.1 wt% of Fe in FeI_2@DWCNTs, 0.97 wt% of Co in CoI_2@DWCNTs and 0.33 wt% of K in KI@DWCNTs. Then the volume ratio of each metal iodides based on these weight% values was calculated in order to compare with what the TEM images actually show, giving a ranking as follows:

KI@DWCNTs < CoI_2@DWCNTs < CdI_2@DWCNTs < FeI_2@DWCNTs < PbI_2@DWCNTs < NiI_2@DWCNTs.

It can be seen that, though the estimation of filling rates based on the HRTEM data is not accurate, the ranking of filling rates achieved by various metal iodides based on this method is valid as supported by the elemental analysis results.

Then, data on surface tension, viscosity, and vapour pressure of the filling materials as discussed in section 2.7.1 are also listed in Table 2.7, as well as melting point and boiling point temperatures of the filling materials. None of them are able to correlate with the filling-rate-based ranking, which is surprising at least for viscosity and surface tension which are presumably important when considering capillarity- and wetting-driven events, as CNT filling mechanisms were supposed to be.

Table 2.7: Some properties of the filling materials. Iodine-based filling materials are listed according to their filling rate as already reported in Table 2.3, and reported again in second left column. The far right column reports the ranking number according to the redox potential value.

Filling material	Estimated filling rate (%)	Melting point (°C)	Boiling point (°C)	Surface tension[a] (mJ/m^2)	Viscosity[a] (mN.s/m^2)	Vapour pressure[a] (Pa)	Redox potential[b] (V) and related ranking	
NiI_2	51±5	797	n.a.	54	n.a.	26400	-0.002	*1*
AgI	38±5	558	1506	171	3.58	0.2	-0.526	*6*
SnI_2	34±5	320	714	43	n.a.	31.8	-0.358	*4*
PbI_2	32±5	402	953	50	n.a.	22.7	-0.489	*5*
FeI_2	27±5	587	827	71	n.a.	320	-0.298	*3*
CdI_2	22±5	387	742	47	17.7	91.5	-0.638	*7*
CoI_2	14±5	520	570	53	n.a.	8.8	-0.139	*2*
LiI	<1	469	1171	94	2.12	0.1	-2.414	*8*
KI	<1	681	1330	70	1.6	35.4	-2.749	*9*
$PbCl_2$	1~5	501	950	138	4.57	34.9		
PbF_2	<1	824	1293	125	n.a.	192		
I_2	27±5	113.7	184.3	37	n.a.	1094	0.000	

[a] *All the data are obtained at the melting point of the filling material.*

[b] *For the couple [metal iodide / metal], when relevant (E_{I_2/I^-} is set to 0V as it is used as a reference couple for the calculations).*

n.a. = not available

Hence, chemical reactivity was also considered as a possible relevant factor, and redox potential of the couple [metal iodide / metal] was chosen as the parameter to account for it. Calculated redox potentials of the filling materials as discussed in section 2.7.1 are reported in Table 2.7, and provide another ranking whose values are listed in decreasing order in the far right column for easier comparison with the filling rate-based ranking. From this comparison, it appears that both rankings compare fairly well (yet with a few anomalies):

- The highest filling rate, achieved for NiI_2 (51%), corresponds to the highest redox potential value;
- The large group gathering AgI, SnI_2, PbI_2, and FeI_2 (27-38%) corresponds to ranking from #3 to 6 for both the filling rate and the redox potential (while the position of AgI in the list represents a first anomaly);
- The small group including CdI_2 and CoI_2 with low filling rates in the range 14-22% shows the second anomaly: while CdI_2 is ranked #6 and 7 according to the filling rate and redox

potential respectively, CoI_2 is ranked #7 according to the filling rate, but is ranked #2 according to the redox potential;

- The lowest filling rates (for KI and LiI: less than 1%) correspond to the lowest redox potentials.

This result shows a good correlation between filling rate and redox potential. This correlation can relate to the need for the tubes to be opened, as the prerequisite for the nanocapillarity-driven filling to occur. Hence, the ability of the filling material in opening the nanotubes is of an utmost importance giving that our starting DWCNTs are initially closed. In a sense, considering that molten halides are supposed to be ionic liquids, redox potential can be considered as an indicator of the reactivity of the halides towards polyaromatic carbon.

The first anomaly regarding the ranking of AgI, which is at the top of its group regarding the filling rate (~38%) but at the bottom of it regarding the redox potential (-0.526 V), could be explained by considering the surface tension values. Indeed, all the metal iodides investigated exhibit surface tension values in the range 43-94 $mJ.m^{-2}$ except AgI which exhibits a very high value of 171 $mJ.m^{-2}$. It is then reasonable to consider that such a difference significantly favors the capillary filling event for AgI with respect to the others: according to Jurin's law (see Section 1.2.5 in Chapter 1), the height reached by a liquid in a capillary increases with the surface tension of the liquid, for a given capillary diameter [2].

A second anomaly was pointed out above for CoI_2, since it is ranked #7 according to the filling rate but ranked #2 according to the redox potential. This could be explained by the high propensity of CoI_2 to dimerize even before the melting point is reached [30] assuming that the dimerization is detrimental to the opening and then the filling event (for example by increasing the viscosity as this is the case for polymers when the chain length increases, and also possibly decreasing the reactivity). It is worth noting that a similar behaviour was also observed for FeI_2 [31] but its ability to dimerize is lower compared to CoI_2 [32], which is consistent with the observation that the filling rate for this compound is not affected.

Finally, it is also worth noting that in case of filling DWCNTs with NiI_2, it is likely that the opening of the tubes starts first with gaseous I_2 resulting from the decomposition of NiI_2 which is was evidenced in section 2.5 and explained in section 2.7.2, and then compete with the opening effect due to molten NiI_2. Gaseous I_2 may indeed react with the tube to open them and then fill them, as ascertained from the literature [5,13,33] and the current study (see Table 2.7, confirmed by the results shown in section 2.5 on the reference experiments consisting in filling DWCNTs while starting from pure iodine as filling material). As a result, the material found to fill the DWCNTs was both iodine and NiI_2 (in proportions ~35/65) as ascertained by EELS. Therefore, this competition has hindered the actual filling rate that could have been achieved with NiI_2 only, which could have been higher than observed, based on the highest redox potential of this compound within the whole metal iodide series.

In this work, the reactivity of the metal iodides with the DWCNTs resulting in giving access to the tube inner cavity was chosen to be represented by the redox potential values (calculated at the same temperature for all the compounds). One may wonder why not representing it in a more straightforward way by the Gibbs free energy of the reactions involving graphitic carbon and the different metal halides, resulting in the formation of carbon tetraiodide CI_4 at the corresponding melting temperature ($4MI + C = 4M + CI_4$ (for monoiodide) or $2MI_2 + C = 2M + CI_4$ (for diiodide)). Alternatively, the formation of metal carbide and iodine (vapour) could be considered. However, due to the absence of such carbide phases in all the filled CNT products, we have discarded this possibility. The problem is that, once calculated (see Table 2.8), the related ΔG values for this reaction are all positive, suggesting that the related reactions are all thermodynamically infeasible. However, it is clear from our experiments and previous ones from the literature [5,6,25] that iodine, either gaseous or molten, is able to open and then fill DWCNTs (and SWCNTs). The reason for this apparent contradiction probably comes from the fact that in available thermodynamics databases, data related to sp^2-hybridized carbon is represented by genuine graphite, which is far from being valid for CNTs, and specifically for DWCNTs and SWCNTs. First, sp^2 carbon networks in DWCNTs and SWCNTs are bent following a nanometre-range radius of curvature, and second, according to Euler's rule, carbon nanotubes include 6 pentagons at each tip in order to close the nanostructure. For both configurations (*i.e.*, "bent graphene", and pentagons), C-C bonds are heavily strained (specifically in pentagons), which is known to significantly enhance their reactivity [34], and then is likely to turn the free Gibbs energy of the reaction with metal iodides down to negative values.

Table 2.8: ΔG for reaction $\frac{4}{x}MI_x + C = \frac{4}{x}M + CI_4$ (MI_x is the filling material) at the melting point of the filling material.

Iodide name	ΔG kJ/mol
NiI_2	361
AgI	545
SnI_2	537
PbI_2	580
FeI_2	467
CdI_2	639
CoI_2	418
KI	1434
LiI	1314

In summary, filling DWCNTs with various iodides was performed and the relationships between presumably relevant physical and chemical properties of the iodides and the filling rate were investigated. It is found that the filling rate is mostly driven by the redox potential of the [metal iodide / metal] couple of the filling material at the molten state, which relates to the reactivity of metal iodides towards carbon, thanks to the enhanced reactivity of carbon with respect to graphite when involved in DWCNTs (and SWCNTs). Therefore, the ranking based on the filling rate and that based on the redox potential are fairly well related. Few anomalies in the correlation exist, though, which can be explained by considering other parameters such as surface tension, vapour pressure, or ability to dimerize.

2.6.3 Influence of the properties of host CNTs on the filling rate

Thanks to our selection of host tubes, the parameters that can be discussed are:

- the number of walls (from 1 to more than 10)
- the inner diameter (from 0.5 to 70 nm)
- the chemical nature of the inner tube wall (carbon or BN)
- The surface energetics of the inner surface of host tubes

Regarding the latter parameter, yet no values are provided since no attempt of measuring it was made, a large variation is expected by comparing CNTs with concentric texture (whose inner surface energetics is driven by that of graphene surface, in the range of 60 mJ/m^2 [35], even if the curvature may induce some modification), CNTs with herringbone texture (whose inner surface energetics is driven by that of graphene edges), and that of BNNT (whose inner surface energetics is driven by that of hexagonal boron nitride layer surface, which is depleted in π electrons with respect to graphene surface, providing a surface energy of ~47 mJ/m^2 [36]).

By comparing the estimated filling rates with PbI_2 for various types of host CNTs as shown in Table 2.4 (reminded below), the following ranking is obtained:

PbI_2@SWCNTs = PbI_2@DWCNTs > PbI_2@FWCNTs > PbI_2@h-MWCNTs > PbI_2@c-MWCNTs-a.

Reminder of Table 2.4

sample	*PbI_2@ SWCNTs*	*PbI_2@ DWCNTs*	*PbI_2@ FWCNTs*	*PbI_2@ c-MWNTs-a*	*PbI_2@ h-MWCNTs*	*PbI_2@ BNNTs*	*NiI_2@ BNNTs*
Estimated filling rate (%)	32±5	32±5	25±5	<1	20±5	<1	0
Most frequent nb of walls	1	2	2-6	> 10	Not appropriate	2-4	2-4
Most frequent inner diameters	1.35 nm	1-2 nm	1.5-3.5 nm	2-10 nm	50-70 nm	1.2-3 nm	1.2-3 nm

Thanks to the discussion made in section 2.6.2, it is reasonable to explain the higher filling rates exhibited by PbI_2@SWCNTs, PbI_2@DWCNTs and PbI_2@FWCNTs compared to the c-MWCNTs-a by the limited number of walls, hence making the opening of the tubes by the molten halide possible (easier), whereas c-MWCNTs-a obviously remained closed.

On the other hand, as most h-MWCNTs were naturally opened at one end, the reactivity of the molten halide towards the thick carbon wall was not an issue, and significant filling could occur. More in the detail, we could discuss regarding the filling rate achieved. Indeed, h-MWCNTs were opened, hence filling could occur. Why filling rates higher than 20% were then not achieved could be questioned. This could relate to the Jurin's law (1.4) $h = \frac{2\gamma cos\theta}{rg\rho}$ introduced in chapter 1 which describes that the capillary rise of a liquid in a hollow cylinder is inversely proportional to the radius of the capillary r for a given liquid. Thereby, it is deduced that large-inner-diameter CNTs should fill over a shorter length range than small-inner-diameter CNTs, meaning lower filling efficiency. However, since h could not be calculated due to the lack of needed data, there is a possibility that the filling rate should have been lower than 20% with respect to the specific inner diameter values of h-MWCNTs. In such a case, the relatively high filling rate could be due to the surface energetics, which is higher for h-MWCNTs than for DWCNTs and FWCNTs since the inner surface of the former is mostly made of graphene edges (with respect to graphene faces for FWCNTs and DWCNTs), thereby leading to different γ_{SV} and γ_{SL} for the nanowetting (see chapter 1). This uncertainty regarding which parameter prevails on the filling rate among the surface energetics or the inner tube diameter could have been ruled out by considering c-MWCNTs-a, provided the latter would have been opened. However, naturally opened large c-MWCNTs are not easy to obtain, and subjecting large c-MWCNTs to some chemical procedure (e.g., HNO_3 treatment) to open them comes along with modifications (e.g., the occurrence of amorphous carbon resulting from the oxidation that may clog the opening created, or the functionalization of the opening mouth that might prevent the filling material from entering the cavity) which are likely to make the experiments barely comparable.

A similar uncertainty is stated for the filling mechanisms of BNNTs. Indeed, despite their limited number of walls, BNNTs could not be filled either with NiI_2 or PbI_2 (see section 2.5). This may relate to what was discussed in section 2.7.2: The fact that PbI_2 did not fill BNNTs might be due to the poor reactivity of PbI_2 with boron nitride hence leaving BNNTs unopened, whereas the fact that the BNNT material was heavily destroyed when replacing PbI_2 by NiI_2 could be due to the high reactivity of BN with the iodine species released from NiI_2 decomposition, possibly generating boron triiodide. Alternatively, should the reactivity of PbI_2 towards boron nitride be enough for opening the tube ends, as could be suggested from Figure 2.12c, the reason why the filling rate of PbI_2@BNNTs was still almost nil may also be attributed to the low surface energy of BN relatively to graphene [9].

2.7 Conclusions

In this chapter, various metal halides (metals, alkali metals and transition metals) and iodine have been successfully introduced into DWCNTs mostly via the molten phase method or occasionally by the gas phase method (in the case of iodine). Peculiar structures were observed for the confined NiI_2

and iodine with respect to the bulk filling materials. Especially in the case of the latter, atomic chains with different configurations depending on the size of the inner cavity of the host nanotube were clearly evidenced by ADF images. Furthermore, the influence of various characteristics of the host CNTs and of possibly relevant chemical and physical properties of the filling materials on the filling rate was investigated. It was found that: i) for various types of CNTs filled with PbI_2, the CNT with smaller inner diameter was filled more efficiently; ii) for DWCNTs filled with various halides, the filling rates of the hybrid DWCNTs is mainly related to the reactivity of the halides towards carbon which can be represented by the Gibbs free energies of the decomposition reactions of halides. Within the metal iodides series, the reactivity of the filling material towards carbon was further indicated by the redox potential (E MIx/M) of the filling material and a relationship between the redox potential and the filling rate was demonstrated. Meanwhile, other parameters such as surface tension, viscosity, the possible formation of dimers, or the early release of iodine - among which some were presumably important for nanowetting phenomena - may also play an additional role in the filling process to explain subsidiary effects. Further work on similar investigations involving other halides, other compounds, as well as other host nanotubes with characteristics suitable for allowing more accurate comparisons should now be carried out in order to ascertain the role of some parameters such as the surface energy of the host tube inner surface, but the fact that not all the data (e.g., viscosity at melting temperature) are available in the literature and that thermodynamics databases only consider carbon in the regular graphitic form slows down significantly the progress in the field.

References

[1] E. Dujardin, T. Ebbesen, H. Hiura, K. Tanigaki, Capillarity and wetting of carbon nanotubes, Science, 265 (1994) 1850-1852.

[2] P.-G. De Gennes, F. Brochard-Wyart, D. Quéré, Capillarity and wetting phenomena: drops, bubbles, pearls, waves, Springer Science & Business Media, 2013.

[3] M. Monthioux, E. Flahaut, J.-P. Cleuziou, Hybrid carbon nanotubes: strategy, progress, and perspectives, Journal of materials research, 21 (2006) 2774-2793.

[4] D. Wright, A.E. York, K. Coleman, M.H. Green, J. Hutchison, Capillarity and silver nanowire formation observed in single walled carbon nanotubes, Chemical Communications, (1999) 699-700.

[5] X. Fan, E.C. Dickey, P. Eklund, K. Williams, L. Grigorian, R. Buczko, S. Pantelides, S. Pennycook, Atomic arrangement of iodine atoms inside single-walled carbon nanotubes, Physical review letters, 84 (2000) 4621.

[6] E. Flahaut, C. Laurent, A. Peigney, Catalytic CVD synthesis of double and triple-walled carbon nanotubes by the control of the catalyst preparation, Carbon, 43 (2005) 375-383.

[7] E. Flahaut, F. Agnoli, J. Sloan, C. O'Connor, M. Green, CCVD synthesis and characterization of cobalt-encapsulated nanoparticles, Chemistry of Materials, 14 (2002) 2553-2558.

[8] E. Flahaut, R. Bacsa, A. Peigney, C. Laurent, Gram-scale CCVD synthesis of double-walled carbon nanotubes, Chemical Communications, (2003) 1442-1443.

[9] D. Golberg, Y. Bando, C. Tang, C. Zhi, Boron nitride nanotubes, Advanced Materials, 19 (2007) 2413-2432.

[10] G.F. Vander Voort, Metallography, principles and practice, ASM International, 1984.

[11] C.M. Wood, C. Hogstrand, F. Galvez, R. Munger, The physiology of waterborne silver toxicity in freshwater rainbow trout (Oncorhynchus mykiss) 2. The effects of silver thiosulfate, Aquatic toxicology, 35 (1996) 111-125.

[12] L. Cabana, B. Ballesteros, E. Batista, C. Magén, R. Arenal, J. Oró‐Solé, R. Rurali, G. Tobias, Synthesis of PbI_2 Single‐Layered Inorganic Nanotubes Encapsulated Within Carbon Nanotubes, Advanced Materials, 26 (2014) 2016-2021.

[13] L. Guan, K. Suenaga, Z. Shi, Z. Gu, S. Iijima, Polymorphic structures of iodine and their phase transition in confined nanospace, Nano letters, 7 (2007) 1532-1535.

[14] J. Ketelaar, Die Kristallstruktur des Nickelbromids und-jodids, Zeitschrift für Kristallographie-Crystalline Materials, 88 (1934) 26-34.

[15] E. Flahaut, J. Sloan, S. Friedrichs, A.I. Kirkland, K. Coleman, V. Williams, N. Hanson, J. Hutchison, M.L. Green, Crystallization of 2H and 4H PbI_2 in carbon nanotubes of varying diameters and morphologies, Chemistry of materials, 18 (2006) 2059-2069.

[16] J. Sloan, A.I. Kirkland, J.L. Hutchison, M.L. Green, Aspects of crystal growth within carbon nanotubes, Comptes Rendus Physique, 4 (2003) 1063-1074.

[17] N. Thamavaranukup, H.A. Höppe, L. Ruiz-Gonzalez, P.M. Costa, J. Sloan, A. Kirkland, M.L. Green, Single-walled carbon nanotubes filled with M OH (M= K, Cs) and then washed and refilled with clusters and molecules, Chemical communications, (2004) 1686-1687.

[18] J. Chancolon, F. Archaimbault, A. Pineau, S. Bonnamy, Filling of carbon nanotubes with selenium by vapor phase process, Journal of nanoscience and nanotechnology, 6 (2006) 82-86.

[19] M. Chorro, G. Kané, L. Alvarez, J. Cambedouzou, E. Paineau, A. Rossberg, M. Kociak, R. Aznar, S. Pascarelli, P. Launois, 1D-confinement of polyiodides inside single-wall carbon nanotubes, Carbon, 52 (2013) 100-108.

[20] E. Evans, The Absorption Spectrum of Iodine Vapor at High Temperatures, The Astrophysical Journal, 32 (1910) 1.

[21] D. Choi, Q. Wang, Y. Azuma, Y. Majima, J. Warner, Y. Miyata, H. Shinohara, R. Kitaura, Fabrication and characterization of fully flattened carbon nanotubes: a new graphene

nanoribbon analogue, Scientific reports, 3 (2013) 1617.

[22] H.R. Barzegar, E. Gracia-Espino, A. Yan, C. Ojeda-Aristizabal, G. Dunn, T. Wågberg, A. Zettl, C60/Collapsed Carbon Nanotube Hybrids: A Variant of Peapods, Nano letters, 15 (2015) 829-834.

[23] Q. Wang, R. Kitaura, Y. Yamamoto, S. Arai, H. Shinohara, Synthesis and TEM structural characterization of C60-flattened carbon nanotube nanopeapods, Nano Research, 7 (2014) 1843-1848.

[24] F. Aqra, Surface tension of molten metal halide salts, Journal of Molecular Liquids, 200 (2014) 120-121.

[25] G. Brown, S. Bailey, M. Novotny, R. Carter, E. Flahaut, K. Coleman, J. Hutchison, M. Green, J. Sloan, High yield incorporation and washing properties of halides incorporated into single walled carbon nanotubes, Applied Physics A, 76 (2003) 457-462.

[26] G.J. Janz, C. Dijkhuis, G. Lakshminarayanan, R. Tomkins, J. Wong, Molten salts. Volume 2. Ssection 1. Electrochemistry of molten salts: Gibbs free energies and excess free energies from equilibrium-type cells. Section 2. Surface tension data, Rensselaer Polytechnic Inst., Troy, NY, 1969.

[27] J. Duncan, F. Thomas, The vapour pressures of lead iodide and neodymium tricyclopentadienide, Journal of the Chemical Society (Resumed), (1964) 360-364.

[28] G.J. Janz, Thermodynamic and transport properties for molten salts: correlation equations for critically evaluated density, surface tension, electrical conductance, and viscosity data, Amer Inst of Physics, 1988.

[29] J. McCreary, R. Thorn, Heat and Entropy of Sublimation of Nickel Dichloride, Dibromide, and Di‐iodide; Dissociation Energies of Gaseous $NiCl_2$ and $NiBr_2$, The Journal of Chemical Physics, 48 (1968) 3290-3297.

[30] S.D. Hill, C. Cleland, A. Adams, A. Landsberg, F.E. Block, Vapor pressures and heats of sublimation of cobalt dihalides, Journal of Chemical and Engineering Data, 14 (1969) 84-89.

[31] W. Zaugg, N. Gregory, Thermodynamic Properties of FeI_2 (g) and Fe_2I_4 (g), The Journal of Physical Chemistry, 70 (1966) 490-494.

[32] N. Schiefenhövel, M. Binnewies, F. Janetzko, K. Jug, Zur Thermodynamik der Dimerisierung von Gasfoermigem CrI2, MnI2, FeI_2 und CoI_2: Experimentelle und Quantenchemische Untersuchungen, Zeitschrift für anorganische und allgemeine Chemie, 627 (2001) 1513-1517.

[33] A. Tonkikh, V. Tsebro, E. Obraztsova, K. Suenaga, H. Kataura, A. Nasibulin, E. Kauppinen, E. Obraztsova, Metallization of single-wall carbon nanotube thin films induced by gas phase iodination, Carbon, 94 (2015) 768-774.

[34] Y. Chen, R. Haddon, S. Fang, A.M. Rao, P. Eklund, W. Lee, E. Dickey, E. Grulke, J. Pendergrass, A. Chavan, Chemical attachment of organic functional groups to single-walled carbon nanotube material, Journal of Materials Research, 13 (1998) 2423-2431.

[35] A. Kozbial, Z. Li, C. Conaway, R. McGinley, S. Dhingra, V. Vahdat, F. Zhou, B. D'Urso, H. Liu, L. Li, Study on the Surface Energy of Graphene by Contact Angle Measurements, Langmuir

30 (2014) 8598-8606.

[36] N. Rathod, The effect of surface properties of boron nitride on polymer processability, Master Thesis, The University of British Colombia, Canada (2003).

Chapter 3 In situ *chemistry in X@DWCNTs*

3.1 Introduction

One of the limitations of the molten phase method is that it is hard to directly insert material with high melting point (>1000°C), *e.g.* oxides, fluorides, sulfides, metals, etc. into DWCNTs, while the synthesis of these materials with one-dimensional nanostructures is of great interest due to their peculiar properties. For instance, nanosized FeF_3 provides the possibility for achieving fast reversible conversion reaction when used as cathode material for lithium ion batteries [1]. Semiconducting PbS nanocrystals with narrow band gap energy are widely used in IR detector [2], photovoltaic devices [3], *etc*. and monoatomic Co chains exhibit larger local orbital and spin magnetic moments compared to bulk Co and Co nanoclusters due to the reduced atomic coordination [4]. To overcome the high-temperature issue, we also took advantage of the inner cavity of DWCNTs which not only templates the growth but also acts as a nanoreactor in order to perform chemical reactions. The insertion of materials with high melting point is typically achieved by first filling CNTs with a precursor, and then transforming the precursor into the desired 1D nanostructure by post-treatments. In this chapter, *in situ* sulfurization of PbI_2@DWCNTs, *in situ* reduction of FeI_2@DWCNTs and NiI_2@DWCNTs aiming to obtain encapsulated metal nanocrystals, and *in situ* fluorination of FeI_2@DWCNTs aiming to obtain encapsulated iron fluoride crystals were performed. Various characterizations of these transformed hybrid DWCNTs including HRTEM, EELS, X-EDS, XRD, XPS and Raman Spectroscopy were carried out in order to investigate if the transformations were successful, and the results are reported in this chapter.

3.2 *In situ* sulfurization of PbI_2@DWCNTs

3.2.1 Methods

According to the reaction 3.1 described below, reaction of PbI_2 with sulphur is used in order to synthesize PbS nanocrystals:

$$PbI_2 + S \rightarrow PbS + I_2 \qquad (3.1)$$

To explore a suitable method for preparing PbS@DWCNTs, sulfurization tests were performed under three different experimental conditions:

1. Two separate alumina boats containing successively 1) sulphur powder and 2) the as-prepared PbI_2@DWCNTs were placed into the middle of a horizontal furnace and heated at 400°C for 10h in Ar atmosphere. Then the furnace was naturally cooled down to room temperature under the same Ar atmosphere. The synthesized sample is denoted as sample 1.
2. The sulphur powder and as-prepared PbI_2@DWCNTs were mixed together and transferred into a quartz ampoule. Then the ampoule was evacuated and sealed following the same procedure used for preparing X@DWCNTs as described in chapter 2. Afterwards, the ampoule was placed in a horizontal furnace and heated at 400°C for 10h. Finally, the furnace was naturally cooled down to room temperature. The synthesized sample is denoted as sample 2.
3. The sulphur powder and as-prepared PbI_2@DWCNTs were mixed together and transferred into a quartz ampoule. Then the ampoule was evacuated and sealed following the same procedure used for sample 2. Afterwards, the ampoule was placed in a furnace with a 10° tilt and heated at only 250°C for 72h. Finally, the furnace was naturally cooled down to room temperature.

To remove the unreacted sulphur after the sulfurization, materials were washed in toluene and heated at 60°C for 10 min under stirring. Then the materials were filtered and dried in an oven at 80°C for 24h. The obtained three sulphurized samples starting from PbI_2@DWCNTs synthesized under condition 1, 2 and 3 were denoted as PbS@DWCNTs_1, PbS@DWCNTs_2 and PbS@DWCNTs_3, respectively.

The samples were characterized by the same TEM and EELS facilities as described in Chapter 2. Additionally, a Philips CM20FEG microscope operated at 200 kV was used for X-EDS analysis. XPS spectra of samples were collected on a SpecsLab PHOIBOS 150 spectrometer at the BESSY (German synchroton radiation facility) using monochromatized Al Kα-radiation (hν = 1486.6 eV) and a ‘‘VG Escalab HP” spectrometer using monochromatized Al Kα-radiation (hν = 1486.6 eV). The former has better energy resolution than the latter.

3.2.2 Results and Discussion

Fig. 3.1 shows the HRTEM images of PbS@DWCNTs_1, PbS@DWCNTs_2 and PbS@DWCNTs_3, respectively. It is found that nearly all the nanotubes observed under the microscope are empty in PbS@DWCNTs_1, while nanotubes encapsulating nanocrystals are observed in PbS@DWCNTs_2 and PbS@DWCNTs_3. The absence of encapsulation in PbS@DWCNTs_1 should be due to the fact that the previously encapsulated PbI_2 nanocrystals evaporated under the Ar flow at 400°C for 10h (due to the nanosize, the melting point of PbI_2 nanocrystals may be decreased). Compared to PbS@DWCNTs_3, less filled-tubes are observed in PbS@DWCNTs_2 based on the visual inspection of HRTEM images.

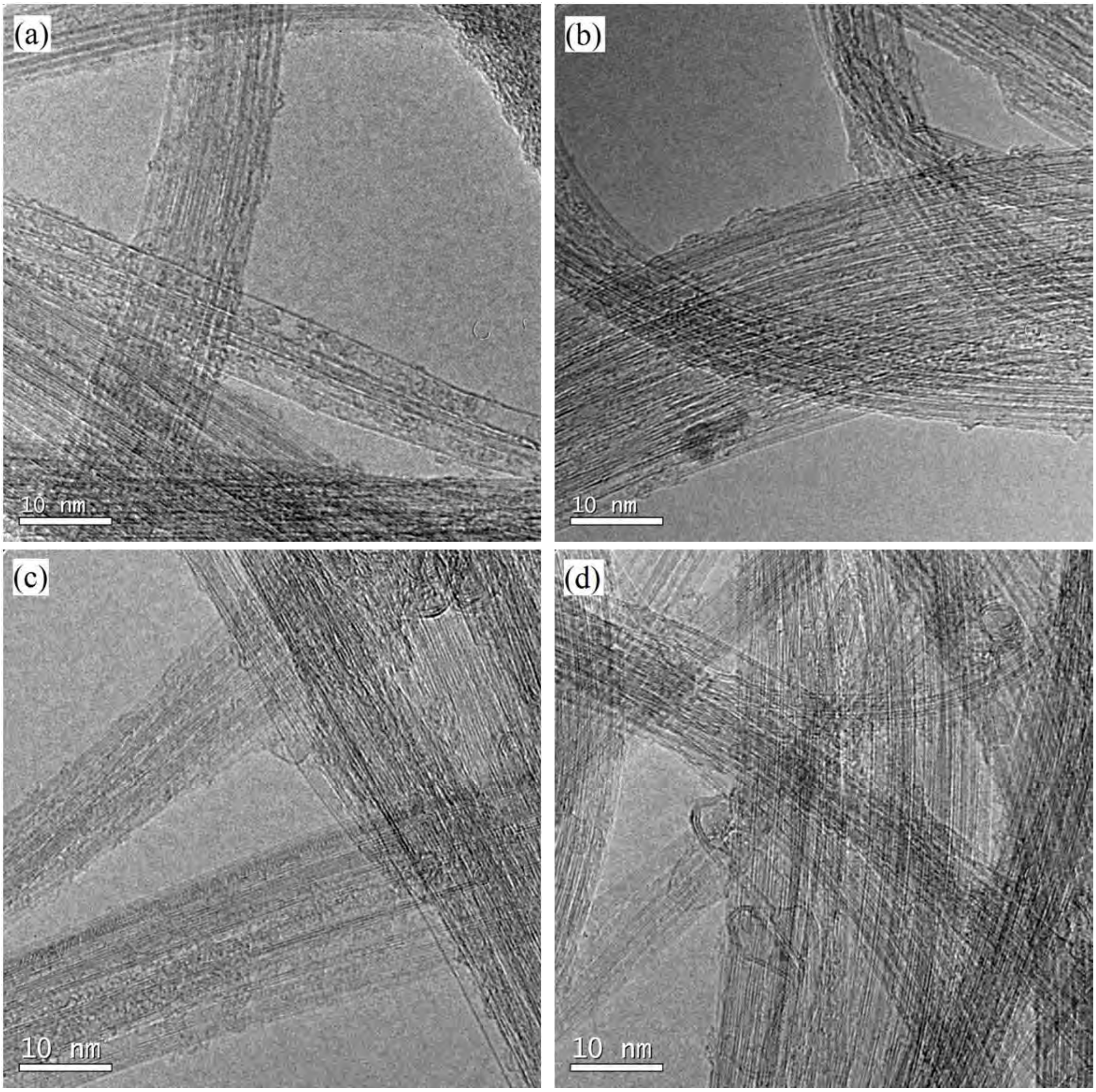

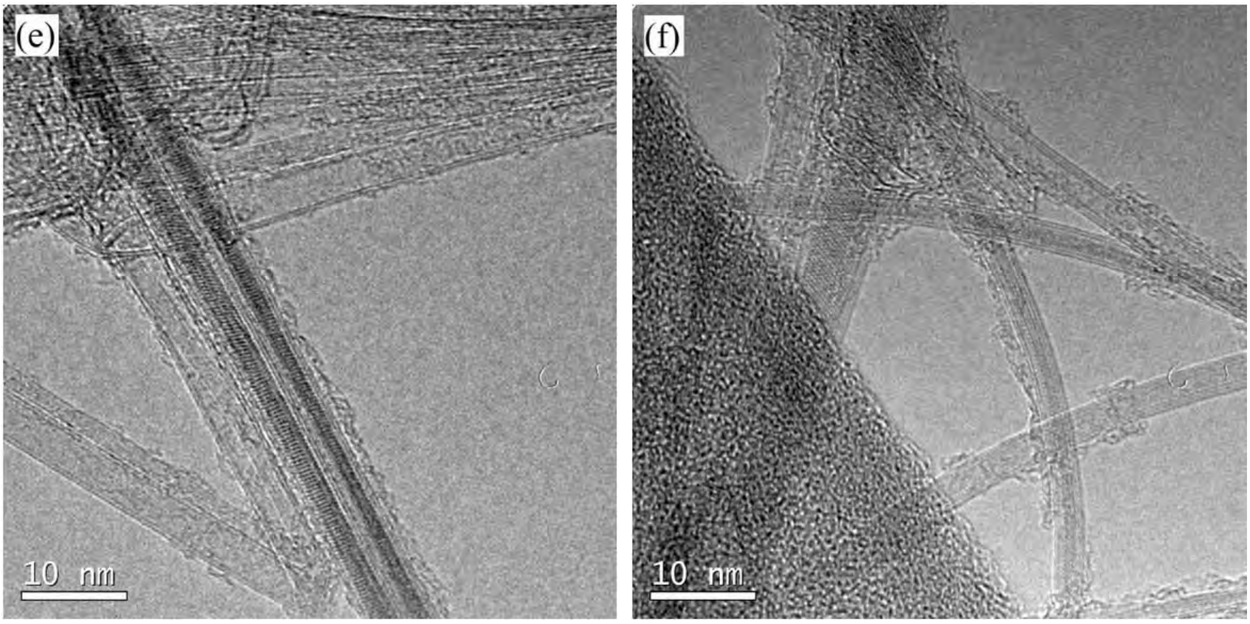

Fig. 3.1 - HRTEM images of (a) and (b) PbS@DWCNTs_1, (c) and (d) PbS@DWCNTs_2, (e) and (f) PbS@DWCNTs_3.

PbS@DWCNTs_3 being the most promising sample, it was further investigated by EELS analysis. The carbon (C) K edge is located around 284 eV, the sulphur (S) L edge is located around 165 eV, the iodine (I) M edge is located around 619 eV and the lead (Pb) M edge is located around 2484 eV. The EELS spectra (Fig. 3.2b and d) collected from CNT bundles encapsulating crystals (Fig. 3.2a and c) in PbS@DWCNTs_3 identify the presence of both sulphur and iodine in the encapsulated nanocrystals. The presence of carbon originates from the carbon nanotubes. However, the presence of Pb is hard to be detected by EELS because of its high ionization energy. Therefore, X-EDS analysis was used to investigate the elemental composition of the filled CNTs.

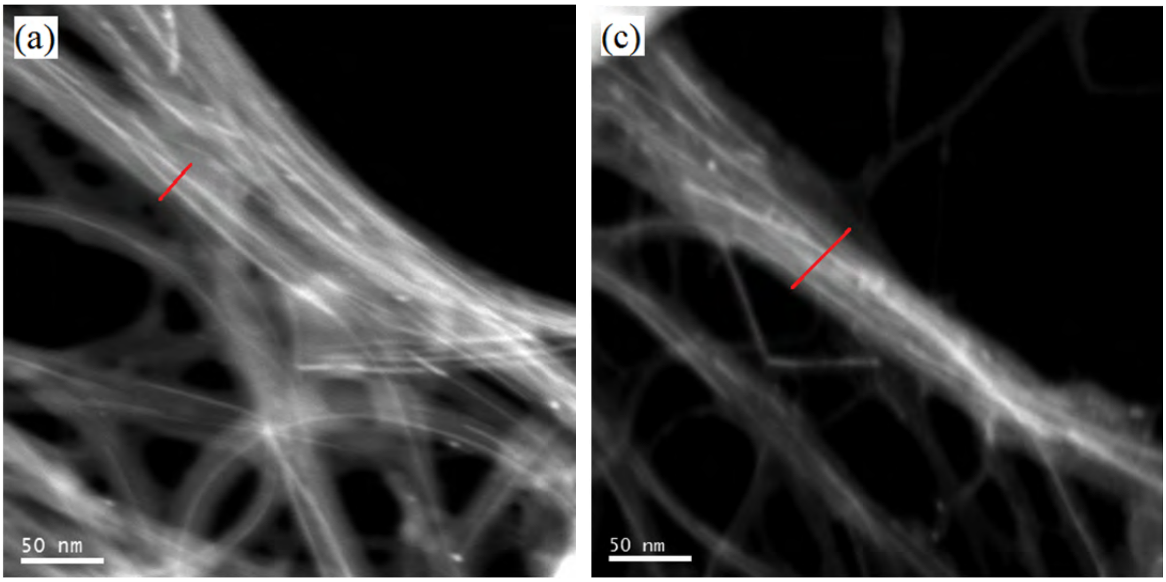

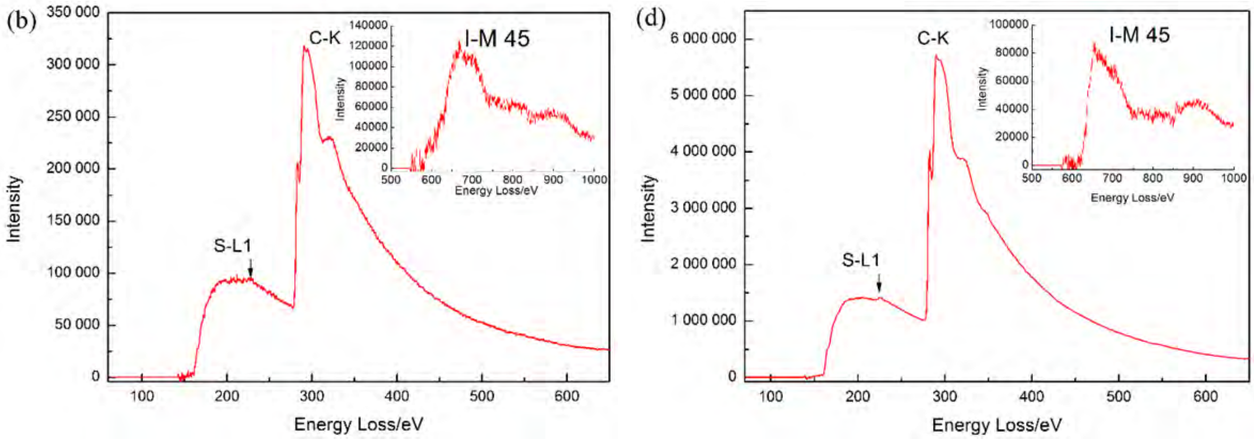

Fig. 3.2 - (a) and (c) High angle ADF (HAADF) images (FEI Tecnai-F20 equipped with a HAADF detector) of CNT bundles accommodating nanocrystals in PbS@DWCNTs_3; (b) and (d) EEL spectra obtained by summing the spectra collected along the red line shown in (a) and (c), respectively.

Typical STEM images and X-EDS spectra of PbS@DWCNTs_2 and PbS@DWCNTs_3 are shown in Fig. 3.3 and Fig. 3.4, respectively.

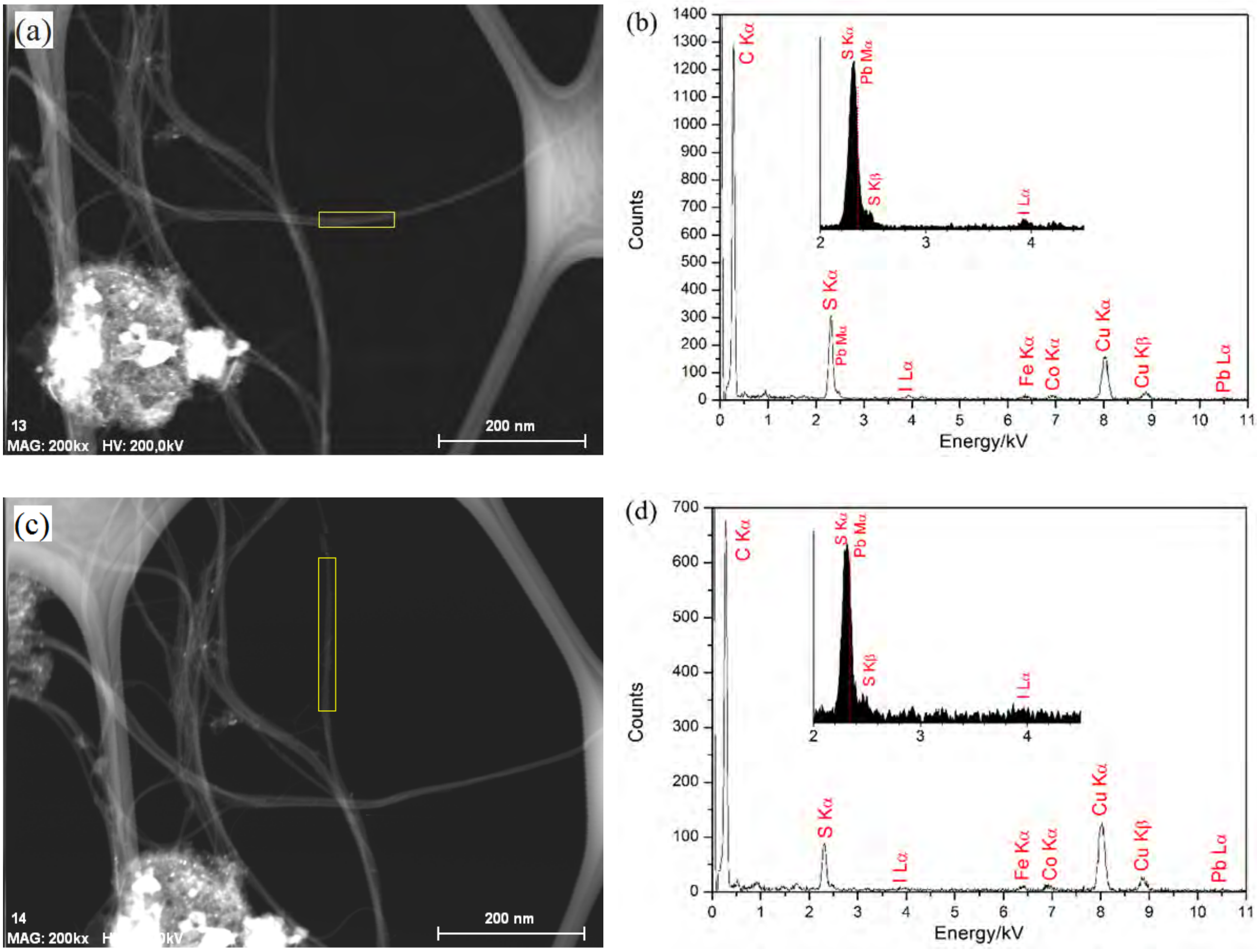

Fig. 3.3 - (a) and (c) STEM images of PbS@DWCNTs_2; (b) and (d) X-EDS spectra collected from the DWCNT bundles boxed in (a) and (c).

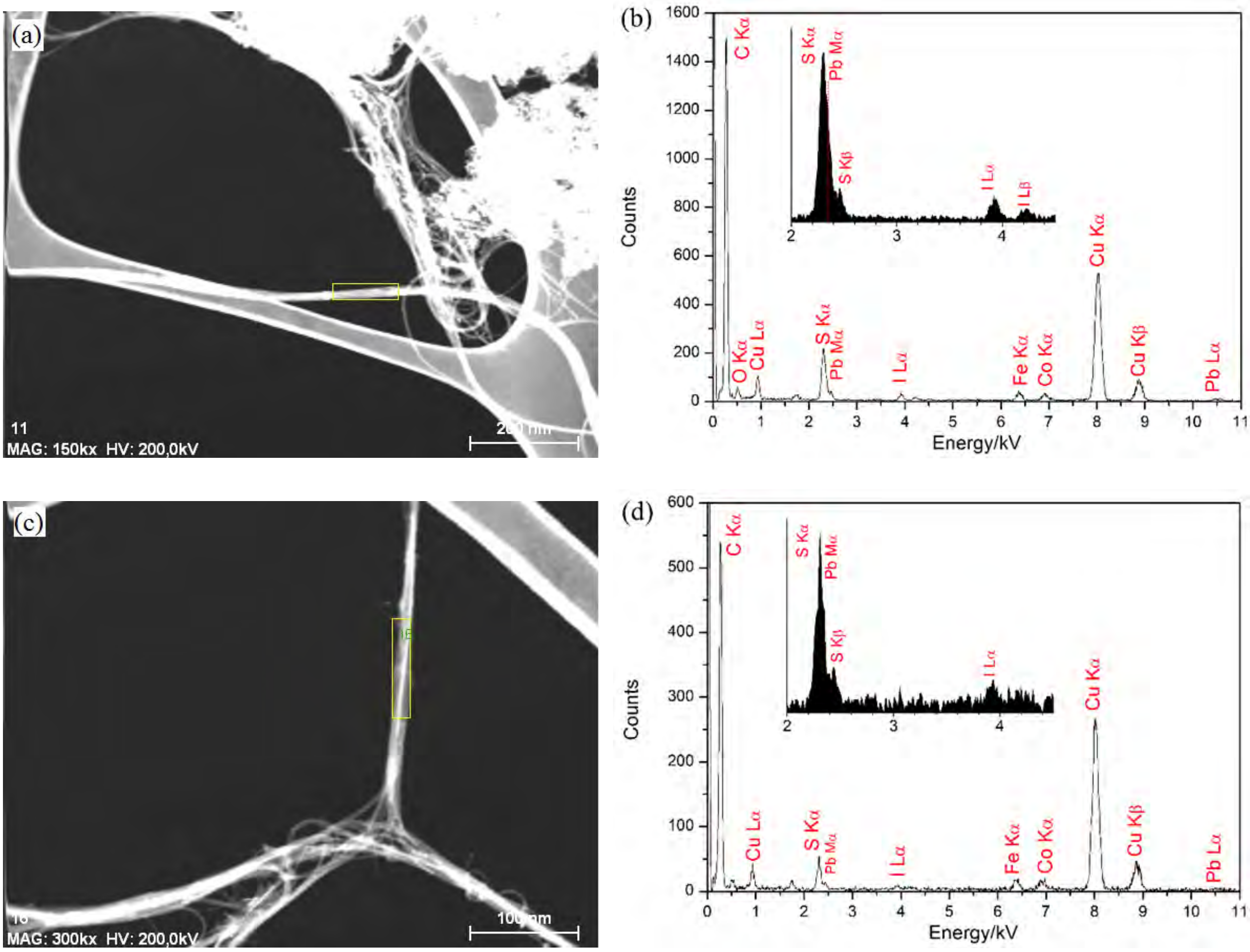

Fig. 3.4 - (a) and (c) STEM images of PbS@DWCNTs_3; (b) and (d) X-EDS spectra collected from the DWCNT bundles boxed in (a) and (c).

It should be noted that the Pb M peak (2.342 keV) is quite close to the S Kα peak (2.307 keV), so Pb is identified by its Lα peak (10.55 keV). As seen, strong S Kα peak, weak I Lα peak and weak Pb Lα peak are present in the spectra collected from CNT bundles in the two samples. The presence of other peaks in the spectra including C Kα peak, O Kα peak, Si Kα peak, Fe Kα peak, Co Kα peak and three peaks of Cu originate from the carbon nanotubes themselves, the X-EDS detector, the specimen holder and the copper grid, respectively. Around 10 spectra were collected from different CNT bundles for each sample and the average atomic ratio among elements C, S, I and Pb was 97.0: 2.9: 0.2: <0.1 (PbS@DWCNTs_2) and 98.2: 1.7: 0.2: <0.1 (PbS@DWCNTs_3), respectively. Combining the EELS and X-EDS analysis, it is deduced that the encapsulated crystals in the sulphurized samples are likely to still be PbI$_2$, but the CNTs in the sulphurized samples were slightly doped with sulphur – although this could not be evidenced by HRTEM images due to the low contrast difference between sulphur and carbon atoms.

Furthermore, the sample PbS@DWCNTs_3 was investigated by X-ray Photoelectron Spectroscopy (XPS). The raw DWCNTs and starting PbI_2@DWCNTs were also investigated by XPS for comparison (Fig.3.5).

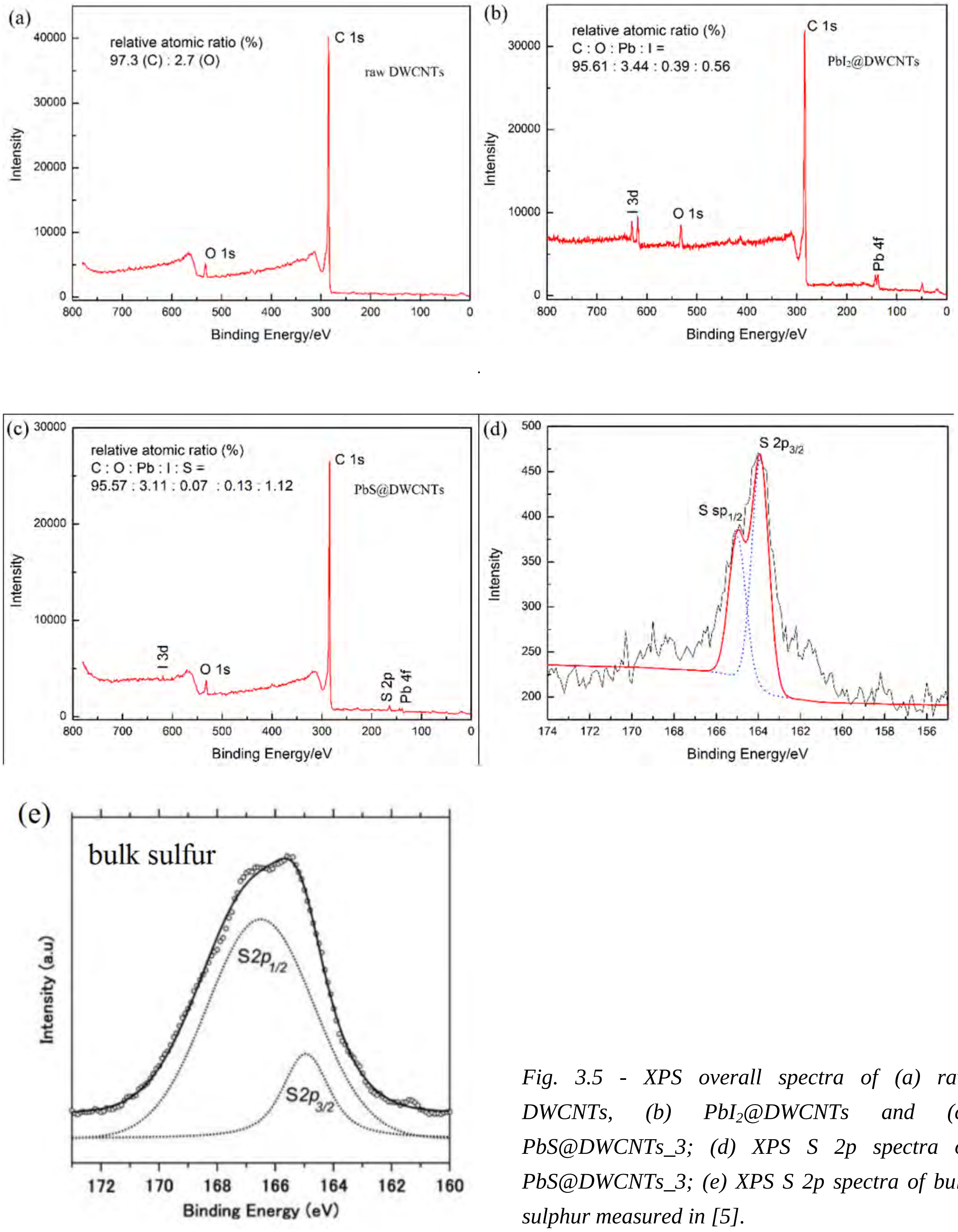

Fig. 3.5 - XPS overall spectra of (a) raw DWCNTs, (b) PbI_2@DWCNTs and (c) PbS@DWCNTs_3; (d) XPS S 2p spectra of PbS@DWCNTs_3; (e) XPS S 2p spectra of bulk sulphur measured in [5].

Compared with the overall spectrum of raw DWCNTs (Fig. 3.5a), signals of lead and iodine are present in the spectrum of PbI_2@DWCNT (Fig. 3.5b) confirming the encapsulation of PbI_2 and signals of sulphur, lead and iodine are present in the spectrum of PbS@DWCNT_3 (Fig. 3.5c), which is in agreement with the X-EDS results. The signal of oxygen is attributed to air or possibly SO_3 adsorbed by CNTs. In addition, the atomic concentration of sulphur in sample PbS@DWCNTs_3 is much higher than that of lead and iodine, indicating again that the CNTs were slightly doped with sulphur due to the sulfurization step, while the synthesis of PbS nanocrystals was not successful. The S 2p spectrum of PbS@DWCNTs_3 is shown in Fig. 3.5d and it can be seen that the binding energies of the S 2p core-level are split into two components (S $2p_{1/2}$ and S $2p_{3/2}$) arising from spin-orbit coupling. The S 2p spectrum of bulk sulphur (α-S_8; the most stable, ring-shaped sulphur allotrope) as reported in [5] is shown in the inset of Fig. 3.5d for comparison. The S 2p core-level binding energies for PbS@DWCNTs_3 are 163.9 eV (S $2p_{3/2}$) and 165 eV (S $2p_{1/2}$) respectively, which are lower than those of the bulk sulphur (165 eV, S $2p_{3/2}$; 166.5 eV, S $2p_{1/2}$) [5], suggesting that the sulphur atoms are bonded to CNTs rather than existing as sulphur molecules. It should also be noted that the S 2p core-level binding energies of PbS nanocrystals were reported to be 160.3 eV (S $2p_{3/2}$) and 161.5 eV (S $2p_{1/2}$), respectively. Therefore, we can assess that encapsulated PbS crystals are not present in our samples. The failure in obtaining PbS crystals is attributed to the slow diffusion of sulphur and slow kinetics of reaction between lead iodide and sulphur within the protection of carbon sheath (a control experiment performed with bulk PbI_2 and S in experimental conditions (1) was successful to prepare PbS). The XPS C 1s core-level spectra of raw DWCNTs, PbI_2@DWCNTs and PbS@DWCNTs_3 are compared in Fig. 3.6 while a shift of binding energy is not observed, possibly because the low atomic percent of sulphur in PbS@DWCNTs_3 is not able to modify the electronic property of DWCNTs.

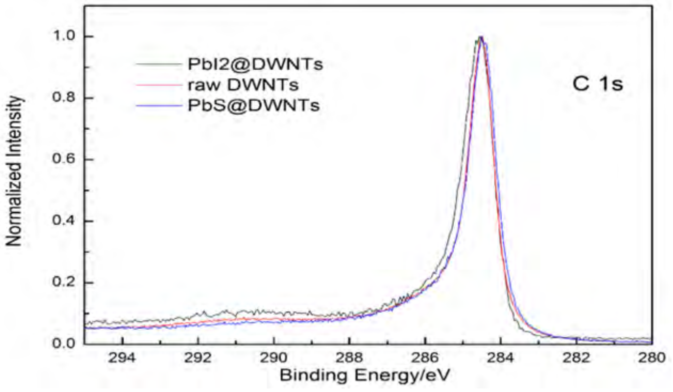

Fig. 3.6 – XPS C 1s spectra of raw DWCNTs (red), PbI_2@DWCNTs (black) and PbS@DWCNTs_3 (blue).

To conclude, it seems that the *in situ* transformation of PbI_2 into PbS was not successful in the different experimental conditions investigated here. Other experiments initially planned (use of H_2S instead of S) could unfortunately not be performed to investigate further this question.

3.3 *In situ* H_2-reduction

3.3.1 Methods

According to reactions 3.2 and 3.3 described below, hydrogen as a common reducing agent is used to reduce the encapsulated FeI_2/NiI_2 into Fe/Ni:

$$FeI_2@DWCNTs + H_2 \rightarrow Fe@DWCNTs + 2HI \tag{3.2}$$

$$NiI_2@DWCNTs + H_2 \rightarrow Ni@DWCNTs + 2HI \tag{3.3}$$

To perform the reduction, an alumina boat containing the as-prepared FeI_2@DWCNTs or NiI_2@DWCNTs was placed at the middle of a horizontal furnace which was under H_2 atmosphere all along the heating program (flow rate: 5L/h). To explore the suitable experimental condition for reduction of the metal iodide to form metal nanocrystals, the furnace was heated at different temperatures for different durations. For the reduction of FeI_2 @DWCNTs, the sample was heated at 400°C for 7 or 24 hours respectively, or at 500°C for 24 hours. The obtained reduced samples were denoted as Fe@DWCNTs_400_7, Fe@DWCNTs_400_24, and Fe@DWCNTs_500_24, respectively. For reduction of NiI_2@DWCNTs, the sample was heated at 300°C for 8 hours, at 400°C for 7 hours or 24 hours respectively, at 500°C for 7 hours or 24 hours respectively. The obtained reduced samples were denoted as Ni@DWCNTs_300, Ni@DWCNTs_400_7, Ni@DWCNTs_400_24, Ni@DWCNTs_500_7, and Ni@DWCNTs_500_24, respectively.

In addition, the electrochemical reduction of FeI_2@DWCNTs was also investigated. Briefly, the powder of FeI_2@DWCNTs was pressed onto a Pt substrate, which served as the working electrode. Another Pt substrate was used as counter electrode. A Pt wire was used as quasi-reference electrode. 1M KCl solution was used as the electrolyte. A potential of -1.5 V vs the reference electrode supplied by a VMP3 potentiostat (Biologic, USA) was imposed on the working electrode for 30 min. Finally, the sample was peeled off the substrate and filtered with water to remove the residual KCl and dried at 80 °C for 24h. The obtained reduced sample was denoted as Fe@DWCNTs_EC. Characterisations were carried-out using the same TEM and EELS facilities described in Chapter 2.

3.3.2 Results and Discussion

3.3.2.1 In situ reduction of FeI_2@DWCNTs

Some examples of ADF images and a related EEL spectrum of starting FeI_2@DWCNTs are presented in Fig. 3.7 for comparison with the reduced materials which will follow.

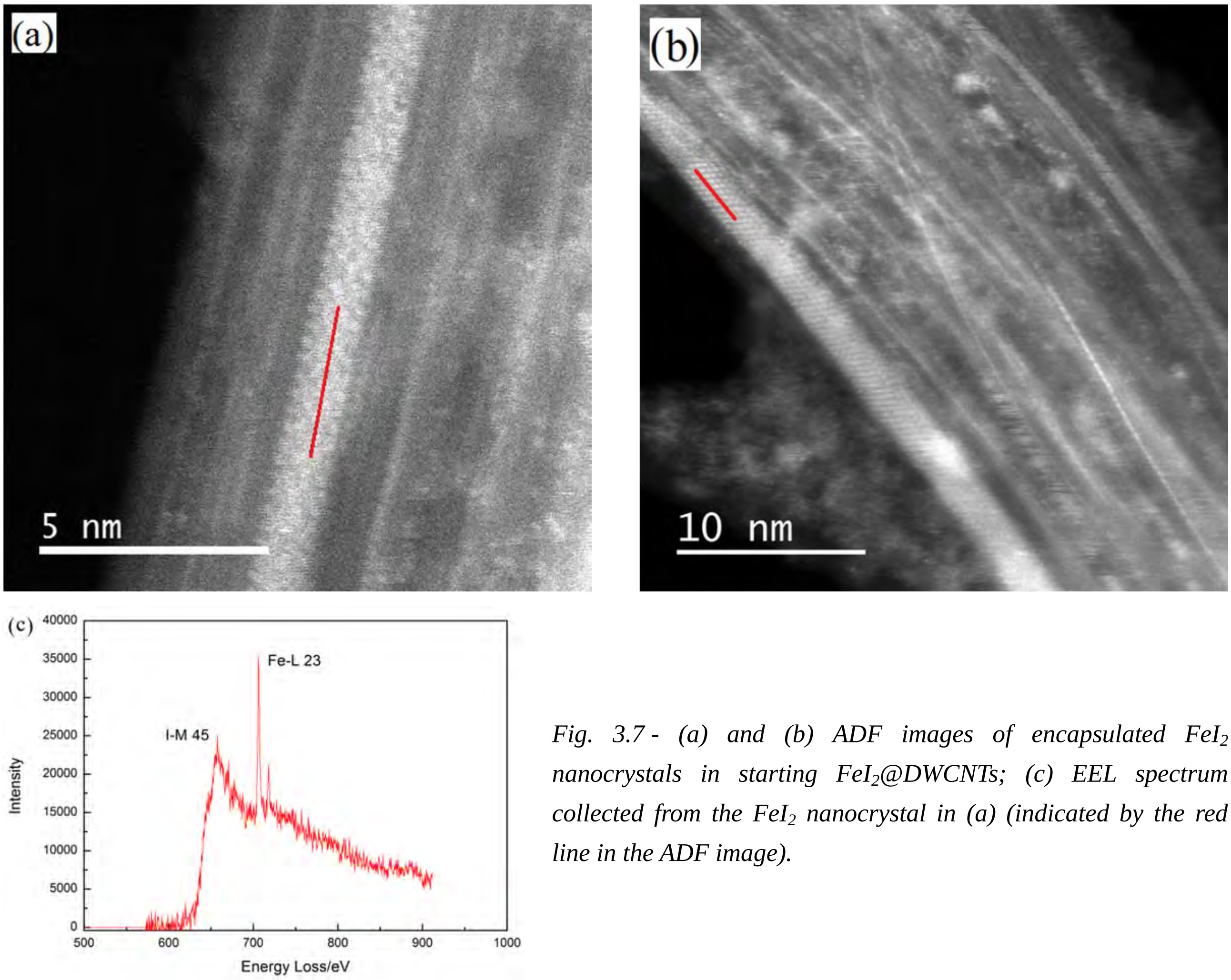

Fig. 3.7 - (a) and (b) ADF images of encapsulated FeI_2 nanocrystals in starting FeI_2@DWCNTs; (c) EEL spectrum collected from the FeI_2 nanocrystal in (a) (indicated by the red line in the ADF image).

Fig. 3.8 illustrates the HRTEM image, HAADF image and EEL spectrum of Fe@DWCNTs_400_7. A small cluster encapsulated within a MWCNT which is boxed in Fig. 3.8a was identified to be pure Fe by EELS (Fig. 3.8c). Typically, the oxygen (O) K edge is located around 532 eV, the iodine (I) M45 edge is located around 619 eV, the iron (Fe) L23 edge is located around 708 eV. In contrast with the nanocrystals on the left (red arrow in Fig. 3.8a) which was identified as FeI_2 by EELS analysis, the Fe cluster appears amorphous, which may be because the removal of iodine atoms by H_2 leads to the collapse of the crystalline FeI_2, and then the recrystallization of the remaining iron atoms did not occur. However, most of the encapsulations in Fe@DWCNTs_400_7 still remain as FeI_2, as verified by EELS analysis. One point to be mentioned is that for all reduced samples obtained in our work, more than 20 filled-tubes were investigated by EELS analysis in order to identify if the reduction was successful, which can be considered as a coarse statistical analysis.

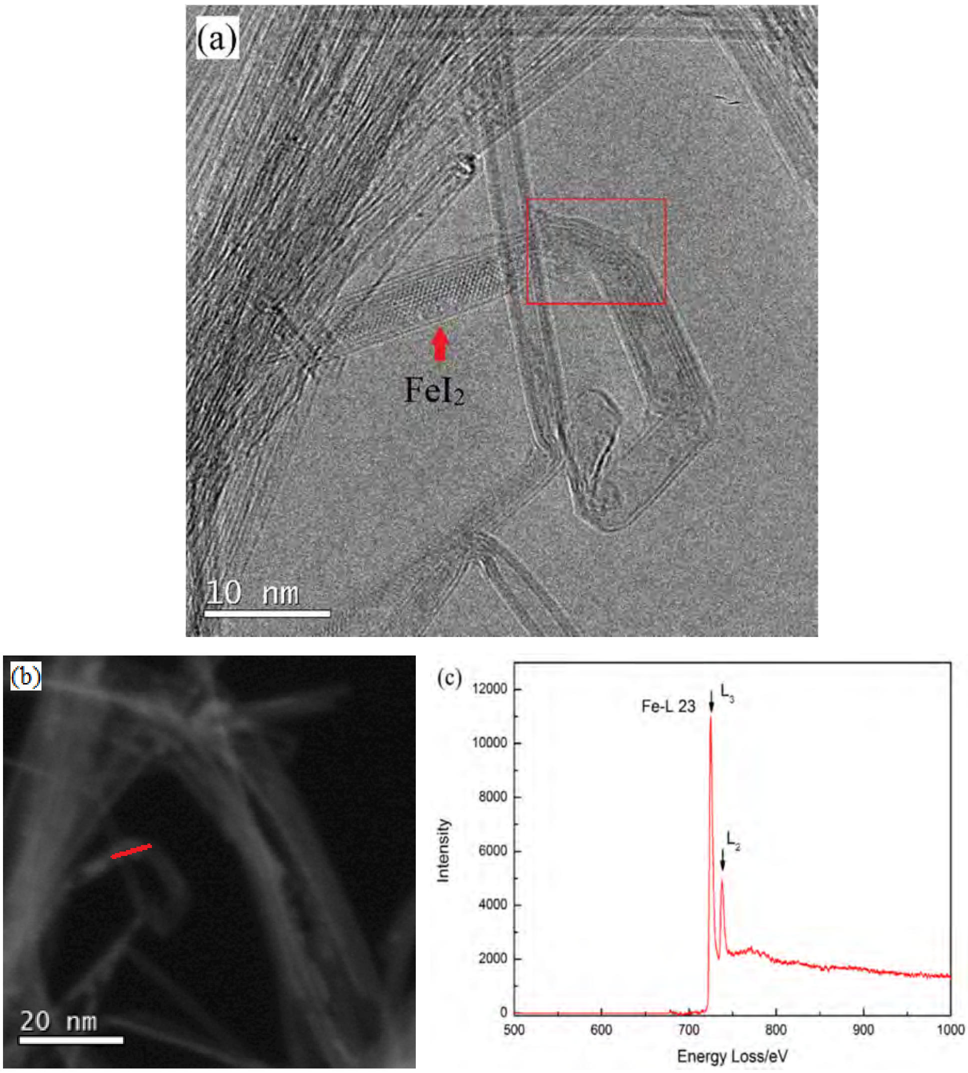

Fig. 3.8 - (a) HRTEM image of an encapsulated Fe cluster in Fe@DWCNTs_400_7; (b) HAADF image of the Fe cluster; (c) EEL spectrum collected from the Fe cluster.

In the case of Fe@DWCNTs_400_24, Fe nanocrystals encapsulated within DWCNTs are observed and confirmed by EEL spectra, as demonstrated in Fig. 3.9. The obtained Fe nanocrystals are not as continuous as the pristine FeI_2 nanocrystals, with a length not exceeding 10 nm. The reason for the occurrence of such short Fe nanocrystals is that the diffusion of H_2 into the cavity of CNTs and the kinetics of the reaction between FeI_2 and H_2 are slowed down due to the presence of the carbon sheath (i.e., it occurs only through the CNT tip, which is presumably opened by the contact with the metal iodide, presumably thanks to the higher reactivity of the CNT tip with respect to the CNT wall – see Chapter 2), hence only the tip of the encapsulated crystal facing the opening of the CNT tip is subjected to H_2, and then H_2 can only diffuse through the solid crystal and in-between the crystal/CNT wall interspace. This causes only a segment in a continuous FeI_2 nanowire to be reduced by H_2 even after a 24-h reaction.

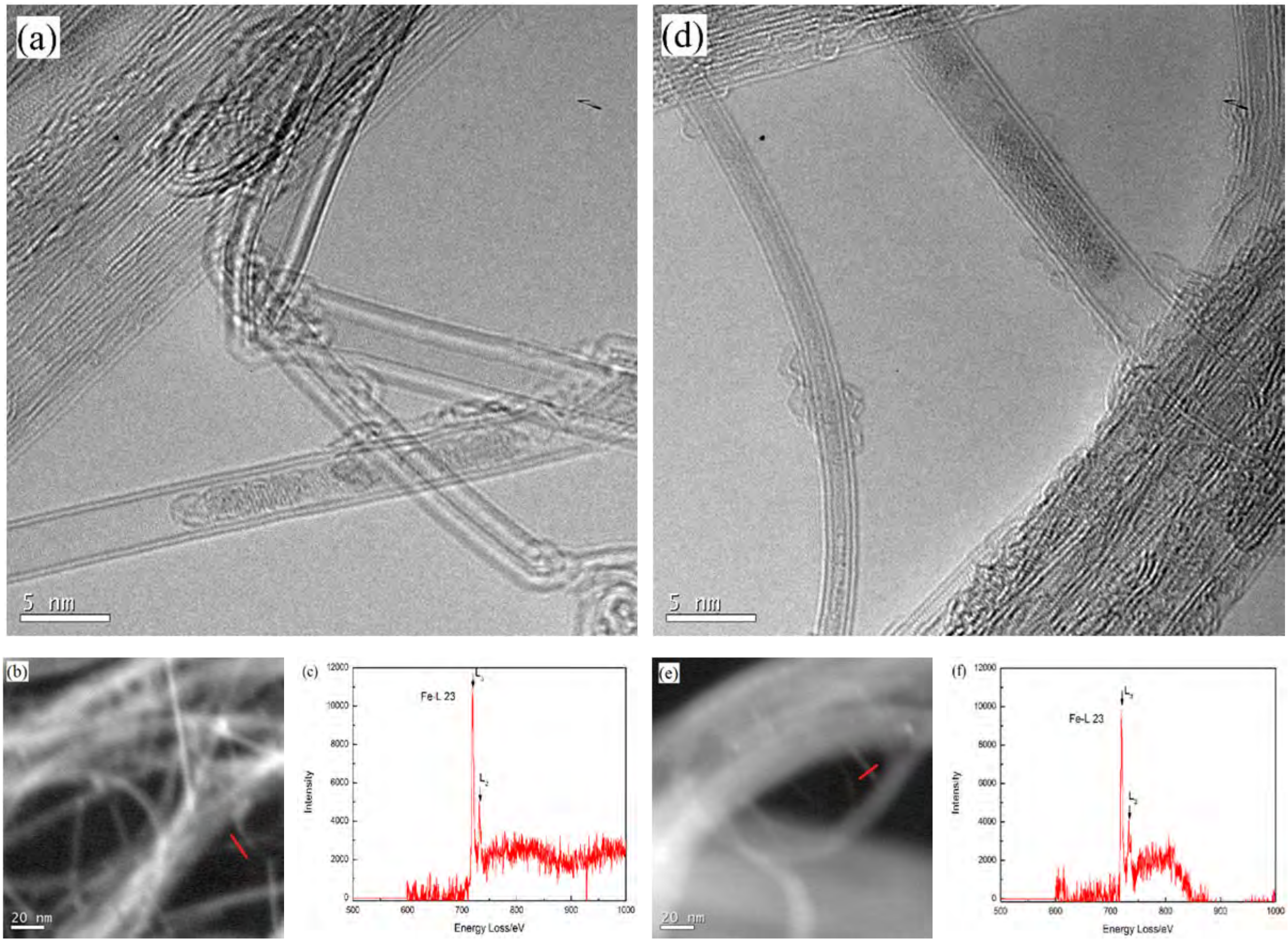

Fig. 3.9 - (a) and (d) are HRTEM images of Fe nanocrystals encapsulated within DWCNTs in Fe@DWCNTs_400_24, in (d) the crystals encapsulated within the left tube are identified as FeI_2 by EELS; (b) and (e) are HAADF images of Fe nanocrystals showed in (a) and (d); (c) and (f) are EEL spectra collected from the Fe nanocrystals (indicated by the red line in HAADF images).

Through the coarse statistical analysis, it is found that more Fe nanocrystals are present in Fe@DWCNTs_400_24 compared to Fe@DWCNTs_400_7, owing to the longer reduction time while abundant FeI_2 nanocrystals still exist in the sample. In the case of Fe@DWCNTs_500_24, Fe nanocrystals encapsulated within DWCNTs are also observed (see Fig. 3.10), exhibiting similar structure as the Fe crystals present in Fe@DWCNTs_400_24.

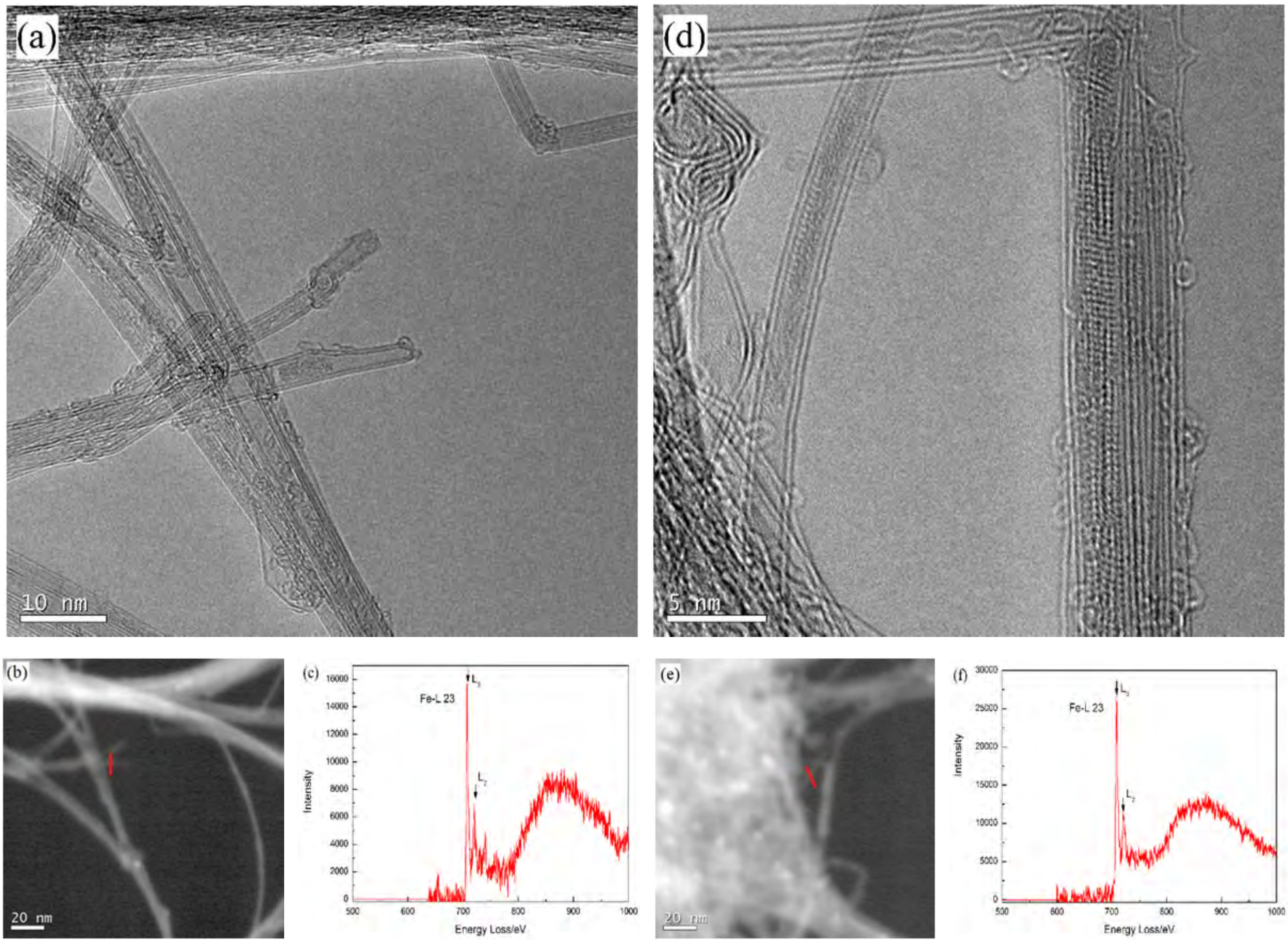

Fig. 3.10 - (a) and (d) are HRTEM images of Fe nanocrystals encapsulated within DWCNTs in Fe@DWCNTs_500_24, in (d) the crystals on the right-hand side are identified as FeI_2 by EELS; (b) and (e) are HAADF images of Fe nanocrystals showed in (a) and (d); (c) and (f) are EEL spectra collected from the Fe nanocrystals (indicated by the red line in HAADF images).

In addition, the amount of Fe nanocrystals in Fe@DWCNTs_500_24 increased only slightly with respect to Fe@DWCNTs_400_24 according to the EELS analysis, which can also be explained by the reason that confinement by DWCNTs slows down the interaction kinetic between FeI_2 and H_2. To verify this, a control experiment of reduction of bulk FeI_2 in the same conditions used for

Fe@DWCNTs_500_24 was performed, and the obtained product was found to be Fe(0) by XRD analysis. It is worth noting that no Fe nanoparticles were found outside the CNTs in the reduced Fe@DWCNTs materials. Only few large Fe oxide particles were found, which are believed to originate from the oxidation in air of the residual (non-encapsulated) FeI_2 which may have survived in spite of the washing step.

The idea of reducing FeI_2@DWCNTs electrochemically was inspired by the work of Holloway *et al.* [6]. In their study, encapsulated CuI within SWCNTs was found to undergo both reduction and oxidation in $NaClO_4$ solution when a potential window from -1.5V to 1.5V vs SCE (Saturated Calomel reference Electrode) was applied to the working electrode containing CuI@SWCNTs. Such chemical transformation of CuI was attributed to the electron transfer occurring between the SWCNTs which are electrochemically opened at the ends by the applied potential and the confined CuI. It should be noted that the electrochemical opening of the SWCNTs can only occur when the applied potential is beyond the window from -1.2V to 1.2V *vs* the SCE[1]. In our work, a constant voltage of -1.5V *vs* our reference electrode[2] was used aiming to open the DWCNTs firstly then to induce the electron transfer between the DWCNTs and confined FeI_2 given that the standard redox potential of Fe^{2+}/Fe is -0.244V *vs* SCE. However, iron oxides instead of iron were obtained in the electrochemically reduced sample, as shown in Fig. 3.5. Amorphous encapsulations within the cavity of nanotubes are observed in ADF image of Fe@DWCNTs_EC and the EEL spectrum collected from the amorphous encapsulations identify the presence of Fe and O. The reason for the presence of encapsulated Fe oxides could be that iron produced from the reduction of encapsulated FeI_2 is oxidized by the oxygen dissolved in the electrolyte which originates from the breakdown of water. The metallic iron formed may also have oxidized later in air, prior to EELS analysis.

To obtain Fe nanocrystals, post-reduction and annealing treatment are required. A drawback of this experiment is that the use of Pt quasi-reference electrode makes the calculation of potential

---

[1]. "Intuitively, the application of a sufficiently oxidizing potential to the SWCNTs is thought to induce the opening of the fullerene-like caps at the tube ends by removing electrons from the bonding HOMO. Perhaps less immediately obvious is the opening of the tubes by the application of a sufficiently reducing potential, which may involve the addition of electrons into the antibonding LUMO again resulting in the opening of the endcaps." (From reference [6]).

[2]. The disadvantage of the utilization of a Pt wire as quasi-reference electrode is that we cannot calculate the potential unless a reference redox system is used *in situ*, or measuring the potential after the experiment by using a reference redox system or a conventional reference electrode.

difficult. Therefore, this experiment is just a preliminary test for confirming the feasibility of electrochemical reduction of FeI_2@DWCNTs. To understand the mechanism involved in the electrochemical reduction process, further work is required using a proper 3-electrode electrochemical setup.

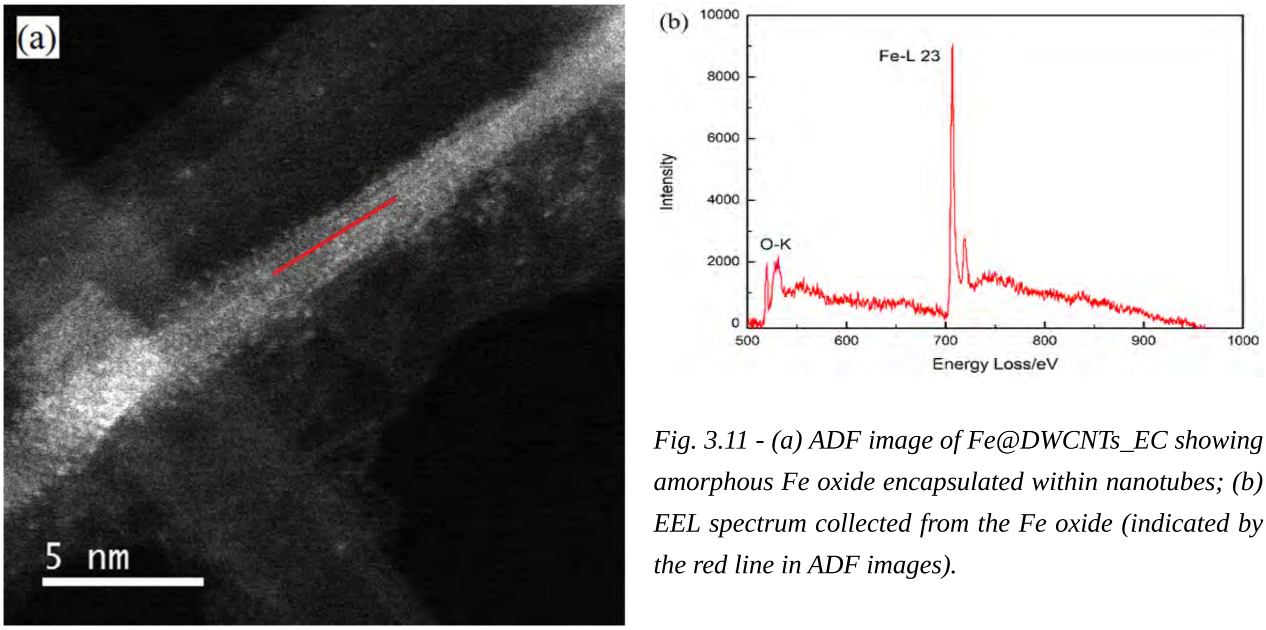

Fig. 3.11 - (a) ADF image of Fe@DWCNTs_EC showing amorphous Fe oxide encapsulated within nanotubes; (b) EEL spectrum collected from the Fe oxide (indicated by the red line in ADF images).

3.3.2.2 In situ reduction of NiI_2@DWCNTs

Fig. 3.12 displays TEM images, HAADF images and EEL spectra of Ni@DWCNTs_300, Ni@DWCNTs_400_7 and Ni@DWCNTs_500_7, respectively.

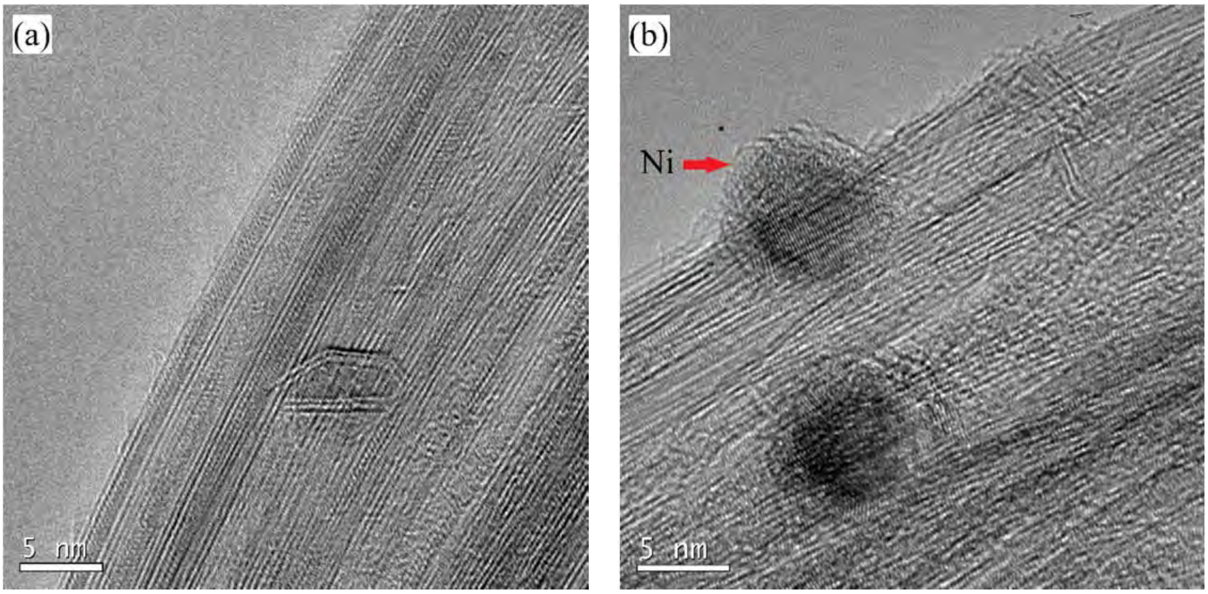

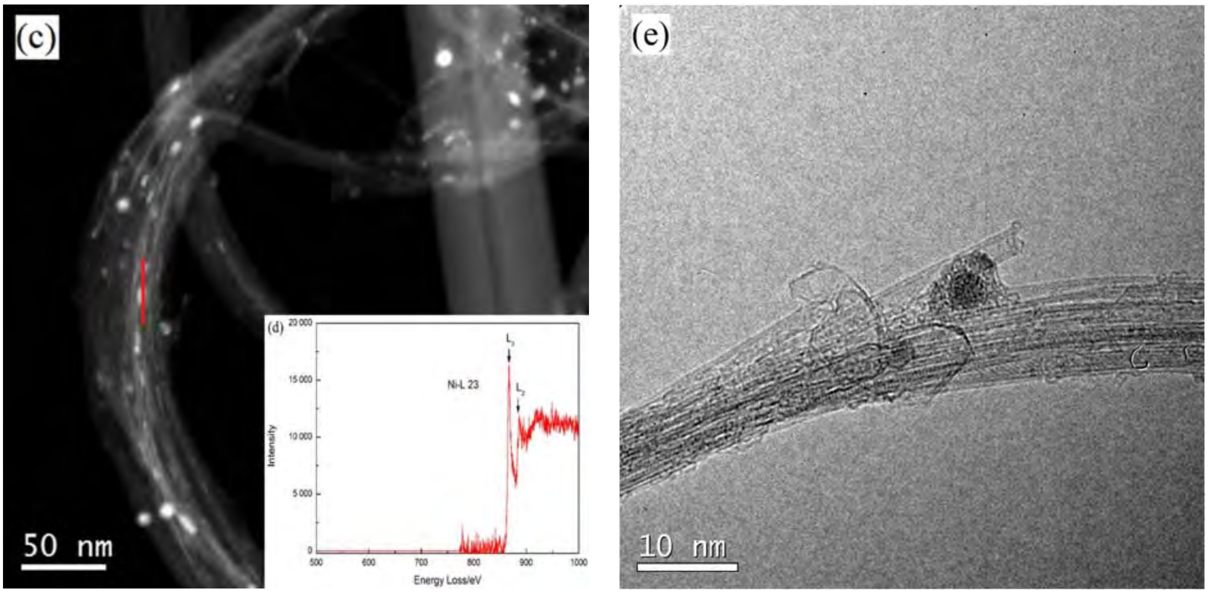

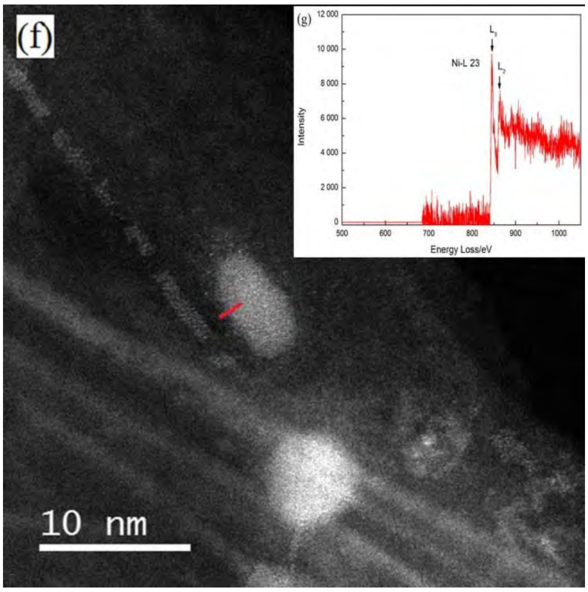

Fig. 3.12 - (a) HRTEM image of Ni@DWCNTs_300_7 showing the absence of Ni particles; (b) HRTEM image of Ni@DWCNTs_400_7 showing the presence of Ni particles associated with a DWCNT bundle; (c) HAADF image of Ni@DWCNTs_400_7 showing DWCNT bundles coated with Ni particles; (d) EEL spectrum collected from Ni particles indicated by the red line in (c); (e) HRTEM image of Ni@DWCNTs_500_7 showing the presence of a Ni particle associated with a DWCNT bundle; (f) ADF image of a Ni particle present in Ni@DWCNTs_500_7; (g) EEL spectrum collected from Ni particles indicated by the red line in (c).

It can be seen that particles attached to the surface of CNTs are present in Ni@DWCNTs_400_7 and Ni@DWCNTs_500_7, while they are absent in pristine NiI_2@DWCNTs and Ni@DWCNTs_300. These particles are identified as Ni particles by EEL spectra. Typically, the nickel (Ni) L23 edge is located around 855 eV. This can be explained if we assume that a minimum temperature is required to make possible the reduction of NiI_2 inside DWCNTs. However, we think that another mechanism is also possible. It should be reminded that the spontaneous decomposition of NiI_2 was observed during the filling step (see Chapter 2). Hence, it is possible that the decomposition of NiI_2 which was able to form encapsulated nanocrystals from the molten phase at 827°C or lower occurred at 400°C because of the nanosize of the crystals which makes their thermal stability even lower with respect to bulk NiI_2 whereas decomposition did not occur at 300°C. Once the encapsulated NiI_2 is decomposed into Ni and I_2, there is a chance that Ni will be pushed out from the nanotubes by the iodine gas, leading to the formation of Ni particles coating the surface of nanotubes. Moreover, the decomposition of encapsulated NiI_2 in Ni@DWCNTs_400_7 material is also supposed to induce the formation of Ni crystals confined within nanotubes. In order to confirm our hypothesis of a mechanism based on the decomposition of encapsulated NiI_2, the as-prepared NiI_2@DWCNTs was heated at 500°C under dynamic vacuum (non-reducing atmosphere) for two hours, and the obtained product was investigated by TEM. It can be seen from Fig. 3.13 that both particles and nanocrystals of pure Ni (i.e., O was not detected in EELS) which are identified by EEL spectra are present in the sample.

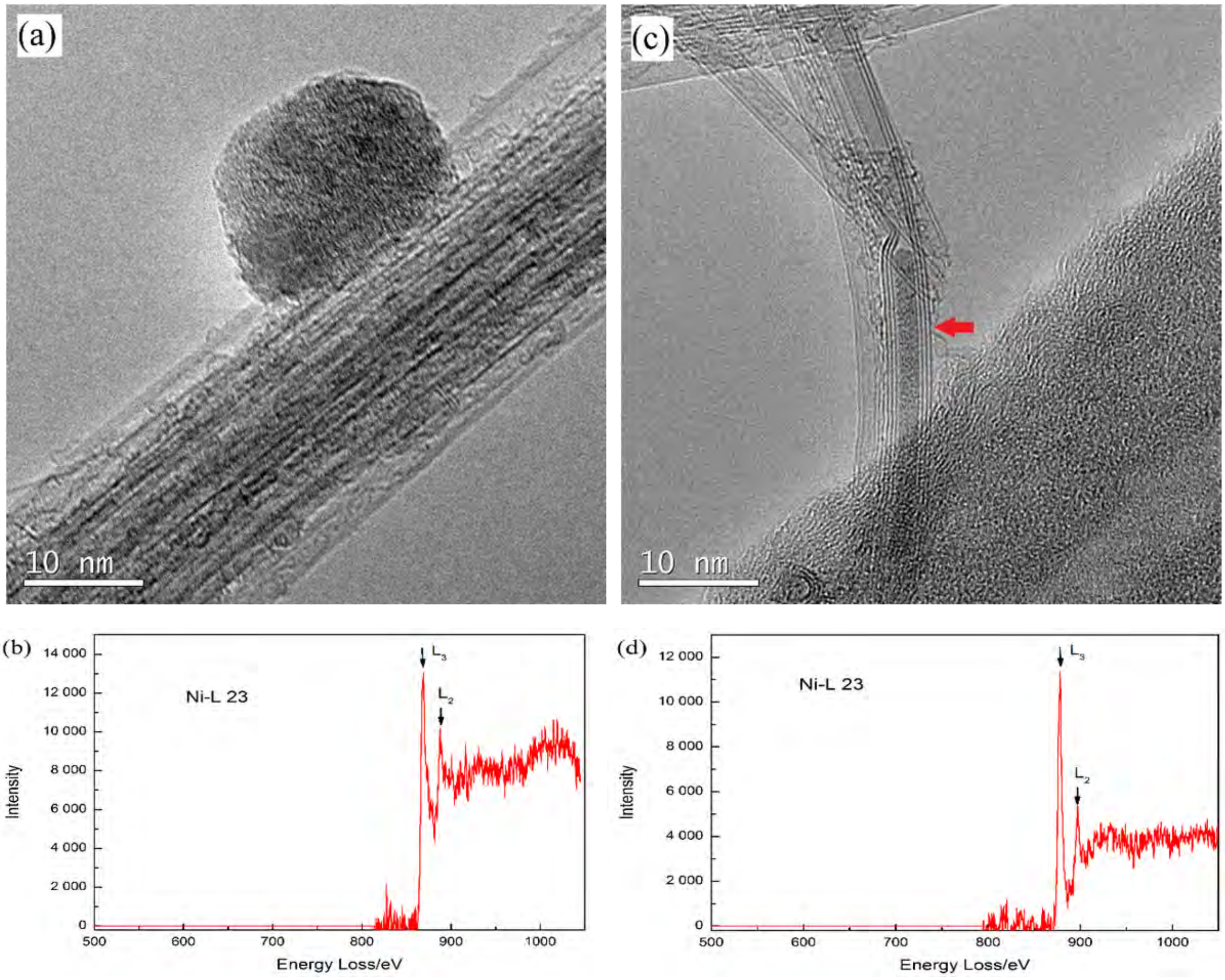

Fig. 3.13 - HRTEM images of (a) Ni particle and (c) Ni nanocrystals (arrowed region) present in the sample obtained by decomposing NiI_2@DWCNTs at 500°C under dynamic vacuum for two hours; (b) and (d) are corresponding EEL spectra collected from Ni particle (a) and Ni nanocrystals (c).

Some tubes are segmentally filled in Ni@DWCNTs_500_7 while showing peculiar contrast variations as demonstrated by ADF images such as Figs. 3.14a-b. The elemental composition of the segments along the axis of the nanocrystals following the axis of the nanotube was investigated by EELS analysis. Four typical EEL spectra collected from different segments encapsulated in the same tube as shown in Fig. 3.14b are displayed as Fig. 3.14c-f. It can be seen that the elemental composition of the encapsulated segments varies along the axis direction. The encapsulation of iodine in position 1 (Fig. 3.14c) may result from the decomposition of previously existing NiI_2 nanocrystals, in which case resulting Ni was pushed out from the tube while iodine has remained within the cavity of the tube. Segment in position 2 (Fig. 3.14d) still corresponds to NiI_2 having not been subjected to reduction yet. Since the position 3 is void, neither Ni edge nor I edge is present in the spectrum (Fig. 3.14e). When it comes to position 4 (Fig. 3.14f), the segment is supposed to be an intermediate (NiI_x, $x<2$) between NiI_2 and Ni since the I M45/Ni L23 intensity ratio is much lower than for genuine NiI_2. Such an intermediate may originate from the uncomplete reduction of NiI_2 by H_2 or decomposition of NiI_2. Thus, the transition from NiI_2 to I_2 or to NiI_x ($x<2$) within the same tube indicates the anisotropic reactivity of encapsulated NiI_2 along the axis direction of nanotubes.

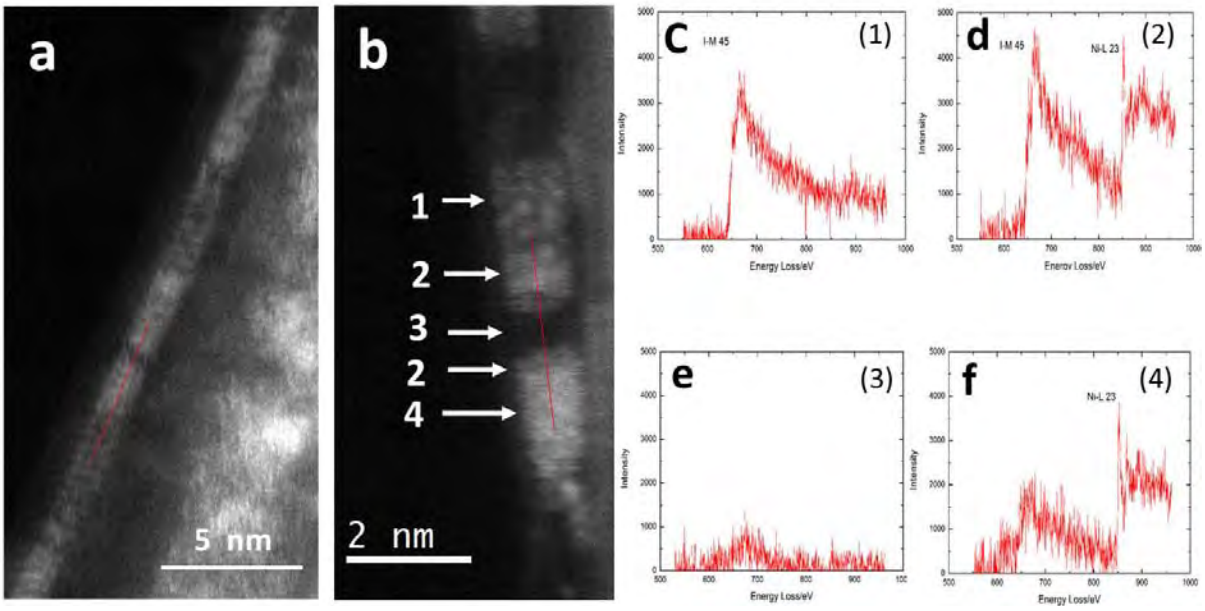

Fig. 3.14 - (a) and (b) ADF images of encapsulated crystals showing contrast variations in Ni@DWCNTs_500_7; (c) to (f) are the corresponding EEL spectra collected from positions 1 to 4 indicated by arrows in (b), respectively. Meanwhile, the absence of any signal in spectrum (e) demonstrates the spatial resolution of the electron probe.

Apart from the Ni particles outside bundles, Ni crystals are also observed in Ni@DWCNTs_400_7 and Ni@DWCNTs_500_7 while they are not in Ni@DWCNTs_300_7. Such crystals exhibit significant contrast difference compared to the confined NiI_2 nanocrystals, as shown in TEM images (Figs. 3.15a and d).

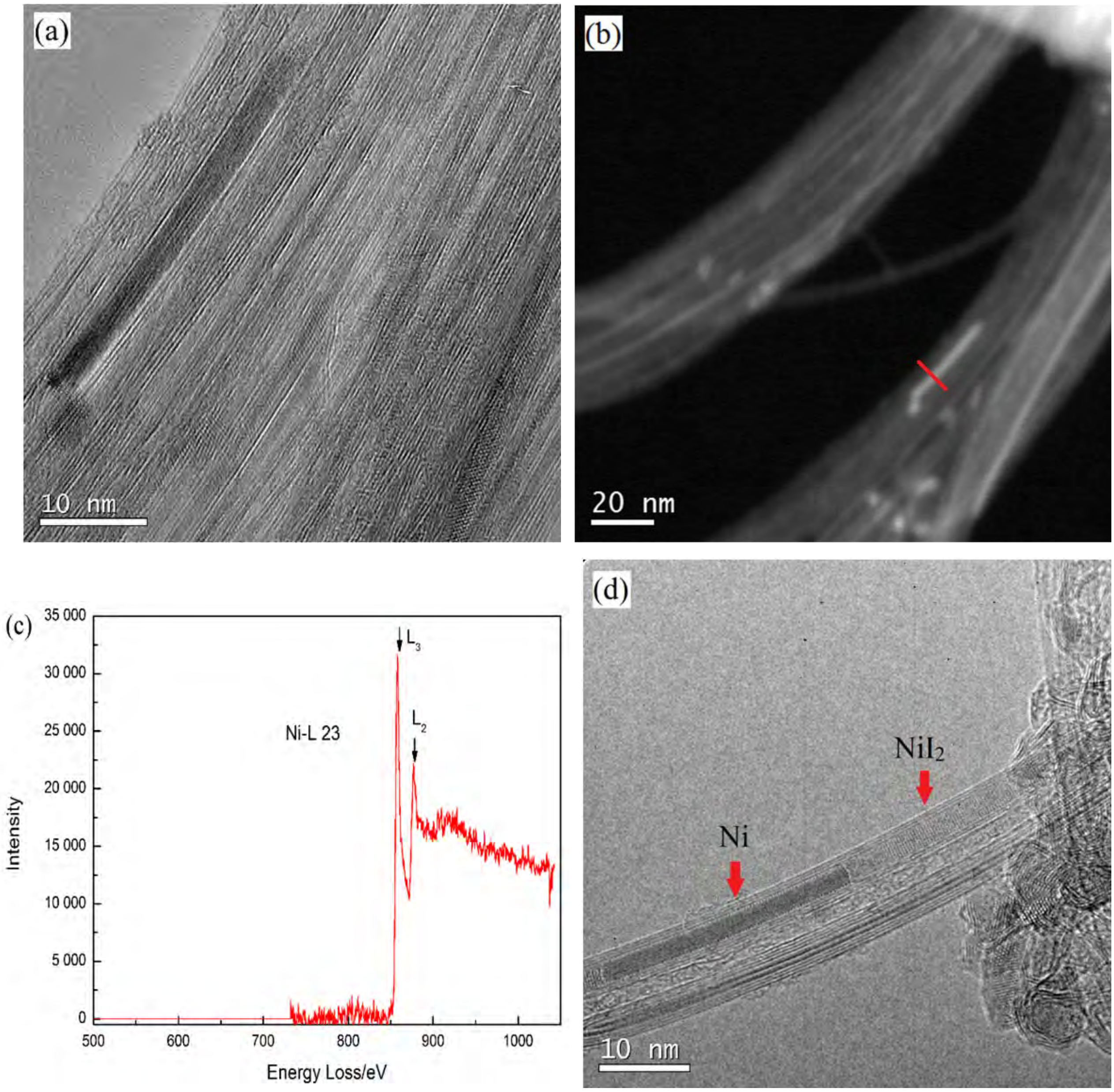

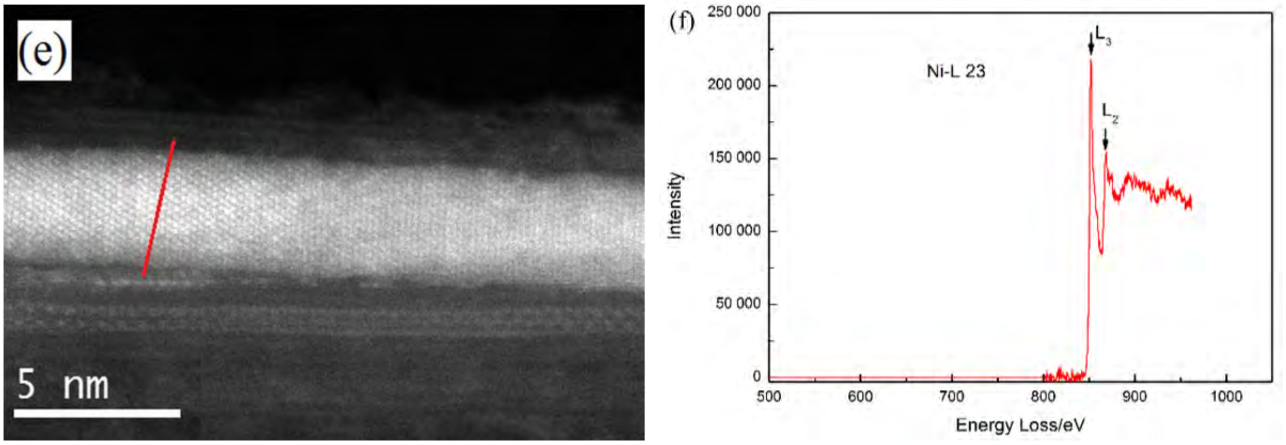

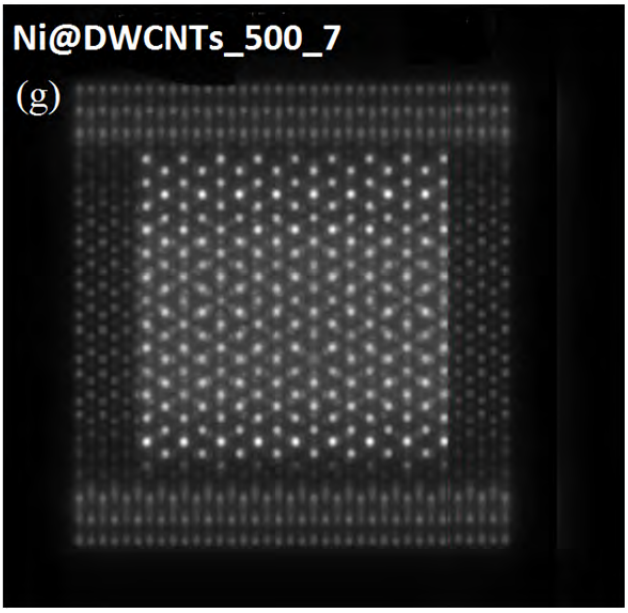

Fig. 3.15 - (a) and (d) are HRTEM images of Ni/NiI$_2$ *nanocrystals encapsulated within DWCNTs in Ni@DWCNTs_400_7 and Ni@DWCNTs_500_7, respectively; (b) HAADF image of Ni nanocrystals present in Ni@DWCNTs_400_7; (e) ADF image displaying the crystal structure of Ni crystals present in Ni@DWCNTs_500_7; (c) and (f) are EEL spectra collected from the Ni nanocrystals shown in (b) and (e) respectively; (g) Projected atomistic model derived from the Ni crystal imaged in (e) based on the structure of bulk Ni. However, in order to accommodate the structure, the distances between the Ni atom columns in the projection have to be stretched by 25-29%.*

Typical HAADF image or ADF image and EEL spectra of the encapsulated Ni nanocrystals are illustrated by Figs. 3.15b and 3.15e, and Figs. 3.9c and 3.9f, respectively. According to the coarse statistical analysis, more Ni nanocrystals are present in Ni@DWCNTs_500_7 than in Ni@DWCNTs_400_7, which should be ascribed to both the higher chemical reactivity of H_2 towards NiI_2 and lower thermal stability of NiI_2 at higher temperature. It is worth noting that the projected structure of the encapsulated Ni crystal imaged in Fig.3.15e was tentatively modelled based on the regular structure of bulk Ni crystal. Quite interestingly, the projection fits well the experimental image provided the distances between the Ni atom columns are stretched by 25-29%. This a huge strain, and it is likely that the actual structure is actually an unprecedented one, yet to determine.

When the reduction time is increased to 24 h, the amount of both Ni particles and Ni nanocrystals in the reduced samples increased as well, which is indicated by the EELS analysis.

This suggests that increasing the reduction time is beneficial to improve the yield of Ni nanocrystals. In addition, compared to Ni@DWCNTs_400_24, more Ni crystals are present in Ni@DWCNTs_500_24, which is consistent with the observations for Ni@DWCNTs_400_7 and Ni@DWCNTs_500_7.

Typical TEM images and EEL spectra of encapsulated Ni nanocrystals in Ni@DWCNTs_400_24 and Ni@DWCNTs_500_24 are illustrated in Fig. 3.16.

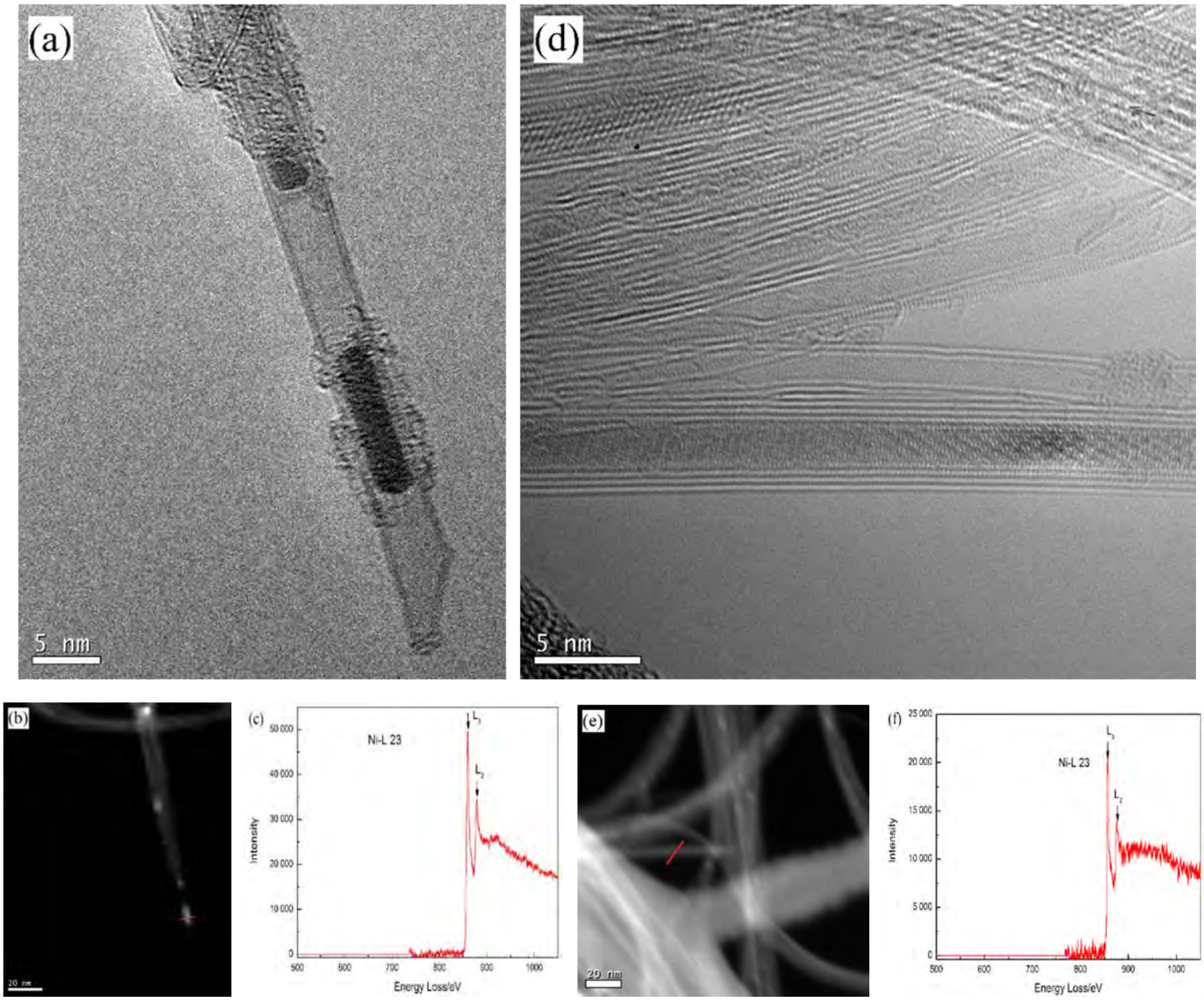

Fig. 3.16 - (a) and (d) are HRTEM images of Ni nanocrystals encapsulated within DWCNTs in Ni@DWCNTs_400_24 and Ni@DWCNTs_500_24, respectively; (b) and (e) are HAADF images of the Ni nanocrystals shown in (a) and (d); (c) and (f) are EEL spectra collected from the Ni nanocrystals shown in (b) and (e).

The contrast difference between NiI_2 and Ni is also visible in TEM images such as Fig. 3.15d, which is in agreement with observation for samples reduced for 7h. It must be noted that in Fig. 3.15d however, only local EELS analysis can assess the presence of Ni(0) because twists of the crystal or any other modification of orientation may also lead to contrast differences. However, NiI_2 is still present in all the reduced samples, which can be explained by the same reason as described for reduced FeI_2@DWCNTs samples, *i.e.* the diffusion of H_2 and kinetics between NiI_2 and H_2 are slowed down due to the presence of the carbon sheath. To verify this, a control experiment of reduction of bulk NiI_2 in the same condition used for Ni@DWCNTs_500_24 was performed and the obtained product was clearly identified as Ni(0) by XRD analysis.

The EEL spectrum of bulk NiI_2 is presented in Fig. 3.17 as a reference. It should be pointed out that the accuracy of EELS quantification in our work is not good enough to determine the exact elemental composition of the analyzed compound. That is why the atomic ratio between I and Ni in the bulk NiI_2 is not indicated to be 2:1 by EELS quantification.

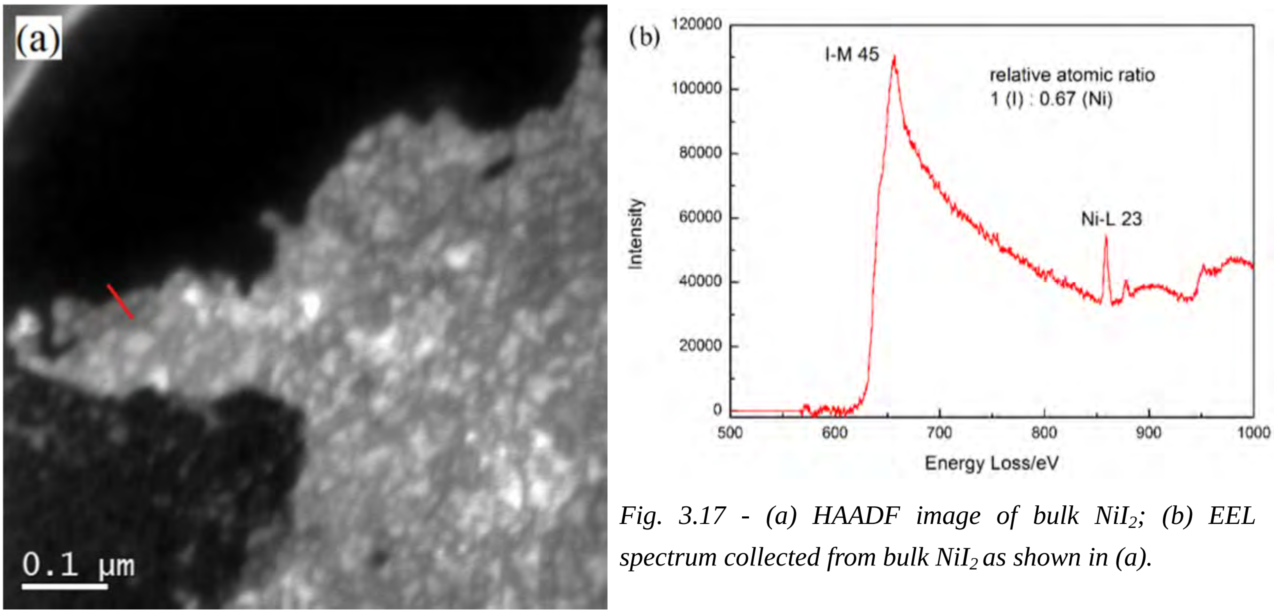

Fig. 3.17 - (a) HAADF image of bulk NiI_2; (b) EEL spectrum collected from bulk NiI_2 as shown in (a).

NiI_x (x<2) intermediate is also observed in Ni@DWCNTs_400_24 and Ni@DWCNTs_500_24. A meaningful example is provided in Fig. 3.18. An encapsulated crystal showing different contrasts is displayed in Fig. 3.18a and the elemental compositions of the two positions arrowed (red arrows) obtained by EELS quantification are 10 at% of iodine and 90 at% of nickel (dark crystal, 1), 60 at% of iodine and 40% of nickel (light crystal, 2), respectively.

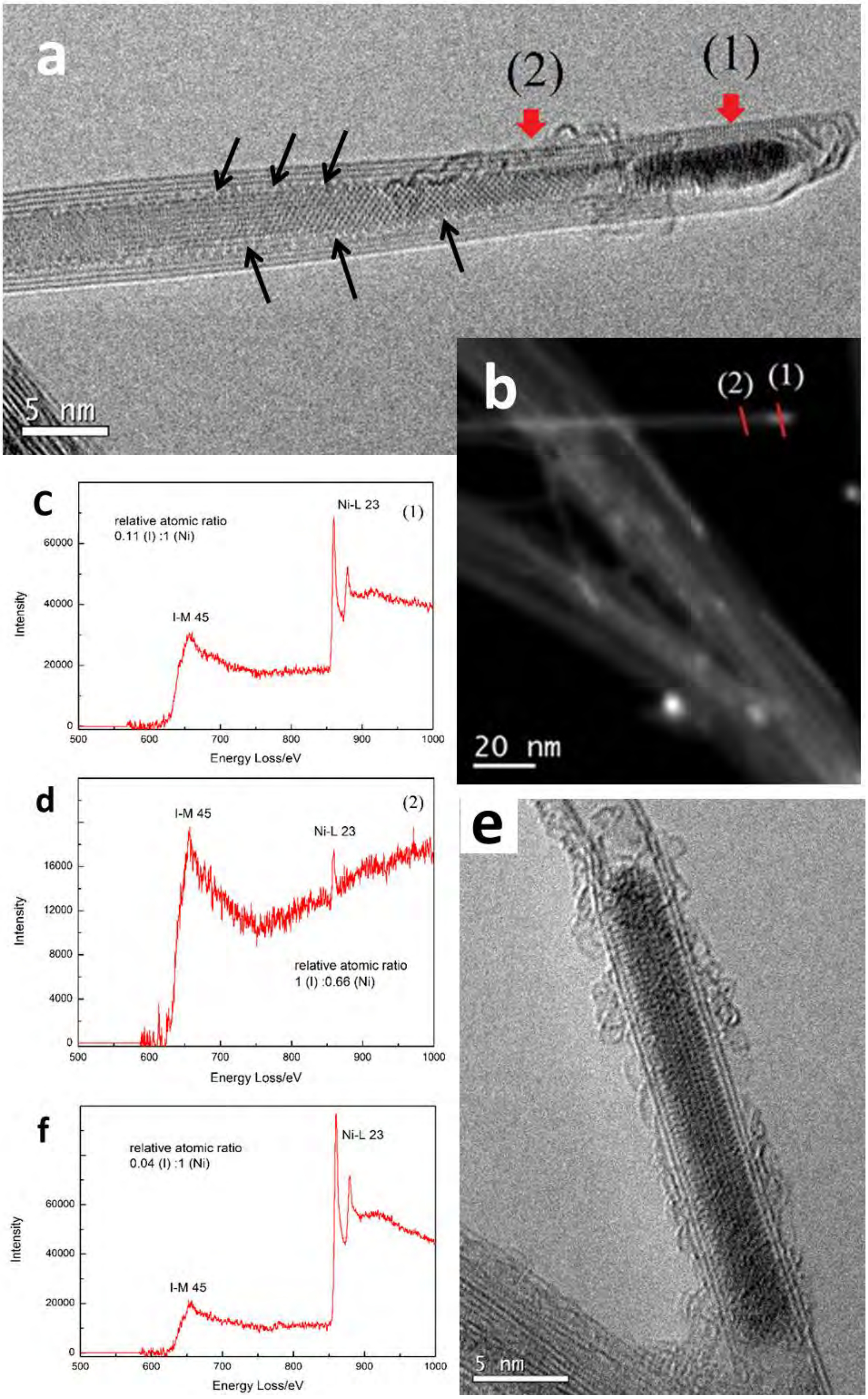

Fig. 3.18 - (a) and (b) HRTEM and HAADF images of a NiI_x crystal with various compositions; (c) and (d) EEL spectra collected from fragment (1) and (2) labelled in (a) and (b); (e) HRTEM image of another intermediate NiI_x ($x<2$) crystal encapsulated within a DWCNT; (f) EEL spectrum collected from the crystals shown in (e).

The results suggest that the diffusion of hydrogen into the cavity of CNTs starts from the tip of the tube where chemically weaker structural defects such as pentagons are located, as already stated in Section 3.3.2.1. However, the diffusion of H_2 is very slow as it has to proceed through the NiI_2 crystal (and/or in the crystal/inner tube interspace, as suggested by the peculiar contrast at this very location – black arrows in Fig. 3.18a) thus resulting in incomplete removal of iodine atoms for the short segment (1) near the tip while leaving the rest of the crystal with the unchanged NiI_2 composition (2). Another example of intermediate NiI_x ($x<2$) is shown in Fig. 3.18e and it is indicated to be composed of 4 at% of iodine and 96 at% of nickel by EELS quantification (Fig. 3.18f).

3.4 *In situ* fluorination

Filling CNTs directly with FeF_3 by the molten phase route is impossible due to the too high melting temperature required (1327°C). To obtain FeF_3 nanocrystals, *in situ* fluorination of FeI_2 nanocrystals encapsulated within CNTs provides a possible solution. In this way, the inner cavity of CNTs is used as a reactor permitting the transformation from FeI_2 to FeF_3 to occur. However, such *in situ* fluorination has been rarely reported before since CNTs may be damaged during the fluorination process, which makes it a challenge. Thanks to the long-date collaboration with the Institut de Chimie de Clermont-Ferrand (ICCF, UMR 6296) [K. Guerin, M. Dubois] and the PhD work of Lea Doubtsof, a possible way to transform FeI_2 into FeF_3 without damaging the CNTs was investigated. It is worth noting that DWCNTs are good candidates for such *in situ* fluorination because their fluorination temperature relatively high (200~300°C) [7], thereby preventing the concomitant fluorination of the CNTs with respect to the fluorination temperature to be used (see Section 3.4.1 below).

3.4.1 Methods

Various sources of fluorine can be used to transform FeI_2 into FeF_3, such as fluorine gas, gaseous or liquid HF, solid TbF_4 and XeF_2, *etc.*, all of which are available from the *'Fluorination and Fluorinated materials'* Group from ICCF. In this work, fluorine gas was chosen to perform the fluorination due to its easy diffusion within the inner cavity of CNTs and its purity preventing the hydration of the formed fluoride. In addition, the gas-solid reaction has the advantage of avoiding the filtration and washing step when liquid or solid fluorinating agents are used. Meanwhile, the molecular fluorine involved in a fluorination reaction provides the highest degree of stable oxidation for a given compound, while hydrofluoric acid leads to the production of the element with the same oxidation state as that of its precursor.

Differing from the sample used for *in situ* reduction which was prepared by filling raw DWCNTs with FeI_2, the sample used for fluorination was prepared by filling purified DWCNTs with FeI_2 (denoted as FeI_2@DWCNTs-p). The purified DWCNTs were obtained by the following steps: first, an alumina boat containing a very thin layer of dry, raw DWCNT powders was placed into a tubular furnace with good air convection which was preheated at 550°C. After heating at 550°C for 30 min, the boat was removed from the furnace and the powder was transferred into HCl solution to eliminate residual metal oxide nanoparticles generated during the previous step. The above procedure was repeated a few times in order to prepare a large enough amount of purified DWCNTs in order to perform the filling experiment. Then all collected fractions of DWCNT suspension in HCl were filtered and washed together with deionized water until neutral pH was reached. Finally, the wet product was freeze-dried. Sample FeI_2@DWCNTs-p was synthesized following the same procedures described according to Lea Doubtsof's thesis (unpublished data), the related fluorination reaction involved in Chapter 2.

in this work can be described as follows:

$$FeI_2\text{@DWCNTs-p} + 13/2\ F_2 \rightarrow FeF_3\text{@DWCNTs-p} + 2IF_5 \qquad (3.4)$$

To perform the fluorination, sample FeI_2@DWCNTs-p was heated at 50°C in a stream of fluorine gas for 24h. A weight loss of 22% with respect to the starting FeI_2@DWCNTs-p for the product after fluorination was measured, which was expected for the reaction (3.4).

Room-temperature Raman spectra were measured using the Ar/Kr laser lines at 514.5 nm (2.41 eV) on a Jobin-Yvon T64000 spectrometer equipped with a charge coupled device (CCD) multichannel detector.

3.4.2 Results and Discussion

TEM images of purified DWCNTs, FeI_2@DWCNTs-p and FeF_3@DWCNTs-p are shown in Fig.

3.19. It can be seen that the tubes form large bundles and amorphous/disorganized carbon which is present in raw DWCNTs is rarely observed in purified DWCNTs, indicating that oxidation in air is efficient to clean-up the CNTs [8].

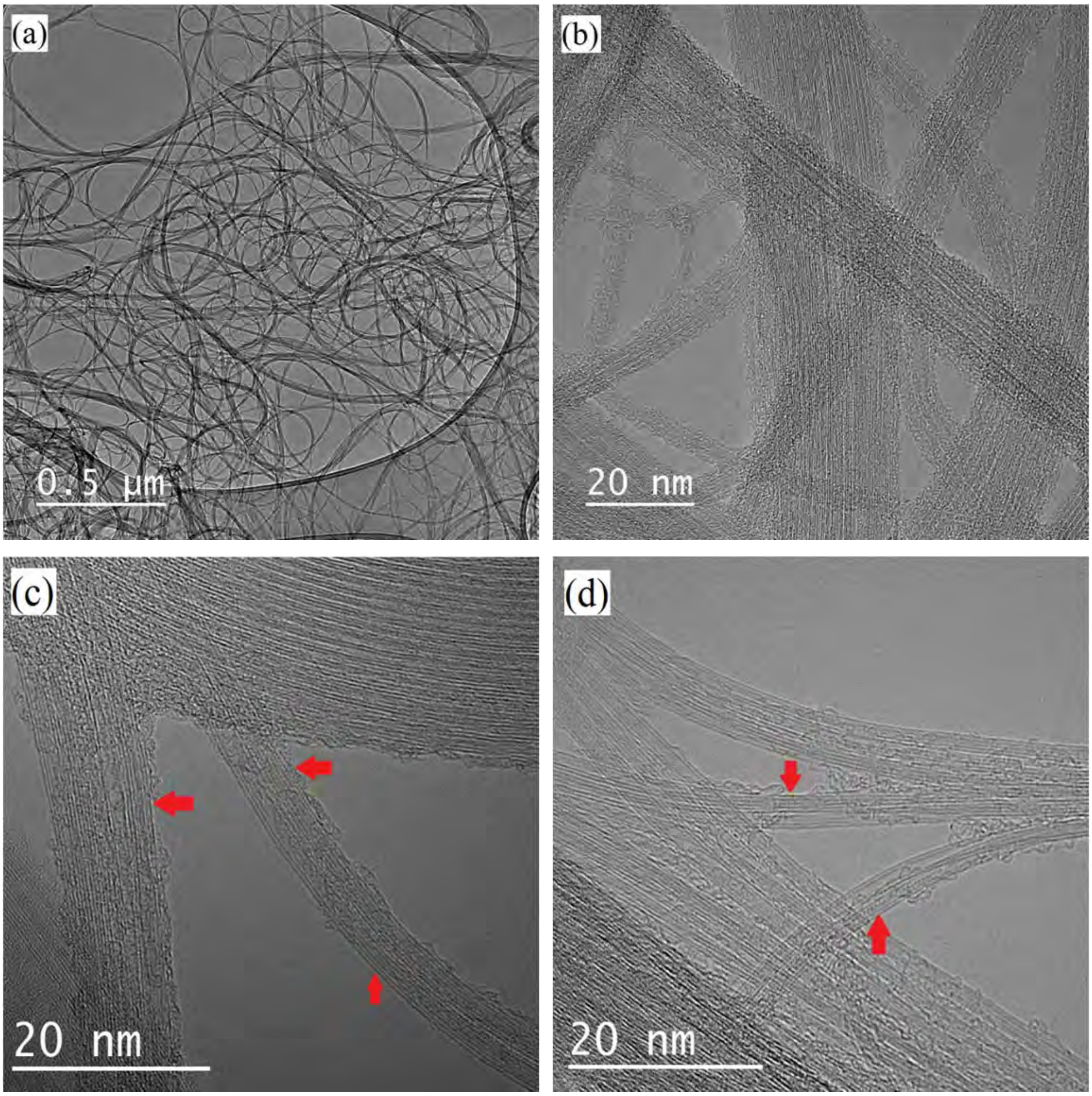

Fig. 3.19 – (a) and (b) TEM images of purified DWCNTs; (c) FeI_2@DWCNTs-p and (d) FeF_3@DWCNTs-p (d). Filled-tubes are pointed by red arrows in (c) and (d).

Amorphous coatings on the CNTs were observed in purified DWCNTs and such potential coating problem was also reported by Tran *et al.* [9] when attempt to purify MWCNTs in air was made. Compared to starting FeI_2@DWCNTs-p, the one-dimensional morphology of CNTs in FeF_3@DWCNTs-p still remains, and no deterioration of the outer wall of CNT which would indicate a significant fluorination is observed, suggesting that the fluorination condition used in our work is mild enough. Filled nanotubes are observed in both samples (arrowed regions in Fig. 3.19 c and d) but unambiguous imaging of materials encapsulated within DWCNTs in TEM mode is quite hard for both samples due to the presence of amorphous coatings. This is especially true in the case of FeF_3@DWCNTs-p, because the contribution to the contrast brought by F atoms is low because of its small atomic number (Z=9). Therefore, it is necessary to switch to STEM mode for better imaging of the encapsulations. Typical ADF images of samples FeI_2@DWCNTs-p and FeF_3@DWCNTs-p are shown in Fig. 3.20. As it can be seen, tubes are clearly observed to be filled with nanocrystals in both samples.

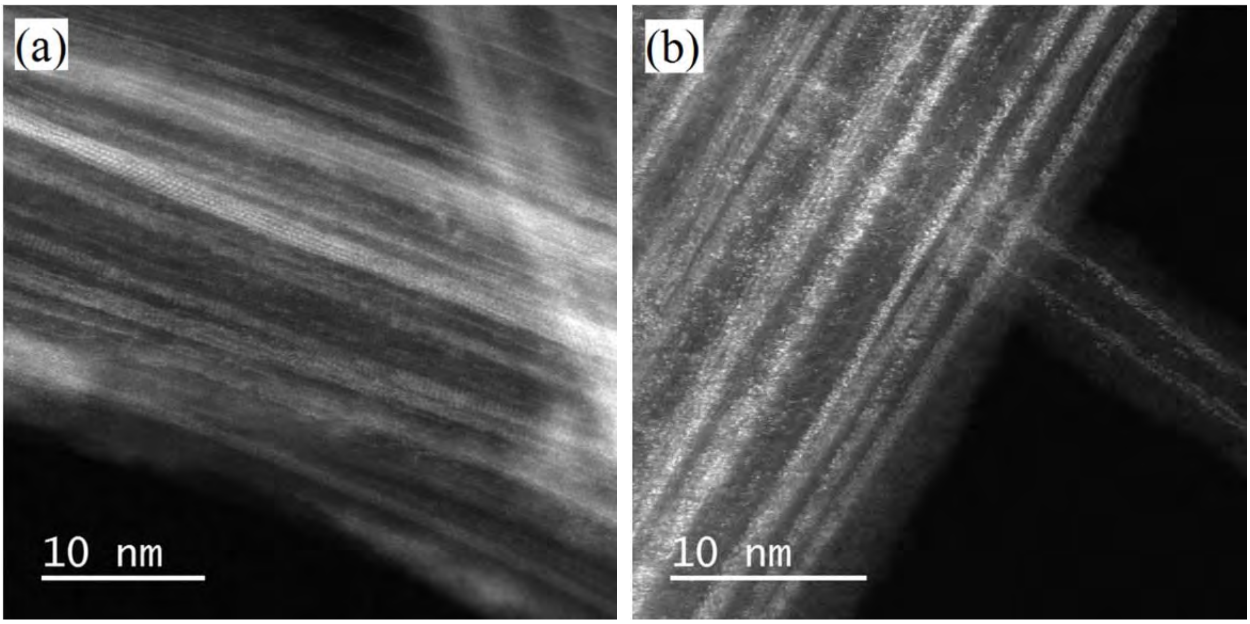

Fig. 3.20 - ADF images of (a) FeI_2@DWCNTs-p and (b) FeF_3@DWCNTs-p showing the encapsulated (here amorphous-like) material in both samples.

To verify whether the encapsulated FeI_2 is successfully or not transformed into FeF_3 after the fluorination, X-EDS analysis is performed on samples FeI_2@DWCNTs-p and FeF_3@DWCNTs-p. Fe Kα peak and I Lα peak are present in the X-EDS spectra collected from DWCNT bundles in FeI_2@DWCNTs-p (Fig. 3.21), confirming the encapsulation of FeI_2 in CNTs. The presence of other peaks in the spectra including C Kα peak, O Kα peak, Si Kα peak and three peaks of Cu in the spectra originate from the carbon nanotubes themselves, air adsorbed in the CNTs or in the column of the TEM, the EDS detector and the copper grid, respectively.

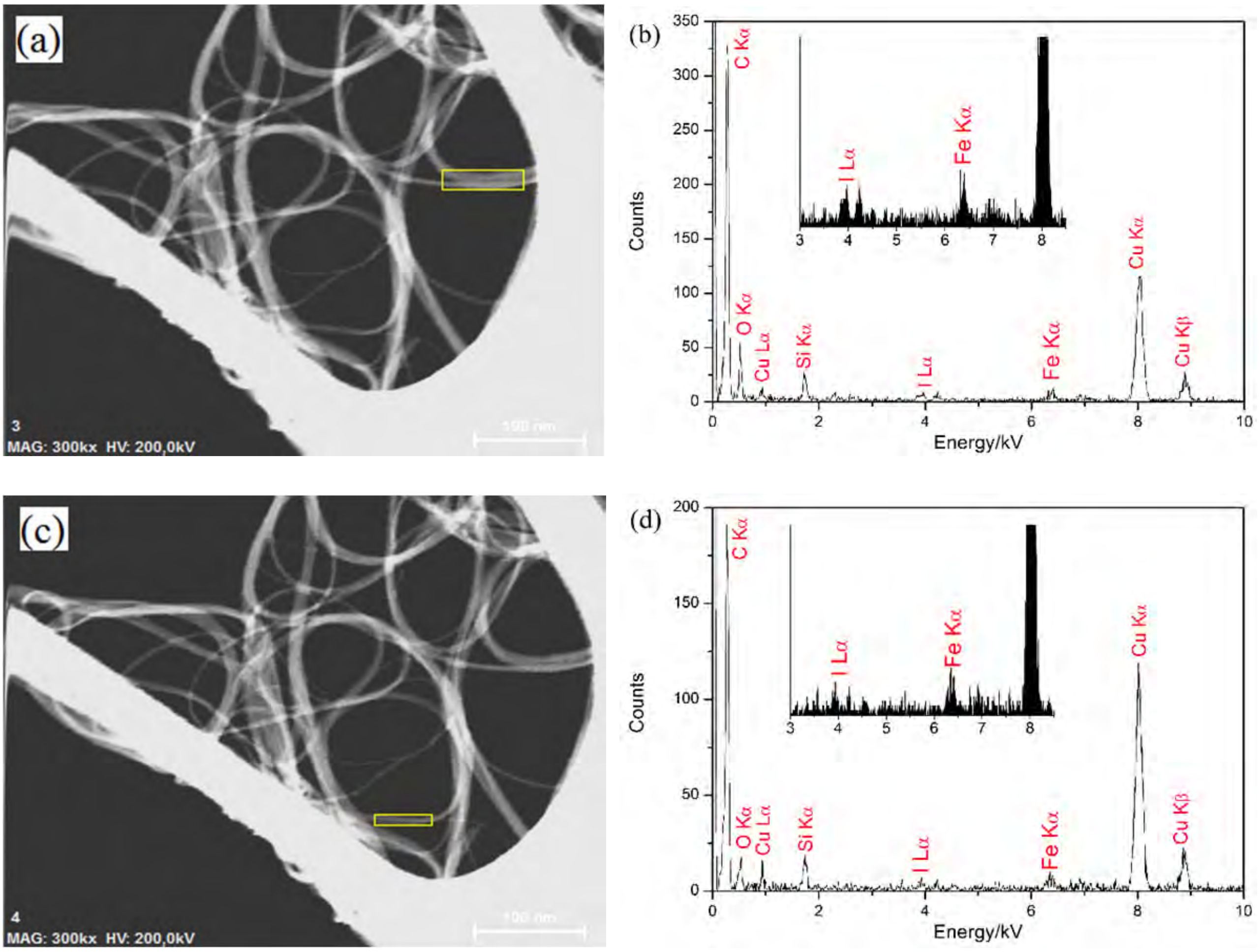

Fig. 3.21 - (a) and (c) are STEM images of FeI_2@DWCNTs-p and (b) and (d) are X-EDS spectra collected from the DWCNT bundles boxed in (a) and (c). The insets in (b) and (d) are enlarged spectra of the region from 3 to 8.5 kV showing the peaks of I and Fe.

Meanwhile, Fe Kα peak and F Kα peak are present in the EDS spectra collected from large DWCNT bundles in FeF_3@DWCNTs-p (Fig. 3.22), suggesting the possible presence of confined FeF_3 crystals after fluorination. However, I Lα peak is present in the spectra of FeF_3@DWCNTs-p as well indicating that some encapsulated FeI_2 crystals are not fluorinated, which can be explained by the same reason as for the *in situ* reduction reaction, i.e., the diffusion of F_2 and reaction kinetics between FeI_2 and F_2 are slowed down due to the presence of the carbon sheath and difficult access to the whole crystal at once.

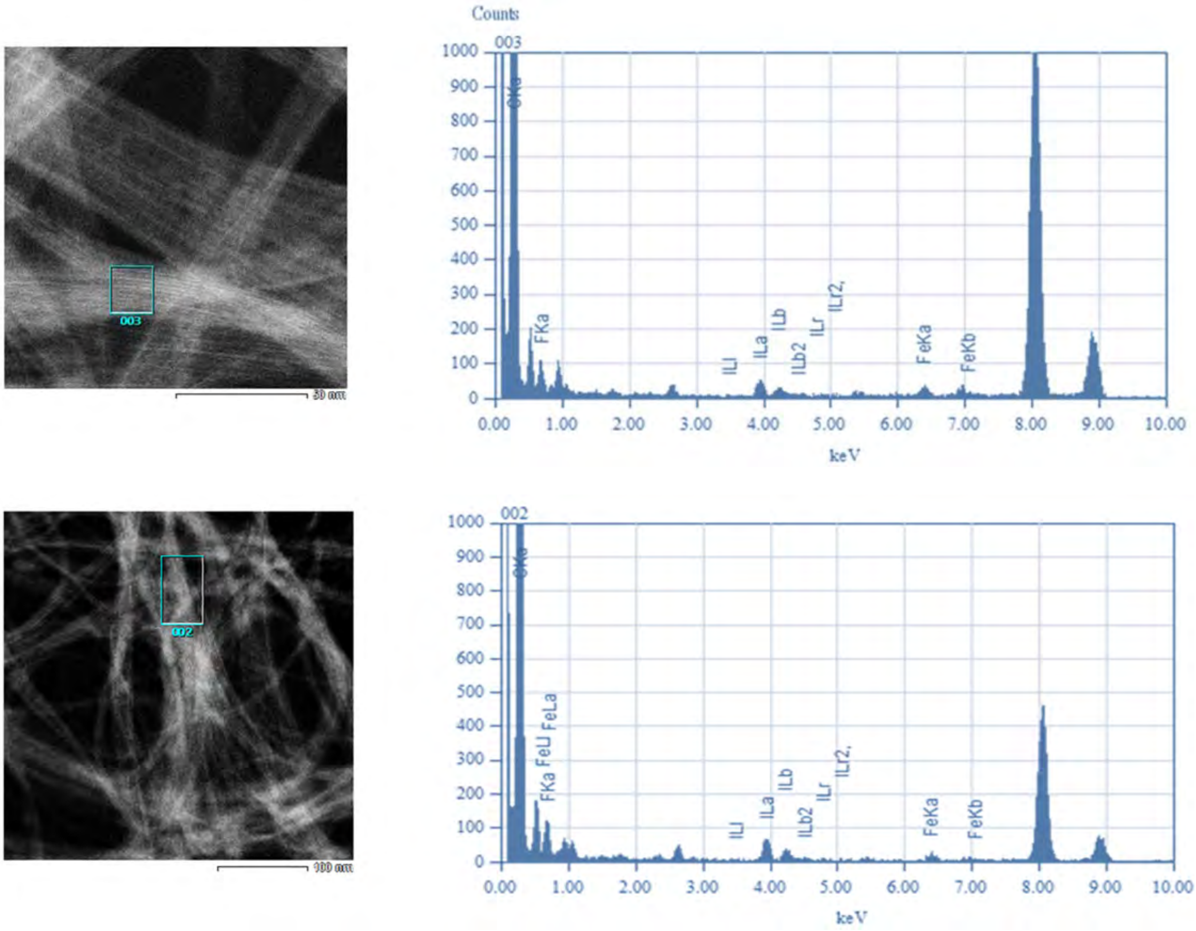

Fig. 3.22 - (a) and (c) are STEM images of FeF_3@DWCNTs-p and (b) and (d) are X-EDS spectra collected from the DWCNT bundles boxed in (a) and (c).

To further confirm the existence of a FeF_3 phase in FeF_3@DWCNTs and ascertain its structural state (amorphous or crystallized), X-ray diffraction (XRD) was performed by ICCF under the large energy flow of the CRYSTAL line at synchrotron SOLEIL. Pair Distribution Function (PDF, in which peaks are related to the distances between two types of atoms in the material structure) data were obtained, which are currently still being analysed at ICCF.

Raman Spectroscopy is known as a powerful tool to investigate the electronic properties of filled CNTs. Many studies have reported that a charge transfer between SWCNTs or DWCNTs and the encapsulated halides [10], iodine [11], oxides [12], organometallic compounds [13], *etc*. resulted in a shift of the Raman G band. Fig. 3.23 illustrates the Raman spectra of the starting purified DWCNTs, FeI_2@DWCNTs-p and FeF_3@DWCNTs-p, respectively. As known, the Raman spectrum in the radial breathing mode (RBM) range gives information about the diameter distribution of SWCNTs or DWCNTs (inner and outer tubes), and the main peaks in the blue region of the RBM bands shown in Fig. 3.23a correspond to the inner tubes of DWCNTs, while the lower frequency peaks in the purple region are related to the outer tubes of DWCNTs. Regarding the pink region, a peak centred at ~110 cm^{-1} appears in the spectra of FeI_2@DWCNTs-p and FeF_3@DWCNTs-p while absent in the spectrum of purified DWCNTs, which can be assigned to the I_n^- species contained in the encapsulated FeI_2 crystals [11, 14]. Comparing the RBM peaks of the three samples, no noticeable change in the position or the number of the main peaks is observed, which can be considered as an indication of an undetectable amount of charge transfer occurring between the CNTs and encapsulated materials [15]. A similar result is observed for the G bands of the three samples, as shown in Fig. 3.23b.

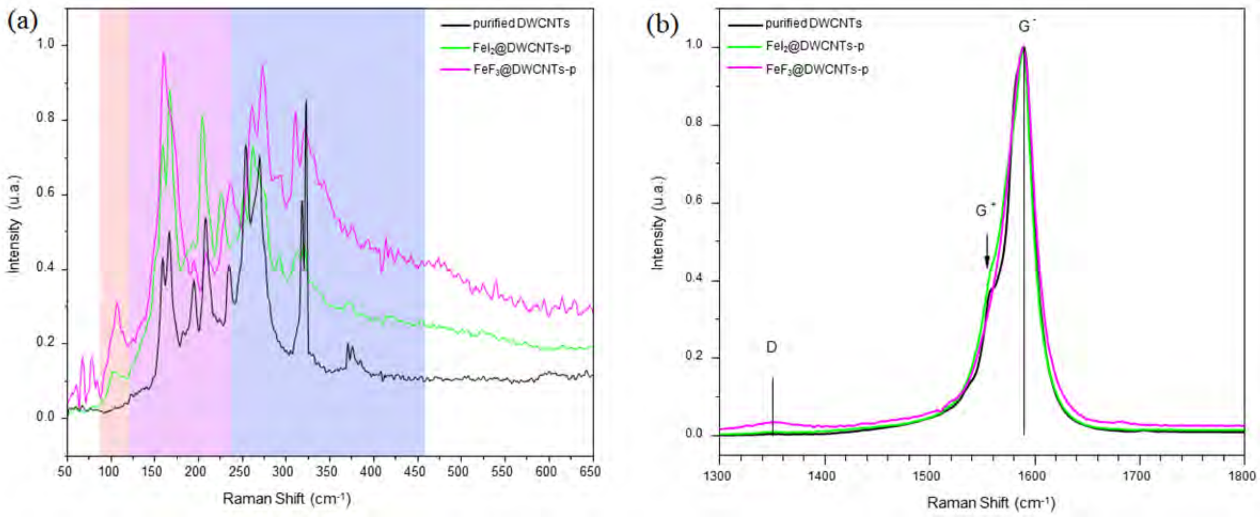

Fig. 3.23 - Raman spectra of purified DWCNTs, FeI_2@DWCNTs-p and FeF_3@DWCNTs-p recorded at 514.5 nm: (a) RBM region and (b) tangential mode region.

The positions of G^- bands in the spectra are 1590 cm^{-1} (purified DWCNTs), 1591 cm^{-1} (FeI_2@DWCNTs-p) and 1589 cm^{-1} (FeF_3@DWCNTs-p), respectively, indicating that almost no charge transfer or weak charge transfer occurs between the CNTs and encapsulated materials. In case of weak charge transfer, it means that encapsulated FeI_2 is able to induce weak p-doping (input of holes) whereas encapsulated FeF_3 is able to induce weak n-doping (input of electrons). More Raman spectra excited at other wavelengths are necessary for further understanding of the interactions between CNTs and encapsulated materials. However, Raman spectra should be interpreted with caution because the RBM bands are acquired from different areas hence could be naturally different since the samples are often not homogeneous and Raman is resonant for CNTs meaning that a single nanotube could give a rather intense signal. Therefore, only analysis on the very same CNT bundles before and after transformation could help drawing strong conclusions, which is in fact impossible due to the experimental procedures used here.

3.5 Conclusion

In summary, various *in situ* transformations including *in situ* sulfurization, *in situ* reduction and *in situ* fluorination on metal iodide-based hybrid DWCNTs were performed. In the case of *in situ* sulfurization of PbI_2@DWCNTs, the synthesis of PbS nanocrystals was not successful in the different experimental conditions investigated but slight doping of the DWCNTs with sulphur was evidenced. Further work on optimizing the experimental conditions is required in order to successfully obtain PbS nanocrystals. In the case of *in situ* reduction, Fe and Ni nanocrystals encapsulated within DWCNTs were synthesized by reducing DWCNTs filled with the corresponding iodides in H_2 atmosphere. In the case of *in situ* fluorination, FeF_3 nanocrystals encapsulated within DWCNTs have been possibly synthesized by reacting the FeI_2@DWCNTs with F_2 gas but this needs to be confirmed by structure analysis (XRD). Regarding the *in situ* reduction, higher temperature and longer reduction time could improve the yield of metal nanocrystals, while the experimental conditions need to be optimized since metal iodides were still present in the reduced samples even in the strongest conditions investigated. Compared to FeI_2, NiI_2 could be reduced by H_2 more easily since more Ni nanocrystals were found in the reduced samples. The reason could be the propensity of NiI_2 to spontaneously decompose (see Chapter 2) which leaves iodine available and facilitates its removal as HI while leaving Ni behind. Meanwhile, interesting intermediate NiI_x ($x<2$) with different elemental compositions encapsulated within CNTs were observed in the reduced NiI_2@DWCNTs samples. Regarding *in situ* fluorination, it is also necessary to optimize the experimental conditions since iron iodide crystals were still present in the DWCNTs after fluorination. This is however challenging because increasing the temperature, in particular, is difficult because this would also lead to the fluorination of the CNTs themselves – which was to be avoided in this work. For both unsuccessful (sulfurization) and successful (H_2 reduction and fluorination) *in situ* chemical transformations investigated it is a common conclusion that the difficult access of the encapsulated crystals by the reactant (only through the tube tip once opened by the contact with the metal halide – see Chapter 2) and then the difficult progression of the reactant in the tube cavity in order to access the whole encapsulated materials (which only can occur by diffusion through the crystal or the crystal/inner tube interspace) are responsible for slowing down the reaction kinetics, resulting in the concomitant occurrence of both transformed, partially transformed and untransformed filling materials. This is consistent with the fact that the most successful *in situ* transformation was achieved with NiI_2, in relation with its propensity to partially decompose even before the melting temperature is reached, giving the reactant an easier access to the whole filling material by creating some porosity. This work also highlights that some of the conclusions of earlier works published in the literature may have to be revisited, as the increasing availability of modern tools (and especially very localised EELS analysis) make possible a more thorough analysis of filled CNTs, clearly showing that the global picture is more complex than the simplified description sometimes given.

References

[1] H. Song, G. Yang, H. Cui, C. Wang, Honeycomb-like porous iron fluoride hybrid nanostructures: excellent Li-storage properties and investigation of the multi-electron reversible conversion reaction mechanism, Journal of Materials Chemistry A, 3 (2015) 19832-19841.

[2] J. Liu, H. Yu, Z. Wu, W. Wang, J. Peng, Y. Cao, Size-tunable near-infrared PbS nanoparticles synthesized from lead carboxylate and sulfur with oleylamine as stabilizer, Nanotechnology, 19 (2008) 345602.

[3] S.A. McDonald, G. Konstantatos, S. Zhang, P.W. Cyr, E.J. Klem, L. Levina, E.H. Sargent, Solution-processed PbS quantum dot infrared photodetectors and photovoltaics, Nature materials, 4 (2005) 138-142.

[4] P. Gambardella, A. Dallmeyer, K. Maiti, M. Malagoli, W. Eberhardt, K. Kern, C. Carbone, Ferromagnetism in one-dimensional monatomic metal chains, Nature, 416 (2002) 301-304.

[5] T. Fujimori, A. Morelos-Gomez, Z. Zhu, H. Muramatsu, R. Futamura, K. Urita, M. Terrones, T. Hayashi, M. Endo, S.Y. Hong, Y.C. Choi, D. Tomanek, K. Kaneko, Conducting linear chains of sulphur inside carbon nanotubes, Nature Commun, 4 (2013) 2162.

[6] A.F. Holloway, K. Toghill, G.G. Wildgoose, R.G. Compton, M.A. Ward, G. Tobias, S.A. Llewellyn, B. Ballesteros, M.L. Green, A. Crossley, Electrochemical opening of single-walled carbon nanotubes filled with metal halides and with closed ends, The Journal of Physical Chemistry C, 112 (2008) 10389-10397.

[7] K.D. Sattler, Carbon Nanomaterials Sourcebook: Graphene, Fullerenes, Nanotubes, and Nanodiamonds, CRC Press, 2016.

[8] T. Bortolamiol, P. Lukanov, A.-M. Galibert, B. Soula, P. Lonchambon, L. Datas, E. Flahaut,

Double-walled carbon nanotubes: quantitative purification assessment, balance between purification and degradation and solution filling as an evidence of opening, Carbon, 78 (2014) 79-90.

[9] M.Q. Tran, C. Tridech, A. Alfrey, A. Bismarck, M.S. Shaffer, Thermal oxidative cutting of multi-walled carbon nanotubes, Carbon, 45 (2007) 2341-2350.

[10] M. Kharlamova, L. Yashina, A. Lukashin, Charge transfer in single-walled carbon nanotubes filled with cadmium halogenides, Journal of Materials Science, 48 (2013) 8412-8419.

[11] J. Cambedouzou, J.-L. Sauvajol, A. Rahmani, E. Flahaut, A. Peigney, C. Laurent, Raman spectroscopy of iodine-doped double-walled carbon nanotubes, Physical Review B, 69 (2004) 235422.

[12] J. Mittal, M. Monthioux, H. Allouche, O. Stephan, Room temperature filling of single-wall carbon nanotubes with chromium oxide in open air, Chemical physics letters, 339 (2001) 311-318.

[13] H. Shiozawa, T. Pichler, C. Kramberger, A. Grüneis, M. Knupfer, B. Büchner, V. Zolyomi, J. Koltai, J. Kürti, D. Batchelor, Fine tuning the charge transfer in carbon nanotubes via the interconversion of encapsulated molecules, Physical Review B, 77 (2008) 153402.

[14] L. Grigorian, K. Williams, S. Fang, G. Sumanasekera, A. Loper, E.C. Dickey, S. Pennycook, P. Eklund, Reversible intercalation of charged iodine chains into carbon nanotube ropes, Physical review letters, 80 (1998) 5560.

[15] M. Sendova, E. Flahaut, B. DeBono, Raman spectroscopy of PbI_2-filled double-walled carbon nanotubes, Journal of applied physics, 98 (2005) 104304-104304.

General Conclusions and Perspectives

In this thesis, we proved that the filling of DWCNTs with metal iodides and iodine is an easy approach to synthesize various 1D nanowires of metal iodides as well as iodine phases with different structures and configurations, owing to the templating effect of the elongated inner cavity of DWCNTs. In addition, we also proved that the hollow core of DWCNTs can act as a nanoreactor allowing chemical reactions to occur.

In order to find out which factors prevail in controlling the filling process and understand the filling mechanisms better, a series of filling experiments using the molten phase method was performed and the filling rate achieved in each filling experiment was estimated from the HRTEM data while investigating various parameters among the possibly most relevant ones.

Firstly, parameters related to the characteristics of the host nanotubes were considered (number of walls, inner diameter, surface energy of the tube inner surface, chemical nature of the tube material) by taking various carbon nanotube types (DWCNTs, FWCNTs, concentric-type MWCNTs, hexagonal-type MWCNTs) and boron nitride nanotubes as potential host tubes, for filling them systematically with a single material, PbI_2 (and NiI_2, in a lesser extent, since only DWCNTs and BNNTs were tentatively filled with it). Secondly, parameters related to the characteristics of the filling materials were also considered by filling a single type of carbon nanotubes (DWCNTs) only, with a variety of halides providing a range of values in several properties (viscosity, vapour pressure, surface tension, redox potential).
A general finding was that the key parameter driving the filling event is the **chemical reactivity** of the filling halides towards the material making the tube wall, due to the need to give access to the inner cavity of the host tubes by opening their tips. For carbon nanotubes, it was demonstrated that such a characteristic is conveniently represented by considering the <u>**redox potential**</u> of the couple metal iodide / metal, calculated at the highest temperature used among all the filling conditions (in order to make the comparison possible). One limitation of our approach which is using redox potentials to compare the reactivity of different metal halides is that either the cation or the anion has to be in common (and at the same oxidation state as well) because the corresponding redox

couple is used as a reference. This thus makes possible to compare for example “metal iodide” between each others (the iodide anion being in common), or “iron compounds” between each others – with some limitations ($FeCl_2$ and FeI_2 for example, where Fe(II) is involved, but not $FeCl_2$ and FeI_3). As far as opening the tubes is concerned, the **number of walls** was therefore found to be another key parameter, as a too large number of walls could not allow the opening to occur. In this regard, the **thermal stability** (revealed by the **Gibbs free energy**) of the filling material appears to be important, as high stability is rather detrimental to filling. This is (i) either because the species resulting from the decomposition is not as chemically reactive as the original halide towards polyaromatic carbon (this is presumably the case for CoI_2, which was found to dimerise before the melting point is reached, assuming that the resulting dimers are not reactive enough towards carbon, hence explaining an unexpectedly low filling rate with respect to the high redox potential value of CoI_2), (ii) or because the resulting species are too much aggressive towards the host tubes (as it is the case towards boron nitride for iodine species resulting from the decomposition of NiI_2), (iii) or, finally, because the resulting species compete with the original halide in the filling event (as it is the case for NiI_2, whose early decomposition results in filling DWCNTs with iodine in addition to NiI_2).

Hence, those three parameters (redox potential, thermal stability of the filling material, and number of walls of the host CNT) prevail, meaning that the other parameters only have a subsidiary importance – if any - in the filling mechanisms. In this regard, our results provided some hints, yet no certainties:

- High values of s**urface tension** could be favourable to capillary filling, in accordance with the Jurin's law. This is how the high filling rate with AgI could be explained whereas its redox potential value was not favourable.
- Low values of **surface energy** of the host tube inner surface could be detrimental to capillary filling. This is how the almost nil filling rate of BNNTs with PbI_2 could be explained (whereas the reactivity of PbI_2 with boron nitride is not an issue, since BNNTs were found to be opened, either because of the mechanical grinding required before use, or due to the reaction with PbI_2). A counterpart is that high values of surface energy of the host tube inner surface should then be favourable to capillary filling, which could be the reason why the

filling rate of opened herringbone-MWCNTs is high in spite of its large inner diameter (which is a supposedly an unfavourable feature, again considering the Jurin's law).

For the other parameters (the host nanotube **inner diameter value**, which is supposed to be more favourable when the diameter is lower according to Jurin's law, and the molten filling material **viscosity**) our set of experiments has not succeeded in determining whether they could play a role or not, either because the adequate comparable experiments were not possible to perform due to the lack of the suitable host nanotube variety (e.g., MWCNTs naturally opened with a large range of inner diameters), or because of the lack of physical parameter data (*e.g.*, the viscosity values were not available in the literature for 7 over 12 of our filling material series gathered in Table 2.7).

Peculiar structures were observed for the confined NiI_2 and iodine with respect to the bulk filling materials when characterizing the hybrid DWCNT samples with TEM. Particularly when iodine was introduced into CNTs starting from either molten iodine, gaseous iodine or as by-product from the decomposition of molten NiI_2, various structures including atomic iodine chains either single and straight or twins (or triple) and helical, iodine crystals with structure differing from that of bulk iodine, iodine crystals with orthorhombic structure as in bulk, and finally iodine nanotubes - which may not exist without the protection of the carbon sheath were observed.

Among the iodine structures, the single straight chain was the most abundant whatever the way iodine was introduced in the system, while the helical double- and triple-chains were less frequent, and only observed when iodine was initially introduced as a phase (i.e., not as a decomposition by-product of NiI_2). Instead of invoking a possible role of the iodine starting state, this discrimination is more likely to result from the competition between iodine and molten NiI_2 in the filling event. The type of iodine structure appeared to be closely dependent on the host tube inner diameter:

- single chains were only found to exist in CNTs within inner diameters less than ~1nm;
- helical double- and triple-chains were no longer found when tube inner diameters were larger than ~1.5 nm;
- A so-called "Phase III" (according to Guan et al[11]) may occur for inner tube diameters larger than 1nm, partly presumably resulting from the electron irradiation (in the TEM) of the multiple-chains

- The orthorhombic structure (the only one similar to that of bulk iodine) needs inner tube diameters larger than 1.5 nm to develop;
- A new hybrid CNT made of a large nanotube (SWCNT or DWCNT) subsequently collapsed and flattened for energetics reasons, hence exhibiting longitudinal edge channels on both sides of the ribbon, and then with these channels filled with iodine.

As already stated with the occurrence of Phase III, iodine structures other than the single straight chain seem to be more or less electron sensitive and may degrade until full amorphisation depending on the energy of the TEM electron probe used.

In order to investigate the possibility of *in situ* transformations of encapsulated nanocrystals, three different chemical treatments were applied: *in situ* sulfurization (on encapsulated PbI_2, aiming at obtaining the semi-conducting phase PbS), *in situ* reduction (on encapsulated FeI_2 and NiI_2, aiming at obtaining metallic Fe and Ni nanomagnets respectively), and *in situ* fluorination (on FeI_2, aiming at obtaining nanosized FeF_3 as an efficient electrode component for Li-ion batteries). None of the target materials could have been inserted into the CNTs directly due to their high melting points (>1000°C).

Our *in situ* sulfurization procedure (by means of molten sulphur), failed at obtaining encapsulated PbS but resulted in introducing a small amount of sulphur in the tube cavities and probably in the groove channels between tubes in bundles as well.

Our *in situ* reduction procedure (by means of gaseous H_2) was more successful in obtaining significant amounts of Fe and – even more abundantly - Ni encapsulated nanocrystals. After optimisation of the procedure, NiI_2 could be reduced more easily than FeI_2. This was possibly related to the propensity of NiI_2 to spontaneously decompose which leaves iodine available for easier removal as HI, while leaving Ni behind. Interesting encapsulated intermediate NiI_x crystals with various under-stoichiometry levels ($0<x<2$) demonstrated that the reduction reaction is directional and progressive, first occurring at the nanocrystal tip facing the nanotube end by which H_2 enters the cavity, and then progressing through the crystal structure. Resulting encapsulated Ni crystals exhibited peculiar crystalline structure, either similar to bulk Ni crystal but with up to 20% stretched atom distances, or unprecedented and yet to determine.

Finally, *in situ* fluorination (by mean of gaseous F_2) was not clearly demonstrated to be efficient with producing FeF_3 crystal yet, since all data are still under analysis at ICCF. However, evidences for chemical changes (addition of F) and slight electronic structure modification (slight downshift of the Raman G band) brought by the fluorination procedure to the encapsulated material have been evidenced, and further analysis should be performed soon to investigate this.

For all *in situ* chemical transformation attempts investigated, it is a common conclusion that the access to the encapsulated crystals by the reactant is the main issue, along with the progression of the reactant through the crystal structure to be transformed. The progression of the reactant in the tube cavity in order to access the whole encapsulated materials is difficult as it can only occur by diffusion through the crystal, or the crystal/inner tube interspace (which is usually tiny). This is certainly the main reason why *in situ* sulfurization has failed since operated by means of liquid (molten) sulphur for which access and diffusion are much more critical issues than for gaseous reactants. Also, this is responsible for slowing down the reaction kinetics, resulting in the concomitant occurrence of both transformed and untransformed filling materials. This is consistent with the fact that the most successful *in situ* transformation was achieved with NiI_2, in relationship with its propensity to partially decompose even before the melting temperature is reached, giving the reactant an easier access to the whole filling material by creating some porosity (in addition to leaving iodine readily available for easier removal as HI).

Our work during the past three years gave a new insight into the mechanisms involved when filling CNTs via the molten method and provided some routes to synthesize 1D metal nanocrystals while demonstrating the inefficiency of others. Among the possible factors investigated, some were demonstrated to be important in the course of successful filling, but uncertainty remains for others. One main reason is the lack of availability of the related physical parameters data in the literature. Carrying-out a systematic work for measuring basic parameters such as viscosity, surface tension and vapour pressure at melting temperature for a large variety of potential filling materials would be very useful. Meanwhile, in order to further understand the filling mechanisms, carrying out similar investigations involving other halides and other compounds would be helpful with bringing more data and more observations so that to possibly obtain statistical evidences likely to overcome the lack of parametric data. This additional work should include considering a more extended range of host carbon nanotube grades allowing more accurate and more reliable comparisons.

In the close future, some of the materials we have been able to prepare would be quite interesting to study for their collective and individual properties: For instance, as encapsulated iodine was demonstrated to be electron acceptor and able of charge transfer in the literature since 1998 and until today where it is used for high conductivity CNT-based fibres[3], checking whether our iodine-filled CNTs also exhibit evidences for charge transfer as a bulk would be a compulsory start. This could be done by investigating (Raman, electrical measurements) the same CNT buckypaper before and after filling with iodine. Then, it would be quite interesting to systematically study the ability of each of the various iodine structures evidenced in our work regarding the extent in charge transfer. This would be possible by contacting individual bundles of filled CNTs first, then individual filled CNTs, after depositing them onto a silicon nitride membrane thin enough for allowing TEM investigation yet strong enough for withstanding the contacting procedure. Such membranes are available nowadays. The same could apply to sulphur-filled CNTs. Another interesting material worth investigating we have produced are the encapsulated Ni nanocrystals. Obviously, their magnetic properties and magneto-transport should be measured. First, thanks to a specific TEM mode (electron holography), evidencing whether the encapsulated Ni crystals actually behave like ferromagnetic nanomagnets could be possible even without needing to contact them. Then the material could be investigated following a similar operating procedure as for the iodine filled CNTs: "blind" investigation of the bulk materials (Raman, SQUID) and then investigation of individual Ni-filled CNTs (Raman, magneto-transport), while lying onto electron-transparent membranes in order to be able to check how filled (number and length of the encapsulated nanocrystals) the contacted CNTs are. These 1D nanocrystals are expected to exhibit peculiar properties with respect to bulk materials and once they can be synthesized in relatively large quantities, practical applications of filled CNTs in various fields could be tested in demonstrators such as photovoltaic devices, energy storage devices, magnetic storage devices, and so on. Most of the characterisations described in the last paragraph are currently in progress with different collaborators but the results, not know at the time of writing this conclusion, could unfortunately not be included in the manuscript.

---

[3] Y. Zhao, J. Wei, R. Vajtai, P. M. Ajayan, E. V. Barrera, Iodine doped carbon nanotube cables exceeding specific electrical conductivity of metals, Scientific Reports 1, 83 (2011).

Appendix *METHODOLOGY*

A.1 Principles of TEM Imaging and Related Techniques

Transmission electron microscope is undoubtedly an invaluable tool for determining the location of the filling and revealing the structure and chemistry of the encapsulated materials. Compared to the conventional visible-light microscope, the smallest distance that can be resolved (i.e., resolution) endowed by an electron microscope is much smaller, even smaller than the diameter of certain atoms, due to the extremely short wavelength of the electron beam with respect to visible light. Therefore, an electron microscope enables scientists to "see" details well below the atomic level. Of course, it is impossible to really see the electrons with eyes but a fluorescent screen, a CCD camera or other image devices can help. Then how to form a TEM image? First of all, an electron source is required to produce the electron beam. At present, either thermionic sources using a LaB_6 crystal as electron emitter, or field-emission sources for which the electron emitter is a fine tungsten needle are the most suitable and commonly used sources for obtaining good images and other signals in an electron microscope. Compared to the thermionic sources, field-emission sources emit more monochromatic electrons (i.e., more coherent beam), hence inducing better high-resolution imaging and analytical performance. It is essential to integrate the electron source into a gun assembly to control the beam and direct it into the condenser lenses whose role is to take the electrons from the source and transfer them to the observed sample (specimen). All lenses in the TEM behave similarly to a convex or converging glass lens in a light microscope and the paths of electron beam controlled by them obey the laws of classic optic. Differing from a light microscope, the lenses in the TEM are electromagnetic and their strength can be changed by changing the current. The electron gun and the condenser lenses constitute the illumination system of an electron microscope and this system can be operated in two principle modes: parallel beam and convergent beam. The first mode is used primarily for TEM imaging and selected-area diffraction (SAD), while the second is used mainly for scanning TEM (STEM) imaging, analysis via X-ray and electron spectrometry, and convergent-beam electron diffraction (CBED).

After the illumination system, the electron beam arrives at the heart of the TEM, that is the objective lens and the stage where the holder containing the specimen is inserted. In this part, the electrons as negatively charged particles with high energy, and the beam interacts with the specimen and various signals are thus produced (as described in Fig. A.1), which contains all the structural, chemical and other information from the specimen. Among these signals, elastically scattered electrons (with same energy as the electrons in incident beam) are the major source of contrast in TEM images and inelastically scattered electrons (with lower energy than the electrons in incident beam) can provide spectroscopic information about the chemistry and electronic structure of the specimen. On the other hand, owing to the wave-particle duality of electrons, the beam can be diffracted by the atoms in the specimen demonstrating the wave nature. The well-known Bragg equation (Eq. A.1) describing the relationship for the wavelength λ of the incident beam (depending on the operating voltage), the lattice spacing of (hkl) atomic planes, and the angle θ between the incident beam and the (hkl) atomic planes are mainly involed in the diffraction in the TEM:

$$2 \; . \; d_{hkl} \; . \; sin\theta = \lambda \tag{A.1}$$

When the beams diffracted in a single direction by a particular plane of atoms travel through the objective lens, they are focused to a single point (diffraction spot) in the back focal plane of the lens. Since the atomic planes in the specimen are variously oriented, groups of spots are obtained, forming the diffraction pattern (DP) in the back focal plane of the objective lens. Therefore, crystallographic information such as crystal structure, lattice distance, and specimen shape can be deduced from the DP. In addition, if an aperture is put in the back focal plane, then only specific diffraction spots which correspond to specific (hkl) atomic planes are permitted to pass through the aperture and imaged by the following parts of TEM. Following this principle, a dark-field image can be obtained by selecting desired spots with an aperture and the obtained image shows the specific orientations of a single-phase specimen.

The third component of the TEM is the imaging system, in which the image or the DP produced by the objective lens is magnified and then projected onto the viewing screen. To magnifying the image or DP, the intermediate lenses or diffraction lenses are employed, respectively. Finally, the projector lens is used for projection. The above three systems are often called the 'column', for obvious reasons. Fig. A.2 depicts the major components consisting of a TEM, arranged vertically from top to bottom and Fig. A.3 illustrated the simplified ray diagrams in the TEM for obtaining a DP and an image on the viewing screen.

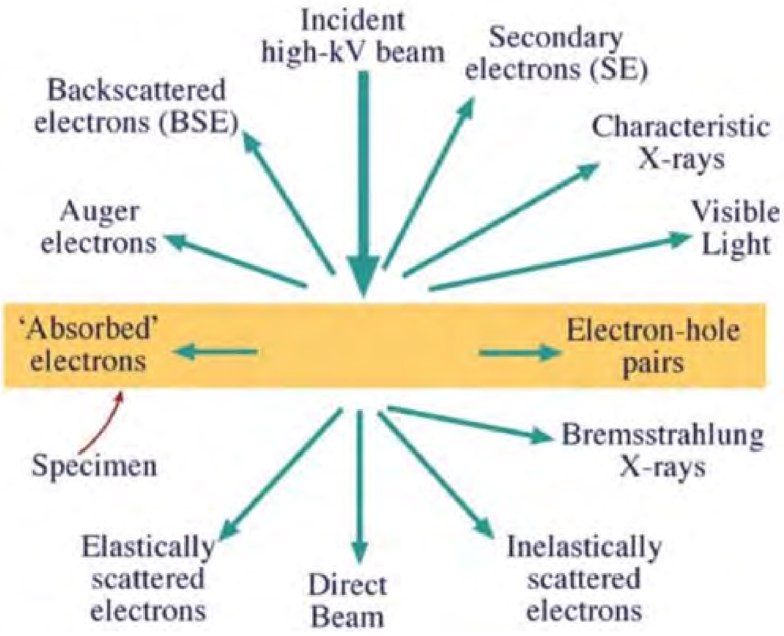

Fig. A.1 - Signals generated when a high-energy beam of electrons interacts with a thin specimen.

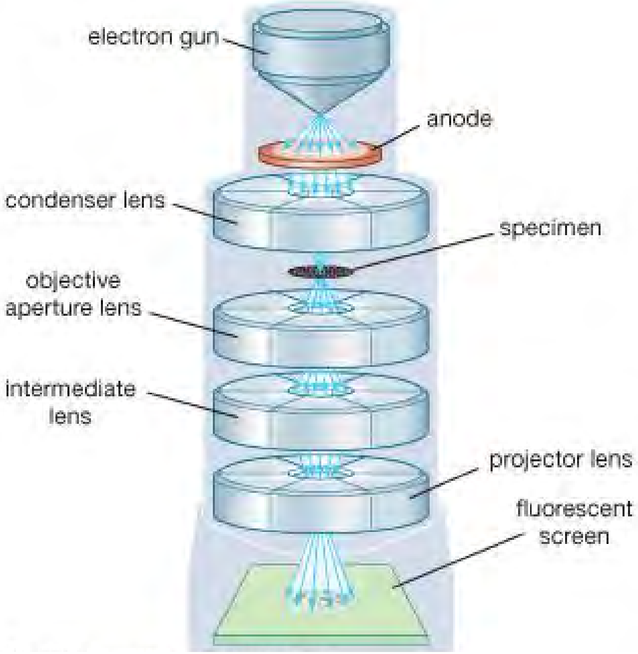

Fig. A.2 - Sketch of the structure of TEM

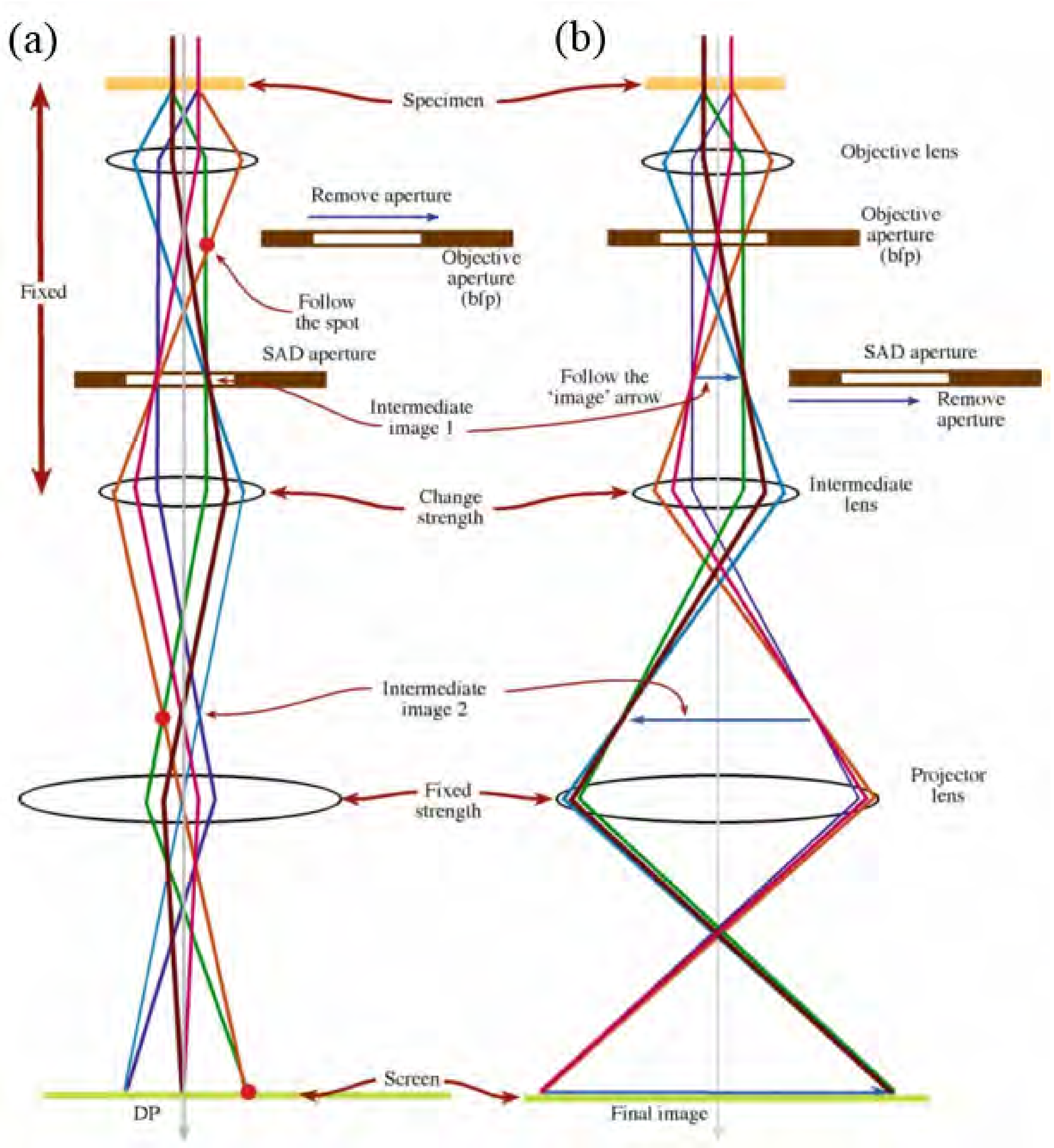

Fig. A.3 - The simplified ray paths in the TEM illustrating how to obtain (a) the DP and (b) the image on the viewing screen. In each case the intermediate lens selects either the back focal plane (BFP) (a) or the image plane (b) of the objective lens as its object. The vertical grey line in each diagram is the imaginary 'optic axis' in the column of TEM. The imaging systems shown here are highly simplified. Most TEMs have many more imaging lenses, which give greater flexibility in terms of magnification and focusing range for both images and DPs. The SAD and objective diaphragms are also shown appropriately inserted or retracted.

The electron travelling paths under the control of lenses in the TEM described above lie in the assumption that all the lenses in the TEM behave as ideal lenses without any defect. In practice, the lenses suffer various defects, such as spherical aberration, chromatic aberration, and astigmatism and among these, spherical aberration (Cs) has a major influence on the limitation of resolution that the microscope can reach. The occurrence of spherical aberration results from the fact that the lens magnetic field is higher for off-axis rays. For electrons further off the axis, they are more strongly bent back toward the axis. Consequently, a point object is imaged as a disk of finite size, which limits our ability to magnify detail because the detail is degraded by the imaging process. In other word, the resolution of TEM becomes worse. Spherical aberration is most important in the objective lens because it degrades the detail that we can resolve in TEM images: all the other lenses magnify any error it generates. During the STEM imaging process, the spherical aberration of the condenser lenses are not in favor of the formation of smallest probes with the highest current thus hindering the microscope performance largely. Fortunately, this aberration can be corrected now thanks to the incorporation of a C_s corrector. With this development, the resolution limit for some modern 'Cs corrected' TEM or STEM can be as low as 0.1 nm or < 0.1 nm.

When the microscope is operated in a conventional TEM mode, with the help of high-resolution transmission electron microscopy (HRTEM) images revealing the detail of the specimen at atomic level can be obtained. If the microscope is operated in a STEM mode, not only atomic resolution images can be obtained, but also information on elemental composition and electronic structure of the specimen can be acquired with the help of analytical techniques such as mapping by energy dispersive X-ray spectroscopy (EDS), electron energy loss spectroscopy (EELS), etc.. The working principle of STEM is similar as that of normal scanning electron microscope (SEM), which is using a focused beam to scan over the sample in a raster while some desired signal is collected to form an image. As in the SEM, backscattered or secondary electrons can be used for imaging; but higher signal levels and better spatial resolution can be obtained by detecting transmitted electrons. In contrast to producing a TEM image by lenses, an electron detector which acts as the interface between the electrons coming from the specimen and the image viewed on the display screen is used to create a STEM image. There are three types of detectors available for STEM, bright field (BF) detector, annular dark field (ADF) detector and high-angle ADF (HAADF) detector. The former intercepts the direct-beam electrons which help build the STEM-BF image, while the ADF detector picks up most of the scattered electrons to form an ADF image. For electrons scattered out to so high angles that beyond the gathering range of ADF detector, the HAADF detector is required and the formed image is called HAADF image or Z-contrast image. Each detector provides a different and complementary view of the specimen and having multiple detectors operating simultaneously is allowed in STEM, which makes the collection of the maximum information from each scan possible.

In order to identify the elemental compositions of the specimen, the characteristic X-rays as shown in Fig. A.1 are important signals. How are these rays generated? First of all, since the energy of the electron in the beam is much higher than the critical ionization energy of most atoms, the electron in the beam will transfer partial energy to the inner-shell electron of atom in the specimen, leaving the atom in an excited state, i.e., ionized. Then the ionized atom can return almost to its ground state by filling-in the hole with an electron from an outer shell. This transition is accompanied by the emission of either an X-ray or an Auger electron. In both the X-ray and Auger cases, the energy of the emission is characteristic of the difference in energy between the two-electron shells involved and this energy difference is unique to the atom. To accomplish the element analytical goal, a X-ray energy-dispersive spectrometer is integrated with the STEM, which uses a Si semiconductor detector or a Ge detector. The detector can generate voltage pulses that are proportional to the X-ray energy and the pulses are subsequently processed by electronics to translate the X-ray energy into a signal in a specific channel in a computer-controlled storage system. The counts in the energy channels are then displayed as a spectrum. With the EDS system, we can acquire a single spectrum or spectrum-line profiles on a selected area in a STEM image, or even carrying out mapping, or compositional imaging on the selected area. These spectra and images can be processed firstly with qualitative analysis by identifying the characteristic peaks in the spectra and then quantitative analysis for obtaining further elemental information of the specimen.

However, it is challenging to analyze light elements by EDS, which is the major drawback. Thus techniques that are sensitive for light-element analysis are required. To this end, EELS is a preferable technique. In fact, it can detect and quantify all the elements in the periodic table in addition to light elements and offers better spatial resolution and analytical sensitivity (both at the single-atom level). Furthermore, not only the elemental composition, but also details about electronic structure, bonding and atomic distribution of the specimen, as well as the specimen thickness can be provided by EELS. Despite of these advantages, very thin specimens are required in EELS and more complicated operation is involved for this technique with respect to EDS, which are disadvantages of EELS. Therefore, EELS and EDS are highly complementary techniques.

The EELS system is based on the magnetic prism which acts as a spectrometer and a lens. When the forward transmitted electrons travel through the prism, they are deflected and the deflection angle for electrons which lose energy is different from that for electrons not suffering any loss. This process resembles the dispersion of white light by a glass prism. Then the dispersed electrons are focused in the dispersion plane, forming a spectrum consisting of a distribution of electron density (I) versus energy loss (E). A typical EEL spectrum can be divided into two regions at the arbitrary break point of ~ 50 eV, low-loss region and high-loss region. In the former, a very intense zero-loss peak is present, which corresponds to the elastic, forward scattered electrons, but also electrons losing a few energy. Apart from the zero-loss peak, plasmon peak is also a strong feature in the low-loss region, which arises from the interaction between beam electrons and outer-shell electrons of atoms in the specimen.

In the high-loss region of the spectrum, signals constituted by the electrons going through the interaction with the inner-shell atomic electrons, as described in the process for how to generate characteristic X-rays are termed as ionization or core-loss edges, which are the predominant feature in this region. The edges are identified as the energy loss at which there is a discrete increase in the slope of the spectrum, and the onset energy of an edge corresponds to the critical ionization energy of an atom, which is unique to the atom. Hence, determination of elemental composition in the specimen using ionization edges is quite straightforward. Then, beyond the ionization edge are found strong oscillations within 50 eV of the onset of the edge due to bonding effect which are called energy-loss near-edge structure (ELNES). Finally, small intensity oscillations may also be observed after 50 eV of the edge onset, as a result of the diffraction effects from the atoms surrounding the ionized atom. These oscillations extend out for several hundred eV as the edge intensity diminishes thus called extended energy-loss fine structure (EXELFS).

A.2 Methodology for the Image Simulation and Structure Modelling of Confined Foreign Phases

The fragments of the filling material are generated from published crystal structures obtained from the *Inorganic Crystal Structure Database* (available at cds.rsc.org). The CNTs are generated using Nanotube Modeller software. The inner diameters of the CNTs are measured from the experimental image but typically "expand" the modelled CNT relative to the experimentally measured one by ca. 8% to allow for curvature of the CNT walls. The models are assembled in CrystalMaker software and then simulated using either an optimized code for parallelisation via GPU acceleration written by Adam Dyson (a PhD student of Dr. Jeremy Sloan in Warwick University, UK) which is published in *https://github.com/ADyson/clTEM* or SimulaTEM for phase-contrast images (sometimes also JEMS) using representative values for accelerating voltage, Cs and defocus where appropriate. Nearly all simulation programs are some variation of the multi-slice approximation approach described in Earl J. Kirkland’s textbook “Advanced Computing in Electron Microscopy”.

Résumé en Français

Introduction générale

Les nanotubes de carbone (CNTs) attirent depuis 1991 l'attention de la communauté scientifique, principalement en raison de leurs propriétés physiques remarquables. En pratique, pour pouvoir réellement les utiliser dans diverses applications, il est souvent nécessaire de les modifier de diverses manières. L'une d'entre elles consiste à les remplir avec des matériaux, avec l'idée que les propriétés du CNT hôte peuvent être modifiées du fait de l'interaction avec le matériau de remplissage. En outre, l'utilisation du canal interne comme moule permet une stratégie alternative pour la synthèse de nanocristaux 1D originaux et de diamètre contrôlé.

Le remplissage des CNTs pour préparer des hybrides X@CNTs peut se faire par différents moyens, parmi lesquels la mise en œuvre d'une phase fondue (sels fondus) est très souvent employée en raison de sa simplicité, de sa polyvalence et de la possibilité d'obtenir des taux de remplissage élevés. Le remplissage des CNTs par un liquide est induit par la force capillaire, et donc souvent décrit par l'équation de Laplace-Young, mais les mécanismes détaillés du remplissage des CNTs par capillarité ne sont pas encore clairs. L'encapsulation de matériaux à haut point de fusion (> 950°C) nécessite de travailler avec un précurseur et de procéder à des traitements de transformation ultérieurs. L'objectif de ce travail vise ainsi à mieux comprendre les phénomènes à la base du remplissage des nanotubes par des composés liquides (fondus) ainsi que les mécanismes des réactions chimiques effectuées *in situ* dans la cavité intérieure des nanotubes. Avec un tel objectif, les iodures métalliques ont été choisis comme composés modèles car ils combinent des propriétés physico-chimiques bien adaptées avec une forte densité électronique de l'iode, rendant cet élément particulièrement facile à mettre en évidence par microscopie électronique en transmission à haute résolution (HRTEM), un outil central dans ces travaux.

Ce manuscrit de thèse se compose donc de 3 chapitres. Le **Chapitre 1** est une introduction générale au remplissage des nanotubes de carbone, qui décrit l'état de l'art des stratégies de remplissage, ainsi que quelques exemples de propriétés et applications des CNTs remplis. Le **Chapitre 2** s'intéresse (1) aux mécanismes de remplissage par la méthode des sels fondus en comparant une série d'halogénures métalliques, mais aussi une variété de nanotubes hôtes et (2) aux structures particulières des nanostructures hybrides X@CNTs ainsi préparées. Le **Chapitre 3** traite de trois différentes tentatives de transformations *in situ* d'hybrides X@DWCNTs sélectionnés (où

DWCNTs désigne des nanotubes de carbone biparois). Enfin, une conclusion générale résume nos résultats et présente nos perspectives, en particulier les travaux en cours liés à la caractérisation des hybrides X@DWCNTs, qui n'ont malheureusement pas pu figurer dans ce manuscrit.

Chapitre 1 Introduction générale au remplissage des nanotubes de carbone

Les premiers exemples de remplissage ont été signalés en 1993 [1-3] lorsque plusieurs tentatives pour introduire des métaux ou des composés dans des NTC multi-parois (MWCNT) ont été rapportées. En 1998, deux exemples de CNTs monoparoi (SWCNTs) remplis ont été signalés (voir Fig. 1.1). L'un d'entre eux était la découverte inattendue de la capacité des fullerènes à diffuser et s'arranger dans les SWCNTs, formant ainsi les fameux "peapods" [4]. L'autre, portant sur la réduction par l'hydrogène de SWCNTs préalablement remplis par $RuCl_3$ (en solution) a été publié la même année [5]. Par la suite, de nombreux autres exemples de remplissage de CNTs ont été décrits.

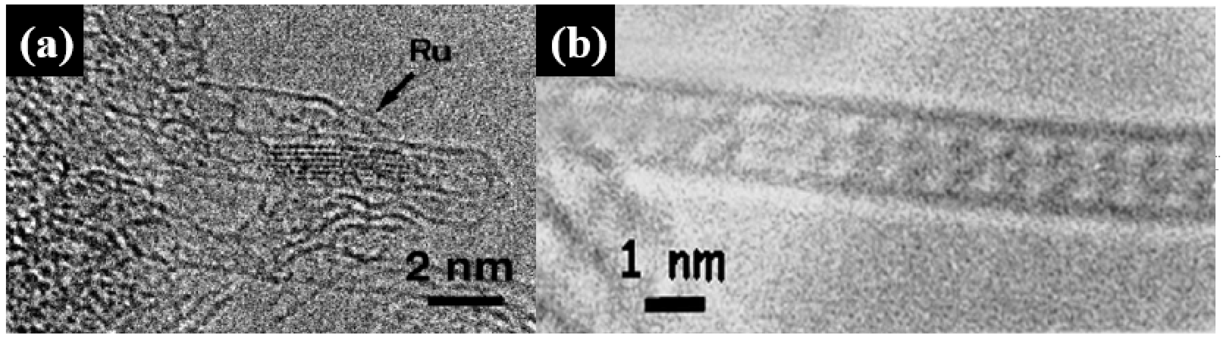

Fig. 1.1 - images MET des deux premiers signalements de remplissage de SWCNT en 1998 (a) Ru@SWCNT, le métal Ru a été introduit initialement sous forme de $RuCl_3$ [9] ; (b) C_{60}@SWCNT ("peapods") [8].

En règle générale, il existe deux voies possibles pour remplir les CNTs, soit *in situ* pendant leur synthèse, soit *ex situ a posteriori*. Par rapport à la méthode *in situ*, l'approche *ex situ* est beaucoup plus souple car elle permet dans l'idéal d'insérer presque tous types de composés dans presque n'importe quel genre de nanotubes. Au cours du processus de remplissage *ex situ*, la capacité des CNTs d'agir comme des capillaires est pleinement exploitée. Plusieurs méthodes de remplissage *ex situ* ont été employées jusqu'à présent y compris par exemple la méthode en phase gaz, la méthode mettant en œuvre une solution ou une suspension, et finalement la méthode en sels fondus. Expérimentalement, l'insertion d'atomes, de molécules ou encore de composés a été obtenue, et la figure 1.2 en montre quelques exemples.

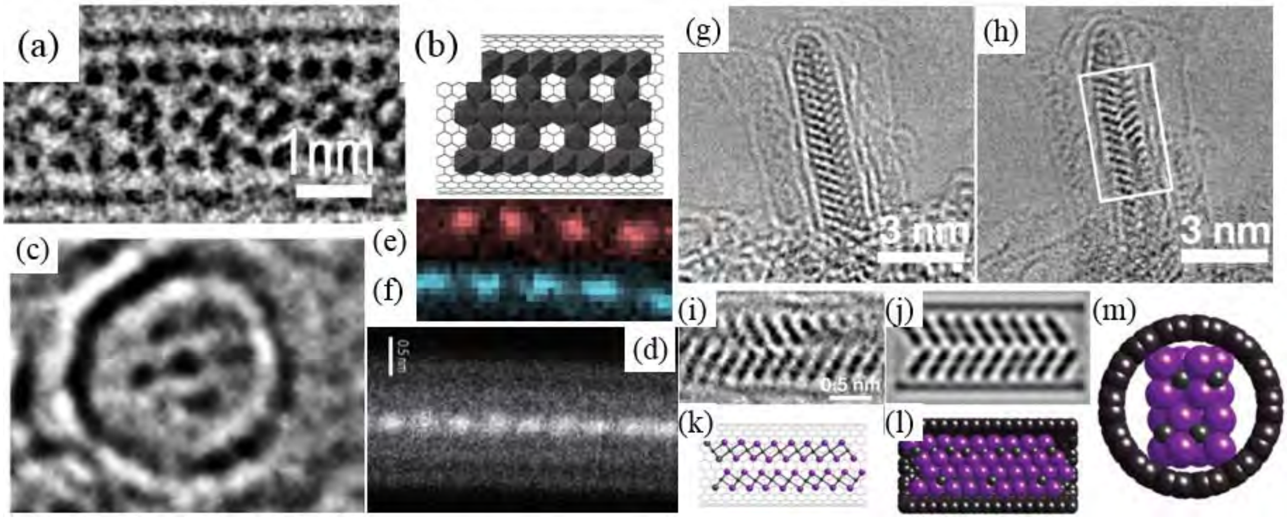

Fig. 1.2 - (a) et (b) image HRTEM et modèle structural d'un SWCNT rempli de cristaux de $NdCl_3$ et le modèle de structure simulée [7] ; (c) image HRTEM d'un SWCNT rempli de $HoCl_3$ présentant une symétrie d'ordre 5 déformée. Chaque tache sombre est supposé être la projection d'une seule chaîne 1D de polyèdres $HoCl_x$ [6]; (d) image en mode "Annular Dark Field" (ADF) d'une chaîne de CsI encapsulée au sein d'un DWCNT et cartographies chimiques EELS associées du Cs (e) et I (f), respectivement, obtenues à partir de l'image (d) [8]; (g) et (h) images HRTEM d'une extrémité d'un SWCNT contenant PbI_2 (h) obtenues à deux focalisations différentes ; (i) image agrandie de la zone encadrée (h) ; (j) image simulée correspondant à (i) basée sur le modèle structural suggéré pour PbI_2 en (k) ; (k, l, m) modèles structuraux représentés sous différentes formes [9].

Des propriétés et comportements particuliers des hybrides X@SWCNTs/DWCNTs ont été découverts. Par exemple, la diffusion et la coalescence de fullerènes à l'intérieur du tube suite à l'irradiation par un faisceau au cours de l'observation en MET [10, 11] ont été observées. Le remplissage de tapis ou couches minces de SWCNTs par de l'iode fondu ou gazeux conduit à une augmentation très nette de la conductivité électrique [12, 13]. Plus intéressant encore, un comportement conducteur de chaînes de soufre encapsulées à l'intérieur de SWCNTs ou DWCNTs a été démontré, alors que le soufre "macroscopique" est isolant à l'ambiante [14], et des clusters de nickel encapsulés dans des SWCNTs ont un comportement superparamagnétique et une coercivité supérieure au Ni "massif" [15]. En raison des comportements particuliers et des propriétés des CNTs remplis, ils peuvent être utilisés dans de nombreux domaines tels que pour la biomédecine, pour des supports de catalyseurs, pour le stockage de l'énergie, l'émission d'électrons par effet de champ, la réalisation des sondes de microscopie en champ proche, pour des dispositifs électroniques ou encore des capteurs [6].

Malgré les résultats obtenus à ce jour dans le domaine du remplissage des CNTs, beaucoup de questions demeurent sans réponse. Par exemple, peu de travaux ont été consacrés à l'identification des propriétés physiques et chimiques pertinentes des composés à insérer sur le taux de remplissage. La mesure à l'échelle microscopique des propriétés physiques du cristal encapsulé dans un nanotube individuel n'est pas facile à réaliser en raison de la nécessité de faire appel à des équipements très sophistiqués tels que la nanolithographie, et des dispositifs spécifiquement conçus pour ce type de mesures. En outre, des nanofils de métaux de transition sont censés présenter des propriétés magnétiques intéressantes car différentes de celles de leurs homologues macroscopiques, mais la synthèse (réussie) de ce type de nanofils encapsulés dans des SWCNTs ou DWCNTs n'est que très peu rapportée. Ceci a donc constitué la motivation pour mener ces travaux sur le remplissage de CNTs mono et biparois par des métaux, en particulier magnétiques.

Références

[1] S. Seraphin, D. Zhou, J. Jiao, J.C. Withers, R. Loutfy, Selective encapsulation of the carbides of yttrium and titanium into carbon nanoclusters, Applied physics letters, 63 (1993) 2073-2075.

[2] P.M. Ajayan, Capillarity-induced filling of carbon nanotubes, Nature, 361 (1993) 333-334.

[3] Y. Saito, T. Yoshikawa, Bamboo-shaped carbon tube filled partially with nickel, Journal of crystal growth, 134 (1993) 154-156.

[4] B.W. Smith, M. Monthioux, D.E. Luzzi, Encapsulated C60 in carbon nanotubes, Nature, 396 (1998) 323-324.

[5] M.H. Green, The opening and filling of single walled carbon nanotubes (SWTs), Chemical Communications, (1998) 347-348.

[6] M. Monthioux, E. Flahaut, J.-P. Cleuziou, Hybrid carbon nanotubes: strategy, progress, and perspectives, Journal of materials research, 21 (2006) 2774-2793.

[7] G. Brown, S. Bailey, M. Novotny, R. Carter, E. Flahaut, K. Coleman, J. Hutchison, M. Green, J. Sloan, High yield incorporation and washing properties of halides incorporated into single walled carbon nanotubes, Applied Physics A, 76 (2003) 457-462.

[8] R. Senga, H.-P. Komsa, Z. Liu, K. Hirose-Takai, A.V. Krasheninnikov, K. Suenaga, Atomic structure and dynamic behaviour of truly one-dimensional ionic chains inside carbon nanotubes, Nature materials, 13 (2014) 1050-1054.

[9] E. Flahaut, J. Sloan, S. Friedrichs, A.I. Kirkland, K. Coleman, V. Williams, N. Hanson, J. Hutchison, M.L. Green, Crystallization of 2H and 4H PbI2 in carbon nanotubes of varying diameters and morphologies, Chemistry of materials, 18 (2006) 2059-2069.

[10] B.W. Smith, M. Monthioux, D.E. Luzzi, Carbon nanotube encapsulated fullerenes: a unique class of hybrid materials, Chemical Physics Letters, 315 (1999) 31-36.

[11] D.E. Luzzi, B.W. Smith, Carbon cage structures in single wall carbon nanotubes: a new class of materials, Carbon, 38 (2000) 1751-1756.

[12] L. Grigorian, K. Williams, S. Fang, G. Sumanasekera, A. Loper, E.C. Dickey, S. Pennycook, P. Eklund, Reversible intercalation of charged iodine chains into carbon nanotube ropes, Physical review letters, 80 (1998) 5560.

[13] A. Tonkikh, V. Tsebro, E. Obraztsova, K. Suenaga, H. Kataura, A. Nasibulin, E. Kauppinen, E. Obraztsova, Metallization of single-wall carbon nanotube thin films induced by gas phase iodination, Carbon, 94 (2015) 768-774.

[14] T. Fujimori, A. Morelos-Gomez, Z. Zhu, H. Muramatsu, R. Futamura, K. Urita, M. Terrones, T. Hayashi, M. Endo,

S.Y. Hong, Y.C. Choi, D. Tomanek, K. Kaneko, Conducting linear chains of sulphur inside carbon nanotubes, Nat Commun, 4 (2013) 2162.

[15] H. Shiozawa, A. Briones-Leon, O. Domanov, G. Zechner, Y. Sato, K. Suenaga, T. Saito, M. Eisterer, E. Weschke, W. Lang, Nickel clusters embedded in carbon nanotubes as high performance magnets, Scientific reports, 5 (2015).

Chapitre 2 Etude des mécanismes de remplissage des DWCNTs par différents composés et des structures particulières résultantes

2.1 Introduction

Bien que divers exemples de remplissage de CNTs ont déjà été publiés, les mécanismes de remplissage ne sont pas encore bien compris, surtout lorsqu’on considère la méthode mettant en œuvre des liquides (solutions, sels fondus). Les travaux pionniers dans ce domaine ont proposé que le remplissage de la cavité interne d'un CNT peut être décrit par un effet de mouillage nanocapillaire, effet décrit par l’équation de Laplace [1, 2], et d'où il découle que les facteurs qui peuvent jouer un rôle dans le processus de remplissage sont nombreux (par exemple, morphologie du CNT, tension superficielle, viscosité, pression de vapeur, etc. [3]). Parmi ces paramètres, la question de savoir le(s)quel(s) est(sont) le(s) plus pertinent(s) n'est pas encore réglée. Dans ce chapitre, le remplissage de CNTs par divers halogénures métalliques ainsi que par l'iode a été effectué via la méthode en sel fondu, et le taux de remplissage atteint dans chaque cas a été estimé à partir de données de MET haute résolution (HRTEM).

Tout d’abord, afin d’évaluer l’importance dans le processus de remplissage des paramètres liés aux CNTs comme le nombre de parois, le diamètre intérieur, ou encore l'énergie de la surface interne des CNTs, nous avons comparé le remplissage de divers types de nanotubes par un seul composé, PbI_2 : DWCNTs, nanotubes de carbone à "peu de parois" de texture concentrique (FWCNTs), MWCNTs de texture concentrique (c-MWCNTs-a) ou "en arêtes de poisson" (h-MWCNTs), et enfin des nanotubes de nitrure de bore (BNNTs). En second lieu, afin d’évaluer l’influence des propriétés physiques et chimiques les plus pertinentes des composés sur les mécanismes de remplissage et les taux de remplissage, les DWCNTs ont été choisis comme tubes hôtes parce qu’ils sont plus robustes que les SWCNTs grâce à la protection par la paroi externe, tandis que la cavité interne des DWCNTs peut avoir un diamètre aussi petit – ou même plus petit – que dans le cas des SWCNTs, ce qui est plus favorable pour promouvoir des structures particulières, et donc des propriétés originales. Enfin, le remplissage de DWCNTs avec une série d’halogénures métalliques (pour la plupart des iodures, mais également $PbCl_2$, PbF_2, etc.) ainsi que par de l'iode a été réalisé, les données relatives aux propriétés des matériaux de remplissage étant recueillies dans la littérature et les bases de données thermodynamiques.

2.2 Synthèse de X@CNTs ou X@BNNTs (X = halogénure ou iode)

Une ampoule de quartz contenant un mélange de CNTs ou BNNTs bruts et le matériau de remplissage désiré, avec un rapport molaire de 1/1,3 (DWCNTs/halogénures ou iode) a été scellée sous vide avec un chalumeau. L'ampoule a ensuite été soumise à un traitement thermique selon le programme suivant : chauffage à 5° C/min depuis la température ambiante (RT) jusqu'à 30 °C au-dessus du point de fusion (Mp) du composé de remplissage, palier de 24h, refroidissement jusqu'à 20 °C au-dessous de Mp à 0,1 °C/min, puis jusqu'à 120 °C au-dessous de Mp à 1 °C/min, puis finalement à 5 °C/min jusqu'à la température ambiante. Pour l'iode, deux températures de remplissage ont été utilisées : 140 °C et 827 °C (température identique à celle utilisée pour NiI_2) et les échantillons préparés ont été notés comme suit : I@DWCNT_140 et I@DWCNT_827, respectivement. Avec le rapport molaire utilisé, le composé de remplissage était en large excès et une étape de lavage a été nécessaire en fin d'opération afin d'enlever le produit en excès (non encapsulé).

Un synoptique résumant toutes les expériences de remplissage effectuées au cours de ce travail de thèse est représenté sur la Fig. 2.1.

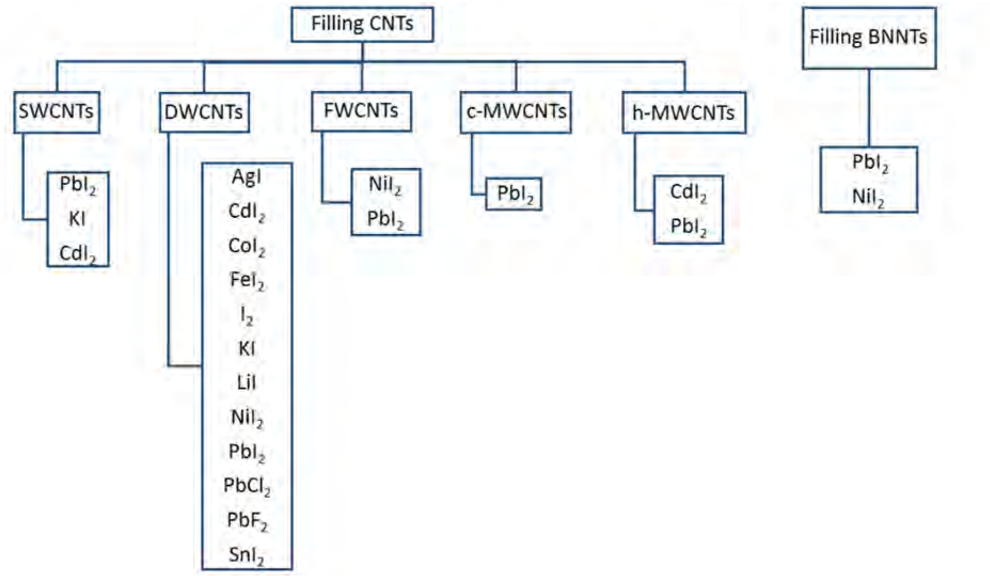

Fig. 2.1 - Synoptique résumant toutes les expériences de remplissage effectuées au cours de cette thèse.

2.3 Caractérisation par microscopie électronique des hybrides X@CNTs et X@BNNTs

Pour estimer le taux de remplissage de chaque échantillon, un minimum de 30 images HRTEM ont été acquises (par échantillon), et le taux de remplissage a été défini comme le rapport de la longueur cumulée de tubes remplis sur la longueur cumulée des tubes présents (remplis + vides) mesurables sur chaque image. Cependant, en raison des limitations inhérentes à la méthode utilisée, nous estimons que le taux de remplissage est obtenu à ± 5 % (% absolu).

Les images HRTEM des DWCNTs remplis montrent que le matériau de remplissage a été correctement inséré dans les nanotubes, confirmant la capacité des iodures métalliques et de l'iode à ouvrir les CNTs, du moins ceux qui ont un nombre limité de parois tels que les DWCNTs. Dans le cas de tentatives de remplissage de DWCNTs avec NiI_2, deux types d'hybrides sont mis en évidence : NiI_2@DWCNT mais aussi un peu de I@DWCNT - résultant de la décomposition spontanée de NiI_2 pendant le processus de remplissage, telle que révélée par l'analyse EELS.

2.4 Structures de NiI_2 et de l'iode confinés à l'intérieur de CNTs

2.4.1 NiI_2 encapsulé

La structure cristallographique de NiI_2 est lamellaire, de type $CdCl_2$, et uniquement du groupe d'espace R-3mH. Presque tous les cristaux de NiI_2 encapsulés peuvent être reliés à ce groupe d'espace R-3mH avec 4-5 atomes d'épaisseur, ou plus selon le diamètre intérieur du CNT hôte. De nombreux cristaux de NiI_2 sont observés déformés (twistés) à l'intérieur des CNTs. Par exemple, les fragments dans les zones I et II (Fig. 2.2, voir encarts) montrent différentes projections de la même structure. Les images ADF simulées et les modèles structuraux dérivés de ces deux régions (Fig. 2.3) révèlent que le fragment II est imagé parallèlement à une projection inhabituelle ([2 1 -0,5]) pour la structure "massive" R-3mH, alors que le fragment I est orienté perpendiculairement au II (voir vue perpendiculaire à l'axe du CNT). De plus, le nanocristal de NiI_2 dans la zone I a 5 atomes d'épaisseur, et diffère ainsi du fragment dans la zone II qui n'a que 4 atomes d'épaisseur. Ceci peut découler de différentes orientations possibles des nanocristaux, tel que proposé sur la figure 2.3.

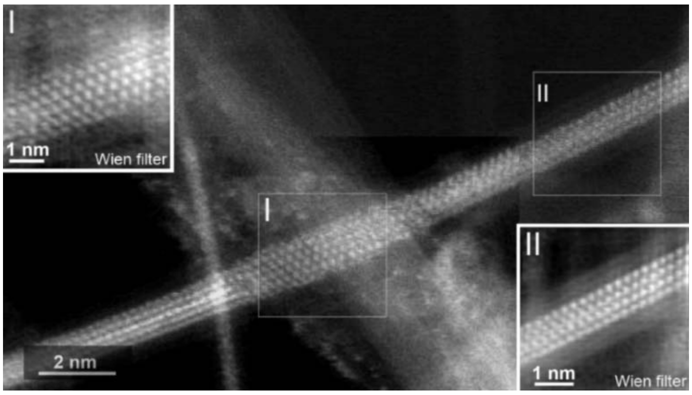

Fig. 2.2 - image ADF d’un nanocristal encapsulé de NiI_2 nanocristallins. Les encarts correspondent à l'application d'un filtre de Wien dans les zones I et II (programme "HRTEM Filter" développé par D. R. G. Mitchell (http://www.dmscripting.com/hrtem_filter.html).

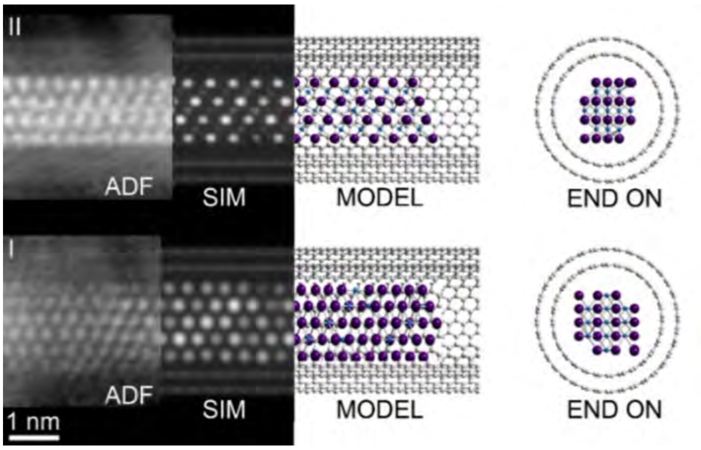

Fig. 2.3 – Modèles structuraux proposés pour les nanocristaux dans les zones I et II.

2.4.2 Encapsulation de l'iode

Des structures particulières ont été observées lorsque de l'iode a été encapsulé dans les CNTs, que ce soit à partir de la décomposition de NiI_2 ou d'iode pur, fondu ou en phase vapeur. La figure 2.4 rassemble des images typiques en champ sombre ou clair illustrant (i) des chaînes d'iode atomique soit simples et droites, soit jumelles (ou triplées) et hélicoïdales, (ii) des cristaux d’iode avec une structure différente de celle de l’iode "massif", (iii) des cristaux d'iode avec une structure orthorhombique identique à celle de l'iode "massif". Un cas intéressant illustré par la fig.2.4f est la présence probable de tubes large mais aplatis, dont le processus d'aplatissement a créé deux canaux longitudinaux latéraux qui se sont remplis d'iode. Ces images montrent aussi que la configuration de l'iode peut varier considérablement avec le diamètre intérieur du CNT hôte.

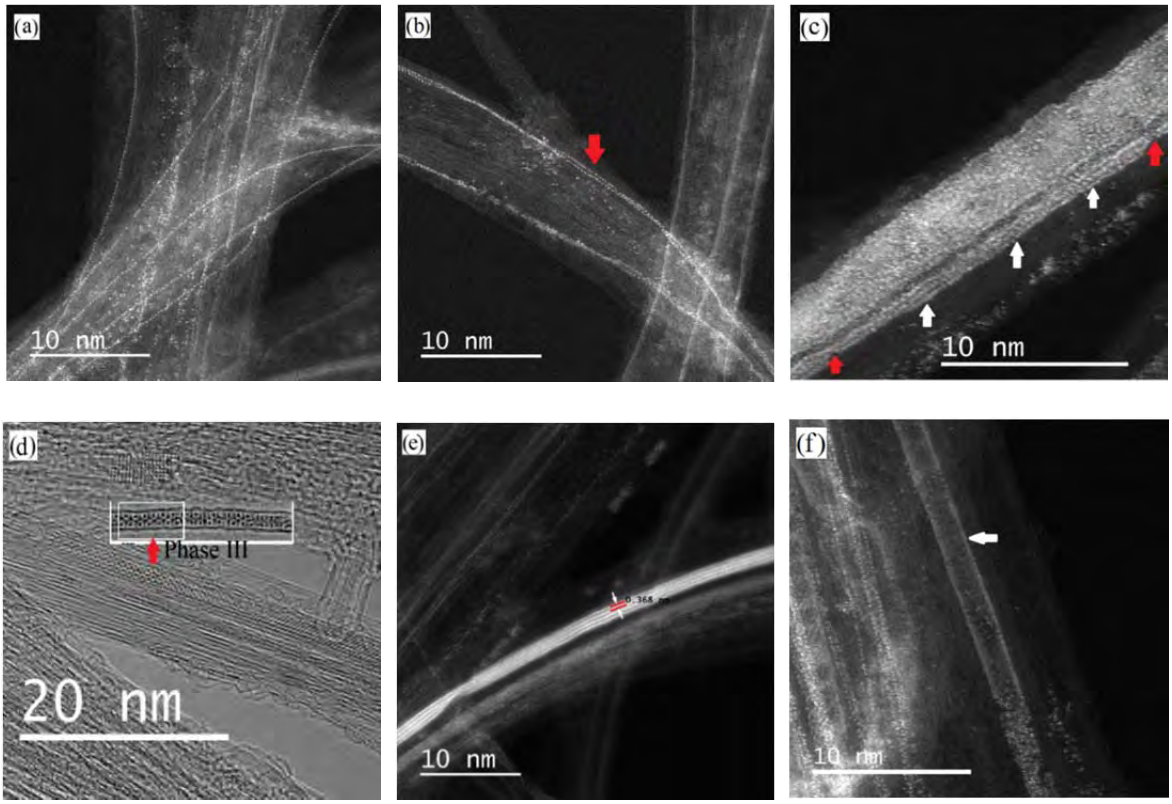

Fig. 2.4 - images en mode ADF (STEM à 200 kV) montrant (a) plusieurs chaînes d'iode seul, (b) des doubles chaînes d'iode hélicoïdales, (flèches), (c) une triple hélice de chaînes d'iode (les deux nœuds des chaînes sont indiqués par des flèches rouges, la configuration des chaînes triples peut être observée clairement dans les régions marquées de flèches blanches), (e) cristaux d'iode avec la structure orthorhombique et (f) des nanotubes larges probablement aplatis et dont les deux canaux latéraux résultant sont remplis d'iode (flèches blanches) ; (d) image HRTEM (200 kV) montrant une phase ordonnée de l'iode présent dans l'échantillon NiI_2*@DWNT. Cette phase ressemble à la structure de Phase III pour l'iode proposée par Guan et al [4] qui est illustrée dans les encarts.*

2.5 Mécanismes de remplissage

2.5.1 Influence des propriétés physiques et chimiques sur le taux de remplissage

Une série d'iodures métalliques ont été classés selon leur taux de remplissage, comme indiqué dans le tableau 2.1. Les paramètres physico-chimiques comme la tension superficielle, la viscosité, les points de fusion et d'ébullition et la pression de vapeur des composés de remplissage ont été recueillis dans la littérature [5, 6] et sont également répertoriés dans le tableau 2.1. Aucun d'entre eux ne permet d'établir de façon évidente une corrélation avec le classement sur la base du taux de remplissage.

La réactivité chimique a donc été également considérée comme un possible facteur pertinent, puisque la première étape du remplissage est forcément l'ouverture des CNTs. Le potentiel redox du couple iodure métallique / métal a été choisi comme paramètre pour en rendre compte puisque l'ouverture des CNTs pourrait se faire par réaction avec l'iode provenant de la décomposition de l'iodure. Les potentiels redox calculés des différents composés de remplissage sont reportés dans le tableau 2.1 et conduisent à un autre classement, dont les valeurs sont listées par ordre décroissant dans la dernière colonne afin de faciliter la comparaison avec le classement basé sur les taux de remplissage.

Tableau 2.1 : Taux de remplissage estimés et propriétés des matériaux de remplissage. Ceux-ci sont répertoriés selon leur taux de remplissage. La colonne de droite indique le classement selon la valeur du potentiel redox.

Matériau de remplissage	Taux de remplissage estimé (%)	Point de fusion (°C)	Point d'ébullition (°C)	Tension de surface[a] (mJ/m^2)	Viscosité[a] (mN.s/m^2)	Tension de vapeur[a] (Pa)	Potentiel redox[b] (V) et classement
NiI_2	51±5	797	n.a.	54	n.a.	26400	-0.002 *1*
AgI	38±5	558	1506	171	3.58	0.2	-0.526 *6*
SnI_2	34±5	320	714	43	n.a.	31.8	-0.358 *4*
PbI_2	32±5	402	953	50	n.a.	22.7	-0.489 *5*
FeI_2	27±5	587	827	71	n.a.	320	-0.298 *3*
CdI_2	22±5	387	742	47	17.7	91.5	-0.638 *7*
CoI_2	14±5	520	570	53	n.a.	8.8	-0.139 *2*
LiI	<1	469	1171	94	2.12	0.1	-2.414 *8*
KI	<1	681	1330	70	1.6	35.4	-2.749 *9*
I_2	27±5	113.7	184.3	37	n.a.	1094	0.000

[a] *Toutes les valeurs s'entendent à la temperature de fusion du matériau de remplissage.*

[b] *Pour le couple [iodure métallique / métal], quand cela est nécessaire , E_{I_2/I^-} est fixé à 0V puisqu'utilisé comme couple de référence pour les calculs.*

n.a. = non disponible

De cette comparaison, il apparaît que les deux classements sont en assez bon accord, avec toutefois quelques anomalies, dont AgI et CoI_2. Ce résultat montre donc une bonne corrélation entre le taux de remplissage et le potentiel redox du couple iodure métallique / métal. Cette corrélation peut être en lien avec la nécessité de premièrement ouvrir les tubes pour que le remplissage par effet capillaire puisse se produire. Par conséquent, nous proposons que la capacité du composé de remplissage à ouvrir les CNTs est primordiale, étant donné que nos DWCNTs sont initialement fermés. D'une certaine manière, et considérant aussi que les halogénures fondus sont censés être des liquides ioniques, le potentiel d’oxydoréduction peut être considéré comme un indicateur de la réactivité des halogénures métalliques vis-à-vis du carbone.

En ce qui concerne l’anomalie observée pour AgI, dont le taux de remplissage était le deuxième plus élevé alors que le potentiel redox est classé $6^{ème}$, elle peut s'expliquer par la forte tension de surface de AgI qui favorise le remplissage capillaire pour ce composé parmi les autres iodures. CoI_2 représente la seconde anomalie car il a été classé n°7 selon le taux de remplissage, mais n°2 en termes de potentiel d’oxydoréduction. Ce désaccord a été attribué à la forte propension des CoI_2 à se dimériser avant même que le point de fusion n'ait été atteint, si l'on fait l'hypothèse que la dimérisation est préjudiciable à l’ouverture, et donc au remplissage, et contribue peut-être aussi à diminuer la réactivité.

2.5.2 Influence des propriétés du CNT hôte sur le taux de remplissage

Grâce à notre sélection de nanotubes, les paramètres qui peuvent être discutés sont : 1) le nombre de parois (de 1 à plus de 10) ; 2) le diamètre intérieur (de 0,5 à 70 nm) ; 3) la nature chimique de la paroi du tube intérieur (carbone ou BN) ; 4) l'énergie de surface de la surface interne du tubes hôte (pour ce dernier paramètre, aucune valeur n'est indiquée puisque nous n'avons pas eu accès à des mesures expérimentales).

En comparant les taux de remplissage estimés avec PbI_2 pour divers types de CNT hôte comme indiqué dans le tableau 2.2, le classement suivant est obtenu :

$$PbI_2@SWCNT = PbI_2@DWCNT > PbI_2@FWCNT > PbI_2@h\text{-}MWCNT > PbI_2@c\text{-}MWCNT\text{-}a$$

Tableau 2.2: Taux de remplissage estimés obtenus pour PbI_2@CNTs, PbI_2@BNNTs et NiI_2@BNNTs, ainsi que quelques caractéristiques des nanotubes utilisés

Echantillon	*PbI_2@ SWCNT*	*PbI_2@ DWCNT*	*PbI_2@ FWCNT*	*PbI_2@ c-MWCNTs-a*	*PbI_2@ h-MWCNT*	*PbI_2@ BNNTs*	*NiI_2@ BNNTs*
Taux de remplissage mesuré (%)	32±5	32±5	25±5	<1	20±5	<1	0
Nombre de parois	1	2	2-6	> 10	N. A.	2-4	2-4
Domaine de diamètre interne	1.35 nm	1-2 nm	1.5-3.5 nm	2-10 nm	50-70 nm	1.2-3 nm	1.2-3 nm

La discussion (section 2.5.1) permet d'expliquer les meilleurs taux de remplissage observés pour

PbI_2@SWCNT, PbI_2@DWCNT et PbI_2@FWCNT par rapport à c-MWCNT-a par le fait que le faible nombre de parois facilite l'ouverture par l'halogénure fondu (les nanotubes c-MWCNTs-a sont restés fermés).

Cependant, comme la plupart des h-MWCNTs étaient naturellement ouverts à une extrémité, la question de la réactivité de l'iodure fondu vis-à-vis du carbone n'entre pas en ligne de compte et des taux de remplissage significatifs sont observés. La question de savoir pourquoi le taux de remplissage ne dépasse pas 20% reste ouverte. Ceci pourrait s'expliquer par l'équation de Jurin : $h = \frac{2\gamma cos\theta}{rg\rho}$ qui montre qu'un grand diamètre intérieur de CNT devrait défavoriser une grande longueur de remplissage - contrairement aux CNTs de petit diamètre - ce qui revient à une efficacité moindre de remplissage. Toutefois, étant donné que h n'a pu être calculée en raison du manque de données nécessaires, il est possible que le taux de remplissage attendu aurait dû être inférieur à 20 % dans le cas particulier des larges valeurs de diamètre intérieur des h-MWCNTs. Dans ce cas, le taux de remplissage relativement élevé pourrait être dû à l'énergie de surface, qui est plus élevée pour les h-MWCNTs que pour les DWCNTs et FWCNTs étant donné que la surface intérieure des premiers est principalement composée de graphène présentant de nombreuses liaisons pendantes. Cette incertitude concernant quel paramètre prévaut sur le taux de remplissage entre les énergies de surface ou le diamètre du tube intérieur pourrait avoir été écartée en considérant les c-MWCNTs-a, à condition que ces derniers n'aient pas été ouverts. Cependant, des c- MWCNTs naturellement ouverts de grand diamètre ne sont pas faciles à obtenir, et soumettre des c-MWCNTs de grand diamètre à un traitement chimique pour les ouvrir conduit à des modifications qui sont susceptibles de rendre les expériences non comparables.

Une incertitude semblable demeure aussi dans le cas des nanotubes de nitrure de bore (BNNT). D'une part le fait que PbI_2 n'a pas rempli ces derniers pourrait provenir de la mauvaise réactivité de PbI_2 avec le nitrure de bore, rendant impossible l'ouverture des BNNTs, ou encore de la faible énergie de surface du BN par rapport au graphène [7]. D'autre part le fait que les BNNTs ont été fortement détruits lors des essais de remplissage par NiI_2 au lieu de PbI_2 pourrait s'expliquer par la forte réactivité de BN avec les espèces de l'iode libérées par la décomposition de NiI_2, avec la possible libération de triiodure de bore.

2.6 Conclusions

Dans ce chapitre, divers halogénures métalliques (métaux, métaux alcalins et métaux de transition) ainsi que de l'iode ont été introduits avec succès dans des DWCNTs (principalement) en utilisant la méthode de la phase fondue, ou occasionnellement par la méthode en phase gaz (pour l'iode). Nous avons mis en évidence des structures particulières pour NiI_2 et l'iode encapsulés, en comparaison avec leurs équivalents macroscopiques. En outre, l'influence de diverses caractéristiques des CNTs ainsi que des propriétés chimiques et physiques les plus pertinentes des matériaux sur le taux de remplissage a été étudiée. Nous avons constaté que : 1) pour divers types de CNTs remplis de PbI_2, les CNTs de plus petits diamètres sont les mieux remplis ; 2) dans la série des iodures métalliques, le taux de remplissage peut être principalement lié au potentiel redox du couple iodure métallique / métal. D'autres paramètres tels que la formation de dimères, la tension superficielle ou la libération anticipée d'iode (comme dans le cas de NiI_2) peuvent également jouer un rôle complémentaire dans le processus de remplissage.

Références

[1] E. Dujardin, T. Ebbesen, H. Hiura, K. Tanigaki, Capillarity and wetting of carbon nanotubes, Science, 265 (1994) 1850-1852.

[2] P.-G. De Gennes, F. Brochard-Wyart, D. Quéré, Capillarity and wetting phenomena: drops, bubbles, pearls, waves, Springer Science & Business Media, 2013.

[3] M. Monthioux, E. Flahaut, J.-P. Cleuziou, Hybrid carbon nanotubes: strategy, progress, and perspectives, Journal of materials research, 21 (2006) 2774-2793.

[4] L. Guan, K. Suenaga, Z. Shi, Z. Gu, S. Iijima, Polymorphic structures of iodine and their phase transition in confined nanospace, Nano letters, 7 (2007) 1532-1535.

[5] F. Aqra, Surface tension of molten metal halide salts, Journal of Molecular Liquids, 200 (2014) 120-121.

[6] G.J. Janz, Thermodynamic and transport properties for molten salts: correlation equations for critically evaluated density, surface tension, electrical conductance, and viscosity data, Amer Inst of Physics, 1988.

[7] D. Golberg, Y. Bando, C. Tang, C. Zhi, Boron nitride nanotubes, Advanced Materials, 19 (2007) 2413-2432.

Chapitre 3 *Chimie* **in situ** *des hybrides X@DWCNTs*

3.1 Introduction

Une des limitations de la méthode "sels fondus" est qu'elle ne permet généralement pas d'insérer dans les CNTs des matériaux de très haut point de fusion (typiquement >1000°C), comme par exemple de nombreux oxydes, la plupart des fluorures, sulfures, et un bon nombre de métaux. Cependant, la synthèse de nanostructures 1D de tels matériaux représente souvent un intérêt tout particulier. Dans ce cas, la stratégie consiste alors à insérer un précurseur, qui sera ensuite transformé *in situ* pour générer le matériau désiré. Dans le chapitre 3, nos travaux de sulfuration *in situ* de PbI_2@DWCNT pour obtenir PbS@DWCNT et la réduction *in situ* de FeI_2@DWCNT et de NiI_2@DWCNT pour obtenir respectivement Fe@DWCNT et Ni@DWCNT sont présentés, ainsi que nos essais de fluoration de FeI_2@DWCNT dans le but d'obtenir FeF_2@DWCNT (collaboration LMI Clermont Ferrand). De nombreuses méthodes de caractérisations sont employées pour s'assurer que la transformation souhaitée a bien eu lieu (MET, EELS, X-EDS, DRX, XPS).

3.2 Sulfuration *in situ* de PbI_2@DWNT

Nous avons souhaité utiliser la réaction de PbI_2 avec le soufre pour obtenir PbS et de l'iode (éliminé) pour obtenir des nanocristaux de PbS. Pour effectuer la sulfuration, une ampoule contenant le mélange de poudres de soufre et de PbI_2@DWCNTs est scellée sous vide puis chauffée dans un four avec une inclinaison de 10 à 250 °C pendant 72 h puis refroidie naturellement à température ambiante. Le soufre en excès a été lavé par du toluène à 60° C pendant 10 min.

Afin de vérifier si la sulfuration a réussi, l'échantillon (supposé être) PbS@DWNT a été étudié par analyse EELS. Le spectre EELS (Fig. 3. 1b) obtenu au niveau de faisceaux de NTC encapsulant des nanocristaux (Fig. 3. 1a) a permis d'identifier la présence de soufre et d’iode. Toutefois, la présence de plomb est difficile à détecter par EELS en raison de son énergie d’ionisation trop élevée. Des analyses XPS complémentaires ont donc été réalisées. Les résultats XPS montrent que la concentration atomique du soufre dans l’échantillon de PbS@DWCNTs est beaucoup plus élevée que celle du plomb et de l’iode, ce qui indique que les CNTs ont été légèrement dopés avec le soufre suite à l’étape de sulfuration, alors que la synthèse de nanocristaux de PbS n’a pas réussi.

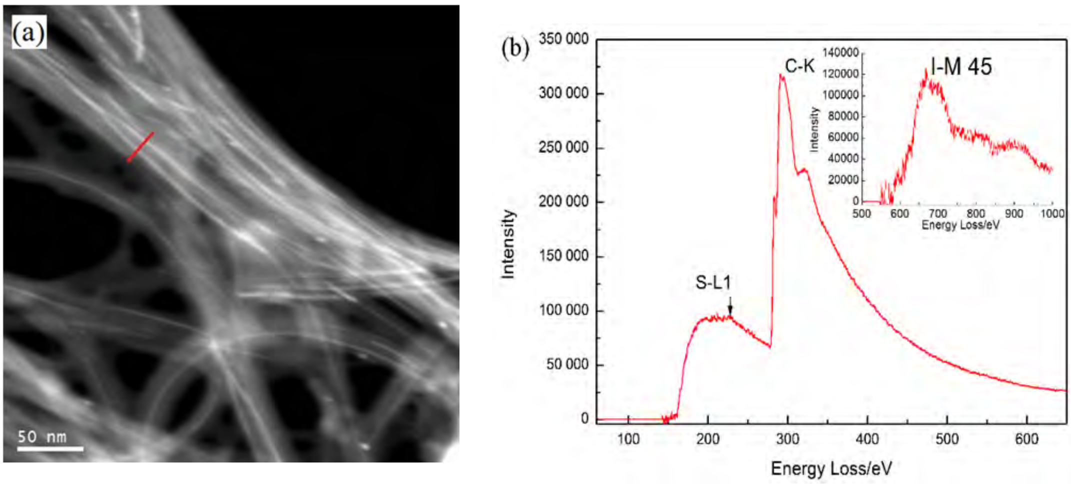

Fig. 3.1 – (a) images HAADF (FEI Tecnai-F20 équipé d’un détecteur HAADF) des faisceaux de NTC susceptibles de contenir des nanocristaux de PbS@DWNT et (b) spectre EELS obtenu en additionnant les spectres collectés le long de la ligne rouge tracée en (a).

La comparaison entre les spectres S 2p de PbS@DWCNT (Fig. 3.2b) et du soufre "massif" [1] (α-S_8; l’allotrope du soufre le plus stable, voir encart de la Fig. 3.2b) suggère que les atomes de soufre sont liés aux CNTs et non pas existants comme des molécules de soufre libre. L’échec de l’obtention des cristaux de PbS est attribué à la diffusion lente du soufre ainsi qu'à la lente cinétique de la réaction entre PbI_2 et S à l'intérieur des CNTs (une expérience de contrôle effectuée avec PbI_2 et S en poudres (hors CNTs) dans les mêmes conditions expérimentales a bien conduit à la synthèse de PbS). Nous avons donc obtenu un dopage des CNTs par le soufre mais pas de preuve évidente de la présence de PbS (qui est certainement tout de même présent mais en très faible proportion).

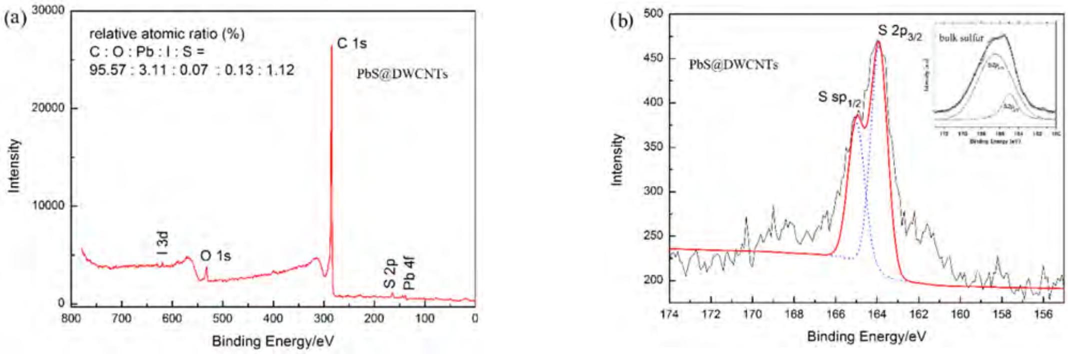

Figure 3.2 - (a) spectre XPS global de PbS@DWNT (b) spectres XPS S 2p de PbS@DWNT, et du soufre "massif" en encart (S 2p) [1].

3.3 Réduction *in situ par* H_2

Nous avons choisi d'utiliser l'hydrogène gazeux comme agent réducteur. Sur le principe, la réduction des nanocristaux de FeI_2 ou NiI_2 encapsulés doit conduire à des nanocristaux de Fe ou Ni, et à la libération d'acide iodhydrique (HI). La réduction est réalisée dans un four horizontal sous atmosphère de H_2 (débit de 5L/h). Nous avons exploré différentes conditions expérimentales pour optimiser la synthèse de ces nanocristaux métalliques : le four a été chauffé à 400° C ou 500° C pendant 24 heures, et les échantillons réduits obtenus ont été notés Fe@DWCNT_400_24, Fe@DWCNT_500_24, Ni@DWCNT_400_24 et enfin Ni@DWCNT_500_24.

3.3.1. Réduction in situ de FeI_2@DWCNT

Tous les échantillons réduits ont été étudiés par METHR et analyse EELS et à titre de comparaison, la proportion de nanocristaux de Fe est plus élevée pour le traitement effectué à la plus haute température (Fe@DWNT_500_24).

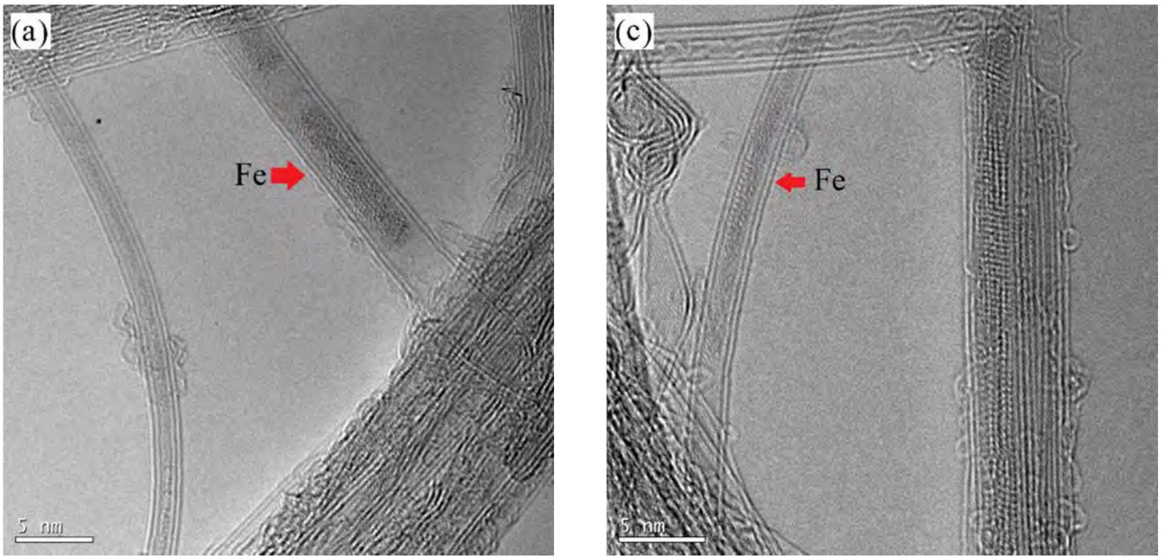

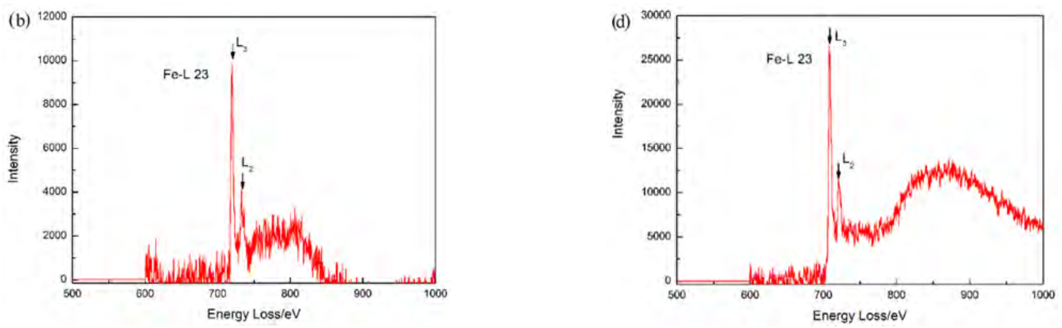

Fig. 3.3 - images HRTEM de (a) un nanocristal de Fe encapsulé dans Fe@DWNT_400_24 et (c) un nanocristal de Fe encapsulé dans Fe@DWNT_500_24; (b) et (d) spectres EELS provenant des nanocristaux de Fe montrés dans les images HRTEM correspondantes.

3.3.2. Réduction In situ de NiI_2@DWCNT

Des nanocristaux de Ni (identifiés par les spectres EELS) sont observés dans les échantillons réduits et la même observation que dans le cas du fer d'une quantité plus importante dans l'échantillons réduit à la plus haute température (500°C) est faite. La Fig. 3.4 montre des images HRTEM et spectres EELS de nanocristaux de Ni encapsulés dans les échantillons Ni@DWCNT_400_24 et Ni@DWCNT_500_24. Ici aussi, la réduction n'est que partielle et il faut noter que NiI_2 est encore présent dans tous les échantillons réduits, ce qui s'explique toujours par la même raison.

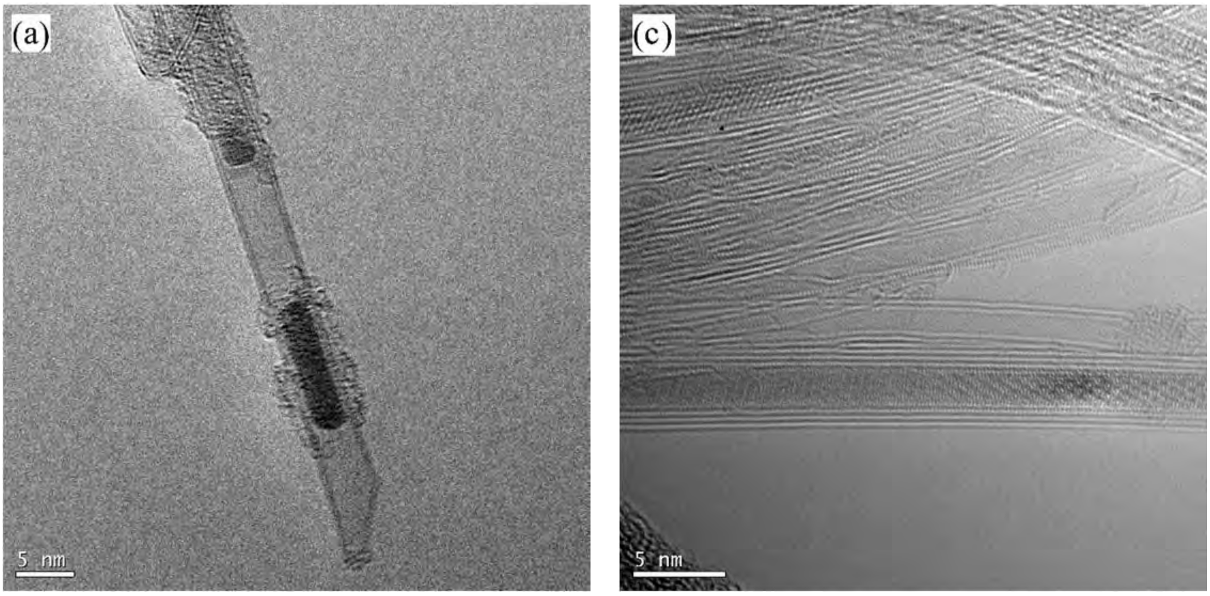

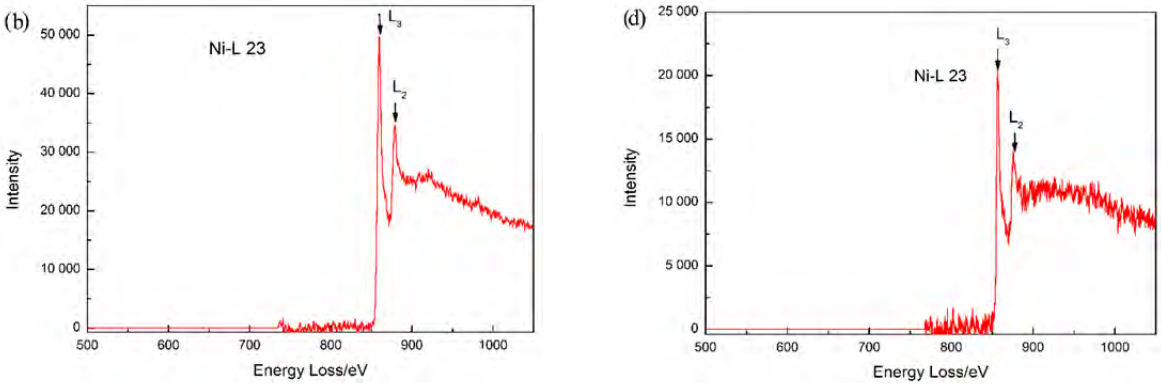

Fig. 3.4 - images HRTEM de (a) un nanocristal de Ni encapsulé dans Ni@DWCNT_400_24 et (c) un nanocristal de Ni encapsulé dans Ni@DWCNT_500_24; (b) et (d) spectres EELS provenant des nanocristaux de Ni montrés dans les images HRTEM correspondantes.

3.4 Fluoration *in situ*

Pour obtenir des nanocristaux de FeF_3 dans des DWCNTs, la fluoration *in situ* de nanocristaux de FeI_2 encapsulés dans des CNTs représente une voie attractive. Une des problématiques concerne la réactivité des CNTs vis-à-vis du fluor et donc la difficulté à fluorer le contenu des CNTs sans fluorer les CNTs eux-mêmes. Ces travaux ont été réalisés grâce à la une collaboration de longue date avec l'Institut de Chimie de Clermont-Ferrand (ICCF, UMR 6296) [K. Guerin, M. Dubois] et le travail de doctorat de Lea Doubtsof. Une méthode possible pour transformer FeI_2 en FeF_3 sans endommager les CNTs a donc été proposée. Il est intéressant de noter que les DWCNTs sont de bons candidats pour cette expérience de fluoration *in situ* car leur température de fluoration est relativement élevée (200 - 300° C) [2].

L'échantillon utilisé pour la fluoration a été préparé en remplissant des DWCNTs purifiés avec FeI_2 (FeI_2@DWCNT-p). Les DWCNTs purifiés ont été obtenus par chauffage sous air de DWCNTs bruts à 550° C pendant 30 min, puis lavage dans une solution de HCl pour éliminer les résidus d'oxyde métallique (CoO) générés lors de l'étape précédente. L'échantillon FeI_2@DWCNT-p a été synthétisé selon les procédures décrites au chapitre 2. La réaction de fluoration impliquée dans ce travail peut être décrite comme suit :

FeI_2@DWNT-p + 13/2 F_2 → FeF_3@DWNT-p + $2Si_5$ (réaction 3.1)

Pour effectuer la fluoration, l'échantillon FeI_2@DWCNT-p a été chauffé à 50 °C dans un courant de fluor gazeux pendant 24h. Une perte de poids de 22 % après fluoration a été mesurée, en accord avec ce qui était prévu pour cette réaction.

Des images MET de DWCNTs purifiés (champ clair) et des images en champ sombre (ADF) des échantillons purifiés (FeI_2@DWCNT-p) et fluoré (FeF_3@DWCNT-p) sont montrées sur la figure 3.5.

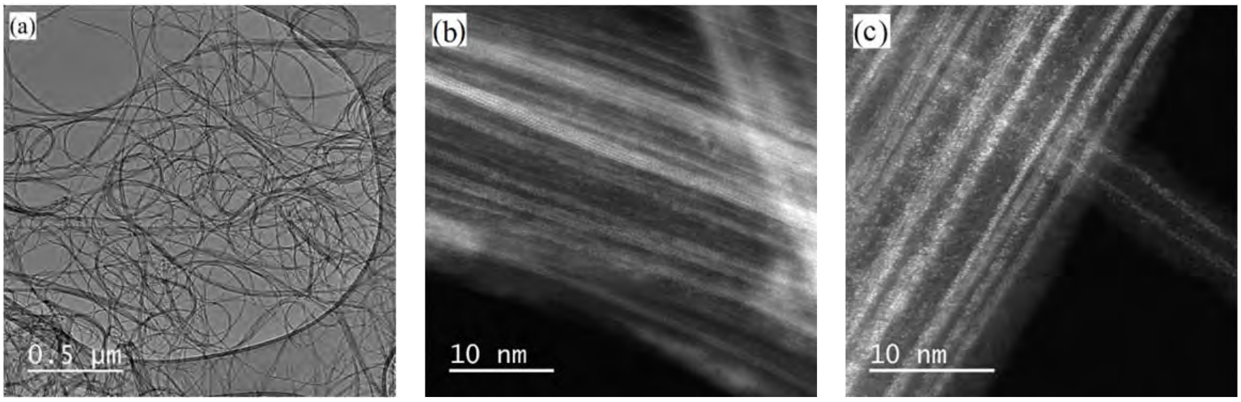

Fig. 3.5 - images MET (a) de DWCNTs purifiés, (b) FeI_2@DWCNT-p (ADF) montrant les nanocristaux encapsulés et (c) de FeF_3@DWNT-p ADF montrant les cristaux encapsulés.

On peut voir que les CNTs forment de gros faisceaux et que le carbone désorganisé présent dans les DWCNTs bruts est rarement observé dans les DWCNTs purifiés, indiquant que l'oxydation sous air est efficace pour purifier les CNTs. Les images en champ sombre montrent que les CNTs sont remplis de nanocristaux dans les deux cas, avant (FeI_2@DWCNT-p) et après (FeF_3@DWCNT-p) fluoration.

Pour vérifier si les nanocristaux de FeI_2 ont bien été transformés en FeF_3 après la fluoration, une analyse X-EDS est effectuée sur des échantillons FeI_2@DWCNT-p et FeF_3@DWCNT-p.

Les pics Fe-Kα I-Lα sont présents dans les spectres EDS obtenus dans des faisceaux de l'échantillon FeI_2@DWCNT-p (Fig. 3.6b), confirmant l'encapsulation de FeI_2 dans les CNTs. Les pics Fe Kα et F Kα sont aussi observés dans les spectres EDS provenant de gros faisceaux de nanotubes pour l'échantillon fluoré (FeF_3@DWCNT-p) (Fig. 3.6 d), ce qui implique la présence de FeF_3 après fluoration. Cependant, le pic I-Lα est toujours présent dans les spectres de FeF_3@DWCNT-p, impliquant que certains nanocristaux de FeI_2 encapsulés ne sont pas fluorés, ce que nous expliquons toujours par les mêmes raisons cinétiques.

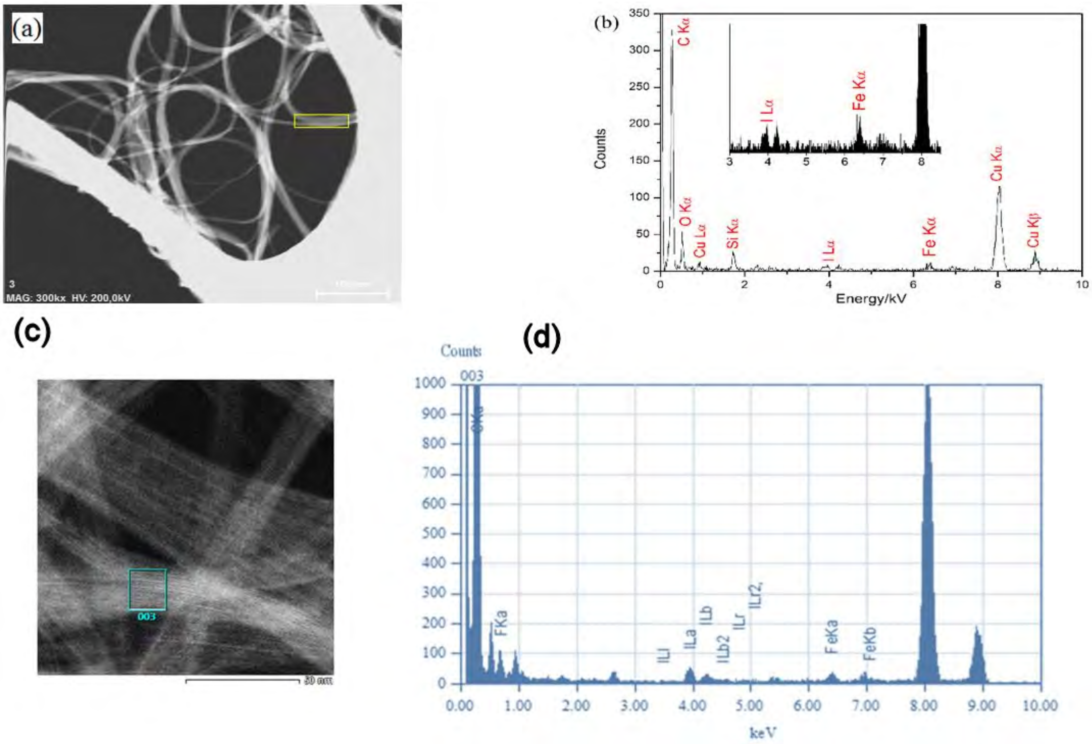

Figure 3.6 - (a) et (c) images STEM de FeI_2*@DWCNT-p et* FeF_3*@DWCNT-p ; (b) et (d) spectres EDS correspondant aux zones encadrées en (a) et (c). L'encart présenté en (b) est un spectre agrandi de la région de 3 à 8,5 kV montrant les pics de I et Fe.*

3.5 Conclusion

En résumé, diverses transformations *in situ*, y compris la sulfuration, la réduction et la fluoration d'hybrides (iodure métallique)@DWCNTs ont été effectuées. Que ces transformations aient été fructueuses (réduction par H_2 et fluoration) ou non (sulfuration), une conclusion générale est que la difficile progression des réactifs et des sous-produits de la réaction dans la cavité interne de CNTs d'aussi petit diamètre que des DWCNTs ralentit énormément la vitesse de la réaction. De ce fait, il est courant que le produit contienne finalement un mélange du produit initial et du produit désiré, ainsi qu'un cortège d'étapes intermédiaires.

References

[1] T. Fujimori, A. Morelos-Gomez, Z. Zhu, H. Muramatsu, R. Futamura, K. Urita, M. Terrones, T. Hayashi, M. Endo, S.Y. Hong, Y.C. Choi, D. Tomanek, K. Kaneko, Conducting linear chains of sulphur inside carbon nanotubes, Nat Commun, 4 (2013) 2162.

[2] K.D. Sattler, Carbon Nanomaterials Sourcebook: Graphene, Fullerenes, Nanotubes, and Nanodiamonds, CRC Press, 2016.

Conclusions générales et perspectives

Dans cette thèse, nous avons prouvé que le remplissage de DWCNTs par des halogénures métalliques et l'iode est une approche facile pour synthétiser diverses nanostructures 1D allant de nanofils d'iodures métalliques à différentes structures de l'iode atomique, du fait de l'effet de confinement dans la cavité interne des CNTs. En outre, nous avons également prouvé que cette même cavité interne peut être utilisée comme un nanoréacteur permettant des réactions chimiques *in situ*.

Une conclusion générale est que la **réactivité chimique** des matériaux de remplissage vis-à-vis du CNT, et en particulier des extrémités initialement fermées, joue un rôle essentiel dans le remplissage des CNTs. Nous avons montré dans le cas des iodures métalliques que le **potentiel d’oxydoréduction** du couple iodure métallique / métal peut être utilisé pour comparer une série de composés d'une même famille (ici les iodures) et même de procéder à un classement des taux de remplissage qui peuvent être attendus. Il resterait à démontrer la validité générale de cette approche en s'intéressant à d'autres familles (par exemple, les chlorures métalliques, ou encore les halogénures d'un métal donné) mais il faut bien garder à l'esprit que le travail de caractérisation à mener est très lourd. En ce qui concerne le **nombre de parois** son augmentation conduit sans trop de surprises à rendre le remplissage plus difficile. Finalement, la **stabilité thermique** (vue sous l'ange de l'**énergie libre de Gibbs**) du matériau de remplissage joue aussi un rôle important puisque le remplissage apparaît d'autant plus difficile que la stabilité du composé est grande. Bien entendu, d'autres paramètres tels que la viscosité, la pression de vapeur saturante, la mouillabilité, seraient très importants à prendre en compte de façon plus détaillée, et certains (tension de surface, énergie des surface) ont d'ailleurs été considérés ici pour expliquer des variations de détails. Mais ces données sont souvent absentes de la littérature, en particulier à la température des sels fondus, ce qui rend la tâche plus difficile qu'il pourrait sembler initialement.

Nous avons mis en évidence dans le cas de l'iode que la source utilisée (iode fondu ou gazeux, ou encore iode provenant de la décomposition d'un iodure (NiI_2 en particulier) joue aussi un rôle considérable sur l'organisation de cet élément dans les CNTs avec des structures allant de simples chaînes atomiques linéaires à des chaînes hélicoïdales jumelles ou triplées ou encore des structures cristallines similaires au matériau massif, ou au contraire très différentes. Ceci ouvre donc des perspectives intéressantes pour la synthèse préférentielle de telle ou telle structure. Enfin, un cas particulier et encore jamais vu dans la littérature a été mis en évidence, qui est la présence probable de tubes larges aplatis en rubans dont les bords forment des canaux longitudinaux qui se sont remplis d'iode. Le choix de l'une ou l'autre des configurations de l'iode est induit par la valeur du diamètre interne de chaque nanotube concerné.

Diverses transformations *in situ* telles que la sulfuration, la réduction et la fluoration d'hybrides iodure métallique@DWCNT ont été effectuées. Que ces transformations aient été fructueuses (réduction par H_2 et fluoration) ou non (sulfuration), la difficile progression des réactifs et des sous-produits de la réaction dans la cavité interne de CNTs d'aussi petits diamètres que des DWCNTs ralentit énormément la vitesse de la réaction. Une transformation totale est probablement possible au prix d'un allongement considérable de la durée du traitement.

Notre travail au cours des trois dernières années a donné un nouvel éclairage sur les mécanismes impliqués lors du remplissage de CNTs par la méthode des sels fondus et a fourni quelques pistes pour la synthèse de nanocristaux métalliques 1D tout en démontrant l’inefficacité de certaines autres. Afin de mieux comprendre les mécanismes de remplissage, travailler à la fois sur d'autres composés et sur d'autres CNTs de diamètre variable serait utile afin d'accumuler davantage de données et de mieux prendre en compte ce paramètre. La difficulté essentielle que nous avons rencontrée en quittant le domaine familier des DWCNTs est de trouver des sources fiables d'échantillons de CNTs dont il serait possible de ne faire varier idéalement qu'une seule caractéristique (le diamètre par exemple).

L'étude des propriétés physiques des hybrides que nous avons préparés, que ce soit à titre individuel ou collectif (poudres, "buckypapers", *etc.*) serait très intéressante. En effet, on peut s'attendre, que ce soit au niveau électrique ou magnétique, à des modifications importantes des propriétés des nanocristaux du fait de la différence importante de structure par rapport au matériau macroscopique. En cas de transfert de charge avec les CNTs, ce sont des modifications des propriétés des CNTs qui peuvent être attendues, et il se pourrait que certains des matériaux hybrides préparés au cours de ces travaux présentent des comportements tout à fait originaux. La plupart des caractérisations décrites dans les perspectives sont actuellement en cours avec différents collaborateurs, mais les résultats, encore inconnus au moment de la rédaction de cette conclusion, n'ont malheureusement pas pu figurer dans le manuscrit.

Publications:

1. *The unexpected complexity of filling double-wall carbon nanotubes with iodine-based 1D nanocrystals*
   Chunyang Nie, Anne-Marie Galibert, Brigitte Soula, Emmanuel Flahaut, Jeremy Sloan, Marc Monthioux.
   IEEE-TNANO Special Issue (submitted)
2. *Importance of Structural Integrity of Carbon Conjugated Mediator for Photocatalytic Hydrogen Generation from Water over CdS-Carbon Nanotube-MoS_2 Composite.*
   Molly Meng-Jung Li, Poppy Mills, Simon M. Fairclough, Alex Robertson, Yung-Kang Peng, Jamie Warner, Chunyang Nie, Emmanuel Flahaut, Shik Chi Edman Tsang.
   Angewandte Chemie (submitted)
3. *The unexpected complexity of filling double-wall carbon nanotubes with iodine-based 1D nanocrystals*
   Chunyang Nie, Anne-Marie Galibert, Brigitte Soula, Emmanuel Flahaut, Jeremy Sloan, Marc Monthioux.
   IEEE-NMDC International conference, Toulouse (France), 9-12 October, 2016, Extend. Abstr. *accepted*.
4. *A new insight on the mechanisms of filling closed carbon nanotubes with molten metal iodides*
   Chunyang Nie, Anne-Marie Galibert, Brigitte Soula, Emmanuel Flahaut, Jeremy Sloan, Marc Monthioux.
   Carbon, 110 (2016) 48

Oral presentations in Conference

1. *Evidences for the unexpected filling of double-wall carbon nanotubes with iodine nanocrystals*
   C. Nie, T. Michel, M. Paillet, A.M. Gilbert, B. Soula, L. Datas, S. Joulié, E. Flahaut, M. Monthioux.
   Hetero NanoCarb 2015, Benasque (Spain), 07-11 December, 2015, Oral
2. *De la complexité du remplissage de nanotubes de carbone biparois par des iodures métalliques*
   C. Nie, A.M. Galibert, B. Soula, L. Datas, J. Sloan, M. Monthioux, E. Flahaut.
   SFEC-Colloque annuel 2016, Carqueiranne (France), 17-20 May, 2016.

Title of the thesis:

"The investigation of 1D nanocrystals confined in carbon nanotubes"

Abstract:

Filling carbon nanotubes (CNTs) has been considered as an easy approach to synthesize various nanocrystals since the inserted materials are forced to adopt a nearly one-dimensional morphology arising from their very high aspect ratio, especially in the case of single-walled CNTs (SWCNTs) or double-walled CNTs (DWCNTs). Nanocrystals/nanowires of transition metals, especially those with very narrow diameters, are predicted to exhibit peculiar magnetic property differing from the bulk metals. Filling CNTs provides a possible way for the synthesis of such metal nanocrystals/nanowires.

There are several methods for filling CNTs including the *in situ* method, gas phase method, molten phase method, solution method, *etc.* Among them, molten phase has been very popular for filling various types of nanotubes due to the possibility to reach high filling rates, simplicity and versatility. However, for materials with high melting point such as metals, it is difficult to insert them into CNTs directly. To solve this problem, we also took advantage of the inner cavity of CNTs which not only templates the growth but also acts as a nanoreactor in order to perform chemical reactions. The insertion of materials with high melting point is typically achieved by first filling CNTs with a precursor, and then transforming the precursor into the desired 1D nanostructure by post-treatments.

In this thesis, (i) filling DWCNTs with iodine and various halides via the molten phase method was performed and the influence of the relevant physical and chemical properties of the halides on the filling rate was investigated. The role of the redox potential as a main parameter driving the filling efficiency is pointed out, and explained; (ii) peculiar structures of the nanocrystals confined within DWCNTs were imaged by transmission electron microscopy (TEM) and corresponding modeling of the observed crystal nanostructures and related TEM images were proposed; (iii) different in situ transformations on the iodide-filled DWCNTs were attempted and the chemical composition of the encapsulated 1D nanocrystals before and after post-filling treatments was systematically identified by means of electron energy loss spectroscopy (EELS).

Key words:

Double-walled carbon nanotubes (DWCNTs), filling, hybrid nanomaterials, 1D nanocrystals, *in situ* transformation, transmission electron microscopy (TEM), energy loss electron spectroscopy (EELS)

Titre de la thèse:

"Etude de nanocristaux unidimensionnels confinés dans des nanotubes de carbone"

Résumé:

Le remplissage des nanotubes de carbone (NTC) est considéré comme une approche relativement simple permettant de synthétiser des nanocristaux du fait de l'effet de confinement 1D imposé par la cavité centrale des NTC, qui peut être seulement de l'ordre du nanomètre ou moins, notamment dans le cas des NTC monoparoi et en particulier des NTC biparois (DWCNT) sur lesquels nous avons concentré nos efforts. De tels nanocristaux devraient avoir des propriétés physiques (électriques, magnétiques) différentes de celles de leurs équivalents à l'état massif du fait de la modification de la coordinence des atomes ou des ions les composant.

Parmi les différentes méthodes existantes pour le remplissage des NTC, (*in situ* pendant la synthèse, *a posteriori* à partir de solutions), la méthode faisant intervenir des matériaux fondus est la plus populaire pour le remplissage par des matériaux inorganiques. Elle permet en effet d'atteindre des taux de remplissage raisonnablement élevés et demeure assez simple à mettre en œuvre. Cependant, elle fait preuve d'un certain nombre de limitations (techniques) qui posent problème dans le cas de matériaux à haut point de fusion (typiquement > 1000°C), dont la réactivité avec le carbone à haute température pourrait être gênante (carboréduction des oxydes par exemples), ou encore dont la faible mouillabilité vis-à-vis du carbone à l'état fondu est rédhibitoire (métaux par exemple). Il est possible de palier à cette difficulté en procédant par étapes successives et en remplissant d'abord les NTC avec un précurseur puis d'utiliser la cavité interne des NTC comme des nanoréacteurs afin de procéder dans un second temps à une transformation *in situ*.

Dans ces travaux, nous avons étudié (1) le remplissage de DWCNT avec de l'iode ainsi qu'avec différents iodures métalliques en mettant en œuvre essentiellement la méthode des sels fondus. Nous avons étudié en détails l'influence des paramètres physico-chimiques du matériau de remplissage (réactivité chimique sous la forme en particulier du potentiel rédox du couple iodure métallique / métal, mais aussi viscosité, tension de surface, pression de vapeur saturante en milieu fondu) mais aussi du NTC (texture cylindrique ou "en arrêtes de poisson", diamètre, nombre de parois) sur le taux de remplissage. (2) Nous avons étudié en détail un certain nombre de structures inhabituelles de nanomatériaux confinés dans les DWCNT, en faisant appel à la modélisation structurale et à la simulation d'images de microscopie électronique sur la base de ces modèles pour guider notre analyse. (3) Nous avons enfin étudié différentes réactions *in situ* dans les DWCNT telles que la sulfuration, la réduction sous hydrogène ou encore la fluoration afin de synthétiser des nanocristaux originaux et de les caractériser en détails à l'aide d'outils tels que par exemple le MET Haute Résolution et la spectroscopie de perte d'énergie des électrons (EELS).

Mots-clés:

Nanotubes de carbone biparois, remplissage, nanomatériaux hybrides, nanocristaux 1D, transformation *in situ*, microscopie électronique par transmission (MET), spectroscopie de perte d'énergie des électrons (EELS)